Technical Report
TR-21-02
December 2022

Post-closure safety for the final repository for spent nuclear fuel at Forsmark

Fuel and canister process report, PSAR version

SVENSK KÄRNBRÄNSLEHANTERING AB

SWEDISH NUCLEAR FUEL
AND WASTE MANAGEMENT CO

Box 3091, SE-169 03 Solna
Phone +46 8 459 84 00
skb.se

ISSN 1404-0344
SKB TR-21-02
ID 1872567
December 2022

Post-closure safety for the final repository for spent nuclear fuel at Forsmark

Fuel and canister process report, PSAR version

Svensk Kärnbränslehantering AB

This report is published on www.skb.se

Contents

1 Introduction

1.1 Role of this process report in the PSAR

1.1.1 Overall methodology

This report documents fuel and canister processes identified as relevant to the long-term safety of a KBS-3 repository. It forms an important part of the PSAR for a final repository at the Forsmark site.[1] The report is an update of the Fuel and canister process report for the safety assessment SR-Site (SKB 2010a). The extent of the update is described in some detail in Section 1.1.5. The detailed assessment methodology, including the role of the process reports in the assessment, is described in Chapter 2 of the PSAR Post-closure safety report (SKB 2022a). The following excerpts describe the methodology and clarify the role of this process report in the assessment.

The repository system broadly defined as the deposited spent nuclear fuel, the engineered barriers surrounding it, the host rock, and the biosphere in the proximity of the repository will evolve over time. Future states of the system will depend on:

- the initial state of the system,
- a number of radiation related, thermal, hydraulic, mechanical, chemical and biological processes acting within the repository system over time, and
- external influences acting on the system.

A previously established methodology in eleven steps has been applied in the PSAR as summarised in Figure 1-1 and described below.

1. Identification of factors to consider (FEP processing).

   This step consists of identifying all the factors that need to be included in the analysis. Experience from earlier safety assessments and KBS-3 specific and international databases of relevant features, events and processes (FEPs) influencing long-term safety are utilised. An SKB FEP database is developed in which the great majority of FEPs are classified as being either initial state FEPs, internal processes or external FEPs. Remaining FEPs are either related to assessment methodology in general or deemed irrelevant for the KBS-3 concept. Based on the results of the FEP processing, an FEP catalogue, containing FEPs to be handled in the safety assessment, has been established. Within the PSAR work, an evaluation was made of the international developments as regards FEPs since the reporting of SR-Site and of review comments on SR-Site. These efforts led to the conclusion that the SR-Site version of the FEP database and the FEP report are adequate also for the PSAR, with a minor modification regarding the canister. See further section 1.1.2 below, Chapter 3 of the PSAR Post-closure safety report (SKB 2022a) and the FEP report (SKB 2010b).

2. Description of the initial state.

   The initial state of the system is described based on the design specifications of the KBS-3 repository, a descriptive model of the repository site and a site-specific layout of the repository. The initial state of the fuel and the engineered components is that immediately after deposition, as summarised in Chapter 5 of the PSAR Post-closure safety report (SKB 2022a). The initial state of the geosphere and the biosphere is that of the natural system prior to excavation as described in the site descriptive model supporting the PSAR, see further Chapter 4 of the PSAR Post-closure safety report (SKB 2022a).

3. Description of external conditions.

   Factors related to external conditions are handled in the categories “climate related issues”, “large-scale geological processes and effects” and “future human actions”. The handling of climate related issues is described in the PSAR Climate report (SKB 2020), whereas the few external, large-scale geosphere processes are addressed in the PSAR Geosphere process report (SKB 2022c). The treatment of future human actions (FHA) is described in the FHA report (SKB 2010c).

[1] The present report is published some time before the submission of the PSAR. In case the need for any changes of the contents of this report arises between its publication and the submission of the PSAR, a report of these changes will be provided in the PSAR.

4. Compilation of process reports.

   The identification of relevant processes is based on earlier assessments and FEP screening. All identified processes within the system boundary relevant to the long-term evolution of the system are described in dedicated Process reports, i.e. this report and process reports for the buffer, backfill and closure (SKB 2022b) and the geosphere (SKB 2022c). Also short-term geosphere processes/alterations due to repository excavation are included. For each process, its general characteristics, the time frame in which it is important, the other processes to which it is coupled, and how the process is handled in the safety assessment, are documented.

5. Definition of safety functions, function indicators and function indicator criteria.

   This step consists of an account of the safety functions of the system and of how they can be evaluated by means of a set of function indicators that are, in principle, measurable or calculable properties of the system. Criteria for the safety function indicators are provided. The Process reports are important references for this step. A FEP chart is developed, showing how FEPs are related to the function indicators.

6. Compilation of input data.

   Data to be used in the quantification of repository evolution and in dose calculations are selected. The process of selection and the data adopted are reported in a dedicated Data report (SKB 2022d). Also, a template for discussion of input data uncertainties has been developed and applied.

7. Definition and analysis of reference evolution.

   A reference evolution, providing a description of a plausible evolution of the repository system, is defined and analysed. The isolation potential of the system over time is analysed, yielding a description of the general system evolution and an evaluation of the safety function indicators. Each process is handled in accordance with the plans outlined in the process reports. Radiological consequences of potential canister failures are not analysed in this step.

8. Selection of scenarios.

   A set of scenarios for the assessment is selected. A comprehensive main scenario is defined in accordance with SSM's regulations SSMFS 2008:21. The main scenario is closely related to the reference evolution analysed in step 7. The selection of additional scenarios is focused on the safety functions of the repository, and the safety function indicators defined in step 4 form an important basis for the selection. For each safety function, an assessment is made as to whether any reasonable situation where it is not maintained can be identified. If this is the case, the corresponding scenario is included in the risk evaluation for the repository, with the overall risk determined by a summation over such scenarios. The set of selected scenarios also includes scenarios explicitly mentioned in applicable regulations; e.g., human intrusion scenarios, and scenarios and variants to explore design issues and the roles of various components in the repository.

9. Analysis of scenarios.

   The main scenario is analysed essentially by referring to the reference evolution in step 7, complemented by consequence calculations for potential canister failures in the reference evolution yielding a calculated risk contribution from the main scenario. The additional scenarios are analysed by focusing on the factors potentially leading to situations in which the safety function in question is not maintained. In most cases, these analyses are carried out by comparison with the evolution for the main scenario, meaning that they only encompass aspects of repository evolution for which the scenario in question differs from the main one. If the scenario leads to canister failures, consequence calculations are carried out. If the likelihood of the scenario is non-negligible, a risk contribution is also calculated.

10. Additional analyses.

    In this step, a number of additional analyses, required to complete the safety assessment, are carried out. These comprise:

    - The selection and analysis of FHA scenarios, including a brief description of the methodology for the selection.
    - Analyses required to demonstrate optimisation and use of best available technique.

- Verification that FEPs omitted in earlier parts of the assessment are negligible in light of the completed scenario and risk analysis.
- A brief account of the time period beyond one million years.
- Natural analogues.

11. Conclusions.

    This step includes integration of the results from the various scenario analyses, development of conclusions regarding safety in relation to acceptance criteria and feedback concerning design, continued site investigations, and the R&D programme.

This fuel and canister process report is one of the process reports required to complete step 4. The purpose of the process reports is to document the scientific knowledge of the processes to a level required for their adequate treatment in the safety assessment. The documentation is not exhaustive from a scientific point of view, since such a treatment is neither necessary for the purposes of the safety assessment nor possible within the scope of an assessment. However, it must be sufficiently detailed to facilitate, by arguments founded on scientific understanding, the treatment of each process in the safety assessment. The purpose is to determine how to handle each process in the safety assessment at an appropriate degree of detail, and to demonstrate how uncertainties are taken care of, given the suggested handling. The handlings established in this report are used in the analysis of the reference evolution, step 7, and in the analyses of scenarios, step 9.

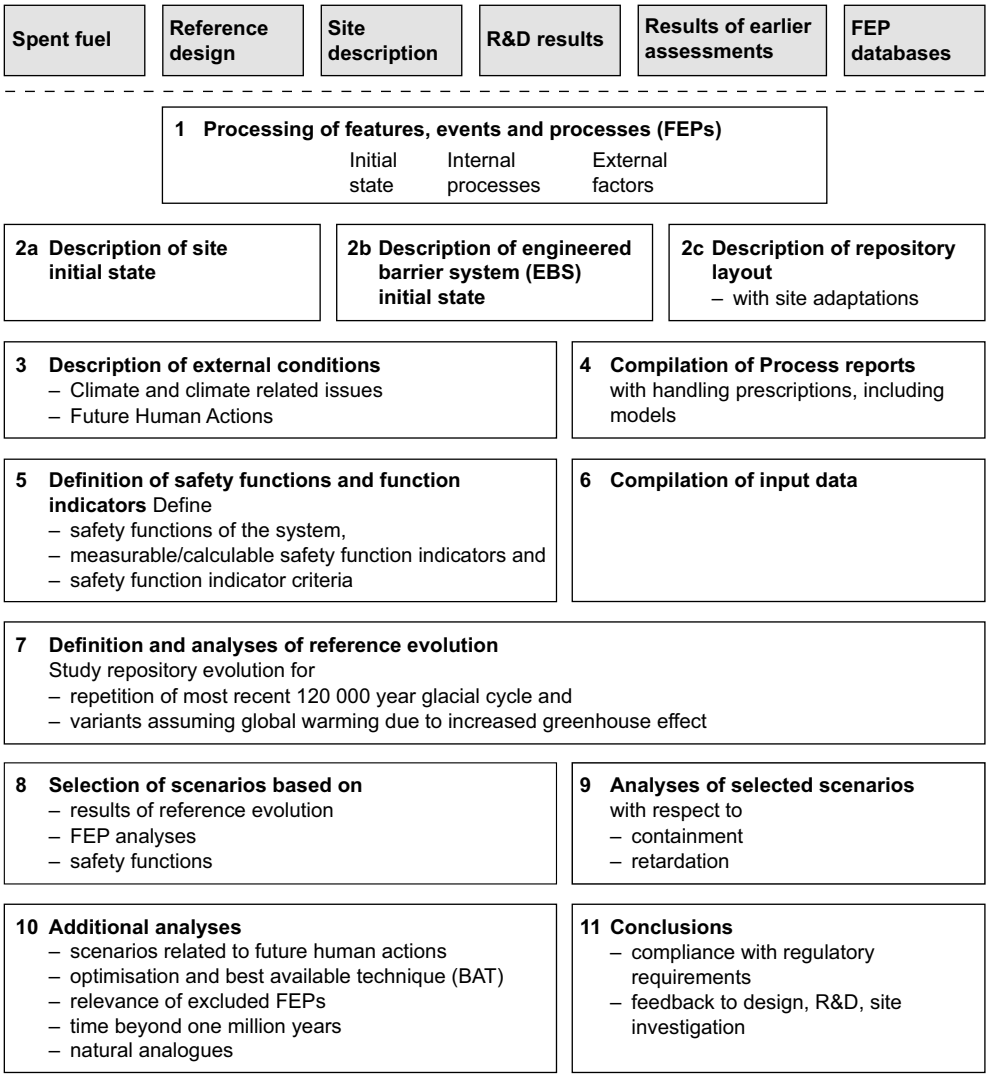

Figure 1-1. *An outline of the eleven main steps of the analysis of post-closure safety in the PSAR. The boxes at the top above the dashed line are inputs to the assessment.*

1.1.2 Identification of processes

The process documentation in this PSAR version of the process report is an update of the descriptions in the SR-Site version (SKB 2010a) and the FEP processing carried out for the previous analyses. In the current assessment, PSAR, no need to modify the list of relevant processes that were included in the SR-Site version of the process report was identified, with one exception: The process "Hydrogen embrittlement of copper canister" has been added to the list of relevant process, see further Chapter 3 of the Post-closure safety report (SKB 2022a).

1.1.3 Relation to specific sites

The PSAR builds on site-specific data and site-descriptive models of the Forsmark site, i.e. the location of the repository facility to which the PSAR applies. The result of the quantitative evaluations of the processes in the different scenarios analysed in the PSAR will, in many cases, be dependent on site-specific data. These data are not given here, but in dedicated model studies. In addition, the most essential data for the safety assessment are thoroughly evaluated in the PSAR Data report (SKB 2022d), step 6 above.

1.1.4 Intended audience for this report

This report is written by, and for, experts in the relevant scientific fields. It should though be possible for a generalist in the area of long-term safety assessments of geologic nuclear waste repositories to comprehend the contents of the report. The report is an important part of the PSAR, providing a scientifically motivated plan for the handling of fuel and canister processes. It is, furthermore, foreseen that the report will be essential for reviewers scrutinising the handling of fuel and canister issues in the PSAR.

1.1.5 Extent of update of the SR-Site Fuel and canister process report

As mentioned above, the present report is an update of the Fuel and canister process report for the safety assessment SR-Site (SKB 2010a). The update is based on requests during the review of SR-Site and on additional findings from SKB's RD&D programme. The general, introductory Sections 1.1 and 1.2 have been updated to reflect the context of the PSAR. The extent of the update of factual information in the remainder of the report is described in Table 1-1.

Table 1-1. Update of factual content relative to the SR-Site version of this report.

Section		Update relative to SR-Site version
1.3	Initial state of the fuel in PSAR	Updated to reflect parts of Chapter 5 in the PSAR Post-closure safety report (SKB 2022a) and new knowledge on radionuclide distribution in the fuel.
1.4	Definition of fuel variables	Only editorial changes.
1.5	Summary of handling of fuel processes in the PSAR	Minor updates to reflect the updated contents of this report.
1.6	Initial state of the canister in the PSAR	Updated to reflect parts of Chapter 5 in the PSAR Post-closure safety report (SKB 2022a).
1.7	Canister performance and safety	Updated to reflect added safety indicator criteria regarding creep in copper and hydrogen embrittlement.
1.8	Definition of canister variables	Minor updates to reflect the updated contents of this report.
1.9	Summary of handling of canister processes in the PSAR	Minor updates to reflect the updated contents of this report.
Fuel processes		
2.1.1	Radioactive decay	Minor update regarding uncertainty of half-life of Se-79, otherwise only editorial changes.
2.1.2	Radiation attenuation/heat generation	Minor updates based on few references, otherwise only editorial changes.
2.1.3	Induced fission (criticality)	Generally updated based on several new references.
2.2.1	Heat transport	Only editorial changes.
2.3.1	Water and gas transport in the canister, boiling/condensation	Minor updates of evolution of failed canister based on Agrenius and Spahiu (2016), otherwise only editorial changes.

Section	Update relative to SR-Site version
2.4.1 Mechanical cladding failure	Updated based on new references as regards delayed hydride cracking (DHC), otherwise only editorial changes.
2.4.2 Structural evolution of the fuel matrix	Only editorial changes.
2.5.1 Advection and diffusion	Minor updates of evolution of failed canister based on Agrenius and Spahiu (2016) and Johansson et al. (2017) otherwise only editorial changes.
2.5.2 Residual gas radiolysis/acid formation	Updated based on new references regarding gas radiolysis.
2.5.3 Water radiolysis	The discussion of the effect of hydrogen on homogeneous alpha radiolysis has been extended based essentially on the findings by Bauhn et al. (2017), otherwise only editorial changes.
2.5.4 Metal corrosion	Updated with new references on metal corrosion in general and on corrosion of Ag in control rods in particular. Updated handling of Ag-108m in the safety assessment.
2.5.5 Fuel dissolution	Updated discussion based on previously available and new experimental data. The handling in the PSAR is essentially the same as that in SR-Site, with the only difference concerning the dissolution rate of a small amount of oxidized fuel matrix in fuel with failed cladding.
2.5.6 Dissolution of the gap inventory	Updated based on several new references.
2.5.7 Speciation of radionuclides, colloid formation	Updated based on several new references. Description of handling of the process and its associated uncertainties in the safety assessment unaltered but clarified.
2.5.8 Helium production	Minor update based on additional information by Lilja (2012a) and a model study by Valls et al. (2014), otherwise only editorial changes.
2.5.9 Chemical alteration of the fuel matrix	Updated based on several new references. The handling in the PSAR is essentially the same as that in SR-Site.
2.6 Radionuclide transport	Only editorial changes.
Canister processes	
3.1.1 Radiation attenuation/heat generation	Minor update based on Renström (2020b) and Jansson et al. (2022).
3.2.1 Heat transport	Minor updates based on Renström (2020a), Ikonen et al. (2018) and Ikonen (2020).
3.4.1 Introduction	Minor updates, mostly editorial.
3.4.2 Deformation of cast iron insert	Updated based on several new references the most important being Jonsson et al. (2018).
3.4.3 Deformation of copper shell from external pressure	Updated based on several new references the most important being Jonsson et al. (2018).
3.4.4 Thermal expansion	Minor update, based mainly on Lilja (2012b).
3.4.5 Deformation from internal corrosion products	Minor update based on additional information from Smart et al. (2012) and Gordon et al. (2017), otherwise only editorial changes.
3.4.6 Radiation effects	Updated based on several new references. The handling in the PSAR is essentially the same as that in SR-Site.
3.4.7 Hydrogen embrittlement of copper	Now included as a separate process.
3.5.1 Corrosion of cast iron insert	Updated mainly with a paragraph on microbially induced corrosion. The handling in the PSAR is the same as that in SR-Site.
3.5.2 Galvanic corrosion	Only editorial changes.
3.5.3 Stress corrosion cracking of cast iron insert	Updated to replace text outdated already to SR-Site (referring to EB welds), with mainly one new reference (Reynaud 2009).
3.5.4 Corrosion of copper canister	Updated based on many new references.
3.5.5 Stress corrosion cracking of the copper canister	Updated based on several new references.
3.5.6 Earth currents – stray current corrosion	Updated based on mainly the analysis in Taxén et al. (2014).
3.5.7 Deposition of salts on the canister surface	Updated based on a few new references. The handling in the PSAR is essentially the same as that in SR-Site.

1.2 Structure for process descriptions

All identified processes are documented using a template, adopted, with minor modifications, from the SR-Site version of the report. The template is described below. The calculations for some of the analysed corrosion processes are described in more detail in Appendix A. The parameter notation and data used in calculations in this report are listed in Appendix B.

Overview/general description

Under this heading, a general description of the knowledge regarding the process is given.

Dependencies between process and fuel and canister variables

For each system component, in this case the fuel and canister systems, a set of physical variables that defines the state of the system is specified. For each process, a table is presented under this heading with documentation of how the process is influenced by the specified set of physical variables and how the process influences the variables. In addition, the handling of each influence in the PSAR is indicated in the table.

Boundary conditions

The boundary conditions for each process are discussed. These refer to the boundaries of the fuel and canister systems, respectively. The processes for which boundary conditions need to be described are, in general, related to transport of material or energy across the boundaries.

Model studies/experimental studies

Model and experimental studies of the process are summarised. This documentation constitutes the major source of information for many of the processes.

Natural analogues/observations in nature

If relevant, natural analogues and/or observations in nature that contribute to the present understanding of the process are documented under this heading.

Time perspective

The timescale or timescales on which the process occurs are documented, if such timescales can be defined.

Handling in the PSAR

Under this heading, the handling in the PSAR is described. Typically, the process is either

- neglected on the basis of the information under the previous headings, or
- included by means of modelling.

The following aspects need to be covered, although no prescribed format for the documentation is given:

Boundary conditions: The handling of boundary conditions is discussed, especially any spatial and temporally varying chemical and hydraulic conditions.

Influences and couplings to other processes: The handling of the documented influences will be discussed, as will couplings to other processes within the system component.

As a result of the information under this sub-heading, a mapping of all processes to method of treatment and, in relevant cases, applicable models will be produced for all processes.

Handling of uncertainties in the PSAR

Given the adopted handling in the PSAR, the handling of different types of uncertainties associated with the process is summarised.

Uncertainties in mechanistic understanding: The uncertainty in the general understanding of the process is discussed based on the available documentation and with the aim of addressing whether the basic scientific mechanisms governing the process are understood to the level necessary for the suggested handling.

Model simplification uncertainties: In most cases, the quantitative representation of a process will contain simplifications. These may be a significant source of uncertainty in the description of the system evolution. These uncertainties are discussed and approaches to addressing them are identified including alternative models or alternative approaches to simplification of a particular conceptual model.

Input data and data uncertainties: The set of input data necessary to quantify the process for the suggested handling is documented. The further treatment of important input data and input data uncertainties is described in a separate report, the PSAR Data report (SKB 2022d), to which reference is made when relevant.

References

A list of references used in the process documentation is given at the end of the report. In the SR-Site version of the report (SKB 2010a), each process also had the sub-heading "*Adequacy of the references supporting the handling in SR-Site*". Under that heading, statements were provided concerning the adequacy of the references in a quality assurance perspective, since some references were not qualified according to the requirements in the SR-Site QA plan. Some of those references are used also in the PSAR version, without repeating the qualification statement from the SR-Site assessment. All new references in the PSAR version are qualified according to the SKB management system, as specified in the PSAR QA plan. The mentioned sub-heading is thus obsolete and is not used in the PSAR version.

1.3 Initial state of the fuel in PSAR

The following is an overview description of the initial state of the fuel, i.e. its state at the time of deposition. Most of the information is taken from the Spent fuel report (SKB 2021a), which can be considered an update of a previous report (SKB 2010d).

1.3.1 General

This repository sub-system comprises the spent fuel and the cavity in the canister. The total quantity of spent fuel obtained from the Swedish nuclear reactors will depend on operating time, energy output and fuel burnup. The existing reactors in Sweden are light water reactors of both boiling water (BWR) and pressurized water (PWR) types. The fuel quantities presented here are based on SKB's scenario for the operation of the nuclear power plants. The maximum enrichment is set to 5 % and the burnup is limited to 60 MWd/kgU for the PWR and BWR uranium oxide (UOX) fuel and 50 MWd/kgHM for the BWR mixed uranium-plutonium oxide (MOX) fuel. It is assumed that the last reactor will be taken out of operation in 2045.

1.3.2 Fuel types

Several types of fuel will be emplaced in the repository. The major portion of the fuel to be deposited is UOX fuel from PWR and BWR reactors. There will also be small amounts (three used fuel elements) of BWR MOX fuel, spent heavy water reactor fuel from the decommissioned Ågesta reactor, and German MOX assemblies (from an exchange project involving reprocessing waste) as well as fuel residues from Studsvik. Since SR-Site, a decision has been taken that all fuel with failed cladding will be handled separately. Thus, special containers with failed fuel are also part of the full spent fuel inventory. The total amount of spent fuel and the total number of fuel elements are given in Table 1-2.

Differences between different fuel types are important for criticality assessments.

To allow for these quantities, the safety assessment assumes a total of 3 982 BWR canisters and 1 707 PWR canisters, in total 5 689 canisters with regular spent fuel corresponding to ca 13 000 tonnes of fuel. In addition there will be a small number of canisters with fuel residues and containers with failed fuel (ie fuel with failed cladding).

Table 1-2. Amount of spent fuel and number of fuel elements. From the Spent fuel report (SKB 2021a).

Fuel type	Number in interim storage (31 December 2015)	Total number for the assumed scenario (includes prognosis)	Total initial weight for the assumed scenario (tonnes of U or HM)
BWR assemblies (incl. 3 BWR MOX)	28 931	47 314	8 367.5
PWR assemblies	3 834	6 793	3 125
Fuel assemblies from Ågesta	222 (1 unirradiated)	222 (1 unirradiated)	20
Fuel residues in protection boxes from Studsvik	20	approximately 37	4
Swap MOX assemblies (BWR)	184	184	14.1
Swap MOX assemblies (PWR)	33	33	8.4

Burnups of regular fuel are expected to vary from about 15 MWd/kgU up to 60 MWd/kgU, with distributions as indicated in Table 1-3.

Table 1-3. Statistical data for burnup of Swedish spent fuel. From the Spent fuel report (SKB 2021a).

	Burnup (MWd/kgU)					
Fuel	Average	Median	1st Quartile	3rd Quartile	Min	Max
BWR produced	36.0	38.8	31.4	41.9	5.4	50.0
BWR prognosis	44.7	48.0	48.0	48.0	11.3	50.0
BWR total	39.4	41.5	34.6	48.0	5.4	50.0
PWR produced	42.6	44	40.1	46.6	14.3	57.8
PWR prognosis	49.9	52.4	50.8	53.5	17.0	56.2
PWR total	45.8	47.3	41.9	52.4	14.3	57.8

1.3.3 Structure of the fuel assemblies

Nuclear fuel, here exemplified by Svea 96 BWR fuel, consists of cylindrical pellets of uranium dioxide. The pellets are 11 mm high and have a diameter of 8 mm. They are stacked in approximately 4-metre-long cladding tubes of Zircaloy, a durable zirconium alloy. The tubes are sealed with welds and bundled together into fuel assemblies. Each assembly contains 96 cladding tubes. The fuel assembly also contains components made of the nickel alloys Inconel and Incoloy, and of stainless steel. Pellets in a cladding tube and a fuel assembly are shown in Figure 1-2. Aspects of importance in the safety assessment, for example the geometrical arrangements and dimensions of the fuel cladding tubes are, as a rule, handled sufficiently pessimistically in analyses of radionuclide release and transport that differences between different fuel types are irrelevant.

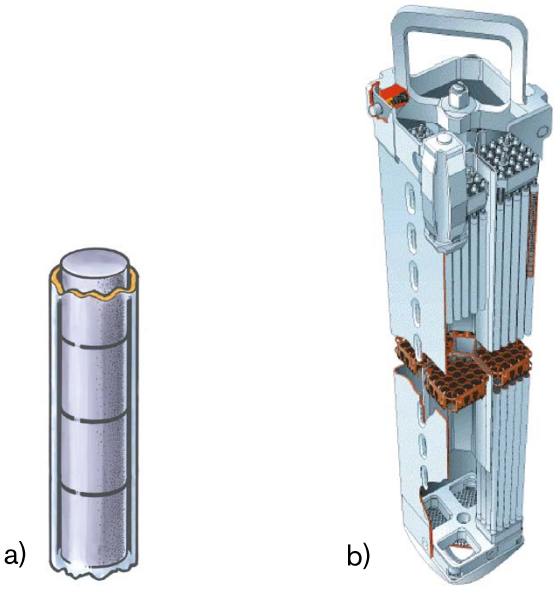

Figure 1-2. *a) Cylindrical fuel pellets in cladding tubes of Zircaloy. The pellets have a diameter of approximately one centimetre. b) Fuel assembly of type Svea 96. The assembly consists of 96 fuel tubes and has a height of approximately 4 metres.*

1.3.4 Description of fuel structure and radionuclide distribution in the structure

Fuel

The nuclear fuel consists of very nearly stoichiometric uranium dioxide in the form of cylindrical pellets. The size of the pellets varies between different fuel types, but is on the order of 1 cm in diameter and 1 cm in length. The grain size is normally in the range of a few µm to about ten µm. The uranium in the present fuel has been enriched in the isotope U-235 from the naturally occurring concentration of 0.7 % up to 3.6 % in BWR fuel (4.2 % in gadolinium-bearing fuel) and 4.46 % in PWR fuel. In the future, the enrichment will be increased to 5 %.

The fuel typically develops a power of 15 to 25 kW per metre of fuel rod during operation, which corresponds to a centre temperature in the fuel pellet of 800 to 1 200 °C. After use in the reactor, the fuel contains 2–6 % fission products, depending on the burnup, and approximately 1 % higher actinides formed by neutron capture and radioactive decay. The average burnup for Swedish nuclear fuel is currently (December 2015) 36 MWd/kgU for BWR fuel and 43 MWd/kgU for PWR fuel. Since the beginning of 1970, the burnup of nuclear fuel has gradually increased. The future average burnup of spent fuel to be deposited in the repository is estimated to 44.7MWd/kgU for BWR fuel and 49.9 MWd/kgU for PWR fuel (see Table 1-3).

The increase of the fuel burnup leads to the formation of the high burnup structure (HBS) in the outer region of the fuel pellet (rim), which consists of small grains of submicron size and a high concentration of pores, 1 to 2 micrometres in size. The rim thickness increases with burnup and at an average burnup of 50 MWd/kgU, it is ca. 50 µm thick. One of the primary driving forces behind HBS formation is the significantly higher burnup experienced by the pellet periphery due to Pu-239 build-up by neutron capture in U-238, followed by its fission (Rondinella and Wiss 2010).

The majority of the fission products and the higher actinides are present in solid solution within the uranium dioxide matrix. Besides the chemical alteration of the uranium dioxide this entails, the fuel has also been altered physically during operation in the reactor. For example, significant cracking has occurred.

Enrichment of radionuclides on the pellet surface

In the case of fuel that has been irradiated at a relatively low temperature, the radial variation in grain size and porosity is small, with moderate grain growth in the centre of the pellet. An exception to this rule is the sharp increase in porosity in the pellet rim. To a depth of a few μm on the rim of the pellet, the porosity is several times higher than inside the fuel. This rim zone also deviates in microstructure from the rest of the pellet in that the original grains have been subdivided into many smaller grains. The reason for this lies in local variations in the fission rate across the diameter of the fuel.

Self-shielding in the fuel leads to a radial variation in the frequency of U-235 fissions, but more importantly, increased formation and fission of plutonium isotopes, in the rim of the fuel pellet. The result is increased burnup and alpha activity at the periphery of the fuel pellets. The increased burnup is also accompanied by a higher content of fission products. This surface layer can have a burnup up to 2.5 times the average (Matzke and Spino 1997), as well as more than four times the average alpha activity (Forsyth 1995).

Radionuclides in the fuel-clad gap

During irradiation in the reactor, a fraction of the radionuclide inventory will have segregated either to the gap between the fuel and the cladding or to the grain boundaries in the fuel. Of these radionuclides, the behaviour of the fission gases is best known. A number of studies of fission gas release (FGR) have been published over the years. The behaviour of other potentially segregated radionuclides is far less well known. This is of concern because these radionuclides will be released more rapidly than the radionuclides that are embedded in the fuel's UO_2 matrix. The fractions of some of the radionuclides that are incompatible with the UO_2 matrix, and thus present in the fuel/cladding gap, are generally considered to be comparable to the fission gas release to the fuel/cladding gap as measured in gas release testing of fuel rods (Johnson and Tait 1997, Johnson and McGinnes 2002, Werme et al. 2004, Johnson et al. 2004, Ferry et al. 2008). This is due to the relatively high high diffusion coefficients for some of the volatile elements, such as I and Cs, at the elevated, in-reactor temperatures. At these temperatures, a fraction of these radionuclides will diffuse to the grain boundaries and then to gap, due to the expected similar behaviour as the fission gases (Johnson et al. 2012). Considering this, and since there are far more data available on fission gas release than on the release from the matrix of other radionuclides, it is of interest to discuss the fission gas release even though the fission gases are of little concern for a long-term safety assessment. Fission gas release is more strongly correlated to the linear power rating than to the burnup of the fuel (Kamimura 1992). Up to about the year 2000, the operating conditions were such that the linear power rating was kept relatively low and the fission gas release minimised. Up to a burnup of about 40 MWd/kgU, the fission gas releases are typically less than one percent (see e.g. Werme et al. 2004, Johnson et al. 2004). In SR-Can (SKB 2006), the fuel was assumed to have a burnup of 38 MWd/kgU. At that time, about 75 % of the Swedish fuel inventory had a burnup of less than 40 MWd/kgU and the number of fuel elements with an average burnup exceeding 50 MWd/kgU was very small. As of June 2005, only 45 fuel elements had a burnup exceeding 50 MWd/kgU. As of December 2015, the number had increased to ca 300. At the time of writing (2019) the number is 577.

It was previously observed, at the time of the SR-Site safety assessment, that for the interval 40 to 50 MWd/kgU, the fission gas release is generally below 1.5 % for PWR fuel, while for BWR fuel it can go as high as 5 % with an average in the range of 2.5 %. As was mentioned earlier, a high linear power rating is expected to increase the FGR. Now, some Swedish reactors have been uprated and as a consequence, the linear power rating is increased and higher FGR is expected. Therefore, for the SR-Site assessment, FGR was calculated for burnups up to 60 MWd/kgU for typical equilibrium cores for Swedish BWR (Oldberg 2009) and PWR reactors (Nordström 2009).

For the PSAR, more experimental data are available for fuels with a burnup above 50 MWd/kgU. Johnson et al. (2012) presents and discusses data from PWR fuel with burnups between ca 58 and 75 MWd/kgU. The measured fission gas releases of these fuels display a significant variation, with the highest values (ca 20 % or more) originating from fuel that had experienced a very high linear power rating (ca 300 W/cm). For other fuels, with a linear power rating between 200 and 230 W/cm, the fission gas release varies between ca 1 and 5 %. These data highlight the importance of the linear power rating in the determination of the FGR and, by extension, the so-called Instant Release Fraction (IRF) of some radionuclides. In the EU-project First Nuclides, both BWR and PWR fuels with high

burnup were studied (Lemmens et al. 2017). The PWR fuels had a burnup of 50–63 MWd/kgU and a linear power rating of 136–306 W/cm (both values rod average). The BWR fuels had a burnup of 42–59 MWd/kgU and a linear power rating of 143–217 W/cm (both values rod average). The PWR fuels had a measured FGR of 2–26 %, while the BWR values are lower, between 1.4 and 3.9 %. It should be noted that the higher PWR values are from a MOX fuel, while the lowest FGR value come from a Cr+Al-doped fuel. Two main conclusions from the First-Nuclides project are 1) that the IRFs of I and Cs are generally below the FGR-values, and 2) there is a positive correlation between the IRFs of I and Cs with linear power ratings above 200 W/cm (Lemmens et al. 2017).

There are relatively few systematic studies of the release of segregated radionuclides other than fission gases from fuel. Only one very comprehensive study has been published (Stroes-Gascoyne 1996). In that publication, the rapid releases of Cs-137, Sr-90, Tc-99, I-129 and C-14 from CANDU fuel were reported. For light water reactor (LWR) fuel, there were far less data available (see e.g. Forsyth and Werme 1992, Gray et al. 1992, Gray 1999, Johnson et al. 2004, 2005, Roudil et al. 2007), but the amount of available data has now increased (Johnson et al. 2012, Kienzler et al. 2017, Lemmens et al. 2017). The inventory of C-14 and Cl-36 in spent fuel originates from neutron activation of impurities (N, Cl), and a fraction of these are also found in the gap. Very few leaching data are available for Cl-36, but this very mobile radionuclide is expected to diffuse rapidly a gas in the reactor, and a large fraction is therefore expected to found in the gap. There is some leaching data for C-14 which is used to estimate the gap inventory (e.g. Johnson et al. 2005).

Based on these studies, it was apparent that the fission gas release and the rapid release of some segregated radionuclides are correlated. This seems to be true for most LWR fuel (Johnson and McGinnes 2002, Lemmens et al. 2017).

Thus, for some radionuclides such as Cs and I, the IRF can be determined based on a correlation with FGR, while for others such as Mo, Tc, Se the relationship seems to be more complex (Werme et al. 2004, Johnson et al. 2004). Mo and Tc are non-volatile at all fuel operating temperatures, so release from UO_2 doesn't occur through volatilisation, but through phase segregation. Therefore, additional leaching data from spent fuels are required to establish the IRF of some radionuclides. One radionuclide of special interest is Se-79. The leaching behaviour and the chemical state of Se in the UO_2 matrix were studied in the First Nuclides project. It was found that the observed very low fractional release of Se (e.g. Johnson et al. 2012) is likely due to the direct chemical bonding of Se to U atoms as a Se(II) (selenide) ion, probably replacing oxygen in the cubic UO_2 lattice (Curti et al. 2015).

As was mentioned by Curti et al. (2015), the calculation of oxygen potential can be used as a first means to evaluate the chemical state of fission products in spent nuclear fuel. This method was utilised by Curti and Kulik (2020) for conventional and Cr-doped UO_2 fuels. The results show that oxygen potentials in spent Cr-doped fuel are similar to conventional spent UO_2 fuels and thus indicates that the Cr-doping should not significantly affect the chemical state of fission products in the spent fuel.

Radionuclide segregation to grain boundaries

In addition to the release of gaseous fission products, other elements that are incompatible with the structure of the uranium dioxide are also segregated to form separate phases. Light water reactor fuel contains inclusions of metal alloys of Mo-Tc-Ru-Rh-Pd (4d metals), known as ε-phases. In standard LWR fuel with average burnup between 40 and 50 MWd/kgU, these particles can be up to micrometres in size and observable by optical microscopy (Forsyth 1995). The fraction of 4d metals, which Forsyth was able to determine by optical microscopy (particles larger than 0.5 μm), corresponded to only 1 % of their calculated total inventory in the fuel. By electron microscopy, it has been possible to determine that ε-phases also occur in the size range 1 to 100 nm (Thomas and Guenther 1989). When fuel is dissolved in nitric acid, the 4d metals form an insoluble residue. By analysing these residues, Forsyth concluded that at least 80 % of the residues consisted of ε-particles. The particle size distribution depends on the temperature at which the fuel operated and can, therefore, vary between fuel samples. A more recent and thorough description of the occurrence of the metal aggregates is given by Spahiu and Evins (2013).

Besides these known segregations, the possibility that other fission products have segregated to the grain boundaries in the uranium dioxide has been discussed. For CANDU fuel, which is irradiated with higher linear power density (20–55 kW/m) than light water reactor fuel, it has been established

by photoelectron spectroscopy that Cs, Rb, Te and Ba are present in the grain boundaries, often with high surface enrichments (Hocking et al. 1994). Gray et al. (1992) determined the grain boundary inventory of Cs in light water reactor fuel to be less than 1 %. The values of gap and grain boundary inventories for Tc and Sr were near their detection limits at less than 0.2 % of their total inventory. An Auger spectroscopy study on fuels with moderate burnup and low fission gas release showed no detectable amounts of Cs, Sr and Tc (Thomas et al. 1992). On a PWR fuel with extremely high fission gas release (18 %; equivalent fuel was also included in the study by Gray et al. (1992), ε-phases were found with high surface concentrations of Cs, Te and Pd (Thomas et al. 1992)). This observation was interpreted as indicating that Cs and other fission products are mainly associated with the ε-phases and, thereby only indirectly with the grain boundaries that contain them. However, considering the similar diffusion coefficients of I, Cs and fission gases, one could argue that fission gas bubbles found in grain boundaries also contain some I and Cs. The implications of this for the IRF is not yet clear since the pores appear to be closed (Roudil et al. 2007), and recent studies indicate a limited contribution from the grain boundaries on the IRF (Roth et al. 2019).

The question of Sr segregation and the differences between Sr and U release from spent fuel in leaching experiments at Studsvik has been discussed extensively. Werme and Forsyth (1988) offer the hypothesis that most of the Sr released comes from selective leaching of cracks and grain boundaries. Attempts have been made to determine grain boundary inventories by microprobe analysis in a fuel with a burnup of 37 MWd/kg U (linear power rating < 20 kW/m) that had been subjected to controlled power ramping to 43 kW/m in the Studsvik R2 reactor (Forsyth et al. 1988). The rod had an appreciable release of Kr and Xe, as well as redistribution of Cs to the fuel-clad gap during the power increase. Sharp concentration gradients within the individual grains could be observed for Xe and Cs, but not for Nd. In the case of Sr, the concentrations were far too close to the detection limit to yield reliable data. Subsequently, a fuel with a burnup of 44–48 MWd/kgU (linear power density < 15 kW/m), was subjected to a similar power ramping to a peak of 43 kW/m (Forsyth et al. 1994). In a corrosion experiment a significant increase, compared to the reference samples, in the release of Cs and Rb was observed, and some increase for Ba and Tc as well as possibly also for Mo. No significant redistribution of Sr was found. In a recent study of up to 5 years fuel leaching under aerobic conditions (Roth et al. 2019) the fractional release rates of Sr are about one order of magnitude higher than the U release rates, indicating that Sr originates not only from matrix dissolution, but also from leaching of segregated oxide phases (grey phases).

New data for Sr release indicates that, for BWR fuel with FGR between ca 1 and 5 %, less than 0.1 % of the Sr inventory is released during 1 year of leaching in aerated conditions (Zwicky et al. 2011, Roth 2015).

The studies presented above thus suggest that there is still some uncertainty concerning the significance of the grain boundary inventory of different radionuclides and that this likely relates to both type and irradiation history of the fuel.

More information regarding IRF values for radionuclides found in the gap and grain boundaries is given in the PSAR Data report (SKB 2022d).

1.4 Definition of fuel variables

The spent fuel is described by the variables in Table 1-4, which together characterise the spent fuel in a suitable manner for the safety assessment. The description applies not only to the spent fuel itself, but also to the cavities in the canister.

The fuel and the cavity in the canister are characterised with respect to radiation by the intensity of α, β, γ and neutron radiation and thermally by the temperature. Hydraulically, it is necessary to characterise the cavity only if the copper canister should be damaged and water should enter. The cavity is then characterised by water flows and water pressures as well as by gas flows and gas pressures, which are jointly termed hydro-variables. Mechanically, the fuel is characterised by stresses in the materials, and chemically by the material composition of the fuel matrix and metal parts, as well as by the radionuclide inventory. The gas composition and, if water enters the canister, the water composition are also relevant for the description.

Table 1-4 Variables for fuel/cavity in the canister.

Variable	Definition
Radiation intensity	Intensity of alpha, beta, gamma and neutron radiation as a function of time and space in the fuel assembly.
Temperature	Temperature as a function of time and space in the fuel assembly.
Hydro-variables (pressure and flow)	Flows, volumes and pressures of water and gas as a function of time and space in the cavities in the fuel and canister.
Fuel geometry	Geometric dimensions of all components of the fuel assembly, such as fuel pellets and Zircaloy cladding. Also includes the detailed geometry, including cracking, of the fuel pellets.
Mechanical stresses	Mechanical stresses as a function of time and space in the fuel assembly.
Radionuclide inventory	Occurrence of radionuclides as a function of time and space in the different parts of the fuel assembly. The distribution of the radionuclides between the pellet matrix and surface is also described here.
Material composition	The materials of which the different components in the fuel assembly are composed, excluding radionuclides.
Water composition	Composition of water (including any radionuclides and dissolved gases) in the fuel and canister cavities.
Gas composition	Composition of gas (including any radionuclides) in the fuel and canister cavities.

1.5 Summary of handling of fuel processes in the PSAR

Table 1-5 summaries the handling of fuel processes in the PSAR, as suggested in this report. In the table, the process is either “mapped” to a model by which it will be quantified or associated with a brief verbal description of how it will be handled.

1.6 Initial state of the canister in the PSAR

The following is an overview description of the initial state of the canister, i.e. its state at the time of deposition. Additional information is given in Pers and Sturek (2021).

1.6.1 Description of cast iron insert and copper canister

The disposal canister for the spent nuclear fuel consists of an outer 5 cm thick copper shell with an insert made from nodular cast iron. The copper shell will act as the corrosion barrier in the repository, while the insert will provide the necessary stability to the whole package when exposed to the different mechanical loads that it may encounter during the one million year time period considered in the safety assessment. The reference design and outer dimensions for the disposal canister are shown in Figure 1-3. As shown in the figure, the insert contains individual channels for each fuel element. For BWR fuel, there are 12 channels in each insert, while for PWR fuel there will be only 4 channels. Figure 1-4 shows the cross section of the BWR and PWR inserts respectively.

The copper in the canister shell is oxygen free phosphorus doped (Cu-OFP) and will fulfil the specifications in EN 1976:1988 for the grade Cu-OFE (UNS10100) with the following additional requirements: 30–100 wt.ppm phosphorus, < 0.6 wt.ppm hydrogen, < 12 wt.ppm sulfur and < 5 wt.ppm oxygen.

The material for nodular cast iron will fulfil the requirements in EN 1563:1997, grade EN-GJS-400-15U regarding mechanical properties. The materials composition is as specified in the old Swedish standard SS140717 since EN 1563 does not have a material specification. As additional requirements, the following have been specified: < 0.05 % Cu, < 6 % C, < 4 % Si and > 90 % Fe.

A summary of the weight for both the BWR and PWR versions of the canister is given in Table 1-6 (Pers and Sturek 2021).

Table 1-5. Process table for the fuel describing how fuel processes will be handled in different time frames and in the special case of failed canisters. Green fields denote processes that are neglected or irrelevant for the time period of concern. Red fields denote processes that are quantified by modelling in the safety assessment. Orange fields denote processes that are neglected subject to a specified condition.

Process	Intact canister	Failed canister
F1 Radioactive decay	Thermal model	COMP23
F2 Radiation attenuation/heat generation	Radiation attenuation: Initial radiation levels given in the SKB (2010d). Heat generation: Included in integrated modelling of thermal evolution.	Neglected when releases occur after period of elevated temperatures.
F3 Induced fission (criticality)	Neglected since there will be insufficient amounts of moderator inside the canister prior to failure.	Neglected since the probability is negligibly small if credit is taken for the burn-up of the fuel.
F4 Heat transport	Included in integrated modelling of thermal evolution.	Neglected when releases occur after period of elevated temperatures.
F5 Water and gas transport in canister cavity, boiling/ condensation	Not relevant	Description in Section 2.3.1, integrated with other relevant processes yielding simplified, pessimistic assumptions on retardation in failed canister depending on failure mode.
F6 Mechanical cladding failure	Not relevant	Pessimistic assumption
F7 Structural evolution of fuel matrix	Not relevant	Negligible for the fuel types and burn-up relevant for the PSAR.
F8 Advection and diffusion	Not relevant	Description in Section 2.3.1, integrated with other relevant processes yielding simplified, pessimistic assumptions on retardation in failed canister depending on failure mode.
F9 Residual gas radiolysis/acid formation	Neglected since only small amounts of corrodants are produced.	Not relevant
F10 Water radiolysis	Neglected	Neglected except for fuel dissolution, see that process.
F11 Metal corrosion	Not relevant	Modelled in COMP23
F12 Fuel dissolution	Not relevant	Modelled as constant, pessimistic dissolution rate in COMP23.
F13 Dissolution of gap inventory	Not relevant	Pessimistic, instantaneous
F14 Speciation of radionuclides, colloid formation	Not relevant	COMP23
F15 Helium production	Neglected since the amount of helium produced will not increase the pressure inside the canister enough to affect its mechanical stability.	Not relevant
F16 Chemical alteration of the fuel matrix	Not relevant	Neglected since it is not deemed to increase the dissolution rate of the fuel.
F17 Radionuclide transport	Not relevant	COMP23

Figure 1-3. *The reference design with a corrosion resistant outer copper shell and a load-bearing insert of nodular cast iron.*

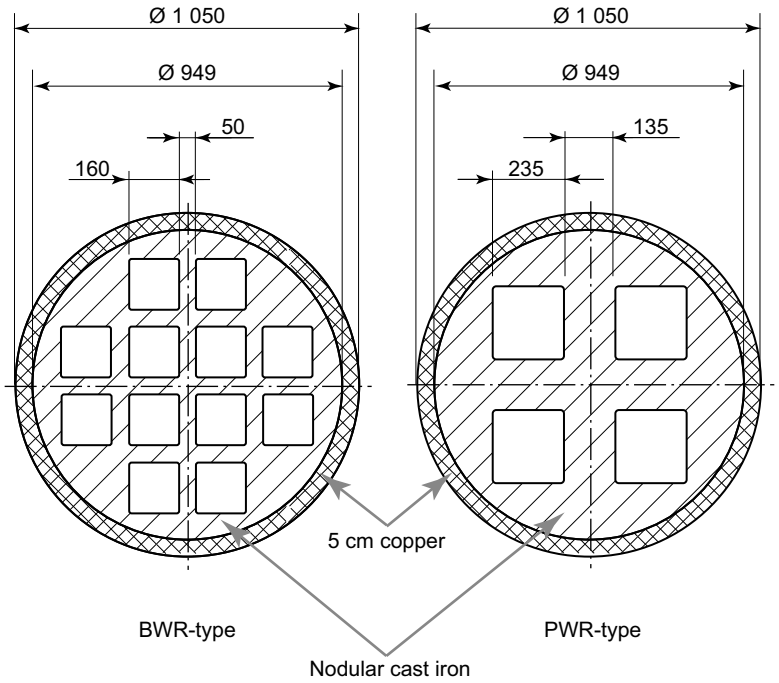

Figure 1-4. *Dimensions (in mm) of the cross section of the BWR and PWR inserts.*

Table 1-6. Weight of canisters.

	Weight (kg)	
	BWR-canister	**PWR-canister**
Insert with lid	13 700	16 400
Copper shell	7 500	7 500
Canister without fuel	21 200	23 900

1.7 Canister performance and safety

A safety function is defined qualitatively as a role through which a repository component contributes to safety. In order to evaluate the canister's performance in the safety assessment, a number of so-called function indicators and criteria that should be fulfilled over time, have been formulated. A safety function indicator is a measurable or calculable property of a repository component that indicates to what extent a safety function is fulfilled. The safety function indicator criterion is a quantitative limit such that if the corresponding function indicator fulfils the criterion, its safety function is fulfilled. For a more elaborate discussion, see the PSAR Post-closure safety report (SKB 2022a). A summary of the canister safety function indicators and safety function indicator criteria relating to the containment potential of the canister is presented in Table 1-7.

Table 1-7. Summary of canister safety function indicators and the criteria they should fulfil.

Function	Indicator and criterion	Rationale
Provide corrosion barrier	Copper thickness > 0	As long as the copper thickness is larger than zero, containment is complete and no releases occur.
Withstand isostatic load	Load < 50 MPa (requirement on buffer and rock). Copper shell resilient to creep deformation during isostatic load. Hydrogen content low.	The evaluation of the design and manufacturing procedures for the ensemble of deposited reference canisters led to the conclusion that the canisters will fulfil the design premise of withstanding an isostatic load of 50 MPa (Pers and Sturek 2021). The copper shell shall maintain its ductile properties for all relevant isostatic loads in the repository. No quantitative indicator is formulated for this function. Rather, for all relevant isostatic loads, creep phenomena need to be evaluated. In this evaluation, all phenomena that may affect the long-term ductility of the copper material, must also be considered. One such phenomenon concerns potential hydrogen embrittlement. Therefore, a dedicated safety function related to the hydrogen content of the copper material is also introduced.
Withstand shear load	No specific safety function indicator criterion for the canister relating to shear movements is formulated. Rather the set of conditions included in the design premises are used as criteria for further analyses. Copper shell sufficiently ductile after shear load. Hydrogen content low.	The evaluation of the design and manufacturing procedures for the ensemble of deposited reference canisters led to the conclusion that the canister will fulfil the following design premise: "*The copper shell shall remain tight and the canister shall maintain its ability to resist loads for 5 cm rock displacements at all angles and a rate of 1 m/s, exerted on the canister by a buffer with an unconfined compressive strength at failure lower than 4 MPa at a deformation rate of 0.8 %/min.*" (Pers and Sturek 2021). No quantitative indicator is formulated for this function. Rather, for all relevant shear loads, creep phenomena need to be evaluated. As for isostatic loads, all phenomena that may affect the long-term ductility of the copper material, must also be considered when evaluating this safety function. One such phenomenon concerns potential hydrogen embrittlement. Therefore, as for the isostatic load, a dedicated safety function related to the hydrogen content of the copper material is also introduced.

1.8 Definition of canister variables

The canister is decribed by the variables in Table 1-8, which, together, characterise the cast iron insert and the copper shell in a suitable manner for the safety assessment.

The fuel and the cavity in the canister are characterised with respect to radiation by the intensity of gamma and neutron radiation and thermally by the temperature. Mechanically, the canister is characterised by stresses in the materials, and chemically by the material composition of the cast iron insert and copper shell.

Table 1-8. Variables for the cast iron insert and copper shell.

Variable	Definition
Radiation intensity	Intensity of gamma and neutron radiation as a function of time and space in the cast iron insert and copper shell.
Temperature	Temperature as a function of time and space in the cast iron insert and copper shell.
Canister geometry	Geometric dimensions of all components of the cast iron insert and copper shell.
Material composition	The detailed composition of the materials used for the cast iron insert and copper shell. Depending on the process, the emphasis may be on the chemical composition or on the physical microstructure. This variable also includes corrosion products of cast iron and of copper.
Mechanical stresses	Mechanical stresses as a function of time and space in the cast iron insert and copper shell.

1.9 Summary of handling of canister processes in the PSAR

Table 1-9 summaries the handling of canister processes in the PSAR, as suggested in this report. In the table, the process is either “mapped” to a model by which it will be quantified or associated with a brief verbal description of how it will be handled.

Table 1-9. Process table for the canister describing how canister processes will be handled in different time frames and in the special case of failed canisters. Green fields denote processes that are neglected or irrelevant for the time period of concern. Red fields denote processes that are quantified by modelling in the safety assessment. Orange fields denote processes that are neglected subject to a specified condition.

Process	Intact canister	Failed canister
C1 Radiation attenuation/ heat generation	Radiation attenuation: Initial radiation levels given in SKB (2010d). Heat generation: Included in integrated modelling of thermal evolution.	Neglected when releases occur after period of elevated temperatures.
C2 Heat transport	Included in integrated modelling of thermal evolution.	Neglected when releases occur after period of elevated temperatures.
C3 Deformation of cast iron insert	Isostatic and shear loads modelled in design analysis of canister (Jonsson et al. 2018). (Uneven loads from uneven swelling of the buffer and lack of straightness of the deposition hole included). Considered as cause for failure when isostatic or shear loads on canister exceed design premises loads.	Description in Section 3.4.2, integrated with other relevant processes yielding simplified, pessimistic assumptions on retardation of radionuclide transport in failed canister depending on failure mode.
C4 Deformation of copper canister from external pressure	Isostatic and shear loads modelled in design analysis of canister (Jonsson et al. 2018). (Uneven loads from uneven swelling of the bufferand lack of straightness of the deposition hole as well as creep in copper included). Considered as cause for failure when isostatic or shear loads on canister exceed design premises loads.	Neglected
C5 Thermal expansion (both cast iron insert and copper canister)	Neglected since the thermal expansion will cause negligible strains in the materials.	Neglected
C6 Deformation from internal corrosion products	Not relevant	Description in Section 3.4.5, and in Section 2.3.1 integrated with other relevant processes yielding simplified, pessimistic assumptions on retardation in failed canister depending on failure mode.
C7 Radiation effects	Neglected based on the specified limit on Cu content for the insert. (Cu impurities promote radiation damage.) Radiation effect on the copper shell neglected due to negligable changes in the material.	Neglected
C8 Corrosion of cast iron insert	Neglected due to limited amount of water giving negligible corrosion effects.	Description in Section 3.5.1, and in Section 2.3.1 integrated with other relevant processes yielding simplified, pessimistic assumptions on retardation in failed canister depending on failure mode.
C9 Galvanic corrosion	Not relevant	Neglected, as influence of galvanic corrosion under oxygen-free, reducing conditions lies within the margins of error for the corrosion rate of the iron insert.
C10 Stress corrosion cracking of cast iron insert	Neglected since stress corrosion cracking is considered unlikely and even if it occurred it would have no consequences for stability of the insert.	Neglected

Process	Intact canister	Failed canister
C11 Corrosion of copper canister	Generally, corrosion is modelled based on mass balance (entrapped O_2) and transport capacity considerations ($H_2S(g)$ and $HS^-(aq)$) whereas reaction rates are disregarded. Sulfide from pyrite in buffer and backfill modelled based on transport capacity. Microbially generated sulfide in buffer (after buffer loss) and backfill, pessimistically bounded by supply of nutrients for microbes. Entrapped O_2 in buffer and backfill: Pessimistically assumed that all O_2 corrodes copper neglecting consumption by pyrite in bentonite, rock minerals and microbial activity. Potentially intruding O_2 during glaciation: Integrated handling of rock, backfill and buffer conditions. Localised O_2 corrosion: Assessed with probabilistic pitting model. Localised sulfide corrosion: described as micro-galvanic corrosion, only possible for very high sulfide fluxes. Corrosion due to radiation: Negligible corrosion depths and minor localised corrosion, based on experimental studies and modelling. Chloride assisted corrosion neglected as long as the combinations of pH and chloride concentration is below (the right-hand side of) the limiting curve (i.e a total copper concentration in solution of less than 10^{-6} mol/kg). Effects of different corrosion behavior of cold worked or welded material neglected due to small (if any) effects on fundamental corrosion properties. Corrosion by water disregarded based on thermo-dynamic considerations.	Not relevant for failed canister.
C12 Stress corrosion cracking, copper canister	For aerobic conditions the possible concentrations of SCC promoting agents close to the canister surface are compared to the threshold concentrations where SCC has been noticed in laboratory experiments. For radiolytic conditions, neglected due to low dose rate and thus insignificant effect on corrosion potential, material defect structure and mechanical properties. For reducing sulfidic conditions, the sulfide flux is compared with experimental threshold values for observed interfacial cracking.	Neglected
C13 Earth currents – stray current corrosion	Negligable increase in corrosion from external electrical field from natural earth currents or present HVDC installations. Future installations mentioned as a stylised case of future human action, with negligible consequences.	Neglected
C14 Deposition of salts on canister surface	Neglected due to small consequences (and only relevant during bentonite saturation phase).	Neglected
C15 Radionuclide transport	Not relevant	COMP23
C16 Hydrogen embrittle-ment of copper canister	Embrittlement due to reduction of oxides neglected since the concentration of oxygen in Cu-OFP is sufficiently low, and since welding under inert gas has been shown as efficient to avoid enhanced oxide concentrations in the weld. The levels of hydrogen potentially absorbed by copper under the H_2 flux generated at the canister surface by radiolysis and sulfide corrosion, are compared with the initial concentration of H in Cu-OFP and/or the concentrations of H known to experimentally affect the material properties and tendency to crack under tensile stress.	Neglected

2 Fuel processes

2.1 Radiation related processes

2.1.1 Radioactive decay

Overview/general description

The process of radioactive decay transforms the radionuclide content of the fuel and of those parts of the canister cavity to which radionuclides have spread. The radioactive disintegrations generate α-, β-, γ- and neutron radiation as well as new nuclides. These may also be radioactive and further decay until a stable nuclide is created.

This process is of fundamental importance, especially since it describes how the radiotoxicity and composition of the fuel evolves over time. The decay products may have chemical properties different from the parent nuclides that can affect their release mechanisms and migration properties. The energy liberated is converted for the most part into heat (Section 2.1.2), and the process thereby also constitutes the basis for the description of the repository's thermal evolution.

Dependencies between process and fuel variables

Table 2-1 shows how the process influences, and is influenced by, all fuel variables.

Table 2-1. Direct dependencies between the process "Radioactive decay" and the defined fuel variables and a short note on the handling in the PSAR.

Variable	Variable influence on process		Process influence on variable	
	Influence present? (Yes/No) Description	Handling of influence (How/If not – why)	Influence present? (Yes/No) Description	Handling of influence (How/If not – why)
Radiation intensity	No.	–	Yes. The radiation intensity is a result of radioactive decay.	The radiation intensity as a function of time is calculated from the radioactive decay of the inventory of radio-nuclides.
Temperature	No.	–	Yes. Most of the decay energy is transformed into heat.	The heat generation (and the temperature in the fuel) is calculated as a function of time from the radioactive decay of the inventory of radionuclides (see above).
Hydrovariables (pressure and flows)	No.	–	No. But indirectly through radiolysis.	–
Fuel geometry	No.	–	No.	–
Mechanical stresses	No.	–	No.	–
Radionuclide inventory	Yes. This is the source of the process.	Obvious.	Yes. The process both consumes and produces radionuclides.	The radionuclide inventory is calculated as a function of time (see above).
Material composition	No.	–	No.	–
Water composition	No.	–	Yes. Negligible compared to other processes influencing the water composition.	Neglected.
Gas composition	No.	–	Yes. Negligible compared to other processes influencing the gas composition.	Neglected.

Boundary conditions

There are no boundary conditions of relevance for this process. (The initial condition is the radionuclide inventory in the fuel at the time of deposition of the fuel in the repository.)

Model studies/experimental studies

Radioactive decay has been thoroughly studied experimentally over a long period of time. The theoretical understanding of the process is good and fully sufficient for the needs of the safety assessment.

Natural analogues/observations in nature

Radioactive substances occur naturally, and it is by studies of these that the knowledge of radioactivity grew during the first few decades of the 20th century.

Time perspective

The time it takes for half of all radioactive atoms of a certain nuclide to decay is called the half-life of the radionuclide. The half-lives of various radionuclides vary from fractions of a second to millions of years.

Handling in the PSAR

The process is included in integrated model calculations of the thermal evolution of the repository and of radionuclide transport (See Sections 2.2.1 and 2.6, respectively, for details regarding modelling).

Boundary conditions: As stated above, there are no boundary conditions of relevance for this process.

Handling of variables influencing this process: According to the influence table above, only the radionuclide inventory is of relevance. This variable is trivially included in the models of radioactive decay.

Handling of uncertainties in the PSAR

Uncertainties in mechanistic understanding

The mechanistic understanding of the process is sufficient for the needs of the safety assessment.

Model simplification uncertainties

The radioactive decay as a function of time can be calculated with great accuracy when the nuclide content is known (See Sections 2.2.1 and 2.6 for details regarding modelling).

Input data and data uncertainties

The half-lives of the relevant radionuclides are generally known with good accuracy. The most important exception to this rule is Se-79, where the reported half-life has a range from 1.1×10^6 years (Jiang et al. 1997) to 1.24×10^5 years (He et al. 2000). More recently published data are 2.80×10^5 years (He et al. 2002), 3.77×10^5 years (Bienvenue et al. 2007) and 3.27×10^5 years (Jörg et al. 2010).

In 1995 an international collaboration was formed, the Decay Data Evaluation Project, which includes members of the BNM-CEA/LNHB (France), PTB (Germany), INEEL (USA), KRI (Russia), LBNL (USA), NPL (United Kingdom), CIEMAT (Spain), with the objective of providing carefully produced (http://www.nucleide.org/DDEP.htm). In their evaluation, the adopted value is the weighted mean of these two latest values available in 2007, giving $3.56(40) \times 10^5$ years. No new evaluation including the 2010 value has been done after 2007 by DDEP; anyhow the average of the two latest values would be $3.52(44) \times 10^5$ years, which is quite similar to the 2007 average.

For other radionuclides, the evaluations published by the Decay Data Evaluation Project will be used when available. Uncertainties concerning the inventory at deposition and half-lives are discussed further in the PSAR Data report (SKB 2022d).

2.1.2 Radiation attenuation/heat generation

Overview/general description

The radiation from radioactive decay interacts with the materials in the fuel and the canister cavity. Energy is thereby transferred to the materials and the radiation is attenuated. Most of the transferred energy is converted into thermal energy, i.e. heat is generated. The thermal energy, or heat, that is generated in the fuel after it has been taken out of service is called residual or decay heat and is dependent on the fuel's radionuclide content. This in turn depends on the fuel's burnup and the length of the intermediate storage time before deposition in the repository. At first, the fuel's heat output is dominated by beta and gamma decay, but alpha disintegrations are also of importance in the long term (SKB 2010d). The isotopes which dominate during the first few centuries are Cs-137 (Ba-137m) and Sr-90 (Y-90), both with half-lives of around 30 years, resulting in an approximate halving of the heat output in 30 years.

The process is of fundamental importance since it describes how heat is generated by the radiation. Furthermore, attenuation determines how much of the generated radiation reaches the canister.

Dependencies between process and fuel variables

Table 2-2 shows how the process influences, and is influenced by, all fuel variables.

Boundary conditions

There are no relevant boundary conditions for this process other than the physical boundaries set by the geometries of the components involved and the loss of radiation over the boundary to the canister.

Model studies/experimental studies

The fuel's heat output is directly dependent on the radioactive decay process, as discussed in Section 2.1.1.

Natural analogues/observations in nature

Not applicable.

Time perspective

Heat generation in the fuel is only of importance for a few hundred years. After 1 000 years, heat generation is only about 5 % of that at the time of deposition.

Handling in the PSAR

The process is modelled for the main scenario in PSAR. The need for additional modelling is evaluated in the analysis of additional scenarios.

The total power output of the fuel as a function of time has been calculated on the basis of its radionuclide content, decay energies and half-lives (SKB 2010d). For modelling of the thermal evolution of the repository, this time dependent power output is approximated by a sum of exponential terms. All the heat generated is assumed to be deposited in the fuel rods.

Model: The thermal model is described in Hedin (2004) and Hökmark et al. (2010).

Boundary conditions: Not relevant for this particular part of the thermal model.

Table 2-2. Direct dependencies between the process "Radiation attenuation/heat generation" and the defined fuel variables and a short note on the handling in the PSAR.

Variable	Variable influence on process		Process influence on variable	
	Influence present? (Yes/No) Description	**Handling of influence (How/If not – why)**	**Influence present? (Yes/No) Description**	**Handling of influence (How/If not – why)**
Radiation intensity	Yes. The decay energy deposited in the fuel generates heat.	The heat generation is calculated from the radioactive decay of radionuclides (see SKB 2010d).	Yes. Attenuation lowers the radiation intensity.	Implicit in the model (see Håkansson and Lundgren 2009).
Temperature	No.	–	Yes. Obvious. Heat generation increases the temperature.	Implicit in the model (see SKB 2010d).
Hydrovariables (pressure and flows)	Yes. In a failed canister, the presence of water will influence the radiation attenuation.	Neglected. At the time of water intrusion, the γ-radiation will have decayed. The fuel and the cladding will attenuate α- and β-radiation.	No. But indirectly through temperature.	–
Fuel geometry	Yes. Most of the decay energy is deposited in the fuel and the geometry of the fuel has a small effect.	Neglected.	No.	–
Mechanical stresses	No.	–	Yes. Increased temperature may create increased stresses in the fuel.	Neglected. This is of no importance for the stability of the fuel.
Radionuclide inventory	Yes. The radionuclides are the source of heat.	Implicit in the model (see SKB 2010d).	No. The decay itself influences the radio-nuclide inventory. The generated heat does not.	–
Material composition	Yes. Different materials have different attenuation properties.	Neglected. All fuel elements have essentially the same material composition.	No.	–
Water composition	No.	–	No.	–
Gas composition	No.	–	No.	–

Handling of variables influencing this process: For the thermal modelling, all the radiation energy created in the radioactive decays is assumed to be deposited as heat in the fuel rods, yielding a simplified handling of all influences on the process listed in the influence table above. This handling is pessimistic with respect to the principal calculation end-point of the thermal model, namely the peak canister surface temperature, since no radiation energy is taken to escape the canister as gamma radiation.

Handling of uncertainties in the PSAR

Uncertainties in mechanistic understanding

The mechanistic understanding of the process is sufficient for the needs of the safety assessment.

Model simplification uncertainties

Heat output as a function of time can be calculated with great accuracy when the radionuclide content is known. In the approximate handling through a sum of exponential terms, a sufficient number of terms are included for the approximation error to have negligible influence on the calculation end-point, the peak canister surface temperature. Also, the simplification of assuming that all heat generated is deposited in the fuel rods is pessimistic since, in reality, some energy will be deposited outside the canister and thereby has a smaller influence on the peak canister surface temperature.

Input data and data uncertainties

The uncertainties regarding heat output stem from uncertainties regarding the nuclide content of the fuel, that are discussed in the PSAR Data report (SKB 2022d).

2.1.3 Induced fission (criticality)

Overview/general description

Criticality inside a canister

Neutrons from radioactive disintegrations can cause nuclear fission in certain isotopes in the fuel. As long as the copper canister is intact, the great majority of neutrons generated by these disintegrations will pass out of the fuel without causing fission and the process can be neglected.

In the case of U-235 and Pu-239 in particular, the efficiency of the fission process increases if the neutrons are moderated (slowed down) to lower energies by collisions with light atomic nuclei. This could, to some extent, occur if water were to penetrate a failed canister. The water will then act as a moderator due to its content of light hydrogen nuclei. New neutrons are released by the fissions, and if more neutrons are formed than are consumed the process can become self-sustaining. The system is then said to be critical and large quantities of energy can then be liberated. It is this process that has been utilised under controlled form in the nuclear reactor for energy production.

In the repository, the criteria for safety against criticality must apply. This means that the effective neutron multiplication factor, k_{eff}, including uncertainties, must not exceed 0.95, or, for events that based on their very low frequency are classified as not expected or improbable, k_{eff} should not exceed 0.98. Johansson et al. (2019) have calculated the effective neutron multiplication factor k_{eff} for a number of cases concerning criticality in the spent nuclear fuel repository after disposal. For criticality after disposal the consequence parameters such as the position of the assemblies in the canister, the manufacturing tolerances, the size of the fuel compartments in the insert, temperature, and variation with enrichment were included. The reactivity of the fuel varies somewhat over time but the analysis shows that using a decay time of one year is always pessimistic. The calculations were performed for fuel with an initial enrichment of 5 % U-235. Burn-up credit is used for PWR fuel, while for BWR-fuel credit is taken for the content of burnable absorber (BA). Using burnup credit requires that a certain burnup is reached for the PWR to comply with the acceptance criteria (Table 2-3). BA credit is not coupled to a certain burnup since the reactivity is lowered throughout the irradiation history. The programs used are Scale and CASMO, and the most reactive BWR and PWR fuels are used in the calculations.

The cases with highest k_{eff} are those which involve a water-filled canister. During the operational phase of the repository, no events are identified that can result in a loss of canister integrity and therefore, no water can enter. After closure of the repository, the situation is different and if the copper canisters fail in the repository, water is expected to enter.

The maximum k_{eff} for water-filled BWR- and PWR-canisters, with no changes in geometry, is:

BWR: $k_{eff} = 0.93243$

PWR: $k_{eff} = 0.93235$

These values are relevant for BWR fuel with an enrichment of 3.4 %, and PWR fuel with an enrichment of 2.3 %, that is, for fuel without requirement for BA content or burnup. Water that enters a failed canister in the repository is expected to corrode the cast iron insert and metal components of the fuel.

The effects of this corrosion have been analysed (Agrenius and Spahiu 2016). Using fuel with no BA or burnup requirement, the changes in internal geometry yields the following maximum k_{eff} for water-filled BWR- and PWR-canisters:

BWR: $k_{eff} = 0.95227$

PWR: $k_{eff} = 0.93434$

The effect comes from corrosion of the iron insert and deposition of magnetite which fills the void between fuel and insert. The calculations are done for the situation which results in highest reactivity, which corresponds to when the gap between the corrosion product magnetite and the fuel rods is ca 2 mm. Other potential changes and uncertainties that may increase the reactivity included in the calculations are:

- both magnetite and siderite (Fe-carbonate) forms as corrosion products
- hydrogen dissolved in the water
- carbon in the steel construction parts of the fuel
- statistical uncertainties inherent in the method (Keno uncertainty)
- reduced content of certain isotopes used for burn-credit.

Adding these uncertainties to the k_{eff} calculated for the case with magnetite filling most of the void in the canister still results in k_{eff} less than 0.98 for both canister types. This is in accordance with acceptance criteria for events which are expected to occur with a frequency less than once per 100 years ($f < 10^{-2}$). The analyses clearly show that criticality will not be reached in the repository. Even so, in an unrealistic "What if"-scenario (see the PSAR Post-closure safety report (SKB 2022a)), the effects of a postulated criticality in a failed and water-filled canister are analysed. It is shown that the consequences of a postulated criticality are limited and will not detrimentally affect the neighbouring deposition holes.

The main conclusion of this analysis was that a BWR-canister containing fuel with 5 % U-235 enrichment and Gd as burnable absorber will meet the criticality acceptance criteria. A PWR-canister containing fuel with 5 % enrichment will meet the criteria providing the burnup is higher than 34 MWd/kg (see Table 2-3). Johansson et al. (2019) provides a complete list of uncertainties taken into account for the determination of the burnup requirements for PWR fuel. The calculations have been performed assuming a canister filled with the same fuel; PWR fuel that does not meet the criteria in Table 2-3 can still be encapsulated with fulfilled criticality criteria if placed with other fuel, with lower reactivity. Thus, for these PWR fuels, canister specific calculations will be performed to show that the criticality criteria are met.

Table 2-3. Burnup requirements to avoid criticality for different enrichments.

Enrichment	5.0	4.5	4.0
PWR Burnup requirement (MWd/kgU)	34	24	12

Other cases involving old special types of fuel assemblies (from the Ågesta reactor and German MOX fuel) as well as some other special fuel, e.g. fuel lacking some rods, have also been analysed. The results show that the acceptance criteria will be met also for these cases.

Criticality outside a canister

The possibility of criticality outside the canister has been addressed on several occasions. This scenario was first analysed by Behrenz and Hannerz (1978). They concluded that criticality in the tunnel above the deposition holes is a very remote possibility since no process can be envisaged whereby the necessary local concentration could be achieved.

In 1994, Bowman and Venneri (1994) published a report claiming that autocritical and explosive conditions could be reached during disposal of all categories of waste containing fissile actinides. Van Konynenburg (1995) reviewed that report and found that the authors did not present plausible

explanations of a process or processes that could convert actual disposed waste into a configuration close enough to their hypothetical configuration to make the calculations relevant. These reports were later published in a special issue of Science and Global Security (1996).

Naudet (1991) developed a model for assessing the conditions to achieve a critical state under the conditions in the Oklo reactor zones. Oversby (1996, 1998) adapted the reasoning in Naudet (1991) to an analysis of the risks for criticality in a high level repository and concluded that if the fuel assemblies were damaged and uranium and plutonium leached out, there are no probable courses of events that could lead to criticality.

The possibility of nuclear criticality in the vicinity of the proposed repository at Yucca Mountain has been explored by Nicot (2008), who concluded that external nuclear criticality is not a concern at the proposed Yucca Mountain repository for any of the deposited waste. Some of the waste intended for Yucca Mountain contains higher levels of fissile material than what is intended for disposal in a Swedish repository.

Dependencies between process and fuel variables

Table 2-4 shows how the process influences, and is influenced by, all fuel variables.

Boundary conditions

There are no relevant boundary conditions for the criticality process other than the physical boundaries set by the geometries of the components involved. (Other important factors for this process include the fuel burnup, i.e. the fuel's content of fissile nuclides, and canister failure followed by the ingress of liquid water.)

Model studies/experimental studies

Nuclear fission has been thoroughly studied experimentally over a long period of time, and the theoretical understanding of the process is good and fully sufficient for the needs of the safety assessment. The issue of criticality in the canister has been studied by Johansson et al. (2019).

Criticality in the spent fuel repository is ruled out. However, for this particular process it was deemed pertinent to carry out some calculations to illustrate the effects in an unrealistic "What if"-scenario. The results, based on calculations in Hedin et al. (2013), are further described in the PSAR Post-closure safety report (SKB 2022a). The main conclusions are: In a steady-state case, where temperature is ca 260 °C and the power ca 13 kW, the bentonite in the adjacent deposition holes is not damaged and the spent fuel dissolution rate in the failed canister is assumed to be about one order of magnitude higher than in a sub-critical case. This results in an increased overall risk of a factor of six.

Natural analogues/observations in nature

Criticality has been studied at the natural reactor in Oklo, see Oversby (1996, 1998).

Time perspective

The fraction and type of of fissionable nuclides in the spent fuel changes somewhat with time; there is however no significant decrease over a time span of the safety assessment. Therefore, there is no general decrease of k_{eff} over time and criticality must be considered for the full time period of the safety assemement. The situation where the canister geometries are the same as in the encapsulation plant has been analysed for criticality in a water filled canister (discussed above). In a failed canister in the repository environment, the geometries may change due to iron corrosion. This situation has also been analysed (Agrenius and Spahiu 2016) and it is concluded that during the insert corrosion, k_{eff} will be elevated up to certain point in the evolution, after which it will decrease. The worst situation is expected when the gap between the corrosion product magnetite and the fuel rods is ca 2 mm. This corresponds to ca 9 mm corroded carbon steel, and assuming a steel corrosion rate of 1 µm/year, this means k_{eff} can be expected to increase for ca 9 000 years after canister failure. Depending on the availability of sulfide, the corrosion may proceed much faster (Johansson et al. 2017). This however, only further limits the time during wich k_{eff} will increase but not the maximum k_{eff}.

Handling in the PSAR

In calculations to assure that the criteria with regard to burnup and burnable poison are met, the resulting k_{eff} is lower than 0.98 in all cases. The probability of criticality outside the canister is considered to be negligibly small, based on the results reported in Oversby (1996, 1998), Van Konynenburg (1995) and Nicot (2008).

Table 2-4. Direct dependencies between the process "Induced fission (criticality)" and the defined fuel variables and a short note on the handling in the PSAR.

Variable	Variable influence on process		Process influence on variable	
	Influence present? (Yes/No) Description	**Handling of influence (How/If not – why)**	**Influence present? (Yes/No) Description**	**Handling of influence (How/If not – why)**
Radiation intensity	Yes. Neutron radiation is necessary for criticality to occur.	Neglected. The probability of criticality is considered to be negligibly small (see text).	Yes. Fissions will increase the radiation intensity.	Neglected. The probability of criticality is considered to be negligibly small (see text).
Temperature	No.	–	Yes. The fission energy will heat the fuel.	Neglected. The probability of criticality is considered to be negligibly small (see text).
Hydrovariables (pressure and flows)	Yes. The presence of liquid water is required.	Neglected. The probability of criticality is considered to be negligibly small (see text).	Yes. The heat generation may cause evaporation of water.	Neglected. The probability of criticality is considered to be negligibly small (see text).
Fuel geometry	Yes. Certain fuel geometries are more susceptible to criticality than others.	Neglected. The probability of criticality is considered to be negligibly small (see text).	No.	–
Mechanical stresses	No.	–	Yes. Stresses due to increased temperature.	Neglected. The probability of criticality is considered to be negligibly small (see text).
Radionuclide inventory	Yes. The amount of fissile material as well as other nuclides in the fuel controls the risk for criticality.	Neglected. The probability of criticality is considered to be negligibly small (see text).	Yes. Fissions lead to production of radionuclides.	Neglected. The probability of criticality is considered to be negligibly small (see text).
Material composition	Yes. The amount of fissile material as well as other nuclides in the fuel controls the risk for criticality.	Neglected. The probability of criticality is considered to be negligibly small (see text).	Yes. Fissions lead to production of radionuclides.	Neglected. The probability of criticality is considered to be negligibly small (see text).
Water composition	No.	–	No, but indirectly through increased radiolysis.	Neglected. The probability of criticality is considered to be negligibly small (see text).
Gas composition	No.	–	Yes. Evaporation of water and gaseous radiolysis products.	Neglected. The probability of criticality is considered to be negligibly small (see text).

Boundary conditions: As stated above, there are no relevant boundary conditions for this process other than the physical boundaries set by the geometries of the components involved. These are used in the reported studies of criticality.

Handling of variables influencing this process: All variables influencing criticality according to the influence table above are included in the reported studies of this process.

Handling of uncertainties in the PSAR

Uncertainties in mechanistic understanding

The process has been thoroughly studied within reactor physics. The mechanistic understanding is sufficient for the needs of the safety assessment.

Model simplification uncertainties

The reactivity of the fuel in the canister can be calculated with sufficient accuracy. Model uncertainties have been included in the assessment.

Input data and data uncertainties

Data uncertainties such as variation in burnup axially and horizontally, radionuclide content and manufacturing tolerances for the canister have been included in the assessment.

2.2 Thermal processes

2.2.1 Heat transport

Overview/general description

Heat is transported through the fuel and canister cavity by conduction and radiation to the canister insert and beyond to the near and far field. The process is dependent on the geometric configuration of the fuel and the thermal properties of the materials, which are determined by their compositions. The heat transfer to the canister insert sets the boundary conditions for the process. The result is a temperature change in the fuel/cavity.

The process constitutes a part of the thermal evolution of the repository.

Heat transfer between the fuel and the canister insert will occur through conduction and radiation. Which one of these will dominate will depend on the composition of the residual gas in the cavity and the radiation properties[2] of the metal surfaces on the fuel assemblies and the canister insert. The temperature in the fuel and the cavity will be affected by the entire chain of heat transfers between the different components in the repository. In the longer term perspective, the temperature evolution in the fuel and cavity will be controlled by the thermal power output of the fuel. In the shorter term, changes in the heat transfer properties of different repository components caused by redistribution of water (moisture) will have a greater influence on the temperature of the fuel. The peak temperature in the fuel will be reached within a few tens of years after deposition.

Dependencies between process and fuel variables

Table 2-5 shows how the process influences, and is influenced by, all fuel variables.

[2] Expressed as emissivity, i.e. capacity to emit electromagnetic radiation.

Table 2-5. Direct dependencies between the process "Heat transport" and the defined fuel variables and a short note on the handling in the PSAR.

Variable	Variable influence on process		Process influence on variable	
	Influence present? (Yes/No) Description	Handling of influence (How/If not – why)	Influence present? (Yes/No) Description	Handling of influence (How/If not – why)
Radiation intensity	No, but indirectly through the temperature.	–	No.	–
Temperature	Yes. The temperature and the temperature gradient control heat flow.	The thermal evolution of the fuel and the canister is included in the temperature modelling.	Yes. Heat transport will increase the temperature at distances away from the heat source.	The thermal evolution of the fuel and the canister is included in the temperature modelling.
Hydrovariables (pressure and flows)	Yes. The gas pressure and the possible presence of water in the canister influence the heat transport in the canister cavity.	Included in the temperature modelling.	No, but indirectly through increased temperature which will increase the gas pressure.	–
Fuel geometry	Yes.	Included in the temperature modelling.	No.	–
Mechanical stresses	No.	–	No, but indirectly through increased temperature that may lead to heat induced stresses.	–
Radionuclide inventory	No. The decay influences the temperature.	–	No.	–
Material composition	Yes. Different materials have different thermal properties.	The thermal properties of the canister materials are included in the temperature modelling.	No.	–
Water composition	No.	–	No.	–
Gas composition	Yes. The heat conduction depends on the type of gas in the cavity.	The thermal properties of gas inside the canister are included in the temperature modelling.	No.	–

Boundary conditions

The heat transfer to the canister insert sets the boundary condition for the process.

Model studies/experimental studies

Hedin has developed a model for the thermal evolution of the fuel and the canisteras a part of the integrated near-field evolution model for a KBS-3 repository (Hedin 2004). Simplified finite element calculations of the copper and buffer temperatures have be performed for a parametric study by Renström (2020a). Further work has been performed by for Posiva and SKB in Ikonen et al. (2018) and Ikonen (2020), see Section 3.2.1.

Natural analogues/observations in nature

Not applicable.

Time perspective

The peak temperature of the fuel is reached within a few tens of years after deposition. It then takes several thousand years for the fuel to cool to near-ambient temperatures.

Handling in the PSAR

The process is modelled for the main scenario in PSAR. The need for additional modelling is evaluated in the analysis of additional scenarios.

The process is included in the integrated modelling of the thermal evolution, encompassing the fuel, the canister, the buffer and the host rock. The most important calculation endpoint in the modelling is the peak canister surface temperature, which is insensitive to the handling of heat transport in the canister interior. To calculate the peak canister surface temperature, it is sufficient to know the power output as a function of time from the fuel. All other controlling factors are external to the canister.

Model: The thermal model is described in Hedin (2004) and Hökmark et al. (2010).

Boundary conditions: Heat transfer to the canister insert through both radiation and conduction is explicitly included in the model.

Handling of variables influencing this process: All variables influencing this process according to the influence table above are included in the model. The thermal conductivity in metal parts is assumed to be infinite, whereas heat transfer by radiation and conduction across gaps in the canister interior is handled for the explicit geometries of the fuel and canister.

Intruding water modifies the heat conduction properties in the interior of the canister only marginally. The description of heat conduction for the case of a defective canister is therefore assumed to lie within the frame of the uncertainties for the equivalent description for an intact canister. In addition, all conceivable causes of a canister failure are highly unlikely to occur during the fuel induced thermal transient in the repository.

Handling of uncertainties in the PSAR

Uncertainties in mechanistic understanding

The mechanistic understanding of the process is sufficient for the needs of the safety assessment, especially since the calculation end-point of concern is insensitive to this process.

Model simplification uncertainties

The geometry of the model is simplified to a 2D-format, and heat conduction is neglected in some parts of the canister interior. These simplifications are either irrelevant or pessimistic.

Input data and data uncertainties

Uncertainties surrounding the heat transfer between the cladding tubes and the cast iron insert lead to uncertainties in the assessment of the temperature of the fuel. Compared to the uncertainty regarding heat transfer between the canister surface and the bentonite before full water saturation has been achieved, these uncertainties surrounding the heat transfer from the fuel to the canister insert are small.

As mentioned above, these data do not influence the calculation of the peak canister temperature.

2.3 Hydraulic processes

2.3.1 Water and gas transport in the canister, boiling/condensation

Overview/general description

If the copper canister is penetrated, water can enter the canister cavity as liquid or water vapour. Transport of water, water vapour and other gases in the canister is then determined by the detailed geometry of the canister cavities, the presence of water/vapour in the cavities, and temperature and pressure. Boiling/condensation comprises an integral part of water/gas transport. Pressures and flows of water and gas across the container/buffer interface set the boundary conditions for this process.

The process is strongly coupled to several other processes; for example, corrosion of the canister insert, where water is consumed and hydrogen is formed. It is also of fundamental importance for some

other processes that are dependent on the presence of water in the canister, such as fuel dissolution and radionuclide transport.

If the canister is penetrated, water will enter. The process is controlled by the pressure difference between the buffer and the canister cavity (typically 5–7 MPa) and the hydraulic conductivity in the bentonite. Water ingress can be expected to proceed very slowly. In the presence of water in the canister, gas will be generated both by radiolysis (see Section 2.5.3) and by corrosion of the cast iron insert (Section 3.5.1). The build-up of gas pressure in the canister will lead to a gradual decrease in the inflow of water and, when the pressure is sufficiently high, possibly also to gas transport out of the canister and through the bentonite. The process has been investigated by Wikramaratna et al. (1993) and Bond et al. (1997).

Qualitatively, the course of events can be described as follows: water enters through a penetrating defect in the copper canister and causes anaerobic corrosion of the iron insert surfaces. This leads to hydrogen gas formation, which gradually increases the pressure inside the cavity in the canister and thereby reduces the ingress of water. The corrosion leads to consumption of water and production of hydrogen gas. If the surface area available for corrosion is constant, the rate of water consumption will also be constant and the water level in the canister will reach a peak and then decrease (see also Section 3.5.1). Bond et al. (1997) demonstrate that the timescale for water vapour distribution in the canister interior is considerably shorter than that of water consumption by corrosion, and hence that it is reasonable to assume, as is done in their study, that corrosion occurs uniformly over the surfaces of the canister insert. Depending on the size of the hole in the canister and the corrosion rate, Bond et al. (1997) see three possibilities.

1. If the hole is so small that water is consumed by corrosion at the same rate as it enters, no water will collect inside the canister. The hydrogen gas pressure builds up gradually and approaches the external water pressure asymptotically. The corrosion rate will be governed by the inward diffusion of water vapour, which also declines asymptotically towards zero as the hydrogen pressure builds up.

   The hole sizes for which this scenario applies depend on the corrosion rate. At a corrosion rate of 0.1 μm/year, the area of the hole must be less than about 8 mm^2 for the water pressure and bentonite conductivity assumed in the study. At a corrosion rate of 1 μm/year, (see also Section 3.5.1) the corresponding hole size is about 800 mm^2. When the inward transport of water due to the pressure difference between the inside and outside of the canister is lower than the inward transport of water by diffusion, canister corrosion will be diffusion-controlled (see below).

2. If the hole in the canister is larger than in case 1), but still sufficiently small, water will collect inside the canister. The water will be completely consumed before the pressure in the canister reaches the external pressure. Then the corrosion rate will be limited by the water supply rate, which will decrease with increasing hydrogen gas pressure leading to a decrease in corrosion rate (as in case 1). The hydrogen gas pressure gradually builds up and approaches the external pressure asymptotically, while the corrosion rate declines asymptotically towards zero.

   In the same way as in case 1), the hole size defining this scenario is dependent on the corrosion rate. The combination of a corrosion rate of 0.1 μm/year and a hole size of 20 mm^2 belongs to this category, for example. When the inward transport of water due to the pressure difference between the inside and outside of the canister is lower than the inward transport by diffusion, canister corrosion will be diffusion-controlled (see below).

3. If the hole is sufficiently large in relation to the corrosion rate, the hydrogen gas pressure will reach the external pressure while there is still water in the canister. If the water level is then lower than the hole in the copper canister, hydrogen is expelled, but the internal pressure is still high and prevents new water from entering the canister. If the water level in the canister lies above the hole in the copper canister, water will first be pressured out until the water is on a level with the hole. Then hydrogen will be expelled as long as the corrosion continues, i.e. until all water in the canister has been consumed.

   As in case 1, the hole size for which this scenario applies is dependent on the corrosion rate and can be illustrated by the cases 0.01 μm/year and hole size 5 mm^2, and 1 μm/year and hole size 0.18 m^2, both of which belong to case 3 (see also Section 3.5.1). When the inward transport of water due to the pressure difference between the inside and outside of the canister is lower than the inward transport by diffusion, canister corrosion will be diffusion-controlled (see below).

Even after all liquid water has been consumed, iron corrosion will continue, since water vapour can diffuse into the canister. This case has also been modelled by Bond et al. (1997) for different corrosion rates, hole sizes in the canister, and areas inside the canister available for corrosion.

The continued corrosion will lead to a continuous increase in the hydrogen pressure. The hydrogen pressure and the transport properties of the surrounding barriers will control the hydrogen release from the canister.

Agrenius and Spahiu (2016) describe the potential long-term evolution of a breached canister, according to processes deemed reasonable given the knowledge of corrosion behaviour of cast iron, steel and Zircaloy. The corrosion process will cause the formation of magnetite which is expected to extrude into the free space in the canister. Given the corrosion rates used in the calculation, the magnetite will fill the space in ca. 15 000 years after canister failure. This development has the potential to influence water transport in the canister.

If sulfide is available, or if sulfate reducing bacteria are active in the canister interior, iron corrosion may proceed more rapidly. Sulfide corrosion of iron will likely produce some form of iron monosulfide (FeS), and results indicate that the free space could be filled as quickly as in 13 years, or in ~2 500 years. These times are calculated using the rates of Johansson et al. (2017) and the geometry considerations in Agrenius and Spahiu (2016).

Dependencies between process and fuel variables

Table 2-6 shows how the process influences, and is influenced by, all fuel variables.

Table 2-6. Direct dependencies between the process "Water and gas transport in the canister: boiling/condensation" and the defined fuel variables and a short note on the handling in the PSAR.

Variable	Variable influence on process		Process influence on variable	
	Influence present? (Yes/No) Description	Handling of influence (How/If not – why)	Influence present? (Yes/No) Description	Handling of influence (How/If not – why)
Radiation intensity	No.	–	No.	–
Temperature	Yes. Influences the distribution between water and vapour.	Neglected for an intact canister. For a failed canister the temperature is assumed to be constant at 11 °C.	No.	–
Hydrovariables (pressure and flows)	Yes. Obvious.	Neglected for an intact canister. For a failed canister the development inside the canister is based on the modelling by Bond et al. (1997).	Yes. Obvious.	Neglected for an intact canister. For a failed canister the development inside the canister is based on the modelling by Bond et al. (1997).
Fuel geometry	No.	–	No.	–
Mechanical stresses	No.	–	Yes. Pressure build-up inside the canister.	Neglected for an intact canister. For a failed canister, see 3.5.1.
Radionuclide inventory	No.	–	No.	–
Material composition	No.	–	No.	–
Water composition	Yes. Water composition influences the corrosion rate and the corrosion products formed.	Neglected for an intact canister. For a failed canister see 3.5.1.	Yes. Release of soluble corrosion products.	See 3.5.1.
Gas composition	Yes. Presence of water vapour.	Neglected for an intact canister. For a failed canister see 3.5.1.	Yes. Hydrogen build-up.	See 3.5.1.

The transport of water and water vapour into the canister will lead to corrosion of the insert. The consequences of corrosion, such as the formation of soluble and solid corrosion products, and gaseous hydrogen will influence the water and gas transport inside the canister and, inversely, the products will influence the water and gas transport in the canister cavity.

Boundary conditions

Pressures and flows of water and gas at the canister/buffer interface set the boundary conditions for the process. The geometry of the damage in the copper shell forms an important part of these conditions.

Model studies/experimental studies

The process has been modelled for cracks in the canister by Wikramaratna et al. (1993), and in more detail by Bond et al. (1997). The long-term evolution of the canister has been described recently in Agrenius and Spahiu (2016). The continuous corrosion of the cast iron insert leads to the filling of the gap between fuel element and the insert with corrosion products after a few tenths of thousands years, thus decreasing the water flow through the canister.

No experimental studies of the process of water ingress and water consumption by hydrogen-generating corrosion have been carried out.

Natural analogues/observations in nature

Not applicable.

Time perspective

After canister penetration, the time frame is a matter of hundreds to tens of thousands of years (Bond et al. 1997, Agrenius and Spahiu 2016).

Handling in the PSAR

For an intact canister, the water and gas transport in the cavity will be negligible from the point of view of long-term safety.

In the case of a canister failure, the process is treated in the PSAR Post-closure safety report (SKB 2022a) as a part of an integral description of the evolution of the canister interior after damage. The descriptions will be based on the modelling reported in Bond et al. (1997) and other sources. Other processes included in the integrated description are advection and diffusion, Section 2.5.1, corrosion of the cast iron insert, Section 3.5.1 and deformation of the canister from internal corrosion products, Section 3.4.4. Several alternative evolutions will be considered to account for conceptual uncertainties arising when integrating a number of processes. Gas release through the buffer must also be included in the description. This is discussed further in the PSAR Buffer, backfill and closure process report (SKB 2022b).

The overall important effects of the coupled hydraulic and corrosion processes in the canister interior are *i*) a delay between the occurrence of the penetrating defect in the canister and the onset of radionuclide transport out of the canister and *ii*) the evolution of the hole size as a function of time, which involves also mechanical processes. The purpose of the integral description is to arrive at pessimistic estimates of these two input parameters used in radionuclide transport calculations.

Model: The treatment of a developing penetrating defect in the copper shell is further discussed in the PSAR Data report, (SKB 2022d) based on the modelling in Bond et al. (1997).

Boundary conditions: The boundary conditions mentioned above are explicitly included in the study by Bond et al. (1997).

Handling of variables influencing this process: All variables influencing this process according to the influence table above are included in the study by Bond et al. (1997). The temperature, however, is assumed to be constant and equal to 11 °C, and anaerobic conditions are assumed to prevail in the canister interior.

Handling of uncertainties in the PSAR

Uncertainties in mechanistic understanding

The mechanistic understanding is sufficient for a pessimistic treatment of this process in the safety assessment.

Model simplification uncertainties

The integrated internal evolution of a failed canister, of which this process forms a part, can be estimated with sufficient accuracy for the needs of the safety assessment, through pessimistic assumptions.

Input data and data uncertainties

For the generation of corrosion gases, the corrosion rates are well-determined empirically and can be modelled with a constant corrosion rate if the water supply is not limiting (Smart et al. 2002a, b). If the corrosion rate is greater than the supply of water, the corrosion process will be controlled by the transport of water into the canister (Bond et al. 1997).

Input data and data uncertainties regarding corrosion rates are discussed in Section 3.5.1.

2.4 Mechanical processes

2.4.1 Mechanical cladding failure

Overview/general description

Temperature changes in the fuel and mechanical impacts associated with handling and transport will affect the fuel cladding.

Temperature increases lead to increased gas pressure inside the cladding tubes and can cause failure. Uptake of hydrogen during reactor operation may have led to hydride formation with potential embrittlement, which can lead to failure of the cladding tubes. The increased internal pressure may also lead to delayed failure through creep, or through delayed hydride cracking (DHC). In most cases, the damage will be local and result in a leak in the cladding tube.

The process is of importance for the release of radionuclides from the fuel. This can only happen if the cladding tubes are damaged.

Dependencies between process and fuel variables

Table 2-7 shows how the process influences, and is influenced by, all fuel variables.

Boundary conditions

There are no relevant boundary conditions for this process other than the physical boundaries set by the geometries of the components involved.

Table 2-7. Direct dependencies between the process "Mechanical cladding failure" and the defined fuel variables and a short note on the handling in the PSAR.

Variable	Variable influence on process		Process influence on variable	
	Influence present? (Yes/No) Description	Handling of influence (How/If not – why)	Influence present? (Yes/No) Description	Handling of influence (How/If not – why)
Radiation intensity	No.	–	No.	–
Temperature	No, but indirectly through increase of gas pressure.	–	No.	–
Hydrovariables (pressure and flows)	Yes, increased gas pressure causes increased creep rate.	Neglected. After failure of the copper canister all cladding tubes are assumed to be damaged.	No.	–
Fuel geometry	No.	–	No.	–
Mechanical stresses	No.	–	Yes. Increased mechanical stresses in the cladding due to temperature increase.	Neglected. After failure of the copper canister all cladding tubes are assumed to be damaged.
Radionuclide inventory	No, but indirectly through heat generation and temperature.	–	No.	–
Material composition	Yes. Influence through the alloy used for cladding.	Neglected. After failure of the copper canister all cladding tubes are assumed to be damaged.	–	–
Water composition	No.	–	No.	–
Gas composition	No.	–	No.	–

Model studies/experimental studies

Experimental studies and modelling have been carried out for dry storage purposes (BEFAST III 1997). Hydride formation and delayed failure have been studied for a long time (Northwood and Kosasih 1983, Grigoriev 1996). Rothman (1984) conducted a review of the state of knowledge based on requirements for direct disposal of spent fuel. The conclusion was that failure due to hydride formation, though unlikely, cannot be entirely ruled out.

Due to the possibility of extended storage time in so-called dry casks, there has been a number of studies performed to investigate the delayed hydride cracking (DHC) failure mechanism. Chan (2013) describes all important parameters involved in the DHC failure mechanism. He concludes that studied types of cladding are most susceptible to DHC at temperatures of ca 300 °C. However, given enough time and fulfilling the requirement of hydride content, stress and initial flaw, the process is still possible for lower temperatures. Alvarez Holston and Stjärnsäter (2017) lists the critical parameters for DHC as hydrogen content, temperature, stress intensity factor, and time, and they state that in principle, all spent fuel in the wet pools has sufficient hydrogen content for DHC to operate below 300 °C. Their study showed that the threshold stress intensity factor was lowest at a temperature of 227 °C. To summarize, it can be concluded that the process is most relevant for prolonged storage at elevated temperature (above ca 100 °C). However, the process can still be active at lower temperatures and, considering a situation with high enough hydride content and stress, given enough time the process may cause cladding failure.

Based mainly on fuel and cladding type as well as burnup, it is possible to identify a fraction of spent fuel assemblies that have higher risk for DHC. This fraction has been used as an estimate of the fraction of the Swedish spent fuel that may develop a DHC-related cladding failure in the first 10 000 years of the safety assessment period (Evins 2020). The fraction is pessimistically estimated to between 3 % and 12 %.

Natural analogues/observations in nature

Not applicable.

Time perspective

After encapsulation, delayed hydride cracking (DHC) due to hydrides in the cladding may cause mechanical failure. Since DHC depends on diffusion of H in cladding, this process goes faster the higher the temperature (up until ca 318 °C). This means that it is possible that DHC may cause cladding failure during the time period of elevated temperature, but at the maximum temperature expected in the canister, ca 125 °C, the process is very slow. Therefore it is unlikely that cladding will fail due to this process in the first 100 years in the repository. However, since the process continues even at lower temperatures, it must be assumed that mechanical failure will happen in some fraction of the fuel rods during the time analysed in the safety assessment. The formation of the first crack will lower the hoop stress, which lowers significantly the likelihood for later crack extensions or formation of additional cracks at later times.

Handling in the PSAR

The process is of no importance for long-term safety as long as the copper canister is intact. To permit a discussion of retrieval, it cannot be guaranteed that the cladding will by intact for all fuel rods. However, the cladding will still provide physical protection for the fuel, and that the fuel assemblies retain their original geometry.

After failure of the canister, all cladding tubes will pessimistically be assumed to be damaged in the modelling of radionuclide transport for all cases that contribute to the calculated risk associated with the repository. Thus it is assumed that cladding provides no resistance to radionuclide transport. It is noted that canister failures occur after typically 10^5 years in the such cases, and that a cladding would have to be intact on this time scale to contribute to safety. For a few exploratory “What if” cases involving early canister failure, 12 % of the spent fuel rods are assumed to have failed cladding initially, based on Evins (2020). Cases with all rods initially failed are also explored.

Boundary conditions: As stated above, there are no specific boundary conditions relevant to this process.

Handling of the variables influencing the process: With the pessimistic handling of this process, the variables influencing the process are also treated pessimistically.

Handling of uncertainties in the PSAR

Uncertainties in mechanistic understanding

The understanding of the process is not sufficient to permit reliable quantification. In cases where the process is of importance, i.e. when the copper canister is damaged, it will be handled pessimistically, as described above

Model simplification uncertainties

Not applicable since the process is not modelled.

Input data and data uncertainties

Not applicable since the process is not modelled.

2.4.2 Structural evolution of the fuel matrix

Overview/general description

The time at which the fuel will contact water is estimated to be in the range of thousands to millions of years after deposition. The effects of radioactive decay, mainly alpha decay and build-up of helium in the fuel (see further Section 2.5.8), could possibly change the physical and chemical behaviour of the fuel over these long time periods.

Radiation enhanced diffusion, also referred to as "athermal" diffusion, is too slow to be directly observed experimentally. Various models have, therefore, been proposed to estimate this alpha self-irradiation enhanced diffusion (Ferry et al. 2005). A first upper estimate is based on an extrapolation of the measured athermal diffusion coefficient of uranium atoms during reactor operation. The deduced diffusion coefficient (D_α m^2/s) is, thus, proportional to the alpha activity per volume (A_α Bq/m^3):

$$D_\alpha \approx 2 \times 10^{-41} A_\alpha$$

For UO_2 fuel, this equation gives a diffusion coefficient that decreases from 10^{-25} m^2/s to 10^{-27} m^2/s during the first 10 000 years out of reactor. Ferry et al. (2005) also quantify the atom mobility in the spent fuel through more physical modelling. Taking into account the effects of the alpha particle, the electronic excitation and the recoil atoms, a three orders of magnitude lower diffusion coefficient is obtained:

$$D_\alpha \approx 8 \times 10^{-45} A_\alpha$$

Ferry et al. (2008) describe an experimental study where heavy ion bombardment of iodine implanted UO_2 was used to simulate the effect of alpha irradiation on iodine mobility in UO_2 fuel. To simulate the ballistic effect, the samples were irradiated with 800 keV ions at fluences of 2×10^{16} and 5×10^{16} per cm^2. The irradiation damage was similar to the ballistic damage accumulated in MOX fuel with a burnup of 60 MWd/kgHM after 10 000 years. The iodine profiles were then measured with SIMS (Secondary Ion Mass Spectrometry). No measurable displacement of iodine could be detected (less than 50 nm), which is consistent with a diffusion coefficient of about 10^{-28} m^2/s. Irradiating UO_2 pellets with bromine and silver ions simulated the effect of the electronic stopping power of alpha particles on iodine atom mobility. The Br ions had an energy varying between 170 and 220 MeV at a fluence of 10^{15} per cm^2 and the Ag ions had an energy of 70 MeV at a fluence of 5×10^{15} per cm^2. No mobility of iodine atoms was detected. Ferry et al. (2008) concluded that the athermal diffusion process would make a negligible contribution to the Instant Release Fraction (IRF; see section 1.3.4).

Ferry et al. (2008) confirm this conclusion and stated that "based on theoretical models supported by experiments simulating α-decay effects on atom mobility in spent fuel, the release of fission products to grain-boundaries should not be significant even on the long-term".

Van Brutzel and Crocombette (2007) also modelled athermal diffusion. They studied two mechanisms for accelerated diffusion: the mobility mechanism related to the ballistic collisions during the displacement cascades, and the mobility mechanism related to the thermal diffusion accelerated via the additional point defects created during the irradiation. The values of athermal diffusion coefficients coming from the ballistic collisions and the additional point defects created during the cascades were estimated from these simulations to be less than 10^{-26} m^2/s in all cases, including for 1 year old fuel. Van Brutzel and Crocombette (2007) did not draw any conclusions on the effect of these processes on the long-term evolution of the IRF. Their data, however, support the conclusions in Ferry et al. (2005, 2008).

Martin G et al. (2009) studied the radiation-induced diffusion in uranium dioxide with molecular dynamics modelling. Their results also show that the contribution from radiation-induced diffusion is too low to be important even for the long-term perspective.

The athermal diffusion mechanism will lead to no significant contribution to release if the diffusion coefficient is less than 1×10^{-26} m^2/s. For a diffusion coefficient of 10^{-26} m^2/s, the average movement of an atom, given by $x = (Dt)^{0.5}$, would be 5 nm in 100 years or 0.5 μm in 10^6 years. Therefore, for spent nuclear fuel of the types and burnups that are considered in PSAR, athermal diffusion is not expected to lead to any increase of the instant release fraction even after a million years.

Dependencies between process and fuel variables

Table 2-8 shows how the process influences, and is influenced by, all fuel variables.

Table 2-8. Direct dependencies between the process "Structural evolution of the fuel matrix" and the defined fuel variables and a short note on the handling in the PSAR.

Variable	Variable influence on process		Process influence on variable	
	Influence present? (Yes/No) Description	**Handling of influence (How/If not – why)**	**Influence present? (Yes/No) Description**	**Handling of influence (How/If not – why)**
Radiation intensity	Yes. The alpha decay will cause radiation damage.	The process is neglected for the fuel types and burnup that are relevant for a Swedish repository.	No.	–
Temperature	No. The temperature range will be too low to cause any annealing of any radiation damage.	–	No.	–
Hydrovariables (pressure and flows)	No.	–	No.	–
Fuel geometry	No.	–	No.	–
Mechanical stresses	No.	–	No.	–
Radionuclide inventory	No, but indirectly through the content of alpha emitters.	–	Yes. If the process was significant, the distribution of radio-nuclides in the fuel would be altered.	The process is neglected for the fuel types and burnup that are relevant for a Swedish repository.
Material composition	No.	–	No.	–
Water composition	No.	–	No.	–
Gas composition	No.	–	No.	–

The only variable of importance for this process is the total content of alpha emitters.

Boundary conditions

This is a diffusion process in the fuel rods, meaning that the fuel rod surface is the relevant boundary.

Model studies/experimental studies

The process has been modelled by Ferry et al. (2005), Van Brutzel and Crocombette (2007), and Martin G et al. (2009), see above, and previously by Lovera et al. (2003) and Olander (2004) (not discussed further here). The results of an experimental study are presented in Ferry et al. (2005).

Natural analogues/observations in nature

Attempts have been made by Lovera et al. (2003) to apply their models for alpha self-irradiation enhanced diffusion to data from Oklo. Due to alpha decay of the uranium isotopes, lead is built up in the uraninite. The present relative composition of PbO in Oklo ranges between 5.4 and 7.7 %. Theoretically, there should be 24.6 %, i.e. substantial quantities of the radiogenic lead have left the uraninite. If this loss were through diffusion, the diffusion coefficient would have been in the range of 7.5×10^{-27} m^2/s to 12.2×10^{-27} m^2/s, i.e. within the range of diffusion coefficients proposed for alpha self-irradiation enhanced diffusion.

Lovera et al. (2003) ignored, however, two important facts in their analysis. The Oklo uraninites that contain 5 to 8 % Pb have been subjected to episodic loss of Pb on two occasions after their crystallisation at the end of reactor operation. An intrusion of a swarm of dykes at 860 ± 39 Ma caused the expulsion of Pb from the uraninites. This Pb crystallised as mm-sized galena (PbS) crystals, which have an isotopic composition consistent with the Pb having grown in uraninite from 1 950 Ma to 850 Ma. The isotopic composition of Pb in the uraninites surrounding these galena crystals shows an initiation of growth of radiogenic Pb starting at 850 Ma and indicates that Pb was also lost from the uraninites at a later time. Detailed analysis of the isotopic composition data yields results consistent with loss of Pb at the time of the pan-African event, a regional thermal event, at about 500 Ma. Thus, the present Pb content of the uraninites is due to loss of radiogenic Pb during two high temperature events with relatively short duration, followed by ingrowth of new radiogenic Pb from about 500 Ma ago. The isotopic composition of Pb in the mm-sized galenas is consistent with negligible loss of Pb from the uraninites between 1 950 Ma and 850 Ma. The diffusion coefficient of Pb at low temperature from the uraninites during that time period must have been vanishingly small. A complete discussion of the geochronology and petrography of the Oklo 5 to 6 % Pb uraninites is provided in Evins et al. (2005).

Time perspective

It is a matter of millions of years before the effect will contribute to radionuclide release from the fuel, if at all.

Handling in the PSAR

Based on the findings of Ferry et al. (2005, 2008), Van Brutzel and Crocombette (2007), and Martin G et al. (2009), the process is neglected for the fuel types and burnup that are relevant for a Swedish repository.

Handling of uncertainties in the PSAR

Uncertainties in mechanistic understanding

Bounding estimates allow neglect of this process despite an incomplete mechanistic understanding (see above).

Model simplification uncertainties

Bounding estimates allow neglect of this process despite model simplifications, see above.

Input data and data uncertainties

Bounding estimates allow neglect of this process despite data uncertainties, see above.

2.5 Chemical processes

2.5.1 Advection and diffusion

Overview/general description

Solutes can be transported to and from the interior of the canister by advection and diffusion. These processes are not discussed explicitly, but dealt with integrated with other processes (often with pessimistic simplifications). (See also Section 2.6 for the handling of radionuclide transport).

Dependencies between process and fuel variables

Table 2-9 shows how the process influences, and is influenced by, all fuel variables.

The advection and diffusion in the canister cavity are influenced by the temperature, and require the presence of water or gas.

Table 2-9. Direct dependencies between the process "Advection and diffusion" and the defined fuel variables and a short note on the handling in the PSAR.

Variable	Variable influence on process		Process influence on variable	
	Influence present? (Yes/No) Description	Handling of influence (How/If not – why)	Influence present? (Yes/No) Description	Handling of influence (How/If not – why)
Radiation intensity	No.	–	No.	–
Temperature	Yes.	For an intact canister, the process is neglected. In the case of a canister failure, see Section 2.3.1, Section 2.6 and Chapter 13 in the PSAR Post-closure safety report (SKB 2022a).	No.	–
Hydrovariables (pressure and flows)	Yes.	See above.	No.	–
Fuel geometry	Yes.	See above.	No	–
Mechanical stresses	No.	–	No.	–
Radionuclide inventory	No.	–	Yes. The process redistributes radionuclides in the canister interior.	See above.
Material composition	No.	–	No.	–
Water composition	Yes. Differences in concentration cause diffusion.	See above.	Yes. The process redistributes water solutes in the canister interior.	See above.
Gas composition	No.	–	No.	–

Boundary conditions

Pressures and flows of water and gas as well as concentrations of radionuclides at the transition to the buffer set the boundary conditions for the process.

Model studies/experimental studies

There are no direct modelling or experimental studies for the case of a KBS-3 canister interior.

Natural analogues/observations in nature

Not applicable.

Time perspective

The process requires water intrusion. Even for an initially defective canister, water intrusion into the canister insert is highly unlikely to occur before at least 1 000 years have elapsed after waste deposition in the repository (Bond et al. 1997), and, in the general case, before millions of years. The evolution inside a failed canister involves anaerobic corrosion of cast iron, steel and Zircaloy, accompanied by the formation of corrosion products. Based on the discussion by Agrenius and Spahiu (2016), the canister interior will be filled with magnetite after ca. 15 000 years after water ingress. At this point, diffusion should be the main mode of solute transport inside the canister.

Handling in the PSAR

For an intact canister, the process is neglected.

In the case of a canister failure, the process is treated in the PSAR Post-closure safety report (SKB 2022a) as a part of an integral description of the evolution of the canister interior after damage (see Section 2.3.1). In the treatment of transport of dissolved species, the canister interior is essentially regarded as a well-stirred tank.

For the case of radionuclide transport, see Section 2.6.

Handling of uncertainties in the PSAR

Uncertainties in mechanistic understanding

Advection and diffusion are well-understood mechanisms for solute transport.

Model simplification uncertainties

See Sections 2.3.1 and 2.6.

Input data and data uncertainties

See Sections 2.3.1 and 2.6.

2.5.2 Residual gas radiolysis/acid formation

Overview/general description

Air and water in an intact canister can be decomposed by means of radiolysis. The products can then be converted to corrosive gases such as nitric and nitrous acids. These gases can be of importance for stress corrosion cracking on the canister insert (see Section 3.5.3).

Dependencies between process and fuel variables

Table 2-10 shows how the process influences, and is influenced by, all fuel variables.

Boundary conditions

There are no relevant boundary conditions for this process other than the physical boundary set by the geometries of the components involved.

Model studies/experimental studies

The production of nitric acid has been calculated by Marsh (1990), Henshaw et al. (1990), Henshaw (1994) and, more recently, by Henshaw and Spahiu (2021), for different dose rates and for different quantities of air and water in the canister. Not unexpectedly, the quantity of nitric acid formed is dependent on the presence of sufficient quantities of water and air. The rate at which nitric acid is formed is dependent on the dose rate. The calculations show that with 50 g of water, i.e. the amount of water corresponding to the void volume inside a fuel pin, just under 160 g of nitric acid can be formed (Henshaw et al. 1990). The availability of water and air will limit the amount of nitric acid that can form. Henshaw and Spahiu (2021) also included the effects of Fe corrosion on the formation of corrosive species. As the initial small amount of oxygen is consumed by oxic corrosion of the steel, the anoxic corrosion of steel starts producing hydrogen that suppresses radiolytic oxidant production in the gas phase (Jonsson 2021a). Under such reducing conditions, radiolytic production of NH3 from the nitrogen of air and the hydrogen produced by anoxic iron corrosion starts. The potential consequences of this for copper corrosion is further discussed in Section 3.4.5. The consequence for spent fuel corrosion is limited by the presence of intact cladding during the time these processes are occurring (Evins 2020, Spahiu 2021). The very limited amount of oxidants that would be available for reaction with fuel with leaking cladding would have an insignificant effect on the fuel (Spahiu 2021), a conclusion which is further supported by the availablility of hydrogen that can suppress oxidant production in the gas phase (Jonsson 2021a).

Table 2-10. Direct dependencies between the process "Residual gas radiolysis/acid formation" and the defined fuel variables and a short note on the handling in the PSAR.

Variable	Variable influence on process		Process influence on variable	
	Influence present? (Yes/No) Description	**Handling of influence (How/If not – why)**	**Influence present? (Yes/No) Description**	**Handling of influence (How/If not – why)**
Radiation intensity	Yes. The intensity determines the extent of radiolysis.	The amount of radiolysis product (nitric acid) is estimated based on the availability of nitrogen in the canister.	No.	–
Temperature	No.	–	No.	–
Hydrovariables (pressure and flows)	Yes. The amount of radiolysis products depends on the availability of water and residual gases in the canister.	The amount of radiolysis product (nitric acid) is estimated based on the availability of nitrogen in the canister.	Yes, but any effect is negligible.	Neglected.
Fuel geometry	No. Indirectly through the radiation intensity.	–	No.	–
Mechanical stresses	No.	–	No.	–
Radionuclide inventory	No. Indirectly through the radiation intensity.	–	No.	–
Material composition	No.	–	No.	–
Water composition	Yes. Dissolved solids and gases will influence the radiolysis products formed.	The water trapped inside the canister will be either reactor water or water from the storage pools at Clab. It can, therefore, be assumed to be clean water with very low ionic strength.	Yes. Radiolysis products will be formed in the water.	The amount of radiolysis product (nitric acid) is estimated based on the availability of nitrogen in the canister.
Gas composition	Yes. Gases will influence the radiolysis products formed.	The gas inside the canister is assumed to be at least 90 % Ar and the balance being air.	Yes. Gaseous radiolysis products will be formed.	The amount of radiolysis product (nitric acid) is estimated based on the availability of nitrogen in the canister.

Jones (1959) studied the radiation-induced reactions in the nitrogen/oxygen/water homogeneous system and found that the formation of nitric acid was linear with the absorbed dose. The formation proceeded to a total concentration in the gas-phase that was stoichiometrically equivalent to the amount of hydrogen initially present in the water. In the current plans for the encapsulation plant, the design goal is that no more than 600 g of water should be transferred to the canister with the fuel elements (Posiva SKB 2017). In this case, the availability of water will no longer limit the amount of nitric acid produced. Instead, the availability of nitrogen will be the limiting factor. The void volume in a canister with fuel will be approximately 1 m^3, see further the PSAR Data report (SKB 2022d). This corresponds to about 800/22.4 mol (NTP) of N_2 and for complete conversion of N_2 to HNO_3, $2 \times 800/22.4 = 71.4$ mol HNO_3 or 4 500 g. During the encapsulation, the air in the canister will be replaced by argon gas and at the most 10 % residual air will remain in the canister (Posiva SKB 2017). At that level of residual air, no more than 450 g of nitric acid can be formed. This estimate is based on a scenario which does not account for Fe corrosion inside the sealed canister. If Fe corrosion is included in the calculation, as was done by Henshaw and Spahiu (2021), available nitrogen will also form NH_3 during the period of anoxic corrosion (see further Section 3.4.5), and as a result, less nitric acid is produced.

Natural analogues/observations in nature

Not applicable.

Time perspective

The transformation of residual air and water to nitric acid takes place over the course of years to tens of years (Henshaw et al. 1990, Henshaw 1994), while ammonia builds up to a maximum during the first hundred years (Henshaw and Spahiu 2021), assuming 600 g of water, 10 % air and Fe corrosion in the sealed canister.

Handling in the PSAR

In an intact canister, residual oxygen, water and radiolytically formed nitric acid will be consumed by corrosion reactions with the canister insert. At the expected corrosion rates, it will take about 100 years to consume the oxidants inside the canister. As a consequence, all the oxidants will be consumed before a potential canister failure and will not have to be considered for a failed canister. The total depth of insert penetration by general corrosion is of the order of ten µm, which is negligible. The process is therefore neglected in the safety assessment. The consequences of stress corrosion cracking (SCC) are discussed in Section 3.5.3.

Handling of uncertainties in the PSAR

Uncertainties in mechanistic understanding

The mechanistic understanding is sufficiently good for the purpose of safety assessment.

Model simplification uncertainties

Mass balance considerations put an upper bound on the amount of nitric acid that could be produced.

Input data and data uncertainties

The maximum allowed amount of water in a canister is 600 g. The uncertainty concerns the quantity of water that is actually inadvertently introduced into the canister. This quantity is expected to be much less than the allowed 600 g.

2.5.3 Water radiolysis

Overview/general description

Water that enters a damaged canister and reaches the cavities between the fuel assemblies and the canister insert is affected by the ionising radiation emitted by the spent fuel. This causes the excitation, or ionisation of water molecules followed by breaking of their chemical bonds (*radiolysis*) producing primarily free electrons, OH-radicals and hydrogen atoms. Radicals are atoms or atomic groups resulting from the breaking of a chemical bond and containing a free or unpaired electron, which makes them highly reactive and able to participate in radiolytic chain reactions. Through such reactions with the solution components, a large variety of radicals are formed, as well as the stable molecular species O_2, H_2O_2, and H_2. Mainly gamma radiation, which has low Linear Energy Transfer (LET), and hence a relatively long range, is discussed here since it affects the water in the canister cavities. Homogeneous radiolysis by alpha-emitting nuclides in solution is also included in this section, while radiolysis at the fuel/clad gap is dealt with in Section 2.5.5, when fuel dissolution is discussed.

The production of reducing species by radiolysis results in a build-up of hydrogen gas in the void in the canister, while the simultaneous corrosion of the cast iron insert also produces hydrogen, as well as Fe(II) ions in solution. After some time, the hydrogen gas amounts produced by gamma radiolysis will reach a constant value and the result of continued gamma radiolysis will be reformation of water (Pastina and LaVerne 2001, Christensen and Bjergbakke 1982, 1984).

The quantity of hydrogen gas produced by gamma radiolysis is dependent on the gamma dose rate. The contribution made by radiolysis to hydrogen gas formation is negligible compared with the contribution made by corrosion of the cast iron insert (see Section 3.5.1).

Dependencies between process and fuel variables

Table 2-11 shows how the process influences, and is influenced by, all fuel variables.

The radiation intensity affects the production of radical and molecular radiolysis products. At the time of water intrusion, the gamma field of the spent fuel is expected to have decreased to negligible levels.

Table 2-11. Direct dependencies between the process "Water radiolysis" and the defined fuel variables and a short note on the handling in the PSAR.

Variable	Variable influence on process		Process influence on variable	
	Influence present? (Yes/No) Description	Handling of influence (How/If not – why)	Influence present? (Yes/No) Description	Handling of influence (How/If not – why)
Radiation intensity	Yes. The radiolysis is proportional to the dose rate.	Neglected. In a failed canister the contribution to hydrogen gas production is considerably smaller than the contribution from iron corrosion. For radiolysis effects on fuel dissolution see 2.5.5.	No.	–
Temperature	Yes.	Neglected. See text and row above.	No.	–
Hydrovariables (pressure and flows)	Yes. Presence of water in the canister is required.	Neglected. See text and first row above.	Yes. Radiolytic gas production.	Neglected. See text and first row above.
Fuel geometry	No. Indirectly through radiation intensity.	–	No.	–
Mechanical stresses	No.	–	No.	–
Radionuclide inventory	No. Indirectly through radiation intensity.	–	No.	–
Material composition	No.	–	No. Radiolysis may form corrosive species.	–
Water composition	Water solutes participate in radiolytic reactions.	Neglected. See text and first row above.	Yes. Radiolytic production of water solutes.	Neglected. See text and first row above.
Gas composition	Yes. Gases participate in radiolytic reactions.	Neglected. See above.	Yes. Radiolytic gas production.	Neglected. See text and first row above.

The temperature affects the kinetics of radiolytic reactions and can be accounted for in radiolytic modelling. At the time of water intrusion into the canister, the temperature is expected to have decreased to near ambient values and its influence is expected to be negligible.

The presence of water in the canister is a requirement for the radiolysis process to take place, while the production of radiolytic gases affects the pressure in the canister. As discussed above, the effect on pressure is expected to be negligible in comparison to the production of hydrogen by the corrosion of iron.

The fuel geometry affects the resultant gamma field inside the canister while the overall surface area of the fuel is of importance for the beta and alpha fields.

The influence of the radionuclide inventory is accounted for by the radiation intensity.

The composition of the water influences the yields and reactions of the different radiolytic species produced by radiolysis. The different radiolytic reactions in homogeneous solutions are modelled by kinetic radiolytic modelling with reliable results. The presence of excess dissolved hydrogen in the groundwater solution inside the canister affects the gamma radiolysis of water through reactions of molecular hydrogen with radicals such as by the reaction $OH\cdot + H_2 = H_2O + H\cdot$, which converts the oxidising radical $OH\cdot$ to water and the reducing radical $H\cdot$ (atomic hydrogen).

Boundary conditions

There are no relevant boundary conditions for this process other than the physical boundaries set by the geometries of the components involved.

Model studies/experimental studies

Radiolysis of water has been thoroughly studied by both experiments and modelling. Low LET (Linear Energy Transfer) radiation, such as gamma radiation, does not produce any detectable amounts of the stable species H_2 and H_2O_2 in pure de-aerated water (Allen 1961), because they react via $OH\cdot$ and $H\cdot$ radicals in a chemical chain reaction to reform H_2O. In aerated water, virtually all the hydrated electrons and $H\cdot$ radicals formed are oxidised by O_2, and the main products of low LET water radiolysis in a system open to air are a steady state concentration of H_2O_2 with constant releases of H_2 and O_2 (Spinks and Woods 1990). Thus, in a system open to air the low LET radiation results in an oxidizing aqueous solution.

Experimental and radiolytic modelling studies on gamma radiolysis of water in a closed system, ie not open to air, containing relatively small amounts of dissolved hydrogen (Pastina et al. 1999, Pastina and LaVerne 2001) show that the production of oxidants involves a threshold; i.e. above a certain concentration of dissolved hydrogen no measurable oxidant production occurs. Other closed system studies, involving spent fuel corrosion (mixed α, β, γ radiation field) in the presence of metallic iron (Loida et al. 1996, Grambow et al. 2000) in 5 M NaCl solutions, show that no traces of radiolytic oxygen could be detected in the gas phase. In addition, corrosion products of iron containing Fe(II), such as magnetite and green rust, were found on the iron at the end of long term tests. The presence of such corrosion products on iron surfaces indicates extremely low concentrations of radiolytic oxidants in the solution. In a study involving gamma radiolysis of saline solutions (5 M NaCl) in a closed system, 0.85 mM dissolved hydrogen was added at the start. At the end of the experiment, no additional gas was measured (Kelm and Bohnert 2004). The production of radiolytic gases in 5 M NaCl solutions was shown to restart in the presence of bromide ions (Kelm and Bohnert 2005).

In low LET radiation, the hydroxyl radicals produced are dispersed in the solution and available to react with bromine in solution, thereby cancelling the effect of hydrogen. To test whether bromide ions can have similar effects in a homogenous solution radiated with alpha-emitting nuclides, aqueous solutions of Pu-238 were prepared and the effects on the solution with and without bromine was investigated (Bauhn et al. 2017). It was clear that in the case of homogenous alpha radiolysis, the bromine reaction with the hydroxyl radical did not affect hydrogen peroxide production. The radicals in the case of alpha radiation are produced in narrow tracks in the solution, and will quickly recombine. This means that bromine only has an effect in the case of homogenous low LET radiation. In addition, the produced oxygen and hydrogen peroxide under 10 bar Ar or H_2 atmospheres were quite similar. These results re-open the debate on the effect of hydrogen on homogeneous alpha radiolysis. Pastina and LaVerne (2001) also reported similar production of H_2O_2 in Ar and H_2 giving as possible explanation the inhomogeneous character of alpha radiolysis. Their results were questioned by Trummer and Johnson (2010), who calculated radiolysis in the very small volume irradiated by the accelerator alpha particles (diameter of the beam × mean path length of particles) instead of the whole vessel volume used in the calculations of Pastina and LaVerne (2001) and found perfect agreement of the calculations with experimental results. In the case of the study of Bauhn et al. (2017), there is no doubt about the homogeneus distribution of the Pu(VI) ions in the whole volume of the solution, but still

no measurable effect of hydrogen on homogeneous alpha radiolysis is observed. In summary, these studies show that the hydrogen effect observed in experiments with solid UO_2 or spent nuclear fuel, appears to be a surface-mediated effect, and bromide ions do not react with radicals formed from high LET radiolysis.

Natural analogues/observations in nature

Not applicable.

Time perspective

The process contributes to hydrogen gas formation during the first centuries after deposition. After that, gamma radiation declines to negligible levels.

Handling in the PSAR

In a damaged canister, the contributions made by radiolysis to hydrogen gas production and other effects are neglected, since these effects are considerably smaller than the corresponding effects of corrosion by water of the cast iron insert. The process can be neglected regardless of time for water intrusion, since the presence of Fe(II) and hydrogen from iron corrosion will result in negligible effects from radiolysis. In addition, gamma radiolysis is only relevant for a few hundred years after deposition in the repository.

Radiolysis effects on fuel dissolution are dealt with in Section 2.5.5.

Handling of uncertainties in the PSAR

Uncertainties in mechanistic understanding

The mechanistic understanding of the process is sufficient for the needs of the safety assessment.

Model simplification uncertainties

Not relevant since the process is not modelled.

Input data and data uncertainties

Not relevant since the process is not modelled.

2.5.4 Metal corrosion

Overview/general description

The cladding tubes for the fuel are made of Zircaloy. Other structural elements in the fuel are made of stainless steel, Inconel, Incoloy or Zircaloy. The PWR control rods will also be encapsulated with the PWR fuel elements. These control rods are made of an alloy containing 80 % silver, 15 % indium and 5 % cadmium and have a Zircaloy cladding. Some of the radioactivity in the fuel is present in the cladding tubes and other metal parts as neutron activation products of alloying elements and impurities present in the as-fabricated materials.

If water enters the canister, the metal parts will corrode. The corrosion rate and the release of activation products from the Zircaloy will be controlled by the dissolution rate of the surface film of zirconium dioxide, which is tightly bound to the metal surface. The dissolution of the oxide film will be controlled by the solubility of ZrO_2 in the water in the immediate vicinity of the fuel and the removal of dissolved zirconium species through diffusion or advection. The solubility of ZrO_2 in water is very low, on the order of 10^{-9} M (Brown et al. 2005, Bruno et al. 1997).

Considering the low corrosion rate of Zircaloy and in view of the low solubility of ZrO_2 in water, the rate of the release of activation products from the cladding tubes will be very low.

Dependencies between process and fuel variables

Table 2-12 shows how the process influences, and is influenced by, all fuel variables.

Any water in the canister cavity can lead to corrosion of cladding tubes and other metal parts in the fuel. The process is controlled mainly by the material composition, the chemical environment in the canister cavity, and the temperature.

Table 2-12. Direct dependencies between the process "Metal corrosion" and the defined fuel variables and a short note on the handling in the PSAR.

Variable	Variable influence on process		Process influence on variable	
	Influence present? (Yes/No) Description	**Handling of influence (How/If not – why)**	**Influence present? (Yes/No) Description**	**Handling of influence (How/If not – why)**
Radiation intensity	No. Indirectly through radiolysis that may form corrosive species and water composition.	–	No.	–
Temperature	Yes. Corrosion rates tend to increase with temperature.	Neglected. This effect is limited under anoxic conditions.	No.	–
Hydrovariables (pressure and flows)	Yes. Presence of water is required.	Water is assumed to be present after canister failure.	No.	–
Fuel geometry	No.	–	Yes. Metal corrosion changes the geometry of corroding fuel elements.	Neglected. Changes in fuel geometry does not affect corrosion rates
Mechanical stresses	Yes. May cause stress corrosion cracking of the fuel metal parts.	No credit is given to cladding integrity.	No.	–
Radionuclide inventory	No. Indirectly through the radiation intensity.	–	No.	–
Material composition	Yes. Different alloys may have different corrosion rates. The effect will most likely be negligible.	Corrosion rate estimates based on stainless steel.	No.	–
Water composition	Yes. Metals have different corrosion rates in different waters. The effect will most likely be negligible.	Neglected. Limited influence under anoxic conditions.	Yes. The influence is small due to the low Zr solubility.	See text.
Gas composition	No.	–	No.	–

The process affects the isolating function of cladding tubes and metal parts that enclose the fuel and is, therefore, of importance for the release of radionuclides from the fuel. The corrosion of metal parts also leads to release of the activation products that have formed in the metal parts.

Boundary conditions

There are no relevant boundary conditions for this process other than the physical boundary set by the geometries of the components involved.

Model studies/experimental studies

No studies of the corrosion rate of Zircaloy have been conducted by SKB, but a thorough literature review was performed in 1984 by the Lawrence Livermore National Laboratory for a tuff repository (Rothman 1984). From Rothman's data, the corrosion rate can be estimated to be approximately 2 nm/year, i.e. penetration of the cladding tubes is estimated to require 400 000 years at a tube thickness of 0.8 mm.

Although no detailed studies of corrosion of Zircaloy in the repository environment have been conducted, similar studies have been conducted for titanium (Mattsson and Olefjord 1984, 1990, Mattsson et al. 1990). The corrosion properties of titanium are very similar to those of zirconium, since it is protected against general corrosion by a similarly adherent and insoluble surface film of oxide. The results of the investigations showed that the oxide film remained tightly bound to the underlying metal and that the corrosion rate was extremely low, approximately 2 nm/year. This is very similar to the corrosion rate of Zircaloy based on Rothman's data.

Within the range of possible water compositions inside the canister, there is no reason, within the accuracy of the estimated corrosion rates, to expect a dependence of corrosion rate on water composition and amount of water available as long as water or water vapour are present. Due to passivation of the Zircaloy, any radiolytically produced nitric acid is expected to preferentially corrode the cast iron insert.

The principal uncertainty is whether the corrosion rates observed in short-duration experiments are valid for geological time spans. The corrosion rate of Zircaloy (titanium) is measured over a short period compared with the expected life of the cladding tubes. The greatest uncertainty stems from the extrapolation of these short-term data. Mattsson and Olefjord (1990) derived a logarithmic growth law for the oxide layer on titanium based on measurements over a three-year period. After a rapid growth of an initial passivating film of about 7 nm, further growth takes place extremely slowly. An extrapolation to 10^6 years gives an oxide layer thickness of 12 nm.

Data from Mattsson and Olefjord (1990) also show, that for longer periods of 5 and 6 years, the growth rate deviates from the logarithmic law. After 6 years the film was 0.7 nm thicker than calculated, while the five-year samples showed a considerable distribution (from 4.9 to 15.5 nm) suggesting extrapolation according to a logarithmic law may not always be appropriate. For shorter exposures, the oxide film was amorphous, but after longer exposure periods it was partially crystallised. It is, therefore, possible that the higher growth rate is attributable to more rapid ion transport through grain boundaries. During the first year the film grows about 8 nm leading to passivation of the freshly exposed surface. Consequently, a rate of 8 nm/year can be regarded as an upper limit for the corrosion rate and corresponds to a life of 100 000 years for the Zircaloy cladding. In a review of corrosion rates of titanium in "fresh" groundwaters (Yucca Mountain J-13 groundwater) or "salt waters" (about 1 000 times more concentrated in most species than J-13 water) the corrosion rates were found to have little dependence on exposure temperature (60 °C and 90 °C) or the composition of the test medium (Hua et al. 2005). General corrosion rates, determined from weight loss measurements on planar and creviced specimens from 5 year tests yielded median values of 5 nm/year and 10 nm/year, respectively.

Shoesmith and Zagidulin (2011), points out that an important consideration of the corrosion behaviour of Zircaloy in a geological repository is the properties of the oxide film formed during the irradiation, since this influences the corrosion mechanism. In their review, they conclude that the main mechanism is passive corrosion, and expected that this would lead to corrosion rates of ca 5 nm/year. Due to reducing redox conditions within a failed canister, pitting corrosion of the Zircaloy is not expected (Shoesmith and Zagidulin 2011). If somehow pitting anyway would be possible, even a pessimistically high pitting factor of 10 would mean the cladding would remain intact for 12 000 years after the start of corrosion (Evins 2020).

The European CAST project focused on the inventory, release and speciation of C-14 formed by activation of N-14 in the metallic parts of the fuel. In a state-of-the-art report concerning releases of C-14 from Zircaloy (Gras 2014), it is concluded that the 20 nm/year envelope used in some assessment models for the corrosion rate of Zircaloy seems too pessimistic, since the long-term corrosion rates based on the most recent data are 1–2 nm/year.

The other engineering materials in the fuel are stainless steels or nickel-base alloys. SKB has not conducted any investigations of the corrosion resistance of these materials under repository conditions and, in general, there are few studies under anaerobic conditions.

Corrosion rates of stainless steel in aerated "fresh" waters at 25–100 °C in the interval 0.01–0.25 µm/year are reported in BSC (2004). For aerated interstitial clay waters at 25–75 °C (Casteels et al. 1986) report rates in the interval 0.1–0.96 µm/year. Results from the IAEA project on spent fuel performance assessment and research (SPAR) show corrosion rates of stainless steel during interim storage of spent fuel in the presence of radiolysis on the order of 0.3 µm/year (IAEA 2003). Saline groundwaters may lead to relatively high corrosion rates. A literature review of the corrosion resistance of similar candidate materials for encapsulation of nuclear fuel for the American Nuclear Waste Management Program in aerated "saltwaters" (see above) (BSC 2004) reports corrosion rates from 2 to 11.4 µm/year. Even higher rates for brief exposures in air saturated seawater are reported by Gdowski and Bullen (1988). As with the maximum rate obtained for brief exposures of titanium discussed above, these rates represent pessimistic upper limits, and the long-term rates will be considerably lower.

There is no evidence that stainless steel will de-passivate in saline anaerobic groundwaters. A corrosion rate of 0.8 µm/year for stainless steel in anoxic seawater at 24–40 °C is reported by White et al. (1966). In a state-of-the-art report of the EU-project Cobecoma, in-situ anoxic corrosion experiments in Boom clay revealed that the average uniform corrosion rates of a series of stainless steels at 16 to 140 °C were in the range 0.003–0.15 µm/year. Electrochemical experiments and immersion tests performed to investigate the influence of various factors on the pitting susceptibility of stainless steel and Ni alloys showed that these materials were resistant to pitting under all tested experimental conditions (T_{max} = 140 °C, $[Cl^-]_{max}$ = 50 g/L, $[S_2O_3]_{max}$ = 200 mg/L) (Kursten et al. 2004). Neither appreciable general corrosion rates (< 0.1 µm/year) nor sensitivity to localised corrosion were observed for stainless steel tested in granitic-bentonite water at 90 °C over one year of exposure (Kursten et al. 2004).

Under anoxic conditions Wada et al. (1999) measured very low corrosion rates (< 0.01 µm/year) of 304 SS stainless steel, the material of the hull-end pieces of the fuel elements, in seawater-based groundwater of pH 10. Smart et al. (2004) report anaerobic corrosion rates of stainless steel in alkaline environments in the range of 0.01 to 0.1 µm/year. The corrosion rates under anoxic conditions in neutral to alkaline environments were found to be relatively insensitive to pH within the range 6.4 to 13 (Blackwood et al. 2002).

From these few studies under anoxic conditions, the corrosion rates of stainless steel and nickel-based alloys are estimated to be 0.15 µm/year and within the range 0.01–1 µm/year, where the highest rates occur in saline groundwaters. With this estimate for corrosion rates, the lifetimes of the thinnest nickel alloy parts in fuel elements (0.3 mm), range from a hundred years to ten thousand years, while the lifetimes of thicker stainless steel parts will obviously be longer.

The corrosion of steel (and Zircaloy, see above) was studied in the EU-project CAST. This project focused on the inventory, release and speciation of C-14 formed by activation of N-14 in the metallic parts of the fuel. A state-of-the-art report concerning releases of C-14 from steels (Swanton et al. 2015) was compiled during the first year. In that report it is stated that there is very few data relevant to anoxic corrosion of stainless steel. This lack of data is indicative of the fact that both the general corrosion and localised corrosion rates of stainless steels would be expected to be very low under these conditions and hence they do not pose a risk to the use of stainless steels in industrial engineering applications in these conditions. An overview of the results of the CAST project is given by Norris and Capouet (2018). They state that the corrosion mechanisms for steels and Zircaloy in the near-field will likely remain generally unchanged in the long term, and that the low corrosion rates for these metals can be considered confirmed. The results also highlight the influence of the oxide layer in the C-14 release mechanism of Zircaloy.

The main constituent in the alloy used in the control rods is silver (80 %). Silver is a noble metal and if the alloy is exposed to anoxic groundwaters, no silver corrosion is expected, unless the water contains dissolved sulfides (see e.g. McNeil and Little 1992). In that case, the silver corrosion rate will be controlled by the rate of supply of sulfide.

The irradiated control rod contains the nuclide Ag-108m. However, the distribution of this nuclide in the used control rod is not even. The potential implications of this for the safety assessment calculations are discussed in Evins (2013a).

The corrosion of silver control rods was investigated at Studsvik in a series of experiments (Roth et al. 2015). The experiments started by investigating a piece of an unirradiated control rod both under air and under hydrogen. Then, an irradiated control rod was leached in an autoclave under 0.4 bar hydrogen for 133 days, with sampling at 12, 62 and 133 days. The autoclave was then left alone for an extended time. After ca 2 years, the autoclave was subjected to external gamma radiation at a dose comparative to that from a 100 years old fuel during ca 4 weeks (Askeljung et al. 2019). The external radiation simulated the radiation field from neighbouring fuel rods expected to be surrounding a used control rod in a failed copper canister. The results show that, under air, silver will be released but at a slower rate than the Cd and In also present in the alloy (Roth et al. 2015). None of the autoclave experiments with hydrogen indicates any release of silver from the control rod sample. The concentration of Ag-108m was measured by counting for 65 hours and was always below detection limit (ppt-level) of the gamma counter.

Using the detection limit (ca 1.2×10^{-12} M Ag-108m) to calculate the maximum fraction of released Ag-108m, and the duration of the experiment (2.5 years), the fractional release rate of Ag-108m from the control rod can be estimated to be in the order of 1.7×10^{-8} year^{-1} (Askeljung et al. 2019).

Natural analogues/observations in nature

Not applicable, except for silver and silver alloys. There are, to our knowledge, no systematic studies performed on silver artifacts as analogues.

Time perspective

After water has come into contact with the cladding tubes, corrosion accompanied by release of activation products is expected to proceed at a constant rate for hundreds of thousands of years. The equivalent time frame for stainless steel components or nickel-based alloys is thousands of years.

Handling in the PSAR

Available data suggest a life of the cladding tubes of at least 100 000 years. Although Zircaloy is highly resistant to uniform corrosion, cladding is not assumed to constitute a barrier to radionuclide release from the fuel, due to its potential susceptibility to local corrosion in groundwaters and to hydrogen induced cracking. Following the arguments presented in Johnson and McGinness (2002), the amount of C-14 present in the oxide layer (20 % of the cladding inventory) is assumed to be released immediately upon water contact. New results from the CAST project indicate that this estimate is too high; Necib et al. (2018) suggests below 10 %. Thus, assuming a 20 % instant release for this fraction of the C-14 is pessimistic. The release of the remaining activation products from Zircaloy is assumed to occur at the rate of its uniform corrosion under anoxic conditions. This rate is pessimistically assumed equal to the release rates of activation products from stainless steel. Another reason for this is that the inventory of activation products for all metal parts together is reported in the Spent fuel report (SKB 2021a). The available experimental data suggest that the release of activation products from all metal parts may be modelled in PSAR with a constant fractional release rate in the range of 10^{-2} to 10^{-4} per year. A triangular distribution with a peak at 10^{-3} per year seems to give sufficient margin for assessing defendable release rates of the activation products. In PSAR, however, the cladding tubes are assumed not to have any barrier function against release of radionuclides from the fuel pellets.

Experimental data for silver alloy control rods indicates that if there is a release of Ag-108m, it is below the detection limit of the gamma counter (ie less than ppt-levels; Askeljung et al. 2019). This shows that Ag-108m should not be included in the Instant Release Fractions, as was done for SR-Site, but rather be assigned a certain release rate. For the inventory of Ag-108m in the control rods, the release rate will be assumed to be governed by rate of Ag metal corrosion which for the reducing conditions in a failed canister is expected to be very low. For the initial, reducing conditions of the leaching experiment, silver metal is expected to be the stable (Roth et al. 2015). The calculated fractional release rate will be used for the control rods.

The whole radionuclide inventory contained in CRUD (Chalk River Unidentified Deposits) is assumed to be released instantaneously upon water contact.

Handling of uncertainties in the PSAR

Uncertainties in mechanistic understanding

The mechanistic understanding of the process of Zircaloy and stainless steel corrosion is sufficient for the needs of the safety assessment.

Model simplification uncertainties

The activation products are assumed to be released at a constant rate as the metal corrodes passively. The higher corrosion rates for stainless steel are used as the basis for estimating the release rate of activation products from all metallic parts, including the much more corrosion resistant Zircaloy parts. Release rates are assessed on the basis of lifetime estimate for the thinnest metal parts.

Input data and data uncertainties

The release rates of activation products are based on the corrosion rates of metallic parts under repository conditions. There are sufficient data of good quality to support much lower corrosion rates than the ones assumed here for Zircaloy metal parts (Shoesmith and Zagidulin 2011). The data used for estimation of the corrosion of stainless steel under anoxic conditions are based on the results of Kursten et al. (2004), White et al. (1966), Wada et al. (1999), and Smart et al. (2004). The uncertainties in the measured corrosion rates depend primarily on the method used to measure corrosion rates, especially for very low rates, as discussed in Smart et al. (2004). The uncertainties are further discussed in the PSAR Data report (SKB 2022d).

The release rate of Ag-108m is based on only one experiment, and observation that silver concentrations in aqueous solution were under the detection limit. However, the observations are in line with expectations based on the stability of silver metal under the relevant conditions.

2.5.5 Fuel dissolution

Overview/general description

If water enters the canister cavity, the fuel will start to dissolve, resulting in the release of uranium and other radionuclides contained in the fuel matrix. The process, which requires that the protective cladding tubes have been breached (Section 2.4.1), is controlled primarily by the chemical environment in the fuel-clad gap, particularly the presence of oxidants, and by the fuel composition, where matrix structure and the presence of radionuclides in the fuel matrix are decisive.

The process is of fundamental importance, since it describes the release of radionuclides from the fuel matrix and its contribution to the source term.

Non-matrix-bound activity

Radionuclides that have segregated to the fuel-clad gap will rapidly go into solution. The quantity of activity released is determined by the solubility and availability of segregated radionuclides. Many of the segregated radionuclides in the gap and within grain boundaries in the fuel have high solubility and mobility and are assumed to be released immediately upon water contact. The release from the gap is independent of the dissolution or transformation of the uranium dioxide matrix of the spent fuel and is discussed in more detail in Section 2.5.6.

Matrix-bound activity

The majority of fission products and higher actinides in the fuel exist in solid solution in the uranium dioxide matrix. The release of these radionuclides requires that the uranium dioxide matrix of the spent fuel be dissolved or otherwise altered, for example by oxidation. This can happen only if water has entered the canister and the cladding tubes are breached. The redox conditions under which dissolution of spent fuel occurs are by far the most important factor influencing the dissolution process, since oxidative dissolution (corrosion) of the fuel will release matrix bound activity much faster than non-oxidative, chemical dissolution.

Redox conditions in connection with water ingress: When water comes into contact with the fuel, the uranium dioxide will begin to dissolve. At the time of liquid water ingress, the corrosion of cast iron by water vapour is expected to have produced substantial amounts of hydrogen, part of which will dissolve in the intruding water and be present together with Fe(II) ions.

Any oxygen remaining in the repository near field after closure, at the time of groundwater ingress, will have been consumed by bacteria, reducing minerals in the rock and bentonite, and minimal corrosion of the Cu container (Section 3.5.4). Furthermore, the oxidation of iron by any intruding oxygen will likely proceed much faster than oxidation of UO_2 inside a damaged canister. An estimate of the time required to consume the oxygen in a copper canister shows that any residual oxygen will be consumed by oxidation of copper within a year or so (Kolár and King 1996). The consumption rate in an iron canister should be comparable, since the corrosion rates of iron and copper are comparable (Wersin et al. 1993). There are, therefore, no appreciable uncertainties surrounding the assumption that the water that will come into contact with the fuel will be oxygen-free. Any contribution to the oxidative dissolution of fuel should, therefore, be caused only by the radiolytic oxidants produced by water radiolysis.

Even for an initially defect canister, the first entry of water into the canister insert is not expected to occur until more than a thousand years after deposition (Bond et al. 1997). By that time the predominant form of radiation will arise from alpha decay (Lundgren 2017). Alpha particles have high LET (Linear Transfer Energy) and a very short range. They can cause radiolysis of a thin layer of water (~35μm) near the fuel surface and produce mainly the molecular radiolysis products H_2O_2 and H_2. Several studies have shown a threshold for the alpha activity below which no measurable effect of alpha radiolysis on fuel dissolution can be observed, even in carbonated de-aerated water (Rondinella et al. 2004, Muzeau et al. 2009). Poinssot et al. (2007) give a range of 18 to 33 MBq/g UO_2 for this threshold. This gives a time range of 3 500 to 55 000 years, where 3 500 years corresponds to an alpha activity threshold of 33 MBq/g (representative of a fuel with a burnup of 33 MWd/kgU UOX fuel) and 55 000 years corresponds to a threshold of 18 MBq/g (representative of a fuel burnup of 60 MWd/kgHM MOX). The conclusion, based on these experimental results, is that oxidative dissolution of uranium dioxide (or spent fuel) with an alpha-actvity of less than 18 MBq/g is too low to be experimentally quantified.

Higher burnup may affect the dissolution rate. It increases the content of fission products and higher actinides resulting in a higher radiation field. It also increases the surface area of the fuel, especially at the fuel rim. However, it has been shown that both these factors are counteracted effectively by the doping effect caused by the increase in fission product and actinide content (Ekeroth et al. 2009, Hanson and Stout 2004), as discussed further in the section on Model studies/experimental studies. This means that the matrix dissolution model used in PSAR should be valid also for HBU (High Burn-Up) fuels.

Dependencies between process and fuel variables

Table 2-13 shows how the process influences, and is influenced by, all fuel variables. Further details are given below.

The process is influenced by radiation intensity, which determines the dose rate to water and the production of radiolytic oxidants. As discussed above, the dominating radiation at the time of water intrusion will be alpha radiation and its levels in spent fuel after a few thousand years are not expected to cause measurable oxidative dissolution of the uranium dioxide matrix in the presence of anaerobically corroding iron and its corrosion products (Werme et al. 2004, Spahiu 2012, Spahiu and Evins 2014).

The temperature affects both the kinetics of all chemical reactions, including radiolytic and dissolution/precipitation processes, and the chemical equilibria in a damaged canister. At the time of water contact the temperature in the canister is expected to have decreased to near ambient when its influence will be limited.

The presence of water in a damaged canister is required for the process to take place. Any potential beneficiary effect of secondary phase deposits on the rate of dissolution of spent fuel, e.g. by limiting the amount of water contacting the fuel surface, is pessimistically neglected.

Table 2-13. Direct dependencies between the process "Fuel dissolution" and the defined fuel variables and a short note on the handling in the PSAR.

Variable	Variable influence on process		Process influence on variable	
	Influence present? (Yes/No) Description	**Handling of influence (How/If not – why)**	**Influence present? (Yes/No) Description**	**Handling of influence (How/If not – why)**
Radiation intensity	Yes. Affects radiolysis which influences redox conditions.	Neglected Effects are minimised by the presence of H_2 and Fe^{2+}.	Yes.	Neglected. Small changes in inventory due to dissolution.
Temperature	Yes. Influences kinetics and equilibria.	Neglected. Water ingress is assumed to take place at the earliest 1 000 years after disposal. At that time the temperature of the fuel will have a very limited effect.	No.	–
Hydrovariables (pressure and flows)	Yes. Presence of water required for the process to take place.	Water is assumed to be present after failure.	Yes. Secondary phases may restrict water access to the surface.	Pessimistically neglected.
Fuel geometry	No, but indirectly through radiation field and radiolysis.	–	Yes. Changes in fuel surface area due to dissolution/ precipitation processes.	Pessimistically neglected.
Mechanical stresses	No.	–	No.	–
Radionuclide inventory	No. Indirectly through radiation intensity.	–	Yes.	Neglected. Small changes due to release of radionuclides.
Material composition	No. (Iron corrosion affects redox conditions indirectly through water composition.)	–	Yes. Potential deposition of radionuclides on material surfaces.	Neglected.
Water composition	Yes. Affects radiolytic oxidant production and kinetics of dissolution.	The effect of radiolysis is assumed to be suppressed by the presence of H_2 and Fe^{2+}	Yes. Soluble radionuclides from fuel dissolution.	Source term for radionuclide release.
Gas composition	Yes. Gases such as H_2 participate in radiolytic reactions.	The effects of radiolysis are assumed to be suppressed by the presence of H_2 and Fe^{2+}.	Yes. Release of radioactive gases.	C-14 and Rn are assumed to be released with H_2 when it escapes through the bentonite.

The surface area of the fuel contacting water influences the dissolution rate, while the fuel geometry in the canister determines the resultant radiation field. Any influence of secondary precipitated phases on the fuel surface is pessimistically neglected, while any increase in fuel surface area due to dissolution of material from grain boundaries is considered negligible for the fuel dissolution rates assessed.

Different scenarios for water intrusion into an initially defective canister are analysed by Bond et al. (1997). Based on their analysis, the minimum time before water comes into contact with the fuel can be estimated to be 1 000 years. The radionuclide inventory of the fuel at the time of water intrusion is, therefore, dominated by alpha emitting nuclides, since most of the short-lived beta/gamma emitters will have decayed before water intrusion occurs. The fuel inventory of radionuclides determines the radiation field at the fuel surface and the dose rate to water as a function of time. The decrease of the inventory of a certain radionuclide in the fuel, caused by its dissolution in water, is usually very small. The influence of the doping by fission products and actinides on the stability of the UO_2(s) fuel matrix towards corrosion (oxidative dissolution) is discussed in the section Model studies/experimental studies. In modern fuel types it has become relatively common to include some additives, such as

Cr or Cr+Al, in the UO_2 matrix. The influence of these additives on solid state characteristics and fuel dissolution were studied in the recently finished EU-project DisCo (Evins et al. 2022) and some results are discussed below.

The behaviour of the different materials in the canister, especially the anaerobic corrosion of the cast iron insert, influence fuel dissolution indirectly by changing the water composition and determining the redox conditions inside the canister, see Section 3.5.1. The composition of the different materials is not affected by fuel dissolution other than by the potential deposition of radionuclide precipitates on their surface.

The water composition influences both the radiolytic reactions and the kinetics of matrix dissolution. The most important factors are the redox potential and the concentration of carbonates, but other complexants, such as sulfate, chloride etc, affect the radiolytic reaction chains and, hence, the dissolution process.

The gas produced by the anoxic corrosion of iron influences the fuel dissolution process through changes in water composition. The process of fuel matrix dissolution causes the release of stable and radioactive gases from fission gas bubbles as the dissolution progresses.

Boundary conditions

There are no relevant boundary conditions for this process other than the physical boundary set by the geometries of the components involved. Related transport processes over the canister boundary are handled in Section 2.6.

Model studies/experimental studies

Experimental studies of fuel dissolution under various redox conditions have been conducted for more than 30 years. The majority of data in dilute groundwater conditions have been obtained under oxidising conditions (see for example Forsyth and Werme 1992, Forsyth 1997); presently more effort is being made to perform fuel matrix dissolution experiments under anaerobic or reducing conditions. Since these two different types of experiments give different types of results the following text is divided into two sections. Finally, the influence of hydrogen on oxidative fuel dissolution is discussed.

Experiments open to air

Radiolysis of water in experiments open to air will be influenced by dissolved oxygen. The oxidizing effect of the radiolysis in such an experiment will accelerate fuel dissolution compared to a reducing system. The environment in the repository will be oxygen–free and reducing, and any experiment performed with real spent fuel under air cannot be seen as a system representative of the repository environment. Nevertheless, experiments with real fuel under oxidizing conditions still provide valuable insight into, and understanding of, the processes involved in oxidative fuel dissolution. There are two main areas of interest investigated through these experiments: 1) determination of the so-called Instant Release Fraction (IRF, see section 1.3.4), 2) effects of radionuclide content and fuel structure related to high burnup, and especially the high burnup structure (HBS). The HBS is found in the rim of the fuel pellet (see section1.3.4). Both the smaller grain size and the higher radiation dose at the rim are expected to contribute to higher dissolution rates. Forsyth (1997) investigated the influence of burnup using fuel material from segments of a stringer rod in which burnup varied between 21 and 49 MWd/kg U along the fuel column. The cumulative fractional release under oxidising conditions increased slightly, almost linearly, with burnup values up to 40–44 MWd/kgU, but then decreased for burnups up to 49 MWd/kg U. This study was later extended with data for four higher burnup (55–75 MWd/kg U) fuel samples using the same experimental procedure (Zwicky et al. 2011). The results for the whole series indicate that the releases do not increase proportionally with burnup. The highest cumulative fractional releases are observed for fuels with an intermediate burnup, a slight decrease being observed for fuels with the highest burnup (Ekeroth et al. 2009). A similar trend is observed in two other systematic studies of fuels with burnup in the range 29–60 MWd/kg U (Jégou et al. 2004) and 15–70 MWd/kg U (Hanson 2008).

In experiments carried out within the EU-Project NF-PRO, Clarens et al. (2008) compared the releases from the outer (~1 mm) part of a high burnup fuel (average burnup 65 MWd/kg U) with

releases from the central part of the pellet. The samples were in the form of powder and obtained by core drilling the fuel pellet. The releases of almost all radionuclides were slightly lower from the outer part, which contained the rim and had higher local burnup. Similar trends in flow-through dissolution tests have been reported (Hanson et al. 2004, Hanson and Stout 2004) and the observations are discussed in terms of the influence of non-uranium cations. The content of 2+, 3+ and 4+ non-uranium cations in spent fuel increases with burnup, leading to a decrease in dissolution rate by both a surface area effect (if the dopant is less soluble or dissolves more slowly than UO_2) and by lowering the redox reactivity of U in the oxide, since U(V) and U(VI) are stabilized in the solid through charge balance with the lower valence cations. In a study of Gd-doped UO_2, a substantial decrease in the dissolution rates was observed with increasing dopant concentration (Casella et al. 2008). In a combined electrochemical and spectroscopic study of SIMFUELs with varying composition (He et al. 2007), a measurable, but marginal, effect of doping level on the surface modification of the UO_2 fluorite lattice to UO_{2+x} was observed, in contrast to the more marked influence of doping on the anodic destruction of the UO_2 structure by conversion to the soluble U(VI) ions. The authors assign this influence to the formation of dopant-vacancy clusters that stabilise the fluorite lattice against the formation of destabilising tetragonal distortions and reduce the availability of oxygen vacancies, which facilitate oxidative dissolution. Thermochemical measurements of UO_{2+x} solid solutions with two and three valent oxides (Mazeina et al. 2008), indicate that they are more resistant to oxidation and oxidative leaching than UO_2 because of the additional stability resulting from the energetic contribution of the dopants.

It was recently shown that UO_2 samples that were repeatedly exposed to H_2O_2 exhibited changed redox reactivity (Maier et al 2020). The observed lower yield of dissolved U(VI) indicates a shift to a higher proportion of H_2O_2 being decomposed on the surface, likely due to a change in redox state of U at the surface. These results emphasize the need to further investigate dissolution of U(VI) in bicarbonate solutions. Attempts to dissolve secondary uranyl phases, mainly studtite and metaschoepite, found on a spent fuel pellet leached for 37 years in deionized water, were only partly successful. Even after 119 days of cumulative leaching in this solution, a significant amount of secondary phase remained (Roth et al. 2021). Interestingly, the release rate of some fission products (Cs, I) increased due to the partial dissolution of the secondary phases.

Experiments under anaerobic or reducing conditions

The fractional fuel dissolution rates proposed in Werme et al. (2004) were based on the review of all, at that time, available experimental studies carried out under reducing conditions. Several experimental and modelling studies in the presence of 0.05–43 mM dissolved hydrogen or actively corroding iron, both with relatively fresh spent fuel and alpha-doped UO_2, have been published since Werme et al. (2004) was published and these are discussed briefly below. These experiments involve both real spent fuel and analogues, such as alpha-doped UO_2.

Long-term (1–3 years) fuel leaching experiments performed in sealed vessels, initially under argon atmosphere (Cera et al. 2006), indicate that the rate of fuel dissolution approaches zero for radiolytically produced H_2 concentrations in the range 10^{-5}–10^{-4} M. The data were successfully modelled by including the effect of metallic particles on fuel surface reduction (Eriksen and Jonsson 2007, Eriksen et al. 2008).

The presence of non redox-sensitive fission products in spent fuel, such as Sr and Cs, make it possible to judge the fuel dissolution rate via their releases. A systematic reduction by more than two orders of magnitude of the released fraction of Sr or Cs during successive time intervals was observed in experiments lasting over one-year in the presence of a hydrogen atmosphere (Carbol et al. 2005). The concentrations of nearly all redox-sensitive elements (U, Pu, Np, Tc) are initially established by the dissolution of a pre-oxidised fuel surface layer, but decrease with time to values ~ 10^{-9} M, equivalent to the solubility of UO_2 (am). In all cases the concentrations of higher actinides, such as neptunium and plutonium, are two or more orders of magnitude lower than the uranium concentrations. The ratio between dissolved actinide and uranium concentrations is fairly close to that in the fuel, even though the solubilities of their tetravalent oxides are quite similar (Cui et al. 2008). This suggests that the solubility limiting solid in the experiment is a precipitate with an actinide composition of U:Pu:Np ~ $1:10^{-2}:10^{-3}$, i.e. reflecting the inventory of these actinides in spent fuel. The pre-oxidised layer, with the same actinide composition, rapidly dissolved and then reprecipitated due to reduction. Similar behaviour has been noticed during a long-term leaching experiment on the outer part of a high burnup fuel pellet containing the rim zone (Fors et al. 2008).

The first results from leaching of MOX fuel under a H_2 atmosphere (Carbol et al. 2009b) exhibit similarities to experiments conducted with uranium dioxide fuel and the data indicate lower releases from fuel regions containing Pu-agglomerates.

Several experiments with real spent fuel under hydrogen have been performed recently (Puranen et al. 2017, 2018), and the conclusion is that after the initial release of radionuclides present in the preoxidised layer, further oxidation of the uranium matrix is suppressed by hydrogen. The potential effect of Fe^{2+} in solution was investigated by using magnetite instead of corroding Fe(0); in this case, a continuous release of radionuclides, due to oxidation of the fuel matrix, is seen, indicating that the redox state of the fuel surface is not affected by the Fe^{2+} but rather H_2 (Puranen et al. 2020). New data from a spent fuel with a rod average burnup of ~ 70.2 MWd/kgU and local pellet burnup of 78 MWd/kgU show that the hydrogen effect is effective also for fuels with this very high burnup (Puranen et al. 2022). This study supports the conclusion that very high burnup fuels can be considered to have similar matrix dissolution behaviour as fuels with lower burnup.

As a part of the DisCo project (Evins et al. 2022), the matrix dissolution behaviour of doped fuel, ie fuel with additives, was investigated. One experiment compared fuel doped with Cr and Al (Adopt) with standard UO_2 fuel; the leaching behaviour under hydrogen was remarkably similar (Fidalgo et al. 2020). This shows that Cr and Al doping has an insignificant effect on the matrix dissolution of spent nuclear fuel in the presence of excess hydrogen. However, studies with model materials indicate that there may be some effect for samples doped with Cr and Al. When leached under 6–8 bar of 4.7 %H_2/N_2 (with trace amount of air due to accidental leaks), hydrogen may have been activated thanks to the combination of Cr and Al. The effect was not seen in samples doped only with Cr (Rodriguez-Vallgra et al. 2022). This indicates that the combined doping of Cr and Al may have a benefical effect by enhancing the activation of hydrogen on the spent fuel surface.

Apart from all experiments listed above, a thorough discussion of relevant experiments involving real spent fuel under reducing conditions is also given by Spahiu (2012). The conclusion from these experiments is that hydrogen supresses oxidative fuel dissolution. The possible mechanisms behind this effect is discussed below as well as in Spahiu (2012). Alpha-doped uranium dioxide better simulates the radiation field of several-thousand-year-old fuel. Experimental studies with UO_2, doped with the alpha-emitters U-233 or Pu-238, have been carried out in the presence of low concentrations of dissolved hydrogen, sulfide ions or actively corroding iron. The composition and radiation field of these materials are discussed and presented in Spahiu and Evins (2014) and Lundgren (2017). Experiments with alpha-doped UO_2(s) indicate clearly that the presence of a small amount of sulfide and strict anoxic conditions are sufficient to cancel any oxidising effect due to α-radiolysis from a few thousand year old fuel (Ollila 2006). In most tests with U-233-doped UO_2 (0, 5 and 10 %) under inert (N_2) and reducing (Fe(s)) conditions, very low total uranium concentrations were measured, especially in the presence of an iron strip. The results showed no evidence for enhanced dissolution of samples containing U-233 over those that contained only normal levels of U-235 and U-238 (Ollila et al. 2003, Ollila and Oversby 2006). The experiments were thoroughly analysed for the location of precipitated uranium. Negligible amounts were found on the corroding iron (Ollila and Oversby 2005). The release of U from the samples, especially during the first year or so of testing, appeared to be dominated either by high energy surface sites formed by crushing of the samples or by high-energy interior sites at grain boundaries or associated with crystal imperfections. Estimation of the matrix dissolution rate confirms previously measured low values (Ollila 2006). The first data from corrosion of alpha doped pellets under anoxic and reducing conditions in 0.5 and 1 M NaCl solutions as well as (Na,Ca)Cl solutions of ionic strength 0.625 M are available and they show no influence of the increased salinity on the corrosion rates (Ollila 2008). These samples contained alpha activity that approximated the levels expected 3 000 and 10 000 years after disposal of spent fuel. The tests were performed in the presence of anaerobically corroding iron.

Results from experiments using alpha doped pellets and three types of natural groundwater are also available (Ollila et al. 2013, Evins et al. 2014). The experimental set-up was the same as for the previous experiments, however, one set of experiments used a higher surface area (more sample, same size fraction) to solution volume ratio. The uranium concentrations are still, in all natural groundwaters, very low in these systems indicating a reducing environment and no U(VI) in solution. The results are used to calculate fractional release rates: some samples indicate a slight increase in the rate compared with previous results in synthetic groundwater (Ollila et al. 2013). For the experiments with higher SA/V, rates calculated for fresh water are, on average, 4.4×10^{-7} per year and for saline

water 6.73×10^{-8} per year, while for brackish water there was one experiment yielding ca 1×10^{-6} per year (Table 5-3 in Evins et al. 2014). It should be noted that the experiment yielding the highest rate was possibly influenced by a pre-oxidized layer due to previous storage and handling. Thus, the calculated dissolution rates from experiments using natural groundwaters are, in general, still within the rate distribution discussed in Spahiu and Evins (2014) and proposed in this safety assessment.

The initial tests with 10 % U-233-doped UO_2 under various hydrogen concentrations showed decreasing U concentrations, an absence of oxidants in the autoclave, and no detectable oxidation of the UO_2(s) surface by XPS (X-ray Photoelectron Spectroscopy) analysis (Carbol et al. 2009a, Rondinella et al. 2004). In spite of this, the measurable but very slight increase of U concentrations observed with 10 % U-233-doped pellets makes it difficult to claim a clear hydrogen effect (see discussion on threshold of alpha activity). A UO_2 pellet with a much higher doping level (385 MBq/g corresponding to 50 years old fuel) was also tested (Muzeau et al. 2009), and a very clear effect of α-radiolysis was observed under an Ar atmosphere, with U concentrations increasing quickly with time in carbonate solutions. The same system, tested under a 1 bar H_2 atmosphere, showed a slight decrease, not increase, in U concentration. These authors showed also that a good quality of alpha doped pellets is required, since in some cases materials with a low density compared to the theoretical UO_2 density give very high U releases (Muzeau 2007). Further, they also gave an explanation why even with good quality pellets, the U releases at the start of the test were proportional to the doping level; i.e. the amount of U released in solution from the pellet with 10 % U-233 was higher than that from the pellet with 1 % U-233, while release from depleted UO_2 was lowest (Rondinella et al. 2004). By using XPS measurements, Jégou et al. (2005) and Muzeau et al. (2009) showed that these materials are sensitive to surface oxidation during storage, especially in the presence of a few layers of water undergoing radiolysis. Thus, the short term U releases reflect this storage effect, which prevented achieving the unoxidized UO_2 behaviour sought in the measurements. Another experiment, with spent fuel leached under hydrogen, showed via XPS-measurements that after leaching the spent fuel surface was fully reduced, indicating that oxidation of UO_2 in that system was fully suppressed (Ekeroth et al. 2020).

Recently Odorowski et al. (2017) tested the same highly doped pellets (385 MBq/g) in Callovo-Oxfordian simulated groundwater and in the presence of metallic iron foil under Ar atmosphere from start. The results of the more than one year test showed very low uranium concentrations in solution (4×10^{-10}–4×10^{-9} M), corresponding to the solubility of UO_2(am, hyd), while the analysis of the uranium sorbed or precipitated during the test through autoclave and iron foil acid stripping indicated that very little U was released during the whole test (~ 10 µmol). Most of the U was found sorbed in the Ti walls of the autoclave (7.6 µmol) or on the iron foil (2.4 µmol), corresponding to the calculated values with K_d for sorption of U(IV) on TiO_2. Characterisations of the pellet and iron foil surface showed akaganeite type Fe(III)-hydroxides on the surface of the doped pellet and chukanovite ($CaFe(II)(CO_3)_2$) and aragonite ($CaCO_3$) on the surface of the iron foil. The authors conclude that Fe(II) produced by iron corrosion completely cancels the oxidative dissolution of the highly doped pellets. In another study by the same group (Odorowski et al. 2016) the dissolution of a unirradiated MOX pellet with alpha activity 1.3×10^9 Bq/g was investigated under air and Ar atmospheres in 10 mM bicarbonate solutions and quite similar increasing concentrations of U, Pu and H_2O_2 in solution were measured in both atmospheres. In her PhD thesis, Odorowski (2015) reports similar data as those for the leaching of the 385 MBq/g doped pellet also for the leaching of the unirradiated MOX pellet, which has a much higher alpha dose rate.

The hydrogen effect on alpha radiolysis: Evidence from experiments and models

Several studies have proposed mechanisms for the suppression of fuel oxidation/dissolution based on the catalytic effect of metallic ε-particles (composed of the fission products Mo, Pd, Tc, Rh and Ru) on H_2 activation at the fuel surface. The corrosion potential of SIMFUEL pellets decreased both with increase of number of ε-particles (Broczkowski et al. 2006) and increased dissolved hydrogen concentration (Broczkowski et al. 2005) to values well below the UO_2(s) oxidation threshold, indicating complete inhibition of fuel corrosion. Scanning electrochemical microscopy was used to verify that these effects can be attributed to the reversible decomposition of H_2 on metallic ε-particles (Broczkowski et al. 2007). Thus, from the electrochemical results it was concluded that the hydrogen in these systems was oxidized to $H\cdot$, and eventually H^+ on the noble metal particles, which prevented the oxidation of the fuel by galvanic coupling to the conductive UO_2 matrix (Broczkowski et al. 2010).

A steady-state model for fuel dissolution has been developed using experimentally determined kinetic parameters (Jonsson et al. 2007, Roth and Jonsson 2008 and references therein). Studies of the catalytic effect of pure Pd particles on the reaction between H_2 and H_2O_2 show that the reaction is very fast, practically diffusion controlled and independent of the H_2 pressure in the range 1–40 bar (Nilsson and Jonsson 2008). Based on the reported decrease of the corrosion potential (Broczkowski et al. 2005) and studies with Pd-doped UO_2 (Trummer et al. 2008, 2009) the relevant parameters for the solid phase reduction of oxidised $U(VI)_{surf}$ mediated by hydrogen via ε-particles were estimated. The results of spent fuel dissolution modelling, including the effect of Fe(II) ions on the decrease in steady state H_2O_2 concentrations at the fuel surface and the fuel surface reduction process on ε-particles, have been published (Jonsson et al. 2007). Calculation of maximum fuel dissolution rates using this model shows that an H_2 pressure of 0.1 bar is sufficient to effectively inhibit the oxidative dissolution of spent fuel aged 100 years or more. In the presence of 1 μM Fe(II), even 0.01 bar H_2 will be sufficient to stop fuel dissolution, while for Fe(II) concentrations of 40 μM (as expected inside a failed canister in Sweden), even radiolytically produced hydrogen is sufficient to completely inhibit fuel corrosion (Jonsson et al. 2007).

Experimental data on both spent fuel and alpha-doped UO_2(s) dissolution in the presence of H_2 and actively corroding iron indicate that either the presence of a redox front or that of a “chemical pump” process, during which the oxidised uranium released from the fuel surface is reduced and deposited on the surface of iron, are highly improbable.

- More than 99 % of the U(VI) released at the start of the leaching experiment was deposited on the surface of the fuel itself (Albinsson et al. 2003) and very low uranium levels were recovered in the vessel rinse.
- The transfer of a solution containing relatively low U levels (40–200 ppb) after contact with metallic Fe under 10 bar H_2 pressure to a similar vessel containing spent fuel equilibrated for a long time under the same conditions (Ollila et al. 2003) caused a quick decrease of the uranium concentrations to much lower levels (a few ppb). This suggests that spent fuel surfaces under such conditions have stronger reducing properties for U(VI) carbonate species than Fe surfaces.

Similar observations were made during the simultaneous corrosion of spent fuel and iron (Grambow et al. 1996, 2000). The uranium levels measured in solution were near the UO_2(s) solubility, while the post leaching characterisation of the Fe showed no UO_2(s), even though magnetite and green rust were formed as corrosion products on the steel surface. Under oxygen free conditions it was shown that magnetite reduces U(VI) (Scott et al. 2005), while green rust on iron surfaces was shown to precipitate UO_2(s) (Cui and Spahiu 2002). Despite this, during the co-dissolution of fuel and iron, both radiolytic oxidants and U(VI) were scavenged on the fuel surface and very little, if at all, on the iron surface. The same holds for leaching of U-233-doped UO_2(s). In the presence of iron, extremely low U concentrations were measured in solution and negligible amounts of uranium were detected on iron surfaces (Ollila and Oversby 2005).

All the experiments discussed above, as well as those listed in Spahiu (2012) indicate that hydrogen interacts with radiolytic oxidants produced by alpha radiation at the fuel surface. In doing so, the oxidants are not reacting with uranium and uranium stays reduced, a conclusion which is supported by the study of Ekeroth et al. (2020). The observed effects cannot be explained by hydrogen interacting with radicals in the bulk solution, but rather indicates surface mediated reactions. The possible mechanisms are discussed in Spahiu (2012). Experimental results are available that support two of these mechanisms: activation of hydrogen on noble metal particles in the spent nuclear fuel (e.g. Broczkowski et al. 2010) and catalytic dissociation of hydrogen peroxide on the oxide surface (Nilsson and Jonsson 2011, Lousada et al. 2013, Bauhn et al. 2018a). Based on the new data on the dissociation of H_2O_2 on UO_2 surfaces, its importance as the main radiolytic product causing fuel dissolution was reduced (Lousada et al. 2013). During surface catalytic decomposition, hydrogen peroxide is split in a first step into two hydroxyl radicals sorbed at the surface. Thus, it is possible that hydrogen present in solution reacts with these surface bound hydroxyl radicals, producing water and hydrogen radicals. Using deuterium (D_2) as a tracer of this reaction, Bauhn et al. (2018a, b) showed that HDO was indeed produced, supporting the conclusion that a large part of hydrogen peroxide, instead of oxidizing uranium, reacts with the hydrogen in the system.

Recently, the hydrogen effect has also been observed for an experiment involving an extrenal alpha source situated ~30 µm from a UO_2 surface. The experiment utilised XPS to show that the hydrogen could keep the surface reduced. Important findings in this study are that oxidation of U on the UO_2 surface proceeds via the formation of U(V), and that hydrogen is involved in interfacial redox reactions driven by radiolysis (Hansson et al. 2021).

Involving both metallic particles and H_2O_2 decomposition, Liu et al. (2017) modelled corrosion of spent fuel and alpha-doped UO_2 using the kinetics of the surface reactions in a steady-state model. They found that when including hydrogen in their model, steady state was not achieved, and the corrosion rate decreased with time to negligible levels.

That hydrogen in solution can keep the uranium oxide surface reduced in spite of the radiolytic production of molecular oxidants at the surface of the material implies that the oxidative dissolution rate of spent fuel in a repository environment will be very low, even at early times of canister failure (Spahiu and Evins 2014).

Natural analogues/observations in nature

The oxidation state of uranium in the uranium oxide lattice is an important factor in the process of spent fuel dissolution. In spent nuclear fuel, the uranium is present as U(IV) with a stoichiometry very close to $UO_{2.0}$, while in natural uraninite U(VI) is present to varying degrees. In Oklo, the U(VI)/U(IV) ratio varies from 0.10 to 0.19 (Janeczek et al. 1996) and in Cigar Lake it is even higher (Cramer and Smellie 1994). This is partly a result of autooxidation, stemming from the decay of U(IV) to stable isotopes of Pb, when Pb will take two electrons from a nearby U in order to reach the preferred oxidation state of Pb(II) (Finch and Murakami 1999). In the long term, mainly in the period beyond one million years, the same process will be important for the structure of the spent nuclear fuel. On a much shorter timescale, another similar effect may be achieved by the variety of impurities (fission products) found in the spent fuel matrix. The preferred oxidation state of many of these impurities are such that they will partly oxidize a uranium neighbour (He et al. 2007), as discussed above in the section on Model studies/experimental studies. This effect, important for the dissolution behaviour of spent nuclear fuel, has also been observed in natural uraninite (Janeczek et al. 1996) where impurities, which can be considered chemical analogues to fission products, are common.

A limitation in the studies of natural uraninite in the framework of a safety analysis, is that the conditions under which dissolution and alteration occurred can, in general, not be accurately specified. Therefore, even though natural uraninite is a good analogue for spent fuel in many respects, data on the dissolution and alteration of uraninite that may be used to quantify the dissolution process are rare. Qualitatively, however, it may be noted that laboratory experiments performed to determine dissolution rates of minerals often yield results that indicate a much faster dissolution rate than results from similar studies performed on minerals in a natural setting (White and Brantley 2003).

Time perspective

After water has come into contact with the fuel, fuel transformation will proceed for hundreds of thousands of years.

Handling in the PSAR

The fuel alteration/dissolution rate in the case of a damaged canister will be modelled using a constant fractional dissolution rate with a triangular distribution in log-space. The rate is based on available experimental data from studies performed using spent nuclear fuel and alpha-doped UO_2 under anaerobic and reducing conditions. These studies were performed in the presence of a hydrogen atmosphere or in the presence of actively corroding iron. An alternative approach would be to calculate a rate using a more sophisticated model involving radiolysis; however, it is recognised that any such model needs to incorporate a large number of surface reactions and their associated kinetic constants (e.g, Eriksen et al. 2012). This is true also of the more recent model of Liu et al. (2017), which takes into account various radiolytic yields, surface reaction rate constants and diffusion coefficients. The model calculates rates for open and closed systems, and was also used for evaluating

the effect of metallic particles in the fuel. The results indicate that the activation of hydrogen on metallic particles in the fuel will reduce corrosion rates to a negligible level. However, since uncertainties still remain regarding exact reaction mechanisms, for example concerning hydrogen peroxide decomposition, and there is still a need for experimentally determined kinetic constants, the more direct approach of using only experimental results is favoured here.

Based on experimental results discussed above, in Spahiu (2012) and Spahiu and Evins (2014) the model for fuel dissolution in the current safety assessment should be a constant fractional dissolution rate in the range of 10^{-8} to 10^{-6} per year, with a best estimate of 10^{-7} per year. These are the same values as were used in SR-Site (SKB 2010a).

Using this recommendation, the expected lifetime of the fuel is 10 million years, with a distribution between 1 and 100 million years, in the most likely scenario, i.e. reducing conditions in the repository and the presence of hydrogen gas and/or corroding iron and iron corrosion products. If dilute groundwater reaches the repository, the buffer may be partially or completely eroded, leaving a cavity filled with a slurry of colloidal clay particles in the deposition hole. Should the canister be breached under such circumstances, the clay particles are not expected to affect the fuel corrosion rate. Dissolved U(IV) would, however, be expected to sorb strongly to the clay particles, in analogy with Th (Bradbury and Bayens 2003, Ochs and Talerico 2004). If this happens, U(IV) would be dissolved from UO_2 (s) available in the canister to keep the water saturated with regards to the solubility limiting solid. In the canister, this is assumed to be UO_2 (am), a re-precipitated phase with higher solubility than the crystalline (but defect) UO_2 matrix of the spent nuclear fuel. Sorption on clay particles would cause first the dissolution of the UO2 (am), to saturate the sorption sites on the clay, and when no more of this phase is available, the fuel matrix would start to dissolve. This would affect the fuel dissolution rate, since U(VI) is being transported out from the canister at the rate of advective flow. In this case, the values for UO_2(s) solubility and K_d for U(IV) on clay are taken from the PSAR Data report (SKB 2022d), while the concentration of clay particles and water flow depend on the scenario analysed. This situation is not valid for the whole analysis time, because a few tens of thousands of years after water contact, the fuel channel will be filled with magnetite and water will only diffuse through corrosion products, which get compacted with time (Agrenius and Spahiu 2016).

In the unlikely case of oxygen-containing water coming into contact with spent fuel, the fuel may dissolve with a higher rate. For air-saturated waters, fractional dissolution rates in the range 10^{-5} to 10^{-4} per year, determined experimentally under air-saturated conditions, become appropriate (Forsyth and Werme 1992, Forsyth 1997). In oxidizing conditions, the corrosion of the uranium dioxide causes an increase in concentration of U(VI) in solution followed by the precipitation of solid U(VI) phases on or near the fuel. The composition of these secondary phases will depend on the groundwater composition. In groundwater or bentonite porewater, uranyl oxides/hydroxides (schoepite) will probably form first, while more stable uranyl silicates (for example, uranophane or soddyite) will form after longer times.

A few copper canisters will contain boxes with fuel with cladding that was damaged during irradiation in reactor. These fuels may have a certain fraction of oxidized fuel, which, when water enters the copper canister, will dissolve much more rapidly than the normal fuel matrix. The oxidized fraction of these irregular fuels will be assumed to dissolve at a certain rate (much) faster than that of non-oxidized fuel matrix. The selected rate will be based on information and arguments by Evins and Hedin (2020). It is pessimistically assumed the oxidative alteration has not caused the release of any radionuclides, so that this oxidized fuel fraction still contains its original radionuclide inventory.

Uncertainties

Uncertainties in mechanistic understanding

While there is a sound and increasing experimental database on the effect of the products of anoxic corrosion of iron on spent fuel dissolution, there are some remaining uncertainties concerning the exact mechanism involved. Other uncertainties concern effects of changing surface area and surface reactivity during dissolution, as well as the effects of radiolysis of very old fuel. These uncertainties are covered through the wide spread of two orders of magnitude used in the proposed dissolution rate distribution.

Model simplification uncertainties

A constant fractional dissolution rate of the fuel is assumed in the calculations. The release of uranium and all other nuclides is assumed proportional to their inventory in the fuel matrix. Enhancement of radionuclide release from the outer regions of the fuel matrix (the rim zone) or for the higher burnups relevant for forthcoming discharged fuels are not considered based on the influence of the higher doping level observed in experimental studies.

Input data and data uncertainties

Input data and input data uncertainties are discussed in the PSAR Data report (SKB 2022d).

2.5.6 Dissolution of the gap inventory

Overview/general description

In the event of canister damage, water can enter the canister. If the fuel cladding is breached, the water can come into contact with the fuel. Most of the radionuclides in the fuel are evenly distributed in the UO_2 matrix and are released only when the uranium dioxide fuel matrix dissolves (see Section 2.5.5). A small fraction of the inventory of a few radionuclides has segregated to the fuel-clad gap and possibly also to grain boundaries in the fuel; see Section 1.4.4.

Most segregated radionuclides are also highly soluble and can quickly go into solution upon contact with water, and the release is, therefore, considered as instantaneous in the safety assessment. The quantity of radionuclides released is determined mainly by the availability and solubility of segregated material. In SR-Can, the release of segregated nuclides in fuel was based on a compilation by Werme et al. (2004). For SR-Site, calculations of the fission gas release of BWR and PWR equilibrium cores for various burnup and linear power ratings were carried out (Oldberg 2009, Nordström 2009). These calculations were used as a basis to make a better estimation of the segregated nuclide fraction for the whole fuel inventory (see section 1.4.4 and the PSAR Data report (SKB 2022d).

Dependencies between process and fuel variables

Table 2-14 shows how the process influences, and is influenced by, all fuel variables.

The temperature influences the kinetics of dissolution of the segregated radionuclides. At the time of water intrusion, the temperature is expected to have decreased to near ambient values.

The presence of water in a damaged canister is required for the process to take place.

The fuel surface area in contact with water influences the release of the segregated nuclides. This influence is accounted for in the estimation of the size of the instant release fraction.

The radionuclide inventory in the gap and grain boundaries determines the contribution of the segregated nuclides to the source term, while the dissolution of these radionuclides affects the radionuclide inventory of the fuel.

In principle, the composition of materials, such as fuel cladding, affects the dissolution of that part of the instant release fraction, which has diffused into the zirconium oxide layer during reactor operation.

Upon water contact, some segregated radionuclides, such as C-14 may produce gaseous products such as methane or carbon dioxide.

Boundary conditions

There are no relevant boundary conditions for this process other than the physical boundary set by the geometries of the components involved.

Table 2-14. Direct dependencies between the process "Dissolution of the gap inventory" and the defined fuel variables and a short note on the handling in the PSAR.

Variable	Variable influence on process		Process influence on variable	
	Influence present? (Yes/No) Description	Handling of influence (How/If not – why)	Influence present? (Yes/No) Description	Handling of influence (How/If not – why)
Radiation intensity	No.	–	No.	–
Temperature	Yes.	Neglected. Instant release of the segregated inventory is assumed.	No.	–
Hydrovariables (pressure and flows)	Yes. Presence of water necessary for the process.	Water is assumed to be present after failure.	No.	–
Fuel geometry	Yes.	Neglected. Instant release of the segregated inventory is assumed.	No.	–
Mechanical stresses	No.	–	No.	–
Radionuclide inventory	Yes. Segregated inventory determines release.	Instant release of the segregated inventory is assumed.	Yes. Dissolution decreases radionuclide inventory.	Instant release of the segregated inventory is assumed.
Material composition	Yes.	Instant release of the segregated inventory is assumed.	No.	–
Water composition	Yes. Limited influence of water composition due to fast release.	Instant release of the segregated inventory is assumed.	Yes. Small changes in composition due to limited amounts of segregated nuclides.	Source term for radionuclide release.
Gas composition	No.	–	Yes. Gaseous products potentially formed.	Source term for radiouclide release.

Model studies/experimental studies

The immediate release of caesium and iodine from the fuel on contact with water is experimentally verified (see e.g. Johnson and Tait 1997). Johnson and McGinnes (2002) have made an assessment of the instant release fraction from light water reactor fuel. An experimental study of the dissolution of segregated metallic ε-particles extracted from spent fuel under various redox conditions (Cui et al. 2004) indicates very limited releases for the redox conditions expected in a damaged canister.

The instant release fractions of some radionuclides, for fuels with higher burnup up to 60 MWd/kgU are based on calculations of fission gas release for BWR and PWR equilibrium cores (Oldberg 2009, Nordström 2009). More information is given in the PSAR Data report (SKB 2022d).

It has been experimentally shown that fractions of the content of the fission gases, Cs, I and other elements such as C and Cl, can leave the fuel matrix during reactor operation. It is also known that Tc, Ru, Rh, Pd and Mo form metallic inclusions in the fuel. Experiments investigating the release of segregated nuclides were performed within the framework of the EU project First-Nuclides (Lemmens et al. 2017). Apart from improving the data base for determining the fraction of segregated nuclides, some modelling was also performed to improve understanding of the accessibility and wetting properties of grain boundaries and the processes on the surface of grain boundaries (Kienzler et al. 2017). In summary, the models indicate rapid transport in fractures (a few days) and microcracks (less than 100 days). Thus the dissolution process of the gap inventory is very rapid compared to the full assessment time spanning 1 million years, which is why the gap inventory it

is assumed to be released instantly. The main focus regarding the gap inventory is to determine the size of the segregated fractions of the various radionuclides, and this is considered in the description of the initial state of the spent fuel (Section 1.3.4).

Uncertainties surrounding the extent, and in some cases the very existence of segregations of certain radionuclides, are great. Uncertainties are discussed in greater detail in the PSAR Data report (SKB 2022d).

Natural analogues/observations in nature

Not applicable.

Time perspective

The release of segregated radionuclides occurs relatively rapidly (on the order of days) and is pessimistically assumed to occur instantaneously upon water contact.

Handling in the PSAR

The process is only relevant if containment by the copper shell has been breached.

Immediate release of the instant release fraction of radionuclides upon water contact in a damaged canister will be assumed for all scenarios in PSAR. Input data will be based on distributions for the instant release fractions assessed in the PSAR Data report (SKB 2022d).

Boundary conditions: As stated above, there are no relevant boundary conditions for this process other than the physical boundaries set by the geometries of the components involved. These become irrelevant with the pessimistic handling of the process.

Handling of variables influencing this process: the influences of temperature, fuel geometry, material composition and water composition are pessimistically neglected in the handling of this process. The influence of radionuclide inventory is trivially handled by assessing the fraction of segregated nuclides and assuming it is immediately released upon water contact. The requirement that water is present in the canister interior is handled by assessing a time after which a continuous water pathway has been established between the fuel and the canister interior.

Handling of uncertainties in the PSAR

Uncertainties in mechanistic understanding

The mechanistic understanding of the process is sufficient for the needs of the safety assessment.

Any mechanistic/conceptual uncertainties are handled pessimistically since immediate release upon water contact is assumed.

Model simplification uncertainties

The uncertainties concerning the dissolution process are covered by the pessimistic assumption that the instant release fraction of the radionuclide inventory is released immediately upon water contact.

Input data and data uncertainties

Input data and input data uncertainties for this process are discussed in the Data report (SKB 2022d).

2.5.7 Speciation of radionuclides, colloid formation

Overview/general description

Radionuclides that have segregated from the fuel or are exposed to water in the fuel matrix and other metal parts can dissolve in the water present in the canister cavity and thereby potentially be transported out from the canister into the surrounding environment. If the flow of water through the

canister is slow, the radionuclide concentration is expected to rise until the solubility limit for each respective radionuclide is reached. The distribution of a given nuclide between dissolved and solid phases is determined by the solubilities of the solid phases formed. These are in turn dependent primarily on the chemical environment in the canister cavity and the temperature. The low solubility of many key radionuclides is an important constraint, limiting their concentration inside a breached canister and, hence, their rate of transport out of the canister. Radionuclide solubility refers to the total aqueous concentration of all the chemical species and isotopes of a radioactive element that are in equilibrium with each other and with a pure crystalline or amorphous solid phase containing the given element. If true equilibrium with a characterised solid has been established, chemical thermodynamics allows the estimation of the maximum concentration of all soluble species for a given radionuclide in a specified groundwater composition. The solubility-limited concentrations and chemical speciation of important radionuclides to be used in the safety assessment have been reported in Duro et al. (2006a, b) and Grivé et al. (2010b). In addition, the effect of phosphate and temperature on radionuclide speciation and solubility were investigated by Grivé et al. (2013a).

Radionuclides can be released in the form of colloidal or pseudo-colloidal particles from the spent fuel. Alternatively, colloidal particles may form during the nucleation of new solid phases inside the canister. This is of no importance for radionuclide dispersal from the canister, as long as the bentonite buffer, which acts as an efficient filter for colloids, remains in place.

In the case of an advective flow scenario and major bentonite loss, the relatively high flow lowers further the concentrations of minor radionuclides such as, e.g., thorium, making it difficult to reach saturation with respect to the corresponding solid phases. On the other hand, several major radionuclides, especially the actinides, may reach solubility limits of their amorphous oxides after a certain period of time and form colloidal oxide particles. Pu(IV) especially is known to have a high tendency to form colloids, and the formation of Pu colloids has been considered while modelling experimental data in the SKB fuel programme (Bruno et al. 1998). The measured concentrations of U, Pu and Np in fuel tests simulating conditions inside a damaged canister (Carbol et al. 2009b, Fors et al. 2008, Cui et al. 2008, Puranen 2017, 2018) are very low and the trend observed in their variation with time indicates the formation of an actinide co-precipitate rather than separate oxide phases. The Pu concentrations were almost two orders of magnitude lower than the U concentrations and Np concentrations almost one order of magnitude lower than the Pu concentrations, which is close to the relative proportions of U, Pu and Np in the spent fuel. The measured Pu concentrations under such conditions, expected to be lowered further in the advective flow case by the relatively high flow, do not suggest an over-saturation with respect to the estimated solubility of $Pu(OH)_4(am)$ (Neck et al. 2007) or the solubility product in the SKB database for Pu (Duro et al. 2006a).

The data from Neck et al. (2007) show that measured Pu(IV) concentrations, attributed to the formation of apparently stable Pu(IV) colloids, were one to two orders of magnitude higher than the solubility of $Pu(OH)_4(s)$. These particles appear to behave thermodynamically so that if you dilute them under their solubility product, they dissolve (Zänker and Hennig 2014). Knopp et al. (1999) present data that indicate that Pu(IV) colloids are formed only in oversaturated conditions with respect to $Pu(OH)_4(s)$ and not in undersaturated conditions. In this situation, and based on the observation of Pu(IV) co-precipitatation with U(IV) as is discussed above, the concentration of Pu would be too low for intrinsic Pu colloids to form.

Dependencies between process and fuel variables

Table 2-15 shows how the process influences, and is influenced by, all fuel variables.

The temperature influences both the kinetics of dissolution/precipitation processes as well as the solubility and complexation equilibria. For many solids, even the crystallinity of the solid formed depends on temperature; e.g. $UO_2(s)$ precipitated from near neutral solutions at low temperatures is amorphous and the crystallinity increases with temperature (Rai et al. 2003). At the time of a possible water intrusion into the canister, the temperature is expected to have decreased to near ambient values and its influence on solubility and complexation equilibria is expected to be small.

The presence of water in a damaged canister is necessary for the process to take place and the rate of water renewal affects the precipitation/dissolution process. In view of the large residence times of the groundwater in the canister and the relatively fast kinetics of inorganic ligand complexation

and dissolution/precipitation reactions, the assumption of chemical equilibrium is not expected to introduce uncertainties in the calculation of solubility-limited concentrations. Further, by assuming solubility equilibrium, maximum expected concentrations of a given radionuclide are obtained. Moreover, both the relatively slow crystallisation of amorphous phases to more crystalline ones (Ostwald ripening) and the slow formation of solid phases as silicates, are pessimistically neglected. The amounts of solids precipitated are not expected to be so large as to affect water flow or its presence in the fuel gap and any such influence on fuel dissolution is pessimistically neglected.

Table 2-15. Direct dependencies between the process "Speciation of radionuclides, colloid formation" and the defined fuel variables and a short note on the handling in the PSAR.

Variable	Variable influence on process		Process influence on variable	
	Influence present? (Yes/No) Description	Handling of influence (How/If not – why)	Influence present? (Yes/No) Description	Handling of influence (How/If not – why)
Radiation intensity	No.	–	No.	–
Temperature	Yes.	Neglected. The probability of water ingress during the early times of elevated temperature is very low. After 1 000 years after disposal the temperature of the fuel will have a very limited effect.	No.	–
Hydrovariables (pressure and flows)	Yes. Presence of water necessary for the process.	Water is assumed to be present after failure.	Yes.	Effect of precipitates pessimistically neglected.
Fuel geometry	No.	–	Yes.	Influence of solids pessimistically neglected.
Mechanical stresses	No.	–	No.	–
Radionuclide inventory	No.	–	No.	–
Material composition	No. Indirectly through water composition.	–	Yes. Deposition of precipitated solids on materials.	Modelled using solubility limits.
Water composition	Yes.	Included in the modelling.	Yes. Dissolved radio-nuclides in water.	Source term for radionuclide release.
Gas composition	No. Indirectly through water composition.	–	Yes. Dissolution of gaseous radionuclides.	Source term for radionuclide release.

The radionuclide inventory does not in principle affect the precipitation or complexation processes, but determines the maximum availability for any given radionuclide at a given time.

Due to corrosion of the cast iron insert, reducing conditions are expected to exist inside the canister (see Section 3.5.1). Any oxidised forms of radionuclides released from the fuel will very probably be precipitated in their reduced forms directly on the fuel surface, or by interaction with iron corrosion products present on the surface of the cast iron insert.

The composition of the groundwater inside the canister determines both the composition of radio-nuclide precipitates and their maximum soluble concentration. For redox-sensitive radionuclides, redox conditions are extremely important, and their variation can cause several orders of magnitude difference in the radionuclide concentration in some cases. Groundwater parameters, such as pH and the concentration of strong complexing ligands, (e.g. carbonate), influence most of the equilibria,

especially those of actinide and lanthanide elements. High salinity groundwaters affect the equilibria through their high ionic strength. Moreover, the dissolution/precipitation of radionuclides changes the composition of the groundwater inside the canister.

The presence of dissolved gases affects the redox conditions inside the canister, but is not expected to influence solubility or complexation equilibria. The influence of pressure of the magnitude expected inside the canister on chemical equilibria is negligible (Marion et al. 2005). On the other hand, certain radionuclides may enter the gas phase during the dissolution of either the rapid release fraction (Section 2.5.6) or the fuel matrix (Section 2.5.5) and establish a Henry's Law equilibrium.

Boundary conditions

There are no relevant boundary conditions for this process other than the physical boundary set by the geometries of the components involved.

The presence of liquid water in a breached canister and sufficient progress of fuel dissolution to establish oversaturation with respect to a given element are necessary requirements for the process to take place. The chemical properties of the solution and the temperature influence the solubility of the potential solid phases.

Model studies/experimental studies

The quantitative estimation of radionuclide solubilities requires reliable thermodynamic equilibrium constants, obtained through experimental studies of appropriate chemical systems. The need for chemical equilibrium data in the field of nuclear waste management has contributed to a large number of basic thermodynamic studies on many radionuclides during the last 30 years. Most of this information has been reviewed by international expert teams within the framework of the NEA-TDB project (Grenthe et al. 1992, Silva et al. 1995, Rard et al. 1999, Lemire et al. 2001, 2013, Guillaumont et al. 2003, Olin et al. 2005, Gamsjäger et al. 2005, 2012, Brown et al. 2005, Hummel et al. 2005, Rand et al. 2009). Recent work published by the NEA-TDB includes a 2nd update of the U, Am, Np, Pu and Tc (Grenthe et al. 2020).

In solubility calculations for a safety assessment, potential solubility-limiting phases are postulated for each radioelement. The most likely solid phases expected to form under the conditions that prevail are chosen. For example, amorphous phases are chosen instead of crystalline ones, while stable sulfides and silicates, whose formation is uncertain, are often disregarded entirely in the modelling. The calculations determine the solubility of the radioelement phase in the groundwater in equilibrium with all the soluble species it forms for the given range of conditions, i.e. the speciation of all radionuclides in the aqueous phase is determined simultaneously. Speciation is important for both solubility and the transport properties of the radionuclide in buffer and rock. Special care has been taken to select a reliable and fully consistent thermodynamic database (Duro et al. 2006a, Grivé et al. 2010b) used to derive solubility limits for a range of pure solid phases which could potentially form under the expected conditions. The effects of including phosphate in the solubility calculations (Grivé et al. 2013a) was investigated, with the conclusion that even low concentrations of phosphate would significantly lower the solubility for some radionuclides; exluding phosphates is therefore a pessimistic approach. Notably, the radionuclides that dominate the calculated dose in the safety assessment are not affected by phosphate and thus, the result of the safety assessment is the same with or without taking phosphate into account.

The output of the thermodynamic modelling is compared to literature data on the formation of identified minerals and measured concentrations in natural and laboratory systems. The extensive available spent fuel leaching data obtained under oxidising or initially argon-purged atmospheres for important elements in the safety assessment have been discussed. A review of the solubility limits used in eight international safety assessment exercises has also been carried out (Duro et al. 2006b, Grivé et al. 2010b).

In safety assessments, usually no credit is taken for the expected co-precipitation of elements with similar chemical properties, since the solubilities of the component elements in ideal solid solutions are lower than those of the corresponding pure components. One exception is radium-calcium-barium sulfate co-precipitation (Berner and Curti 2002), for which there is abundant literature (Doerner and

Hoskins 1925, Berner and Curti 2002). Based on the results of Berner and Curti (2002), Berner (2002) proposed a solubility for Ra based on co-precipitation with Ba in the Opalinus Clay safety assessment (Nagra 2002). A second exception is the use of Ra-Ca-carbonate co-precipitation used in the Japanese H 12 analysis (quoted in Duro et al. 2006b). There may still be, however, some uncertainties in using solid solution solubilities for safety assessment purposes at SKB. The NEA state-of-the-art report (Bruno et al. 2007) discusses the possibilities for solid solution formation under repository conditions and suggests that at the relatively low temperatures expected in a repository when ion diffusion in the solid phase is negligible, the transition from adsorbed layer or surface precipitate to solid solution is expected to occur only in solids with high re-crystallisation rates.

For this reason, the case of radium-barium-sulfate co-precipitation, for which there are literature reports of high rates for barite re-crystallisation (Hahn 1936, Goldschmidt 1940), has been investigated in some more detail. As a first stage, a report summarising the thermodynamic and kinetic evidence in the literature for this specific case as well as its application on a KBS-3 repository has been compiled (Grandia et al. 2008). If Ra and Ba are released simultaneously from spent fuel, all existing evidence indicates that Ra will be readily incorporated into the precipitating $BaSO_4$ to form a Ra-Ba-sulfate solid solution. Grandia (2013) discusses this issue in more detail. It is concluded that the behaviour of the system can be described by the established aqueous-solid solution formalism, assuming that the system behaves ideally. However, Ba and Ra have different sources; Ba is a fission product or a daughter of fission products, while Ra is a uranium decay product. If they are not released simultaneously, Ba from fuel dissolution can be expected to have precipitated as barite in sulfate rich solutions when the Ra released from secondary sources such as UO_2 precipitated in the canister, reaches its peak after about 300 000 years.

In order to obtain further evidence for the co-precipitation kinetics in this case, an experimental study of the barite re-crystallisation and its co-precipitation with Ra has been carried out (Bosbach et al. 2010). The experimental investigation of the uptake of Ra-226 and Ba-133 by two different barite powders (0.31 and 3.2 m^2/g) in aqueous solutions shows that there is a significant uptake of Ra into the bulk of barite crystals. In these experiments, the observed rapid kinetics of Ra-uptake in barite was seen to change and drop significantly within 400 days, even though a zero exchange rate could not be unambiguously demonstrated. In a subsequent experiment (Klinkenberg et al. 2014), the solid phases were analysed by microscopic and spectrometric methods and it was shown that Ra uptake was not limited to the surface of the barite particles but involved the entire solid.

Brandt et al. (2015) report results from a ca 2.5 year long experiment at close-to-equilibrium conditions, in which initially, non-equilibrium Ra entrapment occurred, followed by slow recrystallization toward true thermodynamic solid solution equilibrium. This indicates that on a geological timescale, which are relevant for the repository, the binary $(Ba,Ra)SO_4$ solid solution should be treated as thermodynamic equilibrium system.

During a ca 3.8 year (1400 days) long experiment, uptake of Ra into barite was observed to be connected with a change in porosity (Weber et al. 2017). During the course of the experiment the internal structure of the solid was seen to change, so that small fluid inclusions or nanopores, disappeared in favour of larger pores. At later stages of the longterm experiment the Ra distribution becomes homogenous while nano-scale and macro-scale pores disappear. After ca 1200 days, the system appears to reach equilibrium with a $(Ra,Ba)SO_4$ solid solution (Weber et al. 2017). That the internal structure and crystallinity of the solid phase influences the measured recrystallization rate is supported by a recent study which used a barite solid which has been pre-equilibrated for 0.8 years (Heberling et al. 2018) In this case, the authors estimate it would take several thousand years (1400 to 16900 years) for complete bulk barite equilibration in the presence of Ra. These studies confirm the Ra uptake by barite but point toward the influence of solid state characteristics on the kinetics of the Ra uptake and formation of a Ra-Ba solid solution.

Natural analogues/observations in nature

Elemental concentrations in natural systems, such as rocks, minerals or sea water, as well as elemental concentration measurements in relevant natural analogue sites, are discussed for most of the elements in Duro et al. (2006b). The comparison of the results of thermodynamic modelling with data from natural and laboratory systems is used to check the consistency of the models with available experimental data.

Time perspective

If the canister is breached and water comes into contact with fuel, the process continues throughout the life of the repository.

Handling in the PSAR

The process is only relevant if the copper shell has been breached.

The process will be handled by applying concentration limits in the canister cavity water in the radionuclide transport calculations.

Model: Solubility limits for radionuclides inside a failed canister are calculated using Simple Functions (Grivé et al. 2010a) in combination with @Risk, both implemented in Excel. The resulting aqueous concentrations are used as input data to the near-field radionuclide transport model COMP23 (Cliffe and Kelly 2006).

Concentration limits used in the probabilistic calculations are based on a set of four different types of groundwater compositions (temperate, permafrost, glacial, submerged), representing different stages in the hydrogeochemical evolution of Forsmark as reported by Salas et al. (2010). For deterministic calculations, only water representative of the temperate climate is used. These groundwater data, are archived at SKB (Puigdomenech 2012). The data set used by Simple Functions is a combination of an equal amount of data from the four different waters; it is randomly sampled by @Risk to provide the following input data to Simple Functions: pH, Eh, ionic strength, [HCO_3^-], [SO_4^{2-}], [Cl], [Ca], [Na], [Fe], [Si]. For the safety assessment, using version B, the interaction with the corroding canister insert is taken into account which affects the Eh and Fe^{2+} (Grivé et al. 2010a). The Eh is thus buffered by the corroding iron and assumed to be controlled by the equilibrium between magnetite and goethite (Evins 2013b).

The solubility limiting solid phases included in Simple Functions have been selected from a prior expert judgement (Duro et al. 2006a, b, Grivé et al. 2010b). Of these phases the less soluble phase for each radioelement is selected by Simple Functions Spreadsheet. Some radionuclides are not solubility limited in the calculations. Solubility limits are used for the following elements: Ni, Se, Sr, Zr, Nb, Tc, Pd, Ag, Sn, Sm, Ho, Pb, Ra, Th, Pa, U, Np, Pu, Am, Cm. Thermodynamic data for the relevant chemical reactions are also included in Simple Functions (Duro et al. 2006a, Grivé et al. 2010b). The solubility data are qualified in the PSAR Data report (SKB 2022d).

The resulting solubility limits, presented as distributed data sets, are used as input to the near field radionuclide transport model. The median values of the solubility limits for temperate climate conditions are tabulated in the PSAR Radionuclide transport report (SKB 2022e).

Boundary conditions: The process is confined to the canister and no precipitation of radionuclides in the form of solid phases is considered to take place in the buffer or in the far field.

Handling of variables influencing this process: The concentration limits applied are valid for a temperature of 25 °C, which is a reasonable temperature for the canister interior after a few hundred years of deposition (Duro et al. 2006b). The influence of water composition is handled by using four different groundwater compositions representing four environments: temperate, permafrost, glacial and submerged.

Handling of uncertainties in the PSAR

Uncertainties in mechanistic understanding

The calculation of the solubility limits for each element of interest is based on equilibrium chemical thermodynamics and the fundamental understanding of the processes is sufficient for the needs of the safety assessment. Pessimistic assumptions are made whenever there are conceptual uncertainties. For example, all the uranium resulting from spent fuel dissolution is assumed to contribute to the ingrowth of radium, including uranium in precipitated UO_2, thus, neglecting any Ra formation inside grains.

Model simplification uncertainties

The model does not account for any changes in water chemistry. The Simple Functions tool considers only those solid phases that are likely to form under the surrounding conditions of interest for the waste disposal for SKB and the corresponding aqueous species accounting for, at least, 1 % of the total aqueous concentration of the element under study. Thus, there is some uncertainty concerning the influence of change in water chemistry on the speciation. However, the probabilistic approach involving the four main groundwater types expected in Forsmark is expected to cover these uncertainties.

Input data and data uncertainties

Input data and input data uncertainties for this process, i.e. the concentration limits to be used, are discussed in the PSAR Data report (SKB 2022d), based on the data reported in Duro et al. (2006b) and Grivé et al. (2010b). Uncertainties in thermodynamic data are discussed in Grive et al. (2013b).

2.5.8 Helium production

Overview/general description

Helium builds up in spent fuel due to the alpha decay of actinides. Some of that helium may reach the gap between the fuel pellet and the Zircaloy cladding. This leads to a pressure build-up inside the tube, which can in turn lead to mechanical tube rupture (see Section 2.4.1). If, or when, the cladding ruptures, a negligible pressure increase arises in the canister cavity.

Most of the helium, however, will be trapped within the fuel matrix. This self-irradiation and internal pressure build-up has the potential to detrimentally affect the mechanical stability of the UO_2 fuel matrix, open the grain boundaries and, thereby, possible increase the Instant Release Fraction (IRF).

Dependencies between process and fuel variables

Table 2-16 shows how the process influences, and is influenced by, all fuel variables.

Boundary conditions

There are no relevant boundary conditions for this process other than the physical boundary set by the geometries of the components involved.

Model studies/experimental studies

At 1 000 years after discharge from the reactor, fuel with a burnup of 60 MWd/kgU would contain about 9×10^{18} He atoms/g. At an age of 10^5 years, the concentration of He will have increased to about 3.2×10^{19} atoms/g. After a million years, the concentration would be about two times higher than that.

A number of experimental studies of the possible consequences of helium build-up have been performed using He ion implantation (Desgranges et al. 2003, Roudil et al. 2004, Guilbert et al. 2003). The implanted amounts were in the range 2×10^{18} atoms/g to 2×10^{20} atoms/g. Only in one case at 3.6×10^{19} atoms/g (Guilbert et al. 2003) was mechanical damage observed after heating to 500 and 600 °C. After annealing, the samples showed flaking at the surface with the largest effect seen in the 600 °C sample. This was caused by gas bubbles coalescing and growing, initiating a crack in the UO_2, followed by flaking off of the material above the implantation location. Since there was a dramatic difference in the behaviour of the samples heated to 500 and 600 °C, it is by no means clear whether gas bubbles could coalesce at the much lower temperatures that will pertain in the repository. The concentration of He used in these tests was also far greater than the amount which will be present in spent fuel disposed of in the Swedish repository, even at very long times after disposal.

Table 2-16. Direct dependencies between the process "Helium production" and the defined fuel variables and a short note on the handling in the PSAR.

Variable	Variable influence on process		Process influence on variable	
	Influence present? (Yes/No) Description	Handling of influence (How/If not – why)	Influence present? (Yes/No) Description	Handling of influence (How/If not – why)
Radiation intensity	Yes. The alpha decay rate determines the rate of helium build-up.	Neglected. It is pessimistically assumed that all fuel rods are breached as soon as water contacts the fuel. The helium build-up in the canister void is negligibly small.	No.	–
Temperature	No.	–	No.	–
Hydrovariables (pressure and flows)	No.	–	No.	–
Fuel geometry	No.	–	No.	–
Mechanical stresses	No.	–	Yes. Mechanical stresses in the cladding and possibly in the fuel.	Neglected. It is pessimistically assumed that all fuel rods are breached as soon as water contacts the fuel. The helium build-up has no detrimental effect on the mechanical stability of the fuel.
Radionuclide inventory	Yes. Influenced by the content of alpha emitters.	Neglected. See above.	No.	–
Material composition	No.	–	No.	–
Water composition	No.	–	No.	–
Gas composition	No.	–	Yes. May result in He release.	Neglected. Marginal amount in comparison to the H_2.

Ferry et al. (2008) analysed the effect of helium build-up in the central and intermediate zones as well as in the rim structure of the fuel pellet. They conclude that, for the zones of the fuel that have not undergone restructuring, He release through diffusion to the grain boundaries should be relatively low. Therefore, for the central and intermediate zones of the fuel pellet only grain micro-cracking due to over-pressure or formation of gas bubbles with helium should cause significant helium release from the uranium dioxide grains. By assuming a realistic number density and size distribution of intra-granular fission gas bubbles at the end of the irradiation and that all helium atoms formed are trapped in these bubbles, the concentration of helium required to reach a critical bubble pressure is 4×10^{20} atoms/cm^3 (about 3.8×10^{19} atoms/g for 94 % theoretical density) in 10 nm bubbles. For larger bubbles, the critical pressure is about 10^{21} atoms/cm^3 ($\sim 9.6 \times 10^{19}$ atoms/g). Using the data presented by Ferry et al. (2008), one can conclude that the helium produced by alpha-decay is not sufficient to produce micro-cracking of grains in UO_2 fuel for several hundred thousand years.

The rim region of the fuel has undergone fission at a rate up to three times higher than the mean fission rate of the pellet. This is caused by a build-up of fissile plutonium and other actinides due to capture of epithermal neutrons. The higher fission rate causes a restructuring of the fuel matrix yielding sub-micrometre grains and a higher porosity (exceeding 10 %). These large pores form sharp angles at the grain boundary, where crack-tips can be initiation points for crack growth and fracture of the ceramic. Ferry et al. (2008, 2010, 2016) analysed the effect of helium in this region by considering the helium pressure necessary to exceed the fracture toughness of the material. Their conclusion was that even in the rim region, conditions for crack propagation in the grain boundaries would not occur. The rim inventory should, therefore, not contribute to the Instant Release Fraction.

It can be concluded that, for the burnup range relevant for Swedish conditions, the mechanical stability of the spent fuel to be disposed of in Sweden will not be detrimentally affected by the accumulation of He in the fuel after disposal.

The amounts of He formed after 100 000 years (see above) correspond to 1.7 to 2.2 dm^3 (STP) He for each fuel pin. This is equivalent to a pressure rise of 3.4 to 4.4 MPa if released to the void volume (50 cm^3) in the fuel pin. In addition, the fuel pins may also have been pre-pressurised to a few MPa. If all the accumulated helium was released to the void inside the canister, the pressure rise would be 0.20 to 0.25 MPa (or about twice the level due to pre-pressurisation) after 100 000 years, and about 0.4 to 0.5 MPa after 1 000 000 years. This is considerably lower than the pressure external to the canister and will have negligible consequences for its stability.

Lilja (2012a) provided additional information concerning the canister internal overpressure from both accumulated He and initial gas and water (see Section 2.3.1), showing that at 10 000 years, the pressure will have risen to a maximum of 0.55 MPa. At that time, the pressure from the fully water saturated bentonite will be about an order of magnitude larger, and therefore there is no more internal overpressure after that time.

Valls et al. (2014) studied the build-up of He in MOX fuel with a burnup of 50 MWd/kgHM using the code AMBER. In a comparison with a 60 MWd/kgU PWR UOX fuel, it was observed that the total amount of He produced in the MOX fuel (atoms per cm^3) was about half an order of magnitude higher than the PWR fuel. This relationship does not change significantly over time, and stems from the relative abundances of the main He-producing nuclides in the fuel, which in turn stems from the higher Pu-content in the fresh MOX fuel. Since Ferrry et al. (2010) show that the pressure of pores in the UOX rim zone is 10–50 times lower than the critical pressure, the higher pressure of He in MOX pores still would not reach the critical pressure. The calculations show also that the pressure inside the canister due to He generation is at all times much lower than the hydrostatic pressure and/or the bentonite swelling pressure outside the canister.

Natural analogues/observations in nature

Roudil et al. (2008) have studied a sample of natural uranium dioxide (pitchblende) from Pen Ar Ran in France. The sample was 320 Ma old and had not been subjected to any single events that could have caused helium loss. The sample had retained less than 5 % of the total amount of radiogenic helium formed. The retained amount corresponds roughly to the expected solubility of helium in uranium dioxide. The authors deduced a diffusion coefficient that is nine orders of magnitude higher than that expected in well-crystallised UO_2 nuclear fuel. The reason for this is not presently clear.

Time perspective

The helium build-up proceeds continuously as long as there is uranium left in the fuel.

Handling in the PSAR

It is assumed that all fuel rods are breached as soon as water contacts the fuel, i.e. the ability of the cladding to prevent or retard radionuclide transport is pessimistically neglected.

The helium build-up in the canister void is neglected. The helium build-up has no detrimental effect on the mechanical stability of UO_2 fuel. For MOX fuel, the helium production is higher, but probably not high enough to reach the critical pressure needed for bubble rupture (Ferry et al. 2010, Valls et al. 2014). Thus, the radionuclide inventairy in the rim regions for both UOX and MOX fuel are excluded from the instant release fraction.

If the helium is released to the void in the canister, the resulting pressure increase will not have any consequences for the mechanical stability of the canister.

Boundary conditions: As stated above, there are no relevant boundary conditions for this process other than the physical boundaries set by the geometries of the components involved.

Handling of variables influencing this process: The influence of the radionuclide inventory is explicitly included in all estimates justifying the neglect of this process.

Handling of uncertainties in the PSAR

Uncertainties in mechanistic understanding

Uncertainties related to i) the fraction of the created alpha particles that actually contribute to helium pressure build-up, and ii) the impact of this pressure build-up on cladding integrity are treated pessimistically.

The main uncertainty related to the mechanical alterations of the fuel matrix is the uncertainty associated with future burnup levels.

Model simplification uncertainties

The simplifications with respect to cladding barrier function and pressure build-up in the canister interior are pessimistic.

Input data and data uncertainties

Ferry et al. (2008) state that the main uncertainty of their model is the value of the critical bubble pressure, which is based on a fracture stress derived from three-point bending tests on polycrystalline UO_2, and that a larger value is to be expected in mono-crystalline UO_2. For the rim section, a pessimistic expression has been used for the calculation. It would be necessary to validate this model by more microscopic approaches. The degree of confidence in this model is, however, relatively poor due to the lack of other data to confirm the calculations.

2.5.9 Chemical alteration of the fuel matrix

Overview/general description

In nature, coffinite, a uranium silicate, is commonly observed as an alteration product of uraninite (e.g. Janeczek and Ewing 1992, Evins and Jensen 2012). Already in 1992, Janeczek and Ewing (1992) discussed the possibility of spent UO_2 fuel alteration under reducing conditions through the formation of coffinite, $USiO_4 \cdot nH_2O$. The reaction can be written in simplified form as

$$UO_2 + H_4SiO_4 \rightarrow USiO_4 + 2H_2O$$

The significance of this reaction relates to the relative stability of the two solids in the repository environment. In a situation where coffinite is more stable than the spent nuclear fuel, precipitation of coffinite would remove uranium from solution before the solubility limit of UO_2 is reached, thus causing a continued dissolution of the spent fuel. Via this process, fission products and actinides in the UO_2 matrix could potentially be released at a rate higher than expected if UO_2 is the solubility limiting phase, and no oxidation of uranium occurs.

Lately, efforts have been made to fill the gaps concerning thermodynamic data for coffinite. These studies are described below. Using the improved thermodynamic data, some conclusions can be drawn regarding the relative stabilities of the two solids in the chemical environment expected inside a failed canister in the repository.

In oxidizing waters, chemical alteration of UO_2 involves formation of various uranyl minerals, but only when and if the solubility limit for any of these minerals is achieved in the canister interior. Since the waters in the canister interior will be reducing during the time frame of the safety assessment, only coffinitization, which may occur in a reducing environment, is discussed here.

Dependencies between process and fuel variables

Table 2-17 shows how the process influences, and is influenced by, all fuel variables.

Boundary conditions

There are no relevant boundary conditions for this process other than the physical boundary set by the geometries of the components involved.

Table 2-17. Direct dependencies between the process "Chemical alteration of the fuel matrix" and the defined fuel variables and a short note on the handling in the PSAR.

Variable	Variable influence on process		Process influence on variable	
	Influence present? (Yes/No) Description	Handling of influence (How/If not – why)	Influence present? (Yes/No) Description	Handling of influence (How/If not – why)
Radiation intensity	No.	–	No.	–
Temperature	Yes. The process, if it occurs will take place in the long term and at the ambient constant temperature.	The process is neglected. Release of matrix-bound radionuclides will occur during the UO_2 dissolution.	No.	–
Hydrovariables (pressure and flows)	Yes. The process requires supply of silicates.	The process is neglected. Release of matrix-bound radionuclides will occur during the UO_2 dissolution.	No.	–
Fuel geometry	No.	–	No.	–
Mechanical stresses	No.	–	No.	–
Radionuclide inventory	No.	–	No.	–
Material composition	No.	–	No.	–
Water composition	Yes. The process requires sufficiently high silicate content in the water.	The process is neglected. Release of matrix-bound radionuclides will occur during the UO_2 dissolution.	No.	–
Gas composition	No.	–	No.	–

Model studies/experimental studies

Up until 2015, the thermodynamic data for coffinite used in solubility calculations were essentially based on estimations. This is due to two things: 1) Coffinite naturally occurs as fine-grained crystals often intergrown with associated minerals and organic material, which makes it hard to use natural materials to determine thermodynamic properties. 2) It appeared difficult to synthesize pure coffinite in a laboratory. Synthetic coffinite prepared by Fuchs and Hoekstra (1959) contained excess silica and some uraninite. Robit-Pointeau et al. (2006) attempted unsuccessfully to synthesise coffinite, and Hemingway (1982) also reports and references unsuccessful attempts to produce coffinite. Thermodynamic data were therefore estimated largely from other, better known systems, or from geological information (see below). Brookins (1975) calculated a free energy of formation of coffinite (−456 kcal/mol, −1908 kJ/mol) from comparison with Th- and Zr- silicate systems. However, based on observations in natural environments (see below) this value has been deemed improbably low.

Hemingway (1982) proposes a model for the deposition of coffinite, which involves reduction of U(VI) from solution on surfaces with amorphous silica coatings. He also concludes that coffinite should be metastable with respect to uraninite and quartz at all geologically important temperatures. However, Xu and Wang (1999) considered alteration of a mixed-valence uranium oxide (UO_{2+x}) into coffinite and concluded, from their thermodynamic model, that the reaction could only take place at temperatures lower than 130 °C. The understanding of this reaction through thermodynamic modelling has been hampered by the lack of reliable thermodynamic data. However, focused research efforts have improved the situation.

Synthesis of purified (U,Th)SiO_4 (method described by Clavier et al. 2013), used in solubility experiments, allowed through extrapolation, the determination of the solubility constant for pure $USiO_4$ (Szenknect et al. 2013). Through this extrapolation, the free energy of formation from the oxides was determined to 16 ± 3 kJ/mol, suggesting that coffinite is less stable than previous estimates had indicated, and that at room temperature, coffinite is metastable with respect to the crystalline oxides. Synthetic coffinite, large and crystalline enough to allow further study, has now been produced in two different laboratories. The thermodynamic properties of these samples were studied, resulting in the determination of the enthalpy change for the formation from UO_2 and SiO_2 to ca 25 kJ/mol (Guo et al. 2015). This value is higher than previous estimates. Using this new material in solubility experiments, Szenknect et al. (2016) determined the solubility constant for $USiO_4$ (cr) at 25 °C and 1 bar as log K −5.25 ± 0.05, while the standard free energy of formation of coffinite, from the elements, is determined to be −1867.6 ± 3.2 kJ/mol. This can be compared with the previous values, predicted and estimated from other mineral systems and from natural samples (see below): it is higher than the value of ca −1883 kJ/mol given by Grenthe et al. (1992) but lower than the estimated value representing amorphous coffinite of ca −1835 kJ/mol (Langmuir 1997). Szenknect et al. (2016) concludes, through geochemical simulations using the new data, that coffinite should precipitate in solutions supersaturated with respect to UO_2(cr), but undersaturated with respect to UO_2(am) in aqueous solutions with silica concentrations typical of groundwater.

Konings and Plyasunov (2016) commented on the thermodynamic data presented by Szenknect et al. (2016), and pointed out that the entropy was noticeably large and that, taken together with previously reported data, a discrepancy was apparent. They suggest that the effect of observed metastability needs to be clarified. In reply Szenknect et al. (2017) agree that new experimental data are required to solve the “coffinite issue”, but it was also pointed out that entropy values may be influenced by the polycrystalline nature and crystallite size of the studied coffinite samples. The differences noted raises the question of what is the most the appropriate way to estimate entropy.

Recently, experimental evidence of coffinitization of UO_2 was presented (Szenknect et al. 2020). The experiment was performed at pH of ~9 in room temperature and with a Si concentration of ca 1.7 mM. The system was anoxic and slightly reducing (Eh ~ −50 mV). It should be pointed out that at this Eh, which is significantly higher than that expected in the repository, dissolved U is stable as U(VI), while coffinite in this Eh-domain is stable and can co-exist with meta-schoepite. The stability domains were calculated using the newly proposed thermodynamic data (Szenknect et al. 2016).

Natural analogues/observations in nature

As noted above, up until 2015, most information regarding coffinite and 'coffinitization' of uraninite has been extracted from nature and natural samples

Langmuir (1978) points out that the value given by Brookins (1975) for the free energy of coffinite formation implies that uraninite would be unstable towards coffinite if the activity of H_4SiO_4 exceeded $10^{-6.9}$ M (8 ppb SiO_2). Groundwater normally has a much higher silica concentration; Langmuir (1978) gives the average as 17 ppm, while typical values for Scandinavia are 10–15 ppm. Therefore, Langmuir (1978) instead proposed a equilibrium value of silica content of 10^{-3} (60 ppm), since this is the value found in the groundwaters at Grants mineral belt in New Mexico, where both uraninite and coffinite occur in uranium ore deposits. Based on this assumption, Langmuir (1978) estimated a ΔG of formation of −452 kcal/mol (−1 891 kJ/mol), but this value was later corrected by Langmuir and Chatham (1980) to −449.9 kcal/mol (−1 882 kJ/mol). The value given by the OECD/NEA (−1 883.6 kJ/mol; Guillamont et al. 2003) was recalculated , considering auxiliary available data and also based on estimation (Langmuir and Chatham 1980). At both Oklo and Cigar Lake, coffinite is present as a uraninite alteration product (see e.g. Janeczek and Ewing 1992). The alteration in these deposits likely happened through dissolution in heated (hydrothermal) fluids followed by re-precipitation under reducing conditions. There are no indications of a solid state transformation of uraninite to coffinite. The ca 1700 Ma Palmottu mineralisation site is a U-Th deposit in mica gneisses and granites typical of the rocks in the Fennoscandian Shield. The main U-bearing ore minerals at this site are uraninite [UO_{2+x}, $(0.01 < x < 0.25)$] and monazite (a thorium (and uranium) bearing rare earth phosphate). Coffinite is a widespread alteration product of uraninite, which formed soon after the precipitation of its precursor mineral. The majority of the uranium is found as U(IV) phases, uraninite and coffinite, , demonstrating that reducing conditions have prevailed in the bedrock for most of its existence. The alteration of the uraninite at Palmottu proceeded under reducing conditions, observed by the formation of uranous silicate phases instead of uranyl compounds. Evidently the silica-rich residual hydrothermal fluids of the uraniferous pegmatites were responsible for the alteration.

Time perspective

The process cannot start until the copper canister has failed. Then, the process may be initiated only if secondary phases are more stable than the spent nuclear fuel under the prevailing conditions inside the failed canister. The process is likely to be slow and may be ongoing for millions or years.

Handling in the PSAR

Since the alteration of the uranium dioxide fuel to coffinite, if it occurs, will most likely happen through a dissolution and re-precipitation process, any release of matrix-bound radionuclides will occur during the UO_2 dissolution. Based on the new thermodynamic data, coffinite is energetically metastable with respect to UO_2(cr) and SiO_2(cr). Considering that spent nuclear fuel is expected to be very close to UO_2(cr), there is no apparent thermodynamic driving force for bulk coffinitization of spent nuclear fuel. Therefore, the formation of coffinite will not increase the release rate from the fuel and coffinitization of the spent fuel matrix can be disregarded in the safety assessment.

Handling of uncertainties in the PSAR

Uncertainties in mechanistic understanding

Not applicable.

Model simplification uncertainties

Not applicable.

Input data and data uncertainties

Not applicable

2.6 Radionuclide transport

Overview/general description

If water enters a breached canister, corrosion of the cast iron insert and the fuel's metal parts begins, see Sections 3.5.1 and 2.5.4. With time, water may come into contact with the fuel, thereby causing radionuclides to be released as water-soluble species or colloids (Section 2.5.7). Radionuclides are also present in the metal parts of the fuel and released when they corrode.

Released radionuclides can be transported in the interior of the canister and exit through a breach in the copper shell. Radionuclides dissolved in water inside the canister can be transported either advectively with the water, or by diffusion in the water. Transport in water is the predominant mode of mobilisation of radionuclides, although some nuclides occur in gaseous form in the canister and may also be transported in the gas phase; e.g. C-14, Rn-222 and Kr-85.

The geometry of transport pathways in a breached canister is determined by the original geometry of the canister and the fuel modified by any changes caused by corrosion. For water to contact the fuel and release and transport radionuclides there must be penetrating breaches in both the cast iron insert and the Zircaloy cladding. Even if such breaches have occurred, the remaining structures can be expected to constitute a considerable transport barrier, both to the inflow of water (Section 2.3.1) and to the outward transport of soluble nuclides. The structure of the four-metre-long cladding tubes and other metal parts of the fuel, the cast iron insert and the copper canister prevent effective transport. Corrosion deposits from the cast iron insert in particular can be expected to obstruct transport (see Section 3.5.1). The surfaces of all of these structures may act as sorption sites for certain radionuclides.

Dependencies between process and fuel variables

Table 2-18 shows how the process influences, and is influenced by, all fuel variables.

Table 2-18. Direct dependencies between the process "Radionuclide transport" and the defined fuel variables and a short note on the handling in the PSAR.

Variable	Variable influence on process		Process influence on variable	
	Influence present? (Yes/No) Description	Handling of influence (How/If not – why)	Influence present? (Yes/No) Description	Handling of influence (How/If not – why)
Radiation intensity	No.	–	No.	–
Temperature	Yes. Diffusion is temperature dependent.	Neglected. Water ingress is assumed to take place at the earliest 1 000 years after disposal. At that time the temperature will have a very limited effect.	No.	–
Hydrovariables (pressure and flows)	Yes.	Water is assumed to be present after failure.	No.	–
Fuel geometry	No.	–	No.	–
Mechanical stresses	No.	–	No.	–
Radionuclide inventory	Yes. Obvious.	Included in modelling.	No. Obvious.	–
Material composition	No.	–	No.	–
Water composition	Yes. Affects solubility.	Included in modelling.	Yes. Dissolved radio-nuclides in water.	Source term for radionuclide release.
Gas composition	No.	–	Yes.	Release of gaseous radionuclides.

Boundary conditions

The inner boundary is determined by radionuclide inventories in the fuel, and the release rate from the fuel and the concentrations of radionuclides in the water phase inside the canister.

The outer boundary is determined by size and shape of the defect in the copper canister.

Model studies/experimental studies

No direct studies of radionuclide transport are known for the conditions that are expected in a breached canister. The general knowledge of processes such as advection, diffusion and sorption is good, however, and the processes have been thoroughly studied.

Natural analogues/observations in nature

Not applicable.

Time perspective

After the copper shell has been breached, radionuclide transport in the interior of the canister is a relevant process in all of the safety assessment's time perspectives.

Handling in the PSAR

The process is only relevant if the copper shell has been breached.

Radionuclide transport in the interior of the canister is simplified for modelling purposes in the following way: After a given delay time has passed since the breach of the canister's copper shell, the entire cavity initially available in the canister, about 1 m^3, is assumed to be filled with water. The length of this delay time is determined based on the size of the breach in the copper shell and the subsequent water flux.

After the delay time, all the water in the canister is assumed to be available for the fuel dissolution process, i.e. to be in direct contact with all the fuel without being impaired by Zircaloy cladding or other structures. The water is assumed to be thoroughly mixed, i.e. there are no concentration gradients throughout the interior of the canister. The fuel dissolution process then determines the rate of release of matrix-bound radionuclides. Segregated nuclides are assumed to be available for dissolution in water immediately after the end of the delay time. Radionuclides in the structural parts of the fuel are released to the water at the rate of corrosion of these parts. Sorption of radionuclides on the internal parts of the canister is pessimistically neglected.

Transport of radionuclides through the breach in the copper shell is modelled as diffusion with an assumed geometry of the breach.

The modelling is carried out using the transport model COMP23 (Cliffe and Kelly 2006), integrated with the modelling of fuel dissolution, precipitation/dissolution of solubility-limited radionuclides and radioactive decay. Transport through the buffer/backfill and out to the surrounding geosphere is also handled in this model.

The micropores in the buffer are expected to prevent all colloidal transport out of the canister. Colloid transport in the interior of the canister is therefore not dealt with, since the buffer completely envelops the canister. In scenarios where the buffer is assumed to have lost its colloid-filtering capacity, solubility limits are not used (except for uranium).

Radionuclide transport in the gas phase is handled by approximate calculations.

Handling of uncertainties in the PSAR

Uncertainties in mechanistic understanding

The uncertainties surrounding water/gas flux in the interior of the canister (Section 2.3.1), corrosion of the cast iron insert (Section 3.5.1) and corrosion of the metal parts of the fuel (Section 2.5.4) are particularly large. An assessment of the geometric conditions and, therefore, the geometry of the transport pathways is, hence, also uncertain. The sorption properties of the materials in a damaged canister are also difficult to assess.

Model simplification uncertainties

Radionuclide transport in the interior of the canister is, therefore, simplified pessimistically in the safety assessment (see Handling in PSAR above).

Input data and data uncertainties

Input data and input data uncertainties for this process are discussed in the PSAR Data report (SKB 2022d).

3 Cast iron insert and copper canister

3.1 Radiation-related processes

3.1.1 Radiation attenuation/heat generation

Overview/general description

The gamma- and neutron radiation (from the radioactive disintegrations in the fuel) that extend into the canister interacts with the cast iron insert and the copper shell. Energy is thereby transferred to the materials and the radiation is attenuated. Most of the transferred energy is converted into thermal energy to generate heat.

In the cases of alpha and beta disintegrations, most of the radiation energy remains in the fuel since the fuel itself largely attenuates the radiation. In the case of gamma and neutron radiation, some of the surplus energy will escape the fuel and generate heat by attenuation in the canister materials. For gamma radiation, this fraction is estimated to comprise less than 35 % of the total heat output, see information given by Håkansson (2000).

The radiation attenuation in the canister will also have the potential to influence the microstructure and thereby affect the mechanical properties of the canister materials. This is dealt with in Section 3.4.6.

Dependencies between process and canister variables

Table 3-1 shows how the process influences**,** and is influenced by, all canister variables.

The heat generation in the canister materials is caused by the radiation and, consequently, influenced by the radiation intensity and also by the canister geometry (metal thickness) and material. The attenuation/ heat generation may also give rise to changes in the materials properties, see Section 3.4.6.

Table 3-1. Direct dependencies between the process "Radiation attenuation/heat generation" and the defined canister variables and a short note on the handling in the PSAR.

Variable	Variable influence on process		Process influence on variable	
	Influence present? (Yes/No) Description	**Handling of influence (How/If not – why)**	**Influence present? (Yes/No) Description**	**Handling of influence (How/If not – why)**
Radiation intensity	Yes. The radiation intensity causes the heat generation.	In the modelling of heat generation and dissipation, it is assumed that all heat generation takes place in the fuel itself.	No.	–
Temperature	No.	–	Yes. Radiation attenuation results in heat generation.	In the modelling of the temperature distribution in the canister, it is assumed that all heat generation takes place in the fuel itself.
Canister geometry	Yes. The intensity of radiation will depend on the canister geometry, in particular the thickness of the various components.	The canister geometry and the relevant materials are explicitly included in the calculations leading to the neglect of this process.	No.	–
Material composition	Yes. Different materials attenuate radiation to different degrees.	See above.	No.	–
Mechanical stresses	No.	–	No, but indirectly via the temperature.	See Section 3.4.4.

Boundary conditions

Part of the gamma- and neutron radiation from the radioactive disintegrations escapes the fuel into the canister and the canister materials will attenuate the energy. Most of the energy attenuation occurs in the inner parts of the canister. The remaining energy will cross the canister/buffer boundary and be dissipated outside the canister.

Model studies/experimental studies

Calculations of the canister's radiation attenuation (i.e. dose rate calculations) have been performed in Viertel (2016). An investigation the effect of including the spatial distribution of secondary heat power sources emanating from deposited gamma radiation in the canister materials has been performed (Renström 2020b, Jansson et al. 2022), with the conclusion that only a very small amount of gamma energy is deposited outside the canister, meaning that its influence on temperature development at and outside the copper shell can be disregarded.

Natural analogues/observations in nature

Not applicable.

Time perspective

Immediately after deposition, the gamma-radiation is dominated by the decay of Cs-137. This isotope has a half-life of approximately 30 years. In other words, it takes about 300 years for the gamma radiation intensity to come below one permille of the initial intensity.

Handling in the PSAR

In the modelling of heat generation and dissipation, it is assumed that all heat generation takes place in the fuel itself or in a confined volume containing the fuel, relevant for the model in question. With this approach, the temperature in the fuel will be overestimated initially, but this will be of little importance for the temperature distribution in the near field shortly after deposition and beyond.

The process is not explicitly modelled, but the dissipated energy is accounted for. Section 3.4.6 discusses radiation effects on canister materials.

Boundary conditions: The relevant boundary conditions are explicitly included in the calculations leading to the neglect of this process.

Handling of variables influencing this process: The influencing variables, i.e. the radiation intensity, the canister geometry and the relevant materials are explicitly included in the calculations leading to the neglect of this process.

Handling of uncertainties in the PSAR

Uncertainties in mechanistic understanding

The mechanistic understanding of this process is sufficient for the needs of the safety assessment.

Model simplification uncertainties

Not relevant, since the process is not explicitly modelled in the safety assessment. (The model study used to justify the neglect of the process does not entail simplifications of any importance.)

Input data and data uncertainties

Not relevant since the process is not explicitly modelled in the safety assessment. (The available data are sufficiently accurate for the model study used to justify the neglect of the process.)

3.2 Thermal processes

3.2.1 Heat transport

Overview/general description

Heat is transported in the metals in the cast iron insert and copper canister by conduction. As friction stir welding is used there will be gas (air or argon) in the gap between cast iron and copper, resulting in an important contribution to the heat transfer from iron to copper from conduction. There will also be a contribution due to heat conduction through the bottom contact between the insert and the copper canister. Heat transport by convection in the gap between cast iron and copper can be neglected (Ikonen 2020, Renström 2020a).

The process is controlled by, and influences, the temperature distribution in the materials. The heat flow towards adjacent materials, i.e. the fuel and buffer, comprises the boundary conditions. The process is a part of the repository's thermal evolution.

Dependencies between process and canister variables

Table 3-2 shows how the process influences, and is influenced by, all canister variables.

The radioactive decay (to which the radiation intensity is related) constitutes the heat source. The radiation intensity in the canister itself has negligible influence on the process. The heat is transported throught the metals, buffer and rock. The temperature of the canister is determined by the temperature boundary condition at the far-field rock and heat from the fuel. The relative temperature differences between points at different radii from the canister center are determined by the magnitude of the radial heat flow from within the canister and outward (Renström 2020a). The temperature has a negligible influence on the heat transport through conduction, but a larger influence on the transport of heat through radiation.

Table 3-2. Direct dependencies between the process "Heat transport" and the defined canister variables and a short note on the handling in the PSAR.

Variable	Variable influence on process		Process influence on variable	
	Influence present? (Yes/No) Description	**Handling of influence (How/If not – why)**	**Influence present? (Yes/No) Description**	**Handling of influence (How/If not – why)**
Radiation intensity	No. The radioactive decay (to which the radiation intensity is related) constitutes the heat source.	–	No.	–
Temperature	Yes. The heat transport is driven by temperature differences.	The process is included in the modelling of the canister material temperatures.	Yes. Heats and cools the canister materials.	The process is included in the modelling of the canister material temperatures.
Canister geometry	Yes.	The canister geometry and the gap between the copper shell and cast iron insert is included in the temperature modelling.	No, but indirectly via the temperature.	–
Material composition	Yes.	The thermal properties of the copper shell, the cast iron insert and the gap in-between them are included in the temperature modelling.	No.	–
Mechanical stresses	No.	–	No, but indirectly via the temperature.	See Section 3.4.4.

The process is controlled by, and influences, the temperature distribution in the materials.

Due to the high thermal conductivity of iron and copper, very small temperature differentials arise within the metal components.

Boundary conditions

The boundary conditions are the far-field rock temperature and the heat flow from the fuel into the canister and from the canister out into the buffer.

Model studies/experimental studies

In SR-Can temperature calculations were carried out for the thermal evolution after disposal with a model and benchmarking described in Hedin (2004). The calculations were carried out for a heat load of 1 700 W, which is estimated to be the highest heat load in a canister. The canister was assumed to be filled with air. The surface temperature of the outer copper shell was below 100 °C.

Ikonen et al. (2018) have done an updated modelling of the thermal dimensioning for the repository, which includes the temperature evolution within the canister. The description of the interior of the canister is simplified, using a "homogenized part" for the inner part of the insert. To comply to the limit of 100 °C for the copper surface, a safety margin of 5 °C was applied in sensitivity studies in which the required canister and tunnel spacing were calculated.

The sensitivity analysis in Ikonen et al. (2018) shows that eccentricity in the gap between the iron and copper has a minor effect on copper temperature (increase by 0.8 °C for the modelling example with BWR) and will decrease the temperature of the iron. The same result is the outcome of the study by Renström (2020a) where it is shown that the copper temperature is affected by the outer on the outer gap, heat transfer capacity in buffer and rock and the canister spacing.

Ikonen (2020) evaluated the temperature inside the canisters for four Posiva and SKB canister designs. The analyses showed that the variation of the decay power of the fuel element does not change the cast iron temperature remarkably, as long as the sum of the decay power for a canister is constant. Further, the simulation of the evolution of the temperatures in the repository showed maximum temperatures of 112–114 °C for the 2D modelling, while the 3D modelling gave 105 °C as a maximum for the cast iron. The lower temperature in 3D depends on the treatment of boundary conditions, but also on the heat escape through the top and bottom ends of the canister.

Natural analogues/observations in nature

Not applicable.

Time perspective

Heat generation is halved every 30 years during the initial post-closure period. The highest temperatures and the greatest heat flows occur within tens of years after deposition and repository closure.

Handling in the PSAR

A simplified handling of the temperature modelling in the canister materials is adopted in the PSAR. The process is modelled with results from the modelling of the buffer and the host rock as boundary conditions. The most important calculation end-point in that modelling (Hökmark et al. 2010) is the peak buffer inner surface temperature, which is insensitive to the handling of heat transport in the canister interior, which also means that the canister surface peak temperature is insensitive to the temperature distribution in the canister. The peak temperature in the iron insert is of concern for the analyses of canister material properties, and can be described from the maximum copper temperature.

Boundary conditions: The canister outer surface temperature is controlled by the time dependent heat generation rate and by the thermal properties of the canister/buffer interface, the buffer, and the host rock. Heat transfer due to both conduction and radiation at the boundary between the canister and buffer is included in the analysis of the canister surface temperature.

Handling of variables influencing this process: All variables influencing this process according to the influence table (Table 3-2) are included in the modelling of the temperature of the cast iron insert.

The thermal conductivity in metal parts is assumed to be infinite, and heat transfer by radiation and conduction across the gap between copper and iron canister is considered. Heat conduction through the bottom contact between the insert and copper canister is pessimistically neglected, since data are uncertain for this contribution.

The maximum temperature in the iron insert could be estimated by the heat transfer across the gap between the iron insert and the copper shell. The flow of heat is the sum of the radiation and conduction in the gap (Hedin 2004, Ikonen 2006). Any end effects of the canister are ignored, as well the heat flow in the solid metals as the temperature gradients are negligible due to the high thermal conductivity of the metals. This gives

$$\frac{P}{\pi D_{FeCu} L_{fuel}} = \frac{\lambda_{gas}\left(T_{Fe} - T_{Cu}\right)}{d_{FeCu}} + \varepsilon_{tot}\sigma\left(T_{Fe}^4 - T_{Cu}^4\right)$$

where P is the power output from the canister, D_{FeCu} is the average canister diameter for the gap, L_{fuel} is the length of fuel elements generating the heat, λ_{gas} is the thermal conductivity of the gas in the gap, d_{FeCu} is the thickness of the gap, $\varepsilon_{\mathrm{tot}}$ is the combined emissivity of the two materials in the gap (see Appendix B), σ is the Stefan-Boltzmann constant and T_{Fe} and T_{Cu} are the temperatures in the cast iron and copper respectively.

The temperature in the cast iron insert, T_{Fe} can be solved analytically or numerically from this expression. Assuming the maxium canister power output of 1 700 W, argon as the gas in the gap, an emissivity for the iron of 0.6 and pessimistically an emissivity of the copper of 0.02 (corresponding to highly polished copper) and a copper temperature of 102 °C, a calculation gives a maximum iron temperature of 117 °C (references for data, see Appendix B). This is slightly higher than the results in the modelling by Ikonen (2020) as mentioned above.

Handling of uncertainties in the PSAR

Uncertainties in mechanistic understanding

The fundamental understanding of this process is deemed sufficient for the needs of the safety assessment.

Model simplification uncertainties

Model simplifications essentially involve a simplified geometry. The effects of such simplifications have been evaluated by benchmarking against complex models, which demonstrates that they have no significant influence on the calculation result; see further Hedin (2004) and Ikonen (2020).

Input data and data uncertainties

The copper surface temperature is used as input for the calculation of the temperature of the cast iron insert. The uncertainties of the temperature distribution in the buffer/rock system is discussed in Hökmark et al. (2010) and Ikonen et al. (2018). The simplified calculations are based on pessimistic data for copper surface temperature, copper emissivity (polished copper) and size of the copper-iron gap (the Canister production report states the reference design as 0.0015 m (Pers and Sturek 2021).

3.3 Hydraulic processes

Water and gas flux in the interior of the canister is described in Section 2.3.1 and will not be further dealt with here.

3.4 Mechanical processes

3.4.1 Introduction

In the final repository the canister will be subjected to gradual build-up of pressures from swelling bentonite, and from hydrostatic pressure from the groundwater that is expected to increase considerably during future glaciations. There is also a low probability that earthquake induced secondary shear movements in rock fractures intersecting the canister position can transfer loads to the canister. With time the canister temperature decreases to the background repository temperature. As the canister is cylindrical, the loads are distributed and the sizes of deformations are reduced. However, dimensional steps and joints might raise the stress from the primary stress level. Possibly, under conditions of raised temperatures metals can deform by time-depentent viscous creep flow even below yield stress. The canister materials are strong and ductile metals, but their properties and behaviour could still change with time in unfavourable environments. The potential mechanical load situations in the repository imply that the canister could experience elastic deformation, creep, and plastic deformation.

Mechanical interactions at the boundary between the canister and the buffer generate both compressive and shear stresses in the canister. The swelling of the buffer generates mainly compressive stresses. Shear stresses may appear in the event of rock movements.

The mechanical loads on the canister involves the following:

- Bentonite swelling and groundwater pressures are exerted on the canister.
- Glacial pressure load associated with periods of time when a thick layer of ice covers the repository.
- Shear stresses are transferred from rock movements via the buffer to the canister, especially during an earthquake.
- Trapped gas in the buffer exerts pressure on the canister.
- Canister corrosion products exert pressure on the canister.

In strength analyses the loads are generally treated as static or dynamic and as being present for a short or a long time. For each loading type there are one or more possible failure mechanisms. Important factors of material, loading, manufacturing and environment have to be considered for each failure mechanism. Considered failure mechanisms are ductile and brittle rupture, instability, and creep.

Swelling and water pressures are exerted on the canister

Swelling pressure develops as the buffer undergoes saturation through wetting. Water pressure on the canister does not arise until the bentonite is saturated. The total pressure will not exceed the sum of the swelling pressure and the water pressure. During glaciations, the pressure will increase further. This additional pressure will at most correspond to the weight of the ice sheet formed at the repository location.

If the wetting is even, the swelling pressure increases evenly on the canister's periphery, except on the end surfaces where wetting of the buffer takes the longest time because of its thickness. If the wetting is uneven, the build-up of swelling pressure on the canister will be uneven. In the event of unfortunate combinations of wetting areas, the canister may be subjected to uneven stresses. Uneven stresses can also be caused by bent ("banana" shaped) deposition holes or rock fall-out from the walls of the deposition holes.

In the unlikely event that the buffer is water-saturated before the maximum temperature has been reached in the deposition hole, the water will expand, a process that will be hindered by the confined volume. Thus, the pressure could theoretically be very large. However, such a pore pressure increase is compensated by water drainage out through the rock. Scoping calculations show that a high pressure never has time to build up, see the PSAR Buffer, backfill and closure process report (SKB 2022b).

Transfer of shear stresses from the rock via the buffer to the canister

Rock movements in the form of shear along a rock fracture plane intersecting the depositon hole affect the canister via the buffer. The buffer thereby acts to cushion the sharp and hard rock wedge. Since the movement does not change the total volume of the buffer, the effect is essentially a shear deformation, whereby the shear strength of the buffer determines the impact.

Trapped gas in the buffer exerts pressure on the canister

Gas generated or confined at the canister surface exerts a pressure on the canister. This gas pressure is, however, limited to the bentonite's opening pressure (see the PSAR Buffer, backfill and closure process report, SKB 2022b). The gas is released through the bentonite either through temporary channels that form, or by dissolving in the water and diffusing out.

Canister corrosion products exert pressure on the canister

External corrosion of the copper canister increases the canister volume (if the corrosion products are solids that do not dissolve), since the corrosion products have a lower density than copper. This increase causes consolidation of the buffer and an increase in the pressure between buffer and canister. Copper corrosion is, however, of such limited extent (see Section 3.5.4) that even corrosion over hundreds of thousands of years will not lead to more than a marginal increase in pressure, well within the error margins for the estimated buffer pressure on the canister throughout the one million year time period of the safety assessment.

In the event of a defect in the copper shell, a similar effect may occur in the cast iron. Modelling (Bond et al. 1997) on the event of a small breaching hole showed that the influence was not significant.

3.4.2 Deformation of cast iron insert

Overview/general description

The cast iron insert is the most important mechanical barrier in the repository. If it fails mechanically, a number of safety functions can be at risk. Therefore the deformation processes are of central importance to the function of the repository.

When the insert is loaded mechanically, for example when the buffer swells, stresses will be built up, which deform the insert flexibly (elastically) if the stresses are low or permanently (plastically) if the stresses are high. The deformation depends on the geometry, the load, the temperature and the material of the insert.

Under temperate and periglacial climate conditions, the cast iron insert is expected to be subjected to an external load composed of a maximum swelling pressure from the bentonite of up to 10 MPa and a water pressure of 5 MPa. The pressure can be regarded as isostatic, evenly distributed over the entire surface. A canister can be subjected to an increased load during a glaciation. An ice sheet, several kilometres thick floating on the groundwater gives a maximum increase in pressure proportional to its maximum thickness. Pressure increases up to around 30 MPa may occur. It must be noted that the total stress on the canister is the bentonite swelling pressure added to a part of the hydraulic pressure, rather than just the sum (Harrington and Birchall 2007). The reducing factor for the pore water pressure is estimated to be in the range 0.86–0.92 for hydrostatic pressures conceivable in the repository (Harrington and Birchall 2007). Based on an estimated upper bound on the total load from these three causes, a key design requirement for the canister states that it should withstand an isostatic load of 50 MPa (Posiva SKB 2017).

As the bentonite becomes water saturated, uneven pressure distributions can arise. They may be associated with uneven water inflow or with oval or slightly curved deposition holes. In some cases, an uneven stress could possibly persist for a long time. Such loads will, in addition to compressive stresses, also give rise to bending stresses (tensile and compressive stresses).

Deviations from the normal load can also arise due to rock displacements across the deposition hole. This could result in bending and tensile and compressive stresses in the canister insert.

The load situations described above have been discussed and analysed extensively and these scenarios will, therefore, not be discussed in any detail in this report. The main results and conclusion of the mechanical design analysis of the canister (Jonsson et al. 2018) are presented below, see *Model studies/ experimental studies*.

If the copper canister is breached and water contacts the canister insert, it will corrode (see Section 3.5.1). The corrosion rate is low, but leads to a progressive reduction in the mechanical strength of the insert. This will eventually lead to failure. When and how this failure occurs depends on the extent of the breach, the geometry of the corrosion attack, and the load situation for the canister in question.

Dependencies between process and canister variables

Table 3-3 shows how the process influences, and is influenced by, all canister variables.

Table 3-3. Direct dependencies between the process "Deformation of cast iron insert" and the defined canister variables and a short note on the handling in the PSAR.

Variable	Variable influence on process		Process influence on variable	
	Influence present? (Yes/No) Description	Handling of influence (How/If not – why)	Influence present? (Yes/No) Description	Handling of influence (How/If not – why)
Radiation intensity	Yes. Radiation can cause damage at the micro-scale which could affect material properties	Neglected, due to small effects, see Section 3.4.6.	No.	–
Temperature	Yes. The mechanical properties are temperature dependent.	The canister's mechanical stability is modelled using the actual insert properties for temperatures down to 0 °C, see the canister design analysis (Jonsson et al. 2018).	No.	–
Canister geometry	Yes. The geometry and the properties of the material will determine the strength of the canister insert.	The canister's mechanical stability is modelled using the actual canister dimensions.	Yes. A deformation will obviously alter the canister geometry.	Inherent in the model.
Material composition	Yes. The geometry and the material composition will determine the strength of the canister insert.	The canister's mechanical stability is modelled using the actual properties of the canister material.	No.	–
Mechanical stresses	Yes. Stresses are the direct cause of the deformation.	Inherent in the model.	Yes. A deformation will alter the mechanical stresses.	Inherent in the model.

Boundary conditions

The swelling pressure from the bentonite in combination with the hydrostatic pressure from the groundwater will control the development of even and uneven pressure situations.

Rock displacements across the deposition hole can cause an additional load on the canister.

The chemical environment in the sealed canister could in principle be of importance, e.g. through the presence of hydrogen gas.

Model studies/experimental studies

The mechanical external loads on the canister insert after disposal are discussed and analysed in the design analysis (Jonsson et al. 2018). The analyses include:

- asymmetric loads due to uneven water saturation of the buffer,
- asymmetric loads after buffer saturation,
- isostatic pressure load,
- shear load.

The main conclusions are described in the following.

Bending due to uneven buffer swelling

During water saturation, the worst case that may occur is for a curved deposition hole. Simplified calculations of the stresses in the canister insert yield a maximum bending stress σ_b = 105 N/mm^2. The bending stress in the cast iron insert is much lower than the yield strength which ranges between 260 and 280 N/mm^2. As a result, the insert will withstand the stress elastically, without plastic deformation or risk of damage.

Remaining asymmetric loads after buffer swelling

The worst case for asymmetric loads after buffer saturation is a curved deposition hole and a local rock fall out of 3.75 % of the cross-section area (Börgesson et al. 2009). Simplified calculations give a maximum bending stress that is a little higher than the highest bending stress during the water saturation phase, but lower than the yield strength. The insert will withstand them elastically, without plastic deformation or risk of damage. These asymmetric load cases are acting after bentonite saturation for a very long time. The probability of occurrence for these extreme load cases is very low, which means that it is unreasonable to combine them with other low probability cases, like shear loads.

Isostatic loads

As was mentioned above, the design pressure of the canister is 50 MPa external pressure (Posiva SKB 2017) and the highest pressure will occur during a glacial period when the temperature of the insert is expected to be between 0 and 20 °C. The load case will affect all the canisters in the repository. Consequently, the reliability of the mechanical integrity of the canister needs to be high for this load case, since the possible risk concerns all the canisters in the repository. Still, the maximum ice sheet thickness and the resulting pressure can be confidently bound, see the PSAR Climate report (SKB 2020), which merits a moderate safety factor of 1.5 for plastic collapse (Alverlind 2016). Table 3-4 shows the collapse pressure and how it relates to the design premise and the results of practical tests, for BWR canisters. Deterministic calculations have a high safety margin to the design premise. This is compatible with the considerable margins to the design premise found within probabilistic calculations taking parameter uncertainties into accout. The calculated collapse load for the nominal BWR-insert is 88 N/mm^2 (MPa). For the PWR-inserts the collapse load is higher, 128 MPa, and even higher for the steel lids in both designs. The collapse loads have been evaluated at the permanent plastic deformation equal to elastic deformation, double slope method according to ASME (2008).

Large-scale pressure tests have been performed on copper canisters and the collapse pressure is 139 MPa (Nilsson et al. 2005). An earlier collapse simulation by Martin O et al. (2009) evaluated deformations and pressures of the pressure tests. The deformations compare well to the collapse test, but strict ASME definition of the collapse limit line is not applied when evaluating the pressure test or the simulation by Martin O et al. (2009).

The differences between the calculated pressures in Table 3-4 arise from different levels of pessimism, assumption, and evaluation. This is extensively described in Jonsson et al. (2018). The higher collapse pressure of practical test can be due to a higher deformation hardening of the canister materials at pressure compared to material tensile testing.

Since the maximum anticipated isostatic pressure load is 50 MPa the safety factor to collapse is threefold. Interestingly this is the same level of safety a for pressure vessels (SS-EN-13445-3:2014) even if that standard is not directly applicable for the canister. The canister design can be considered very robust and the risk of global collapse due to isostatic pressures is vanishingly small.

Table 3-4. Isostatic collapse pressures in calculations and practical tests for BWR-canisters. Deterministic calculations if not other noted.

Reference	Pressure	Failure mode	Comments
Posiva SKB (2017)	50 MPa		Design requirement
Dillström and Manngård (2017)	88 MPa	Plastic collapse, ASME	Probabilistic simulation Damage tolerance analysis
Alverlind (2016)	90 MPa	Plastic collapse, ASME	Damage tolerance analysis
Hernelind (2015c)	97 MPa	Plastic collapse, ASME	
Nilsson et al. (2005)	139 MPa		Practical tests

The importance of the uncertain factors to which the global collapse load is most sensitive has been evaluated in the probabilistic analyses in Dillström and Manngård (2017). The offset of the channel tubes is the most important factor, followed in order by the radius of the channel tubes and yield stress of the nodular cast iron. The inspection requirements from the 50 MPa isostatic case and damage tolerance analysis are modest, as the acceptable defects depths are larger than 24 mm. The acceptable defect length is 140 mm (Jonsson et al. 2018).

Creep deformation is strongly dependent on temperature and stress. The temperatures in the repository relative to the melting temperature of the cast iron are low; in the range of 0.2–0.3 at which creep cannot contribute much to deformation. In general, it is only under extreme (corrosion and pressure) laboratory conditions that cast iron exhibits high creep rate and brittle fracturing (Forsström 2019). The creep rate is very low (Martinsson et al. 2010). Therefore, the mechanical analyses mentioned above do not include creep of the cast iron.

Shear movements

The integrity of the canister can also be threatened by shear-type rock movements if the shear plane intersects the position of the canister. The detailed background is given in Posiva SKB (2017). The failure mechanisms of the canister due to rock shear are deformation instability (plastic collapse) or mechanisms related to macro defects such as crack initiation and stable crack growth. Mechanisms related to micro defects, such as fatigue or brittle fracture, are ruled out based on the loads in the repository and ductile behaviour of nodular cast iron and copper (Jonsson et al. 2018).

The insert cross section thickness decreases where corners of the square steel profiles point towards the cylindrical insert surface. The thinnest part is denoted edge distance. This decrease in cross section distance can raise the stresses and strains and might cause plastic instability and collapse during a rock shear movement. The stresses and strains depend on the shear amplitude, shear angle, shear velocity and the intersection point. In addition, the buffer properties and behaviour influence the stresses and strains. The most sensitive case for the insert in terms of location and direction of the shear movement is one occurring perpendicular to the canister main axis at 3/4 of its height (Jonsson et al. 2018, Hernelind and Börgesson 2018). The rock shear analyses (Hernelind 2015b, 2017) show that there is a considerable capacity left in the insert structure after a 5 cm rock shear movement. The maximum insert strain value arises between the surface of the insert and the steel profiles. The strain is less than 1 % in the design rock shear load case of 5 cm. In the steel profiles, the maximum strain is 1 % in the rounded corners. Both these calculated strain values are lower than the material standard values of 8 % and the measured values of elongation at failure of test manufactured inserts (Pers and Sturek 2021). The deterministic safety factor of elongation is therefore higher than three.

The properties of the square steel profiles are affected by contact with the liqud cast iron during casting. The steel could become brittle in 3 mm of the 10 mm thickness for the BWR insert. Affected steel profiles have been tested after casting and found to retain their ductility. For the PWR steel profiles the decrease in ductility can be notable due to the longer solidification time of the surrounding cast iron, but the PWR insert has thicker cast iron which lowers the stresses and strains compensating the affected steel profiles (Jonsson et al. 2018).

A deterministic analysis has shown that the shear load case is more sensitive to macro defects in the insert and the failure mechanisms crack initiation and stable crack growth (Dillström and Bolinder 2010). The acceptable defect sizes are smaller for the shear load case compared to the isostatic load case. Table 3-5 shows the variation of the defect sizes of a semi-elliptical defect with the buffer density, for 5 cm rock shear.

Table 3-5. The calculated acceptable defect sizes for rock shear load case for two buffer densities.

Inserts	Shear	Buffer density	Defect depth	Defect length
BWR/PWR	5 cm	2 022 kg/m^3	9 mm	22 mm
BWR/PWR	5 cm	2 050 kg/m^3	7 mm	20 mm

The cast iron shows ductile fracture behaviour. When the deformation release rate (*J-integral*) reaches the initiation toughness, the material exhibits stable crack growth. It is reasonable to use a toughness value of 2 mm for stable crack growth in a ductile material, which is especially true in this case because the inserts are subjected to short-term displacement-controlled loading. A safety factor (SF_J) of 2 is used when calculating the acceptable defect size, according to the ASME Code for a postulated emergency or faulted condition (Jonsson et al. 2018).

The shear load damage tolerance analysis (Dillström 2015) for the different load cases leads to a number of requirements on inspection (Jonsson et al. 2018). Growth of postulated cracks in the insert was further studied in Unosson (2016), where it was shown that crack growths vary between the channel tubes, and that growth of surface cracks in the BWR inserts do not threaten the integrity of the copper shell of the canister.

The probabilities of initiation of crack growth and of 2 mm stable crack growth are much higher than the probability of plastic collapse. The shear displacement and defect size contribute the most to the calculated probabilities of insert failure in the probabilistic rock shear analysis. The shear plane position has no dominant contribution in the probabilistic analysis. The probability of failure using a rock shear displacement of 5 cm is at most around 2×10^{-3} (Dillström 2014).

Impact of hydrogen on material properties

It is well known that hydrogen can embrittle metals, and Section 3.4.7 describes hydrogen embrittlement in copper. Hydrogen can enter a metal during the melting and casting manufacturing process and remain if the section thickness is large. Exposure to certain solutions or hydrogen gas at high temperature and pressure can raise the hydrogen content. The effects of hydrogen on carbon steels are widely studied, while investigations on cast iron are more scarce (Matsunaga et al. 2014).

Experimentally, hydrogen could be “charged” into cast iron using either exposure to high temperature and hydrogen partial pressure (Martinsson et al. 2009) or to specific solutions to promote hydrogen entry into the metal (Martinsson et al. 2009, Sahiluoma et al. 2021, Matsuno et al. 2012), or by electrochemical methods (Martinsson et al. 2009, Wu et al. 2015, Forsström et al. 2019, Sahiluoma et al. 2021). Care must be taken so that the process by which hydrogen is introduced does not induce other changes that impact the mechanical properties. For example, Martinsson et al. (2009) observed grain growth during thermal charging, which lead the authors to choose the electrochemical charging method for further studies (Wu et al. 2015).

Experiments with electrochemical charging of cast iron EN-GJS-400-15U (the type that is specified for the canister insert) have been performed by two groups, using different solutions. Recombination poisons were used in both cases, to inhibit atomic hydrogen at the metal surface from forming molecular hydrogen that could subsequently escape without entering the metal:

- 0.05 or 1 mol/L H_2SO_4 with 10 mg/L thiourea as recombination poison (Forsström et al. 2019, Sahiluoma et al. 2021), with an applied electrochemical potential of −950 mV (vs Hg/Hg_2SO_4), approximately −300 mV (vs SHE).
- 0.5 mol/L Na_2SO_4 with 30 mg/L As_2O_3 as recombination poison (Martinsson et al. 2009, Wu et al. 2015), at a constant cathodic current density of 10 or 20 mA/cm^2.

The initial content of hydrogen in the canister insert material is about 1.7 wt.ppm (Martinsson et al. 2009). The charging introduces the hydrogen superficially with e.g. up to 130 wt.ppm (at ca 60 µm depth) after 8 hours, and after longer charging times the hydrogen had penetrated further and the difference between bulk and surface was smaller. After 504 h maximum values of approximately 20 and 50 wt.ppm were measured for bulk and surface (0.25 mm depth), respectively (Wu et al. 2015). Tensile stresses increase the uptake of hydrogen (Sahiluoma et al. 2021), and by simultaneously applying an electrochemical potential, up to 280 wt.ppm, was achieved (Forsström et al. 2019). The distribution within the material was though not investigated in this study. It is further noted that hydrogen introduced in the iron is escaping rather quickly at higher temperatures, e.g. decreasing to 2.9 wt.ppm (in the bulk) after 624 h at 100 °C (Wu et al. 2015). At room temperature a more limited amount leaves the outer surface, and gives the highest concentration located in the subsurface. Creep testing after hydrogen charging increases the outgassing (Martinsson et al. 2009).

A Japanese group tested three types of cast iron with different amounts of pearlite, using a solution with 20 % NH_4SCN (Matsuno et al. 2012, Matsunaga et al. 2014, Matsuo 2017) at 40 °C, but with no electrical potential applied. The resulting hydrogen content was up to 4.4 wt.ppm (Matsuno et al. 2012), but the authors also noted that the content gradually decreased when the charged specimen was held in ambient air. After 200 hours, the content reached almost the same level as that in an uncharged specimen.

Sahiluoma et al. (2021) investigated the binding of the introduced hydrogen with TDS (thermal desorption spectroscopy) and found mainly two levels of trapping: 1) an energetically deep trap, realeased at 600 K, that was saturated and did not increase even during longer charging times, 2) one shallower trap, released at approximated 450 K which was able to store larger amounts of hydrogen and without saturation. The authors did not investigate the physical depth distribution of the hydrogen, but interpreted the two types of traps such that the shallower types (releasing hydrogen at 450 K) are sites at small cracks or voids forming at the interfaces of graphite nodules and ferrite matrix, while the deeper traps (releasing hydrogen at 600 K) are hydrogen sites within the graphite nodules. The study concluded that an external tensile loading causes the formation of effective trapping sites which are responsible for the increase of hydrogen uptake.

The main effects on the mechanical properties were shown to be a decreased ductility of approximately 50 % (Martinsson et al. 2009, Forsström et al. 2019, Matsuno et al. 2012), especially at lower strain rates (Matsuno et al. 2012), but also a more modest reduction of the yield and tensile strengths (Martinsson et al. 2009, Forsström et al. 2019). The observed effects were similar in creep tests and slow-strain rate tests (Martinsson et al. 2009, Forsström et al. 2019).

The changes in material properties from the introduced hydrogen is traced to the hydrogen storage capacity of graphite and the graphite-matrix interface. Also pearlite can store hydrogen (Matsunaga et al. 2014). When a non-charged specimen fractures, the process is dominated by ductile dimple fractures (Matsunaga et al. 2014, Forsström et al. 2019). For hydrogen-charged specimens the fracture was less ductile, with ligaments between the graphite nodules exhibiting brittle cleavage facets (Forsström et al. 2019) and cracks growing between adjacent graphite nodules (Matsunaga et al. 2014). Martinsson et al. (2009) noted “river patterns” on the fracture surfaces of hydrogen charged specimens, which indicated a brittle failure, and also noted a change in fracture path, such that the non-charged material cracked in the interface between ferrite and graphite while the hydrogen-charged material showed transgranular cracking.

It is clear that hydrogen can enter cast iron and change its mechanical properties, but the results of experimental studies must be regarded in the context of the insert in the repository. As mentioned above, the initial content of hydrogen in the insert is about 1.7 wt.ppm. There are essentially two sources of additional hydrogen that could possibly enter the cast iron insert, in a sealed copper canister, namely water left in the canister at encapsulation and hydrogen produced by corrosion of the fuel Zircaloy cladding during operation.

There is a requirement of a maximum of 600 g of water to be left in the canister at encapsulation (Posiva SKB 2017). This water could be reduced to maximum 67 g hydrogen gas (by corrosion of iron, or radiolysis), which would correspond to 4–5 wt.ppm hydrogen in the insert if evenly spread in the cast iron (the higher value for the BWR insert with less total mass of iron).

The Zircaloy cladding that surrounds the fuel pellet stack corrodes to some degree in the reactor. This corrosion causes a layer of ZrO_2 to form on the outer part of the cladding, as well as release of hydrogen (Shoesmith and Zagidulin 2011). Some of this hydrogen remains in the alloy, and forms hydrides (see Section 2.4.1). The total amount of hydrogen in the cladding is normally within the range of 50–800 wt.ppm (Raynaud and Bielen 2011) which would correspond to 22 to 470 g hydrogen (assuming 432 to 588 kg cladding in one canister; SKB 2010d, Table 2-4). However, to transfer this hydrogen from the cladding to the interior of the insert would require dissolution of the hydrides, and diffusion of hydrogen in the alloy and through the ZrO_2 layer. Considering the low solubility of hydrogen in Zircaloy at the relevant temperatures (Motta et al. 2019) it is estimated that only a very small fraction, if any, of this hydrogen should be considered as a source of hydrogen for embrittlement of the cast iron.

In summary, hydrogen can enter cast iron and affect its mechanical properties. Detrimental effects of concern for the cast iron insert have, however, only been achieved by electrochemical charging in aggressive solutions (with recombination poisons) or at high temperature and partial pressure of hydrogen. Neither of these environments are conceivable for the canister insert in a sealed copper canister. The partial pressure of hydrogen gas from metal corrosion by the remaining water or from hydrides in the Zircaloy is in the order of 0.1 MPa and is not enough to increase the hydrogen content in the iron, at the temperatures that will occur in the interior of the insert (see Section 3.2.1). In fact, the environment of the insert will more closely resemble that used as a baseline for the comparison of results, i.e. distilled water (Forsström et al. 2019, Sahiluoma et al. 2021), where the fracture mechanism is ductile and described as related to shear and coalescence of small microvoids, formed in the ferrite ligaments between the graphite nodules.

Natural analogues/observations in nature

Not applicable.

Time perspective

The load from the groundwater pressure and the bentonite swelling pressure is expected to build up over a period from a few years to some thousands of years after deposition. The maximum glacial load can be expected after tens of thousands of years.

Handling in the PSAR

Isostatic load and uneven loads: The isostatic load on the canister over the one million year assessment period is assessed in the PSAR. This load will be compared to the isostatic collapse load that can be estimated from the experimental and model studies cited above, and which are essentially included in the design analysis of the canister (Jonsson et al. 2018). The comparison will be used to assess whether canister integrity may be jeopardised due to isostatic over-pressure.

Effects of rock shear: The likelihood of violating the criteria for rock shear movements that the canister can sustain will be assessed based on estimated rock and buffer conditions. If violation occurs, the canister integrity will be assumed to be lost.

For the cast iron insert temperatures in the repository, only primary creep with decreasing creep rate is expected and the amount of creep can be calculated with a logarithmic time law and be considered to be negligible for all the load cases (Honeycombe 1968, Martinsson et al. 2010).

All these load situations will also imply loads on the copper shell. The effects on the copper shell are discussed in Section 3.4.3.

The laboratory experiments where hydrogen embrittlement effects are seen, are performed under conditions that are far more aggressive than those possible in a sealed canister, also with the maximum allowed 600 g of water present. Therefore, degraded material properties from high hydrogen content (hydrogen embrittlement) in cast iron is not considered in the PSAR.

Handling of uncertainties in the PSAR

The uncertainties in the analyses of the mechanical behaviour of the cast iron insert are discussed in detail in Jonsson et al. (2018). Therefore, only brief summaries of their conclusions are given below.

Uncertainties in mechanistic understanding

Isostatic load: Although it is uncertain when an isostatic load can occur, the maximum isostatic load is certain and therefore a safety factor of 1.5 against plastic collapse in stress analyses could be sufficient (Jonsson et al. 2018). In practical pressure tests the safety against collapse pressure is higher at three times the isostatic pressure (Nilsson et al. 2005). The understanding of the process is, therefore, sufficient for the needs of the safety assessment.

Uneven swelling loads: By using worst-case scenarios, the need for a detailed mechanistic understanding is not necessary. The understanding is, therefore, sufficient for the needs of the safety assessment.

Effects of rock shear: The analysis methods are well established, although there are some uncertainties. The contact between the channel tubes for the fuel elements are considered as welded to the cast iron. The conclusion in Hernelind (2017) was that the simplified geometry of the steel channel tubes tied to the nodular cast iron without support plates is a satisfactory numerical idealisation of the geometry and mechanical response of the insert and canister.

Model simplification uncertainties

Isostatic load and uneven loads: The 2D analyses have been validated by comparison to full 3D analyses. At the stress levels of relevance, 2D is marginally pessimistic. Also, the simplified tension model applied was validated against a generalised tension model and no effects of the model simplifications could be traced. There are, therefore, no model simplification uncertainties of any importance for the safety assessment.

Uneven swelling loads: The bentonite density distribution, deposition hole deviation and temporary swelling distribution are combined in the most unfavourable way. The model simplifications are hence pessimistic in this case.

Effects of rock shear: When analysing the damage tolerance, the displacements after shearing were used as input for the damage tolerance calculations. The uncertainty in this data transfer was analysed and the differences considered so small that they did not significantly influence the results.

Input data and data uncertainties

Residual stresses can be induced in the insert during casting. The residual stresses affect the acceptable sizes of the through-thickness cracks but do not affect the results for the surface defects (Alverlind 2016).

Nodular cast irons are ductile and can be used at elevated temperatures due to the thermal stability of the ferritic phase of the matrix. At temperatures much higher than those in the repository, the cast iron can become harder and less ductile due to precipitation hardening (ageing). Tensile testing curves can display small serrations at 100–300 °C when alloying elements or impurities interact dynamically with the deformation of the metal crystals (Honeycombe 1968). Only at 250–450 °C the ductility of the nodular cast iron drops noticeably (Lui and Chao 1989). Specific combinations of plastic deformations, rates, and elevated temperatures is needed to affect the mechanical behaviour of the nodular cast iron. Therefore, strain ageing is assessed not to affect the mechanical integrity of the canister in the repository (SKB 2017). This is further corroborated by the results of the investigations in Sarnet (2022), where also some other recent work in the field is assessed.

Isostatic load: The calculations were based on statistically well-documented data. The uncertainties were judged to be small in comparison to the design load of 50 MPa. As mentioned above, the maximum ice sheet thickness and the resulting pressure can be confidently bound, see the PSAR Climate report (SKB 2020).

Uneven swelling loads: The pessimistic approach in the analysis will give pessimistic results with a low probability of occurrence and these uneven loads pose no threat to the canister integrity. The data and the data uncertainties are, therefore, acceptable for safety assessment purposes.

Effects of rock shear: The meshes of the finite element models can impact the calculated stresses and strains. Comparisons were presented in Jonsson et al. (2018). Detailed models with finer meshes have locally higher stresses than the original model in Hernelind (2010). In addition, wedge elements can increase the calculated stress. Poorly behaving elements were disregarded in post processing of the analyses.

Uncertainties in the damage tolerance will result in uncertainties in the acceptable defect sizes. The sources of the uncertainties are variations in bentonite density, effects of strain rate, scatter in strain-stress data, scatter in fracture toughness data and the assumption that the channel tubes are integrated parts of the insert. As a result of this, pessimistic defect sizes are recommended to be used in the safety assessment.

The calculated probabilities of insert failure are much lower using defect distributions and fracture toughness data from PWR-inserts as compared to BWR-inserts (Dillström 2014).

3.4.3 Deformation of copper shell from external pressure

Overview/general description

The copper shell is primarily a corrosion resistant barrier which protects the iron insert with its spent fuel. In addition the canister must withstand the loads associated with handling, transport and deposition. The copper must also possess sufficient ductility to allow straining, either plastically or by creep when the external load against the insert deforms the copper shell. Furthermore, the copper shell must sustain loads caused by deformations of the cast iron insert in response to external loads.

When the load from the groundwater pressure and the swelling of the bentonite develops, the copper will deform until it makes contact with the cast iron insert.

A rock shear movement will also result in deformation of the copper canister.

Dependencies between process and canister variables

Table 3-6 shows how the process influences, and is influenced by, all canister variables.

Table 3-6. Direct dependencies between the process "Deformation of copper shell from external pressure" and the defined canister variables and a short note on the handling in the PSAR.

Variable	Variable influence on process		Process influence on variable	
	Influence present? (Yes/No) Description	Handling of influence (How/If not – why)	Influence present? (Yes/No) Description	Handling of influence (How/If not – why)
Radiation intensity	Yes. Radiation can cause damage at the micro-scale which could affect material properties.	Neglected, due to small effects, see Section 3.4.6.	No.	–
Temperature	Yes. The mechanical properties are temperature dependent.	Neglected. The maximum mechanical load will occur after the period of increased temperature in the repository.	No.	–
Canister geometry	Yes. The geometry and the choice of material will determine the strength of the copper shell.	The canister's mechanical stability is modelled using the actual canister dimensions.	Yes. The copper will be deformed at normal load.	Inherent in the model.
Material composition	Yes. The geometry and the material composition will determine the strength of the copper shell.	The canister's mechanical stability is modelled using the actual canister materials properties.	No.	–
Mechanical stresses	Yes. Stresses are the direct cause of the deformation. High stresses in the material may also lower its strength.	Inherent in the model.	Yes. A deformation will alter the mechanical stresses.	Inherent in the model.

Boundary conditions

The swelling pressure from the bentonite will control the development of even and uneven pressure situations, together with the hydrostatic pressure from the groundwater.

Rock displacements across the deposition hole can cause an additional load on the canister.

Model studies/experimental studies

The behaviour of the copper canister under the possible load situations in the repository are discussed and analysed in Jonsson et al. (2018). The analyses include deformation caused by swelling pressure from the surrounding buffer after water saturation of the buffer, effects of uneven buffer swelling pressure, effects of increased hydrostatic pressure caused by glacial loads, and rock shear movements. The uncertain contribution effects of slits and notches, as well as of cold work are discussed. Copper is fully ductile under repository conditions (Björkblad and Faleskog 2018) and the added phosphorus micro-alloying of the canister copper further improves time-dependent deformation (creep) ductility (Andersson-Östling 2020).

Time-dependent deformation (creep) in copper, after yielding or even below the yield stress, has been studied experimentally and theoretically for more than one hundred years. Increasing creep strain rates at temperatures above ambient temperatures were reported, and empirical equations of copper creep including logarithmic, power law and linear terms were proposed. In the repository, temperatures are 20–30 % of the melting temperature and therefore slipping within crystal grains is the major creep deformation mechanism. At higher temperatures and lower deformation strain rates, crystal defect rearrangements and crystal grain boundary sliding come into play. The development of theories and models incorporating these fundamental deformation processes were presented first in the textbook by Honeycombe (1968).

The long-term creep behaviour of the canister copper can be assessed from short term tests and theoretical reasoning. The ductile behaviour of the canister copper is facilitated by the phosphorus alloying, and it is essential to evaluate how these beneficial material properties develop over time. It has been verified that the basic creep model can be used to extrapolate the creep rate many orders of magnitude in time to the extent that it can handle the time perspective of the repository (Sandström 2012). This means that the finite element model simulation presented in Jonsson et al. (2018) has a good foundation.

Creep ductility has since the 1930s been determined by extrapolations of *the logarithm of the stress* against the logarithm of rupture time where copper has been creep tested under constant stress. Linear dependencies are usually expected for the short term creep tests, but extrapolation, based on such assumption for longer times is now known to be wrong, giving optimistic predictions (Penny and Marriott 1995).

More importantly, the creep behaviour is strongly dependent on stress and temperature, and therefore testing at higher temperatures gives possibilities to assess the behaviour at higher stresses and longer times. There are several extrapolation methods in the literature (Penny and Marriott 1995). Standard extrapolation methods have been applied to SKB's creep rupture data according to Larson-Miller and Manson-Haferd described in Penny and Marriott (1995) on data from Sandström (1999) for longer times and other temperatures than actually creep tested. Even if the method describes the relations between stress, temperature, and creep rupture times, the confidence of the predictions decreases with time, but it gives valuable insights to the general trends of the creep behaviour of copper.

An alternative extrapolation uses the *temperature* against the logarithm of rupture time, and rupture times for lower temperatures could be extrapolated for constant stress using linear regression. Manson and Haferd (1953) put forward an empirical extrapolation method using common coefficients for all stress lines, i.e. all stress data are used in a common, global fit. This type of fit yields a common rupture time constant, t_a, and a common rupture temperature constant, T_A, for all tensile stresses at which the material will ultimately rupture. This latter type of extrapolation has proven to reproduce empirical data well and closer than other methods (Penny and Marriott 1995), probably due to the two independent constants. The coefficients can then be used to construct an extrapolation of log(*stress*) versus log($time_{rupture}$). The rupture time constant 3.15×10^5 years fits to the canister copper batch 400 (Andersson-Östling 2020).

Deterioration of the material properties over time, long-term embrittlement, is implicit in the models behind the global fits according to Larson and Miller (1952) and Manson and Haferd (1953). This is related to the fact that several embrittlement mechanisms are thermally activated.

Manson-Haferd is more pessimistic for temperatures used in the experiments than Larson-Miller. Further, for longer times Manson-Haferd is more pessimistic even at low temperatures, 50–215 °C. The extrapolations suggest that the rupture times at 20 °C for relevant peak stresses in the canister are in the hundred thousand year scale. Applied to the stress situation in the canister for a glacial load, this suggests that if the load were to persist in the hundred thousand year scale, *local* damage cannot be excluded in the regions of highest stress. However, due to the creep deformation, the stress will decrease with time through relaxation, reducing the risk of local damage.

Models of copper creep deformation were calibrated to increase the physical meaning for SKB's copper grade (Sandström and Andersson 2008a) and the influence of microalloying levels of phosphorus on creep was discussed (Sandström and Andersson 2008b).

The material behaviour according to Sandström and Andersson (2008a, b) was implemented in finite element models for creep of the copper canister in the final repository (Hernelind 2015a). For the isostatic load due to buffer swelling, the copper shell is expected to make full contact with the insert about 10 years after buffer saturation at 75 °C. The maximum strain, which is less than 12 %, will occur at the slit (the axial gap) between the tube and lid or bottom. In the cylindrical part, the strain is less than 0.3 %.

The creep results obtained from glacial load analysis are, in summary, that the strain in the copper shell is low where the insert provides support. Only at the ends of the copper shell where the flanges of the lid and the bottom protrude, the strain values increase up to 10–30 %. The simulation result includes plastic strain and creep strain components occurring after 100 000 years at the geometrically

singular point at the root of the weld. Distortion of the model elements at the root of the weld makes interpretation difficult. At one singular point at the root of the weld inner surface of the shell the strain is as high as 60 % (Hernelind 2015a). The high strain is partly due to a steady state creep model instead of a decreasing logarithmic creep model. Such inner surface singular point peak in creep strain value is not expected to cause any global damage.

Uneven swelling can give rise to local creep. Jonsson et al. (2018) show, however, that this will not lead to cracking.

The understanding has also been improved regarding the effect of cold work, and how the dislocations are formed within the grains, rather than in grain boundaries (Sandström 2016) and such features could be implemented in future simulations models. The equations of creep have further been developed (Sandström 2017), to include tertiary creep (Sui et al. 2018) applicable up to 250 °C (Sandström and Sui 2021), and to also describe multiaxial stress states (Sui and Sandström 2018).

A mechanical load also results from internal pressure build-up due to gas formation caused by alpha decay. The void in the canister is, however, sufficiently large to avoid any detrimental build-up of internal gas pressure throughout the assessment period (see Section 2.5.8).

For the rock shear load case, the peak values for plastic deformation (strain) occur at a few “hot spots” and the global values are considerably lower. The shear plane location significantly affects the strains in the copper shell. The highest peak value in the copper shell, 29 %, occurs when the rock shear is perpendicular to the axis of the canister at midpoint, for 10 cm shear. The corresponding global value is less that 10 %. Most of the copper strain for the rock shear load is caused by the immediate plasticity during the rapid rock movement and the creep after the shear will only relax the stresses in the bentonite-copper-iron assembly (Hernelind 2010). The strain rate dependency has been investigated and found not to be significant for the copper shell (Jonsson et al. 2018).

The favourable creep properties (sufficiently high ductility), is achieved by the addition of 30–100 wt.ppm phosphorus, as demonstrated by extensive creep testing. For the assessment of post-closure safety, it needs also to be shown that the favourable material properties do not change over long periods of time. A fundamental knowledge that explains the effects on an atomic level is under development. The effect of the added phosphorus occurs through interaction of phosphorus in and with the grain boundaries, and possibly also with other impurity atoms.

Thermodynamic calculations (Magnusson 2017) show that the only elements present in Cu-OFP that interact with phosphorus are oxygen (by formation of phosphates) and nickel and iron, both of which (also in a mixed form) form stable phosphides. The energy of different positions of the phosphorus atom in the Cu-OFP matrix has been studied with quantum mechanical calculations with the conclusion that a substitutional position is more favourable than an interstitial (Li and Korzhavyi 2015). The stacking fault energy in copper decreases when point defects are present, and the effect of phosphorus is larger than for vacancies, H, O and OH. Decreasing stacking fault energy implies a larger tendency for segregation to grain-boundaries. Further studies (Li 2015) of impurities of 3sp elements (magnesium, aluminium, silicon, phosphorus and sulfur) and their impact on how a grain boundary is held together, show that the impurities in general improve the strength of the grain boundaries with decreasing electronegativity (i.e. from sulfur to magnesium). For phosphorus, however, the stacking fault energy and the tendency of phosphorus to spread evenly in the grain boundary has a major impact, and overall the calculations show that phosphorus will counteract the formation of cavities in the grain boundaries (Li et al. 2017). Further, the segregation energies vary depending on grain-boundary type (Sandström and Lousada 2021), and for Σ9 grain-boundaires also as a function of distance from the grain-boundary plane (Lousada and Korzhavyi 2020a). The release of free energy during cavity formation has been computed, and is found to be lower for copper with phosphorus (Cu-OFP) than for phosphorus free copper (Cu-OF) indicating that cavity generation occurs more readily in the latter material (Sandström and Lousada 2021).

Several attempts have been made to locate the phosphorus, but the detection limits have been too high to see any enrichment to the grain boundaries. Slow strain rate tests (Josefsson and Andersson-Östling 2019) and a long series of creep tests (Andersson-Östling 2020) confirm that phosphorus increase the creep ductility at temperatures relevant in the repository. Also studies of recrystallization support these temperature dependencies (Sundström et al. 2020).

Theoretical corrosion calculations as well as experimental creep and tensile testing show that embedded copper oxides can have a detrimental effect on the copper ductility (Björck et al. 2017). For the current configuration of gas shielding during welding of the copper canister the oxygen concentration of 100 at.ppm fulfils the limit of 5 wt.ppm in the copper material, and copper oxides are eliminated (Björck et al. 2019).

Natural analogues/observations in nature

Not applicable.

Time perspective

The load from the groundwater pressure and the bentonite swelling pressure is expected to build up over a period from a few years up to some thousands of years. The maximum glacial load can be expected after tens of thousands of years.

Handling in the PSAR

Isostatic load and uneven loads: The isostatic load on the canister over the one million year assessment period is assessed in the PSAR. This load will cause the copper to deform until the cast iron insert supports it. This will result in a maximum strain of the copper of about a few percent and, therefore, will not cause failure of the copper canister (Jonsson et al. 2018) and failure of the canister will be controlled by the strength of the cast iron insert.

Effects of rock shear: The likelihood of violating the criteria for rock shear movements that the canister can sustain is assessed based on estimated rock and buffer conditions. If violation occurs, the canister integrity will be assumed to be lost. Creep is not a concern, since the copper deformation is controlled by the surrounding material, which implies small creep rates as soon as the final deformation has been established (Hernelind 2010).

Handling of uncertainties in the PSAR

The uncertainties in the analyses of the mechanical behaviour of the copper shell are discussed in detail in the design analysis Jonsson et al. (2018). Therefore, only brief summaries of their conclusions are given below.

Uncertainties in mechanistic understanding

The tensile and creep behaviour of copper is sufficiently well understood for developing models that reproduce data from laboratory tests (Jin and Sandström 2009, Jonsson et al. 2018). The mechanistic understanding of the long-term behaviour at atomic level is still under development. Assessments of the effects of creep are, however, possible based on empirical and model results, without a detailed understanding at atomic level.

Model simplification uncertainties

The same creep model is used for all load cases. The uncertainty in the model is estimated to be a factor of five in creep rate. However, the performed analyses show low sensitivity for this uncertainty.

Input data and data uncertainties

The residual stresses in the copper shell and the friction stir weld were modest and rather evenly distributed; all values obtained had an absolute value less than 60 MPa (Jonsson et al. 2018). The crucial parameter is the ductility of the copper in terms of the mechanical integrity. The residual stresses in the copper shell have not been included in the mechanical analyses.

The creep rate increases with the temperature even at the low temperatures expected in the repository. The deformation by slipping within the grains has been modelled fundamentally with thermal activation of crystal dislocation movement. The creep strain to close the gap between the copper shell

and the insert is given by the geometric constraints and the fundamental dislocation model gives a logarithmic time law which was observed at creep testing. For the glacial load case, the temperature was pessimistically assumed to be 27 °C, leading to a marginally higher creep rate than at the expected temperature. The evaluation time point for the amount of creep strain was pessimistically set at 100 000 years.

3.4.4 Thermal expansion

Overview/general description

The canisters reach their maximum temperature in the repository after about 10 years. If the radial gap between the cast iron insert and the copper is closed at this temperature due to creep or plastic deformation (see Section 3.4.3), cooling down to ambient temperature will cause a tensile strain in the copper shell due to the fact that the copper will shrink more than the cast iron when the temperature is decreasing. The resulting tensile strain can be estimated using the following formula;

$$\Delta\varepsilon = -\Delta T \Delta\alpha$$

where

$\Delta\varepsilon$ is the increase in tensile strain,

ΔT is the temperature change of the system (10–100 = −90 °C),

$\Delta\alpha$ is the difference in thermal expansion coefficients for the copper shell and the cast iron insert ($17 \times 10^{-6} - 11 \times 10^{-6} = 6 \times 10^{-6}$ °C^{-1}).

This gives

$\Delta\varepsilon = 0.00054 = 0.054$ %

which is negligible for the canister in the repository. A somewhat less pessimistic analysis is presented in the design analysis fo the canister (Jonsson et al. 2018), with a temperature difference of 50 °C giving a strain of approximately 0.026 %.

A corresponding analysis of the axial expansion is perfomed in Lilja (2012b), and results in a strain in the copper of 0.048 %, which likewise is negligible. The analysis is somewhat more detailed, as it considers also the development of the gap between the iron insert and copper shell, as well as different temperatures in the copper shell and the insert.

Dependencies between process and canister variables

Table 3-7 shows how the process influences, and are influenced by, all canister variables.

Table 3-7. Direct dependencies between the process “Thermal expansion” and the defined canister variables and a short note on the handling in the PSAR.

Variable	Variable influence on process		Process influence on variable	
	Influence present? (Yes/No) Description	Handling of influence (How/If not – why)	Influence present? (Yes/No) Description	Handling of influence (How/If not – why)
Radiation intensity	No.	–	No.	–
Temperature	Yes. It is caused by temperature	Neglected based on simple calculations.	No.	–
Canister geometry	Yes. The dimensions and the gap size control the final results.	Neglected based on simple calculations.	No.	–
Material composition	Yes. Determines the thermal expansion properties.	Neglected based on simple calculations.	No.	–
Mechanical stresses	No.	–	Yes. May increase the stress level.	Neglected based on simple calculations.

Boundary conditions

The heat flow from the fuel and the pressure from the groundwater and the swelling of the bentonite will form the boundaries for this process.

Model studies/experimental studies

See Overview/general description.

Natural analogues/observations in nature

Not applicable.

Time perspective

Heating to the maximum temperature takes place very quickly after deposition. Cooling to the ambient temperature takes hundreds to thousands of years.

Handling in the PSAR

The process is neglected based on the calculation results presented above.

Handling of uncertainties in the PSAR

Uncertainties in mechanistic understanding

The mechanistic understanding of this process is sufficient for the needs of the safety assessment.

Model simplification uncertainties

Thermal load solely does not give any significant stresses in the canister with the initial gap between the copper and the insert for the canister reference design. The combined effect of creep, in especially the welding area when the axial gap is closed, and creep when the canister materaials are cooling, would need to be assessed using FEM creep calculations.

Input data and data uncertainties

Not relevant since the process is not modelled in more detail in the safety assessment. The data uncertainties in the calculations used to justify the neglect of the process are insignificant.

Adequacy of references supporting the handling in the PSAR

Not relevant since the process is not explicitly modelled in the safety assessment, based on fundamental knowledge.

3.4.5 Deformation from internal corrosion products

Overview/general description

If the copper canister is breached, water or water vapour will enter into the gap between the canister insert and the copper shell and give rise to anaerobic corrosion of the insert (see Section 3.5.1). If the water is also able to penetrate the insert, anaerobic corrosion of the inside of the channels for the fuel assemblies will occur.

In both cases, this leads to a build-up of corrosion products, which in turn causes mechanical stresses in the canister.

The process is of interest if the initial breaching occurs relatively early and is of limited extent. Under these conditions, the process will delay the occurrence of a large opening in the canister and hence the loss of all resistance to radionuclide transport offered by the canister. (For a canister failure causing a large breaching any transport resistance for radionuclides is neglected.) If the

breaching is caused by a rock shear movement, the transport resistance is assumed to be delayed by the time it takes for water to enter and give a continuous aqueous pathway for transportation of radionuclides. Breaching caused by copper corrosion over an extended area following the loss of the buffer will take of the order of hundreds of thousands of years and the time required to penetrate the insert through corrosion is small in comparison and will be pessimistically disregarded in the safety assessment.

The sequence of events leading to the development of these stresses is expected to proceed as described below for a case with a small initial defect where the buffer is present.

Water runs into the gap between the canister insert and the copper shell and into the canister insert, leading to anaerobic corrosion. This leads to hydrogen gas generation, which increases the pressure inside the canister, whereupon the inflow of water decreases. This gas pressure is, however, limited to the opening pressure of the bentonite (see the PSAR Buffer, backfill and closure process report, SKB 2022b) and will not be able to cause deformation of the outer copper shell. After some time, the transport of water or water vapour into the canister by diffusion will be greater than the leakage of water into the canister due to the pressure difference. The time required for this varies with the size of the penetration in the copper canister and the corrosion rate, and is reasonably expected to be thousands of years. The inward diffusion of water vapour will prevent corrosion from ceasing entirely. The process leads to a slow build-up of corrosion products. These products occupy a larger volume than the equivalent quantity of cast iron, and with time an internal mechanical pressure is built up against the copper canister. This leads to local deformation and may cause ultimately failure of the copper canister.

Dependencies between process and canister variables

Table 3-8 shows how the process influences, and is influenced by, all canister variables.

Boundary conditions

There are no relevant boundary conditions for this process other than the physical boundary set by the geometries of the components involved. The corrosion process is coupled to the inward transport of water for which boundary conditions are discussed in Section 2.3.1.

Table 3-8. Direct dependencies between the process "Deformation from internal corrosion products" and the defined canister variables and a short note on the handling in the PSAR.

Variable	Variable influence on process		Process influence on variable	
	Influence present? (Yes/No) Description	Handling of influence (How/If not – why)	Influence present? (Yes/No) Description	Handling of influence (How/If not – why)
Radiation intensity	No.	–	No.	–
Temperature	No.	–	No.	–
Canister geometry	Yes. The canister geometry determines the size of the gap.	The actual geometries are considered.	Yes. May cause expansion of the copper shell.	Several alternative cases that may lead to an enlargement of the initial failure are discussed.
Material composition	Yes. The material composition and the nature of the corrosion products determine the degree of volume expansion, which leads to deformation.	The actual materials are considered.	No.	–
Mechanical stresses	No.	–	Yes. Stresses will build up in the canister materials.	Several alternative cases that may lead to an enlargement of the initial failure are discussed.

Model studies/experimental studies

Different evolutions of an initial canister defect with subsequent corrosion of the canister insert have been modelled by Bond et al. (1997).

Regardless of the size of the canister penetration and the corrosion rate, a sufficiently large hydrogen gas pressure is expected to build up after some time to prevent liquid water from entering the canister. After that, the corrosion will nevertheless be able to continue due to the fact that water vapour can diffuse into the canister.

Bond et al. (1997) developed a model for this diffusion-limited corrosion. The purpose was to predict how the solid corrosion products build up in the gap between insert and copper canister. The model takes into account the change in the size of the gap during the corrosion process, possible changes in the corrosion rate, and the escape of corrosion-generated hydrogen gas from the canister.

The gap is expected to eventually fill with magnetite, Fe_3O_4, and the calculations were used to analyse the consequences of this for the strength of the canister. Two situations were analysed: one extreme case where the entire outside surface area of the insert corroded and one case where the corrosion was limited to an area around the original defect. The latter case progresses into the former after the copper material around the original defect begins to give way. This is calculated in the model to take around 20 000 years. According to the calculations, it takes at least 100 000 years from the time of the initial penetration before more extensive damage occurs on the copper canister.

Experimental studies of the possible pressure build-up from the corrosion products showed no jacking effects caused by expanding corrosion products (Smart et al. 2003). Further studies by Smart et al. (2006) gave similar results.

Natural analogues/observations in nature

Some archaeological analogues are discussed by Smart et al. (2003) and Smart and Adams (2006).

Time perspective

The process will start immediately after penetration of the outer copper shell.

Handling in the PSAR

For an intact canister, the process is neglected. For canister failures due to rock shear movements or copper corrosion over an extended area following loss of the buffer, a pessimistic approach is used for the potential delay in the loss of transport resistance caused by the process, see further the PSAR Data report (SKB 2022d, Section 4.2).

In the hypothetical case of a small, early canister failure, the process is treated in the SR-Site as a part of the evolution of the canister interior after damage (see Section 2.3.1 and further the PSAR Data report (SKB 2022d, Section 4.2).

Due to the uncertainties in the development of the annulus between the copper and the cast iron, several alternative cases are considered. As a base case, the corrosion in the filled annulus ceases and the insert remains tight. Conceivable alternative cases are:

- Corrosion in the filled annulus continues and the copper shell expands followed by creep relaxation of the bentonite.
- Corrosion in the filled annulus continues and the copper shell expands followed by compression of the bentonite.
- Corrosion in the filled annulus ceases but continues inside the cavity of the insert.

All these evolutions will eventually lead to failure of the cast iron insert and an enlargement of the initially small penetration in the copper shell. This will lead to an increase in the release rate of radionuclides from the canister.

The consequences of all these developments can be bounded by estimating pessimistic values of the time at which the larger failure occurs and of the size of this failure. This is further developed in the PSAR Data report (SKB 2022d, Section 4.2).

Boundary conditions: The inward transport of water is included in the study by Bond et al. (1997).

Handling of variables influencing this process: The influencing variables in the table are included in the modelling by Bond et al. (1997) and in the cases considered in the integrated treatment of the process.

Handling of uncertainties in the PSAR

Uncertainties in mechanistic understanding

Some degree of uncertainty remains concerning the mechanical effects on the copper shell that could be caused by growing corrosion products at the iron-copper interface as corrosion of the iron insert progresses in a breached canister. Laboratory studies indicate that the iron corrosion products do not exert enough pressure to displace the copper shell (Smart et al. 2003, 2006). Dimensional measurements of the copper shell in several packages from the MiniCan field tests, exposing defect model canisters for up to 9 years in the Äspö Hard Rock Laboratory (Äspö HRL), revealed no changes within the 0.5 mm accuracy of the measurements (Smart et al. 2012, Gordon et al. 2017). The remaining uncertainty concerns the development on longer timescales since the corrosion of the iron insert in these experiments was rather limited (locally up to ca 1 mm). However, as discussed above, despite these uncertainties, it is possible to put an upper bound on the consequences of this process in the safety assessment.

Model simplification uncertainties

Modelling requires assumptions regarding the properties of the corrosion products. These, and other aspects of the model, are not verified experimentally.

Rather than attempting a justification of model simplifications, the consequences of this process are given a pessimistic upper bound in the safety assessment, as discussed above.

Input data and data uncertainties

The corrosion rates of freely exposed metal are relatively well known. There are, however, large uncertainties concerning the form and distribution of the corrosion over the insert surface area when the metal is exposed to a limited amount of water or water vapour. There is also uncertainty over the density and porosity of corrosion products and, therefore, the degree of expansion.

Rather than seeking defensible treatment of data uncertainties, the consequences of this process are given a pessimistic upper bound in the safety assessment, as discussed above.

3.4.6 Radiation effects

Overview/general description

Neutron and gamma radiation from the fuel could potentially give rise to material changes in the cast iron insert and the copper shell.

The effects of neutron- and gamma irradiation of the canister materials over a long period of time have been evaluated computationally and discussed by Guinan (2001). By comparing with experiments in the literature, it was concluded that the magnitude of any physical property changes (e.g. yield stress, creep rates, enhanced solute segregation, dimensional changes, or brittleness) resulting from exposure to neutron and gamma radiation over the one million year time period of the safety assessment will be negligible for both the copper and the cast iron. The results computed by Guinan (2001) have later been verified by Yang et al. (2019), using updated software and databases. Both Guinan (2001) and Yang et al. (2019) evaluated the radiation damage at zero Kelvin, meaning that thermal self-annealing of radiation induced defects in the materials were not accounted for. The pessimism in the results computed by both Guinan (2001) and Yang et al. (2019), has been demonstrated by Padovani et al. (2019), who evaluated quantitatively the magnitude of thermal annealing at temperatures

relevant for the repository application, showing that the actual level of radiation damage must be orders of magnitude lower than predicted by Guinan (2001) and Yang et al. (2019). Padovani et al. (2019) also made several attempts to verify the radiation damage induced in copper by repository representative doses of gamma radiation. No difference was found between copper specimens exposed to 100 kGy gamma radiation and reference specimens, however, the experiment was not sensitive enough to detect the very low levels of radiation damage predicted pessimistically by Guinan (2001) and Yang et al. (2019). It should be noted that Guinan (2001) and Yang et al. (2019) assessed the cast iron insert as consisting of pure iron, which is not the case for the KBS-3 inserts.

Precipitation of copper particles is a well-known problem in reactor steel vessels (see e.g. Odette and Lucas 1998, Chaouadi and Gérard 2005). Depending on the Cu content in the material, precipitation may occur as a result of radiation, potentially leading to embrittlement of the material. Such an accelerated ageing process occurs gradually over the lifetime of the reactor; i.e. over a time period of several decades. Brissonneau et al. (2004) suggested that similar ageing processes may be of relevance also in materials to be used for disposal of nuclear waste. The dose rate due to the radioactive decay in the fuel is much lower compared to that in a reactor. The temperature, however, is also lower (about 100 °C compared to 300 °C in a reactor), and Cu supersaturation is more readily achieved. Also the balance between defect production and defect annihilation in the material will be different.

Calculations by Brissonneau et al. (2004) showed that the copper content will have to be lower than 0.05 % to avoid precipitation embrittlement. The underlying calculations have been verified, though shortcomings in the conceptual understanding of the models coupling precipitation of copper particles to changes in mechanical properties have been revealed (Sandberg and Korzhavyi 2009). An experiment with electron irradiation of an FeCu model alloy (0.079 at.% Cu) as well as cast iron (0.028 at.% Cu) was performed. The materials were analysed with atom probe tomography after the irradiation. Copper precipitation was clearly seen in the FeCu material, but not in the cast iron samples (Olsson P et al. 2013, Yang et al. 2022). The clusters in the FeCu material were though small compared to the ones calculated by Sandberg and Korzhavyi (2009), and would have insignificant effect on the mechanical properties. The effect on cast iron would be even lower. The KBS-3 design requirements specify the copper content to be < 0.05 at.%, which would be appropriate to avoid Cu clustering and precipitation, according to both theoretical and experimental investigation of the cast iron evolution (Olsson P et al. 2013, Chang 2015, Yang et al. 2022).

Segregation of phosphorus to grain boundaries can cause intergranular embrittlement in ferritic steels (Wu et al. 1992). In addition to metallurgic segregation to the last solidified regions, radiation can accelerate diffusion of phosphorus to grain boundaries. SKB has not investigated segregation of phosphorus in the cast iron, but the average phosphorus content of 0.025 wt.% in the bulk of the melt (Pers and Sturek 2021) comforms to typical maximum values stated in the ASM Cast Iron Handbook (Stefanescu 2017, p 629) and indicates concentrations of phosphorus lower than the limit for formation of a brittle phase of Fe_3P. The modelling of segregation of phosphorus to grain boundaries in Sandberg and Korzhavyi (2009) is built on the assumption that phosphorus is precipitated in the same way as copper, and the experimental results in Olsson P et al. (2013) indicates the effects of irradiation are small.

Precipitation of more complex intermetallic phases in reactor steels under irradiation has been predicted to occur at later stages (Odette and Nanstad 2009), and clusters enriched in Ni, Si and Mn have been observed (Miller and Russel 2009). A feasibility study to investigate whether such “late blooming” phases (LBP) can occur in the nodular cast iron has been performed, with thermodynamic calculations of phase diagrams (Calphad, CALculations of PHase Diagrams) used together with quantum mechanical calculations for analysis of interactions between dissolved atoms and vacancies in the copper lattice (Korzhavyi et al. 2018). The conclusions were that precipitation of LBP is thermodynamically possible for the “G-phase” (a phase rich in Ni, Mn and Si), M_2P- and M_3P-phosphides (phases where M stands for Cr, Fe, or Ni) and a sulfide phase called MnS. That the phases are thermodynamically stable does not, however, necessarily mean that they will precipitate.

Yang et al. (2019) also discussed the possibility of neutron capture and transmutation resulting in the formation of H and He atoms in the canister materials. In all cases considered, regarding both canister materials and all positions (e.g. the cast iron inner wall and the iron-copper interface), the formation of H and He due to transmutation were found to be many orders of magnitude lower than the hydrogen content of any copper or iron material.

Dependencies between process and canister variables

Table 3-9 shows how the process influences, and is influenced by, all canister variables.

Boundary conditions

There are no relevant boundary conditions for this process other than the physical boundary set by the geometries of the components involved. (Neutron and gamma radiation from the fuel is required for this process to occur.)

Model studies/experimental studies

See Overview/general description.

Natural analogues/observations in nature

Not applicable.

Table 3-9. Direct dependencies between the process "Radiation effects" and the defined canister variables and a short note on the handling in the PSAR.

Variable	Variable influence on process		Process influence on variable	
	Influence present? (Yes/No) Description	**Handling of influence (How/If not – why)**	**Influence present? (Yes/No) Description**	**Handling of influence (How/If not – why)**
Radiation intensity	Yes. It causes the process.	Accounted for in modelling.	No.	–
Temperature	Yes. Temperature affects supersaturation levels and thus thermodynamic driving forces. Thermal self-annealing reduces radiation damage.	Thermal self-annealing is accounted for in modelling	Yes. The heating caused by the process is negligible.	Neglected, based on modelling results.
Canister geometry	Yes. The dimensions of the iron influence the radiation in the copper shell.	Accounted for by modelling the actual geometry.	No.	–
Material composition	Yes. The composition of the insert material influences the radiation in the copper shell.	Accounted for by modelling the iron and copper.	Yes. The radiation will influence the distribution of elements, chemical form as well as micro structure.	Explicitly modelled.
Mechanical stresses	Yes, in principle mechanical stresses could increase the propensity for radiation damage in the canister materials.	Neglected due to small effects.	No.	–

Time perspective

The period of irradiation is dominated by the neutron flux. The neutrons come from spontaneous fission and from (α, n) reactions in the fuel. Both processes diminish greatly with time, and 1 000 years after deposition the radiation dose has declined by a factor of thirty (SKB 2010d). Gamma radiation is dominated by the decay of Cs-137 with a half-life of 30 years.

Handling in the PSAR

The specifications for the material for the cast iron insert require that the copper content be kept below 0.05 %. Embrittlement due to copper precipitation is, therefore, neglected for the cast iron based on the results presented in Brissonneau et al. (2004), and later in Olsson P et al. (2013), Chang

(2015) and Yang et al. (2022). Other effects of radiation to possibly cause embrittlement in the iron (phosphorus segregation and precipitation of phosphides, precipitation of LBP, or direct radiation damage), are neglected due to small effects in the limited radiation field for a limited time.

The process of radiation damage of the copper shell is neglected based on the results presented in Guinan (2001), verified in later studies (Yang et al. 2019, Padovani et al. 2019).

Handling of uncertainties in the PSAR

Uncertainties in mechanistic understanding

The mechanistic understanding of this process is deemed sufficient for the needs of the safety assessment.

Model simplification uncertainties

Not relevant since the process is not further modelled in the safety assessment.

Input data and data uncertainties

Not relevant since the process is not further modelled in the safety assessment.

3.4.7 Hydrogen embrittlement of copper

Overview/general description

Atomic or molecular hydrogen in copper may, if present in sufficient concentrations, negatively influence the mechanical properties of the metal. This is a well-known phenomenon that applies to metals in general. Atomic hydrogen has a very low solubility in the undisturbed copper lattice, but may be trapped at grain boundaries, in lattice dislocations and vacancies, or bind to impurities in the lattice or in grain boundaries. In addition, atomic hydrogen may form molecular hydrogen in microvoids in the metal. This could have a negative effect on mechanical properties and is generally referred to as hydrogen embrittlement. In particular, H reacting with oxygen in the metal may form molecular water in microvoids, which could also have a negative effect on mechanical properties. The latter phenomenon is sometimes called hydrogen sickness. A thorough review and assessment of hydrogen embrittlement of copper in the repository environment was done in Chapter 7 of SKB (2019a), and an abbreviated version of that text is given below.

According to the requirements for the Cu-OFP to be used for the KBS-3 canister, the initial content of hydrogen and oxygen in the material should be less than 0.6 wt.ppm and 5 wt.ppm, respectively. These requirements serve to prevent hydrogen sickness and hydrogen embrittlement. Similar requirements on oxygen content have been applied for many years for copper in various applications. As regards the requirement on hydrogen content, it is noted that there is a variation at least in the range 0.3 – 0.6 wt.ppm in samples of Cu-OFP (Pers and Sturek 2021). It is also noted that it may be demanding to obtain accurate measurements of the H content in Cu (Granfors 2017). The requirement on hydrogen content can likely be relaxed to at least 1 wt.ppm, but this has not been systematically investigated.

Oxygen could be introduced into the copper canister material through the welding of the canister lid and base, and to reduce this phenomenon to harmless levels, the welding is performed in an inert atmosphere. It has recently been demonstrated that essentially oxide free welds can be produced with this technique (Björck et al. 2017, 2019).

The Cu-OFP to be used for the canister material typically contains around 0.5 wt.ppm H. Several studies with the specific aim of increasing the hydrogen content in copper have demonstrated that extreme electrochemical conditions in specially prepared aqueous environments are required to force hydrogen into copper (Martinsson and Sandström 2012, Leijon et al. 2018, Yagodzinskyy et al. 2018). Some of these studies have also demonstrated the impact on the mechanical properties of the increased hydrogen content. Simply exposing copper to hydrogen gas at the highest pressures and temperatures expected under repository conditions (see further below) would not lead to any

significant increase in H content, since the solubility of H in Cu is very low. In two relatively recent studies, it has been suggested that the H content may increase by up to around 0.5 wt.ppm in thin samples when subjected to a combination of aqueous sulfide and tensile stresses for up to four weeks (Forsström et al. 2017, Becker et al. 2020), or a gamma radiation total dose that is representative for the repository (Lousada et al. 2016). The overwhelming part of the H in Cu-OFP is bound to traps in the form of voids, vacancies, dislocations or impurities, in the bulk or at grain boundaries. Leijon et al. (2018) studied the influence of hydrogen charging on the creep properties of Cu-OFP. A hydrogen content of up to 10 wt.ppm was achieved. The focus in the study was on changes of the microstructure.

Hydrogen embrittlement is also discussed as a potential component in SCC in Section 3.5.5.

Dependencies between process and canister variables

Table 3-10 shows how the process influences, and is influenced by, all canister variables.

Table 3-10. Direct dependencies between the process "Hydrogen embrittlement" and the defined canister variables and a short note on the handling in the PSAR.

Variable	Variable influence on process		Process influence on variable	
	Influence present? (Yes/No) Description	**Handling of influence (How/If not – why)**	**Influence present? (Yes/No) Description**	**Handling of influence (How/If not – why)**
Radiation intensity	Yes, in principle, radiation induced atomic displacements may cause redistribution and/or enhanced uptake of hydrogen.	Neglected due to small effects (atomic displacements are infrequent, due to the low radiation intensity and since self-annealing further reduces the effect), see Section 3.4.6.	No.	–
Temperature	Yes. Hydrogen embrittlement in principle occurs through introduction and distribution of hydrogen in the metal in question, which are temperature dependent.	The temperatures relevant to repository conditions are considered in the evaluation of the process.	No.	–
Canister geometry	Yes. The effect of potential hydrogen embrittlement will depend on the canister geometry, in particular the thickness of the copper shell.	The canister geometry and the relevant material properties are considered in the evaluation of this process.	No. (Indirectly, if hydrogen embrittlement were to be sufficiently extensive, it would influence the impact of mechanical stresses on the canister that could in turn influence the canister geometry.)	–
Material composition	Yes. In particular the hydrogen (and oxygen) content is of relevance.	Initial hydrogen (and oxygen) content and potential changes in hydrogen content from external sources are explicitly considered in the evaluation of this process.	Yes, as hydrogen embrittlement is by definition accompanied by an increase or a redistribution of hydrogen in the material.	Initial hydrogen (and oxygen) content and potential changes in hydrogen content from external sources are explicitly considered in the evaluation of this process.
Mechanical stresses	Yes. The effect of increased hydrogen content, e.g. the formation or alteration of fractures in the Cu could be influenced by mechanical stresses.	Mechanical stresses are considered in the evaluation of this process.	Yes, as hydrogen embrittlement could be associated with fracturing and hence influence the mechanical stresses in the copper.	Mechanical stresses are considered in the evaluation of this process.

Boundary conditions

The extent to which hydrogen could enter the copper canister at the surfaces is a key factor when evaluating the potential extent of hydrogen embrittlement in the safety assessment. Therefore, all potentially hydrogen generating processes at the canister surface need to be considered. As further discussed below, this essentially concerns corrosion caused by sulfide and by agents generated through radiolysis of water.

Model studies/experimental studies

Wampler et al. (1976) observed that pores in the form of spherical "bubbles" were formed in pure copper loaded with H by equilibration with H_2 gas at temperatures between 600 and 1000 °C at a pressure of 3 MPa and then cooled to room temperature. Alternative names for bubbles in the literature are pores, blisters and cavities. The concentration of H in the samples after loading was 300 at.ppm or around 5 wt.ppm. Micrographs show bubbles with radii of the order of 0.1 μm. The bubbles formed preferentially at grain boundaries and dislocations. In a particular measurement, the authors report 0.2–0.4 μm bubbles with a density of around $10^9/cm^3$. The internal H_2 pressure of the bubbles is estimated at 100–200 MPa, meaning that the density of hydrogen is near that of liquid H_2.

Electroless copper deposition is mentioned here for the completeness of the discussion because in the past it has been used to study the influence of hydrogen on ductility. Electroless copper deposition involves the simultaneous reduction of copper and hydrogen. Therefore, high atomic and/or molecular hydrogen contents can be found in the powder metallurgical deposits. Electroless copper is characterized by high porosity and low ductility. For example, Okinaka and Straschil (1986) found that the elongation to failure was below 5 % when the hydrogen content exceeded 10 to 25 wt.ppm. Due to its high porosity and impurity contents, electroless copper has poor mechanical properties and is therefore not relevant when discussing the properties of the canister material (Cu-OFP). Electroless copper will thus not be considered further here.

Panagopoulos and Zacharopoulos (1994) charged tensile specimens of pure copper in a solution of 75 % methanol, 22.4 % water, 2.6 % sulfuric acid with 10 mg/L arsenic trioxide as a hydrogen recombination inhibitor with charging currents up to 100 mA/cm^2. The thickness of the tensile specimens was 1.5 mm. The charging time was up to 36 h, and the charging gave a modest reduction of the tensile strength and of the elongation to failure, for example 30 % after 25 h. Higher charging currents did not generate any further reduction in the properties. No measurement of the hydrogen content and no microstructural study were performed.

Martinsson and Sandström (2012) observed formation of near-surface hydrogen bubbles in Cu-OFP that had been electrolytically charged with H with a current density of 10 mA/cm^2 for up to three weeks, in a 10 % H_2SO_4 electrolyte containing 30 mg/L As_2O_3 to supress hydrogen recombination. The hydrogen bubbles are preferentially formed at grain boundaries within 50 μm from the surface and have sizes of the order of 1 μm. An increase in the hydrogen content in comparison to the value for uncharged specimens was only observed for depths of up to 100 μm. This means that the observation of bubbles is an approximate indication of how deep into the material the hydrogen content has been raised. The authors find through modelling that the internal H_2 pressure in the bubbles can at most be around 400 MPa. It is noted that a pressure of 400 MPa corresponds to a molecular density of 0.16 mol/cm^3 at room temperature, whereas metallic copper has a density of around $8.9/63.5 \approx 0.14$ mol/cm^3. The authors noted that during 3 weeks of charging, the average hydrogen content in the topmost 50 μm increased from 0.6 to almost 100 wt.ppm in as-received copper. One important conclusion from the work of Martinsson and Sandström (2012) is thus that the enhanced hydrogen content is located near the surface even after extensive charging. Modelling results show that a steady-state distribution is soon reached and deeper penetration of hydrogen does not take place even if the charging goes on for years (Martinsson et al. 2013). The reason is that the outflow of hydrogen increases with time and soon matches the inflow. From the modelling performed by Martinsson and Sandström (2012), it was concluded that the influx of H was around 1×10^{-10} $kg/(m^2\ s)$, i.e. 1×10^{-11} $mol/(cm^2\ s)$. The charging current 10 mA/cm^2 corresponds, with F = 96 485 C/mol, to 10^{-7} $mol/(cm^2\ s)$, meaning that the hydrogen pick-up factor, i.e. the fraction of the potentially generated H that actually entered the metal, seems to be $\sim 10^{-4}$. It is noted that this is for a charging situation with a clean surface and using a recombination poison to enhance the charging rate.

Yagodzinskyy et al. (2012) continuously charged Cu-OFP with hydrogen at 20 and 50 °C during slow strain rate tensile tests for 14 h. The specimen thickness was 1.5 mm. Pores and intergranular cracks were found to a depth of 110 µm. In comparison to uncharged specimens, the tensile strength at 50 °C was reduced by about 7 % and the elongation to failure by 10 %. No explanation of the observations is presented in the paper, but the following is suggested: The cracked surface layers can be expected to have a much reduced load bearing capacity. If it is reduced by 50 % which is a reasonable value, the drop in tensile strength would be equivalent to that observed based on the relative cross-sectional areas of the embrittled surface layer and uncharged central core. If the flow stress[3] versus strain is known, the homogeneous elongation can be computed with necking or geometric instability criterion by Considère. It states that when the uniform elongation limt is reached, the work hardening is equal to the flow stress. The greater the localisation of strain the lower the elongation in agreement with the observations. Yagodzinskyy et al. (2012) also performed a few creep tests with or without continuous charging. The creep results for specimens without charging are very different from other published results. For example, they reported an exponent for the stress dependence of the creep rate of 3 whereas other literature gives a value above 50 (Andersson-Östling 2020). This difference represents many orders of magnitude in the creep rate. The testing conditions appear to have been quite different from the ones mentioned in the paper, and it is therefore rather difficult to interpret the results. A discrepancy of the same order of magnitude is also found for the tests with continuous charging in comparison to the results of Leijon et al. (2018).

Lousada et al. (2016) studied the influence of gamma irradiation (total dose of 69 kGy over 6 days at a dose rate of 486 Gy/h) on copper surfaces in pure water. An increase in the hydrogen content to up to 0.4 wt.ppm hydrogen was found after the irradiation exposure using thermal desorption spectroscopy (TDS). This was around twice the initial concentration of the specimens (~ 0.2 wt.ppm H). Since neither the uptake of 0.2 wt.ppm hydrogen, nor the absolute final value of 0.4 wt.ppm hydrogen after uptake is larger than the hydrogen concentration already present in the Cu-OFP (ca 0.5 wt.ppm), and since the effect is measured for a repository representative gamma dose (maximum 70 kGy at the canister surface), this process is not regarded as a risk for hydrogen embrittlement. Also, the thickness of the copper canister is 50 mm whereas that of the foils in Lousada et al. (2016) was 0.25 mm. If the same amount of hydrogen was uptaken by the copper shell in the KBS-3 canister, and if the hydrogen would be distributed in a 0.25 mm surface layer, then only a small fraction of the canister cross section would see a mildly increased hydrogen concentration. If the hydrogen would be distributed further into the 5 cm copper shell, the concentration increase would be correspondingly smaller. It is also noted that the TDS spectra of the H release as a function of temperature from irradiated and non-irradiated samples are very similar in shape, suggesting that H exists in the same form and is similarly distributed in the two samples. This is somewhat unexpected since if the difference in total content stems from the irradiation, the additional H would be expected to be closer to the surface whereas the original H would be homogeneously distributed in the sample. The form in which H is bound in the material could also be different. These concerns suggest that it could be premature to draw firm conclusions regarding the extent of hydrogen introduction from this single measurement.

Becker et al. (2020), in a continuation of work described in Becker and Öijerholm (2017) and Forsström et al. (2017), measured the hydrogen content in Cu-OFP samples before and after 4-week exposures to chloride containing 10^{-5} and 10^{-3} mol/L sulfide solutions at 90 °C. Some of the samples were strained in slow strain rate tests (SSRT) during the sulfide exposures. Before exposure, the samples had a hydrogen content of around 0.6 wt.ppm. In short, the following was observed as regards H content:

- Unstrained samples exposed to 10^{-5} mol/L HS^- exhibited a reduction in H content by about 50 % after exposure, which is suggested by the authors as being due to outgassing of initially present H.
- Unstrained samples exposed to 10^{-3} mol/L HS^- have roughly the same H content before and after exposure.
- Strained samples exposed to 10^{-5} mol/L HS^- also have roughly the same H content before and after exposure.
- Strained samples exposed to 10^{-3} mol/L HS^- show an increase in H content by 15–50 % with the higher values in samples taken from the more strained parts of the SSRT specimens.

[3] Flow stress is the instantaneous value of stress required to continue to plastically deform the material.

It appears as at least the combination of high strain rates and high sulfide concentrations may lead to uptake of H in Cu-OFP. The authors also note that the number of samples was limited, and that the results should thus be viewed in the light of this. One may further note that Forsström et al. (2017) measured, for 10^{-5}, 10^{-4} and 10^{-3} mol/L sulfide solutions at 90 °C, but for twice the strain rate as Becker at al. (2020), H increases by up to around 0.6 wt.ppm irrespective of the sulfide concentration. This appears surprising if the source of H is believed to be the corrosion reaction caused by sulfide. In particular in the study by Forsström et al. (2017), the hydrogen increase appears to be independent of the location of the samples taken from the tapered SSRT specimens, which is unexpected since the strain experienced by the different positions varied markedly and they were too far apart for Fickian diffusion of H in the Cu matrix to even out any difference in concentration during the exposure.

Becker et al. (2020) also investigated samples that had been welded in argon or air before exposure to sulfide. Samples welded in air, meaning that copper in the welds was oxidised, exhibited an increase in H content by more than one t.ppm when exposed to 10^{-3} mol/L HS^- whereas samples welded in argon were much less affected by the same exposure. This further demonstrates the importance of welding KBS-3 canisters in an inert atmosphere to avoid the formation of oxides that may potentially bind hydrogen in the repository environment, and/or alter the mechanical properties of the weld.

Yagodzinskyy et al. (2018) electrolytically charged $1 \times 3 \times 10$ mm single crystal copper samples of 99.9999 wt.% purity. The electrolyte was 1 N H_2SO_4 aqueous solution with 20 mg/L $NaAsO_2$ recombination poison and the charging was carried out under controlled electrochemical potential of −350 mV (SHE) at 50 °C for 250 ks (ca 70 h). The average concentration of hydrogen in the charged samples was determined by thermal desorption spectroscopy (TDS) to be about 240 at.ppm, i.e. around 4 wt.ppm. Positron annihilation spectroscopy indicated void formation, and indications of near-surface voids were also observed as spikes in the TDS spectra. The hydrogen was thus believed to be present in part as molecular hydrogen in the voids formed by the electrolytic charging. The H charging rate was 240 at.ppm in 1 mm copper during 250 ks i.e. $240 \times 10^{-6} \times 8.9\ \mathrm{g \times cm^{-3}} / 63.5\ \mathrm{g \times mol^{-1}} \times 0.1\ \mathrm{cm} / 250\,000\ \mathrm{s} \approx 1.3 \times 10^{-11}$ mol/(cm^2 s). The charging current is not given in the paper, however, if it is assumed to have been around 10 mA/cm^2 as in similar experiments, i.e. 10^{-7} mol/(cm^2 s), then in this experiment, as in that of Martinsson and Sandström (2012) described above, a fraction of the order of 10^{-4} of the generated H appears to enter the metal. This assumes that there are no losses of H over the boundaries of the sample, i.e. that all hydrogen that enters through charging stays in the material. The authors found that the hydrogen introduction caused strain hardening with about 6 % increase of the flow stress at the nominal strain of about 2 % in stage I of the plastic deformation, i.e. the very first part of the plastic deformation. The observed increase in the flow stress is very small, only up to 2 MPa. Hydrogen is known to stabilise the formation of vacancies (Ganchenkova et al. 2014, Korzhavyi and Sandström 2014). This mechanism is assumed to explain the small increase in the flow stress. Stage I does not occur in the polycrystalline material that is used for the copper canisters. If the effect also exists in polycrystalline copper, it would be expected to be quite small as well and without technical significance due to the small effect of vacancies compared with the effect of grain boundaries.

In Leijon et al. (2018), creep tests for Cu-OFP were carried out at 23, 50 and 75 °C with and without continuous charging. The hydrogen charging was performed in an electrolyte of 1 N H_2SO_4 solution with 10 mg $NaAsO_2$ (or 5 mg As_2O_3) recombination poison per litre at a controlled potential of −1.1 V (Hg/Hg_2SO_4). The setup was enclosed by a double-wall glass compartment so that the copper specimen was visible. Gas bubbles were observed on the surface of the specimen, making it evident that much of the electrolytically generated hydrogen recombines into molecular hydrogen (H_2) instead of entering the material as atomic hydrogen (H). Creep tests (up to 1000 h) were first performed applying the same tensile stress of 140 N/mm^2 as was used by Yagodzinskyy et al. (2012); however, no surface cracks were observed after these tests. The stress level was then raised to 170 N/mm^2 or above. After the creep testing, the hydrogen content of all charged specimens was measured to ensure that a significant amount of hydrogen had entered the material. Up to 12 wt.ppm was measured. For some charged specimens, intergranular cracks with a maximum depth of 100 µm were found. On the crack surfaces bubbles were frequently observed. Creep deformation was recorded only for two specimens, which showed higher and lower creep rates than for ordinary creep tests in air. These measurements show that the hydrogen charging had a limited effect on the creep properties.

A brief summary of the references discussed above is given in Table 3-11. For each reference the analysed material is specified. When it is available in the report, the longest charging time as well as the measured hydrogen content is provided. In a number of the reports the microstructure has been studied after charging. If mechanical properties were measured, some main findings are shown in Table 3-11.

Table 3-11. Main findings in studies on H charging of copper.

Study reference	Charging method	Material	Max charging time (h)	Max H content (wt.ppm)*	Microstructure	Mechanical properties	Comment
Wampler et al. (1976)	High pressure at T > 600 C	Pure Cu		5	Fine bubbles 0.2–0.4 μm		
Okinawa and Straschil (1986)	Electroless deposition	Powder metallurcial Cu		39	Porous copper	Low ductility above 10–25 wt.ppm H	No relevance for canister Cu
Panagopoulos and Zacharopoulos (1994)	Electrolytic charging 100 mA/cm^2 with recombination inhibitor (As_2O_3)	Pure Cu	36			30 % reduction of tensile strength and elongation after 25 h charging	
Martinsson and Sandström (2012)	Electrolytic charging 10 mA/cm^2 with recombination inhibitor (As_2O_3)	Cu-OFP	500	5	Bubbles and increased hydrogen content < 50 μm from surface		H pick-up factor 10^{-4}
Yagodzinskyy et al. (2012)	Hydrogen charging at 20 and 50 °C during slow strain rate tensile tests	Cu-OFP	14		Intergranular surface cracks < 110 μm from surface	Up to 7 % reduction in tensile strength and 10 % in ductility	
Lousada et al. (2016)	Gamma radiation (69 kGy) in water	99.98 % Cu		0.4	Crystals and localised corrosion features to ~< 1μm depth		
Becker et al. (2020)	Corrosion in sulfide solution, SSRT	Cu-OFP	572	1.1	Surface cracking		
Yagodzinskyy et al. 2018	Electrolytic charging under controlled potential −350 mV (SHE) at 50 °C with recombination inhibitor $NaAsO_2$	6N Cu	69	4	Fine slip bands observed	6 % increase in flow stress	H pick-up factor estimated to be 10^{-4}
Leijon et al. (2018)	Creep testing at 23–75 °C, with and without electrolytic charging at a controlled potential −1.1 V (Hg/Hg_2SO_4) with recombination inhibitors	Cu-OFP	1000	12	Cracks down to < 100 μm		

* Assuming homogeneous charging of the sample.

Finally, it is noted that the influxes of hydrogen in the cited experiments are considerably higher than those expected in the final repository. Relevant repository conditions need to be considered when evaluating the significance of hydrogen embrittlement in the assessment of post-closure safety.

In terms of theoretical understanding of the behaviour of H in Cu, Lousada and Korzhavyi (2020b), among other things, considered the energetics of H on the copper surface versus H in an interstitial position in the Cu matrix. The energy difference between these two states, i.e. the segregation energy of H to a Cu surface, was calculated to be at least 0.5 eV for surface coverages of H of both 25 and 100 %. This suggests that the H concentration in the bulk material in equilibrium with a surface with a high H coverage can be estimated at $\exp(-0.5\text{eV}/kBT) \approx 3.5 \times 10^{-3}$ at.ppm, where k_B is the Boltzmann constant and T the absolute temperature, see further Section 7.4 in SKB (2019). For a more sparsely covered surface, the corresponding H concentration would be even lower. A concentration of 3.5×10^{-3} at.ppm is a very low value and many orders of magnitude smaller than the initial concentration of H in Cu-OFP. These results suggest that any hydrogen generating process on a Cu surface, e.g. a corrosion process, would lead to only a very limited increase in the bulk concentration of H in the copper metal.

Natural analogues/observations in nature

Not applicable.

Time perspective

The significance of hydrogen embrittlement needs to be evaluated on timescales where the formation of atomic or molecular hydrogen may occur at the surface of the copper canister. Since potentially hydrogen-generating copper corrosion by sulfide is relevant on all timescales of the post-closure safety assessment, this applies also to hydrogen embrittlement.

Handling in the PSAR

The potential extent for hydrogen embrittlement of copper is addressed in the PSAR Post-closure safety report (SKB 2022a) by considering the liberation of hydrogen in processes occurring at the canister surface, assessing the fraction of the liberated hydrogen that could enter the copper and the hydrogen concentrations this could lead to in the material. Such concentrations are then compared to the concentration of hydrogen already present in the copper and/or to experimental conditions in which no detrimental effects are found. Two main cases are considered: One where hydrogen diffusing in the copper metal is assumed to be trapped and accumulate in molecular form in “bubbles” preferentially located at grain boundaries and one where only diffusion in the Cu matrix is considered, without trapping.

Embrittlement due to reduction of oxides neglected since the concentration of oxygen in Cu-OFP is sufficiently low, and since welding under inert gas has been shown as efficient to avoid enhanced oxide concentrations in the weld.

Boundary conditions: The boundary conditions concern the potentially hydrogen liberating processes at the copper surface. These are explicitly included in the handling.

Handling of variables influencing this process: The influencing variables, i.e. the canister geometry, the relevant temperature and the relevant material properties are included in the handling of this process.

Handling of uncertainties in the PSAR

Uncertainties in mechanistic understanding

The mechanistic understanding of this process is to some extent incomplete. The handling is though focused on demonstrating that the extent of the process is negligible under repository conditions, see further Section 10.3.13 in the PSAR Post-closure safety report (SKB 2022a).

Model simplification uncertainties

Model simplifications are essentially addressed by choosing input data pessimistically and by considering two bounding cases; one where H is trapped in bubbles and one where only diffusion in the Cu matrix is considered.

Input data and data uncertainties

Bounding cases are sought in the handling of this process, i.e. input data are chosen pessimistically.

3.5 Chemical processes

3.5.1 Corrosion of cast iron insert

Overview/general description

Water in the fuel channels of the insert and in the annulus between the copper shell and the cast iron insert will cause corrosion of the cast iron. This process could potentially affect the integrity and mechanical strength of the insert. Another consequence of corrosion of iron by water is the formation of gaseous hydrogen and solid corrosion products, of which the latter can exert pressure against the copper canister. The process is central to the canister's hydraulic, mechanical and chemical evolution if the copper shell should be breached by rock shear or corrosion.

Corrosion can be caused by water inside an intact canister, which is a possibility that cannot be ruled out since some water may be present in fuel rods. Thus, also after the consumption of oxygen inside the canister by corrosion, this water will cause anaerobic corrosion of the insert.

Corrosion can also be caused by water that has entered a defective canister. Groundwater at repository depth is expected to be oxygen-free (when the initially entrapped oxygen is consumed). The cast iron insert will, therefore, corrode anaerobically to generate hydrogen gas and form a solid corrosion product, most likely magnetite, and also some dissolved ferrous iron. The magnetite is expected to consist of a thin adherent epitaxial layer and an outer, looser layer with poor adhesion. The resistance of the inner layer to ion transport will determine the corrosion rate. Since this layer appears to achieve a constant thickness while the outer non-protective layer continues to thicken as corrosion continues, the corrosion rate is expected to remain constant over a long period, see below. In the case of high sulfide fluxes, e.g. advective conditions transporting sulfide with the groundwater, or the formation of a biofilm of sulfide reducing bacteria (SRB) at or near the insert surface, the corrosion might be controlled by the supply of sulfide, or sulfate and carbon respecively. Alternatively, if the water supply is low, the corrosion rate will be determined by the availability of water.

The corrosion rate of iron under anoxic conditions depends on the pH of the groundwater (or bentonite pore water) and the presence of sulfate reducing bacteria, as described further below.

Dependencies between process and canister variables

Table 3-12 shows how the process influences, and is influenced by, all canister variables.

Table 3-12. Direct dependencies between the process "Corrosion of cast iron insert" and the defined canister variables and a short note on the handling in the PSAR.

Variable	Variable influence on process		Process influence on variable	
	Influence present? (Yes/No) Description	Handling of influence (How/If not – why)	Influence present? (Yes/No) Description	Handling of influence (How/If not – why)
Radiation intensity	Yes. Gamma-radiation may influence the corrosion that takes place during the first several hundred years.	See Section 3.5.3.	No.	–
Temperature	Yes.	Neglected. Corrosion due to water inside an intact canister is restricted by mass balance. The temperature dependence of the corrosion is marginal in the temperature range that needs to be considered for intruding water.	No.	–
Canister geometry	Yes.	See Section 2.3.1.	Yes. The corrosion products have a larger molar volume than the metal.	Neglected. After failure of the copper shell the influence of the corrosion products on the canister geometry and on transport resistance for radionuclides is neglected.
Material composition	Yes. Different materials have different corrosion properties.	Actual and/or similar insert materials are considered in the evaluation.	Yes. Solid corrosion products are formed, and anoxic corrosion may lead to increase of hydrogen content in the iron.	The effect of hydrogen is neglected due to small effects, see Section 3.4.2.
Mechanical stresses	Yes. Possible environmentally assisted cracking.	See Section 3.5.3.	Yes. The corrosion products may exert a pressure on the canister components.	See Section 3.4.5.

Boundary conditions

The boundary conditions for this process are the physical boundary set by the geometries of the components involved, the composition of water in the canister interior, and the radiation field from the fuel elements. In the case of a breached copper shell, the corrosion process of iron is also coupled to the inward transport of water for which boundary conditions are discussed in Section 2.3.1.

Model studies/experimental studies

Corrosion caused by water inside an intact canister: The fuel elements will be dried before being transferred to the canister, but some water may nevertheless be present in fuel rods. A very pessimistic assumption would be that one fuel rod per fuel element is filled with the maximum water volume and is transferred to each canister. The scope of the corrosion this could cause can be modelled using a simple mass balance approach:

The total quantity of water that can be accommodated in the void in a fuel rod is 50 g. It is expected that no more than 12 fuel rods containing that amount of water will be transferred to the canister. The total maximum amount of water will, therefore, be 600 g (Posiva SKB 2017). If this water reacts solely with the iron in the canister and is assumed to form magnetite, a maximum of about 1 400 g of iron could corrode. This will result in a relatively uniform corrosion depth of less than 10 µm

for the cast insert. In the design premises (Posiva SKB 2017) it is specified that the atmosphere in the canister should be replaced by > 90 % argon. The handling is further described in SKB (2021b, Section 3.12).

Corrosion caused by water that has entered a defective canister: Anaerobic corrosion of cast iron has been studied experimentally by Smart et al. (2002a, b), who found that the corrosion rate is well below 1 μm/year after a few thousand hours even at elevated temperatures and in the most corrosive artificial groundwaters tested. In groundwater with high ionic strength and pH 7 to 8, the long-term corrosion rate for cast iron was measured as 0.1 μm/year, whereas at pH 10.5, the rate was as low as 0.01 μm per year.

In the reaction between cast iron and water, magnetite and hydrogen are produced. Initially, the corrosion rate is quite high but falls off rapidly to very low rates as the surface film of magnetite develops. The rate of hydrogen production at the highest measured long-term corrosion rate is about 0.5 $dm^3/(m^2\ y)$ (Smart et al. 2002b). The total internal surface area in the canister insert is approximately 33 m^2 for a BWR insert (approximately half for a PWR insert), which means the annual production of hydrogen would be 16 dm^3 at normal pressure or 0.33 dm^3 at the pressure at repository level (500 m depth).

The corrosion rate of iron under anaerobic conditions has proved to be independent of both the hydrogen gas pressure for repository-relevant conditions (Smart et al. 2002a) and the concentration of Fe^{2+} (Smart et al. 2002a, b) in the system. The long-term corrosion rate is also independent of whether or not the water is present as a liquid or as vapour at high relative humidity (Smart et al. 2002b). This suggests that the corrosion rate is most likely determined by the ion transport properties of the magnetite layer on the iron surface:

The magnetite (Fe_3O_4) consists of a thin, strongly adherent layer and an outer, looser layer with poor adhesion (Smart et al. 2002b). It is suggested that the adherent layer is formed directly on the metal surface, while the looser layer is probably formed by the precipitation of dissolved Fe^{2+}

$$Fe + 2H_2O \rightarrow Fe^{2+} + H_2 + 2OH^-$$

$$Fe^{2+} + 2\ OH^- \rightarrow Fe(OH)_2$$

$$3Fe^{2+} + 4H_2O \rightarrow Fe_3O_4 + 8\ H^+ + 3H_2 + 2e^-$$

The adherent layer forms very quickly and then does not increase further in thickness. Continuing corrosion leads to the thickening of the looser non-protective layer. Corrosion is controlled by ion transport across the adherent layer and should continue at a constant rate over long periods of time.

Microbiologically influenced corrosion: While the laboratory studies referred to above were conducted under abiotic conditions, repository like field-tests performed at the Äspö HRL have shown rather low general corrosion rates (2–3 μm/year by mass-loss) of cast iron either embedded in compact bentonite clay or in the absence of bentonite clay (Gordon et al. 2017). In contrast, rapid corrosion of iron (>500 μm/year) occurred in the presence of low-density bentonite (Smart et al. 2012). This may have been caused by a combination of a density or swelling pressure low enough to support microbial activity, and the presence of organic material in the bentonite clay. On some specimens exposed under advective conditions at or near the corroding surface, localised corrosion has been observed with pits on the mm scale. Although there are some specimens for which galvanic coupling cannot be ruled out with certainty (oxic conditions may have persisted for a few months, see further Smart et al. (2015), the most likely explanation for these observations is the influence of SRB, since both the presence of viable SRB and the formation of iron sulfides has been verified on the surfaces of some of these specimens (Smart et al. 2012, Gordon et al. 2017, Hallbeck et al. 2017).

Natural analogues/observations in nature

There are some studies of archaeological artefacts reported in the literature. Studies by Neff et al. (2003, 2005) and Dillmann et al. (2014) review some newer studies as well as data from their own investigations. Neff et al. (2005) carefully studied the corrosion products on artefacts from the 2nd century AD to the 16th century AD. In a further publication, Neff et al. (2006) analysed archaeological artefacts to determine the average corrosion rate of low carbon steel after long burial periods. The corrosion products found indicate that some corrosion took place with oxygen present. Nevertheless, the conclusion from the study is that the estimated average corrosion rates do not exceed 4 μm/year.

Neff et al. (2003) found that the measured or estimated corrosion rates vary over a relatively large range and the corrosion products, when identified, indicate that oxygen had been present in the system. The reported rates range from 0.01 µm/year to extreme values of 1 000 µm/year. At one site where the conditions had been oxygen free and the carbonate content in the water had been high (10^{-2} M), siderite (Fe-carbonate) is identified as the main corrosion product (Matthiesen et al. 2003, 2007). This site at Nydam Mose in Denmark was waterlogged and the buried objects are military equipment sacrificed in the period 200–500 AD. The estimated corrosion rates range from an upper limit of 5 µm/year down to 0.03 µm/year or less. The average corrosion rate for 151 analysed lances is about 0.2 µm/year.

Dillmann et al. (2014) also discussed the development of localised corrosion of archeological steel artefacts and noted that while short term pitting factors can attain values of 10^2–10^3, the pitting factor generally decreases to less than 10 when corrosion proceeds to mm average depths.

Time perspective

At a corrosion rate of 1 µm/year, metallic iron will be present for tens of thousands of years after failure of the copper canister. Even at the high corrosion rates attributed to microbial influence, the material will be present for hundreds of years.

Handling in the PSAR

Even with a pessimistic assumption of 600 g of water per canister, the effects of the corrosion of the canister insert prior to failure of the copper canister can be neglected due to fast consumption and very limited corrosion effects.

In the case of a canister breach, the process is treated as part of an integral description of the evolution of the canister interior after damage (see further Section 2.3.1).The treatment aims at bounding the consequences of the effects of the set of integrated processes. This is further developed in the PSAR Data report (SKB 2022d, Section 4.2).

Boundary conditions: The boundary conditions mentioned above are included in the integrated treatment, see Section 2.3.1.

Handling of variables influencing this process: Of the influencing variables in the table, the canister geometry and the material properties are included in the integrated treatment, see Section 2.3.1. The temperature, though, is assumed to be constant and equal to about 15 °C and anaerobic conditions are assumed to prevail in the canister interior. Radiation effects are neglected based on the discussion in Section 2.5.3.

Handling of uncertainties in the PSAR

Uncertainties in mechanistic understanding

There are no major uncertainties in the understanding of the corrosion of iron under oxygen free, reducing conditions.

Model simplification uncertainties

In a breached canister, the process is modelled with a constant corrosion rate unless the supply of water is limiting. Several developments, in which this process is integrated with a number of others, are considered in order to bracket the possible scenarios.

Rather than seeking justification of model simplifications, the consequences of this process are given a pessimistic upper bound in the safety assessment, as discussed above.

Input data and data uncertainties

Intact canister: There are uncertainties regarding the quantity of water that could conceivably be left in the canister, even after replacement of the air by argon. The uncertainties are, however, of no importance, since the extent of corrosion pessimistically achievable would be negligible.

Breached canister: The uncertainties regarding the corrosion rate are discussed above, see *Model studies/ experimental studies* and most data indicate a rate of less than 0.1 µm per year. The experimental investigations show that if the protective corrosion product layer of magnetite is damaged, it will reform very quickly and the measured corrosion rates can be assumed to apply even for long periods of time. For the case of SRB biofilm formation on the insert material in a breached canister, some uncertainties remain regarding the mechanism and rate.

3.5.2 Galvanic corrosion

Overview/general description

If the copper shell is breached and groundwater comes into contact with the cast iron insert, electrochemical reactions on the copper surface will influence the corrosion of the insert. The consequences of galvanic corrosion have been investigated by Smart et al. (2005).

If the groundwater contained oxygen, the rate of cast iron corrosion was very high, up to 100 µm per year (Smart et al. 2005). At the time of water intrusion into the canister, however, the water is expected to be oxygen-free and reducing. In oxygen-free water, the measured corrosion rates of cast iron galvanically coupled to copper were in the same range as those measured for cast iron in the absence of galvanic coupling to copper (Smart et al. 2005).

Dependencies between process and canister variables

Table 3-13 shows how the process influences, and is influenced by, all canister variables.

Boundary conditions

The boundary conditions for this process are the physical boundaries set by the geometries of the components involved and the composition of the water in the canister void. The corrosion process is coupled to the inward transport of water for which boundary conditions are discussed in Section 2.3.1.

Model studies/experimental studies

See Overview/general description.

Natural analogues/observations in nature

Not applicable.

Time perspective

The process takes place after canister penetration.

Handling in the PSAR

The influence of galvanic corrosion under oxygen-free, reducing conditions lies within the margins of error for the corrosion rate of the iron insert and is, therefore, not dealt with specifically.

Handling of uncertainties in the PSAR

Uncertainties in mechanistic understanding

There are no major uncertainties in the understanding of galvanic corrosion.

Model simplification uncertainties

In oxygen-free water, the effects will be small and the uncertainties surrounding the exact contribution made by galvanic corrosion are judged to be negligible compared with the uncertainties in assessments of the corrosion rate. A cautious hypothesis for the corrosion rate for anaerobic corrosion of the canister insert will cover any contributions from galvanic corrosion.

Table 3-13. Direct dependencies between the process "Galvanic corrosion" and the defined canister variables and a short note on the handling in the PSAR.

Variable	Variable influence on process		Process influence on variable	
	Influence present? (Yes/No) Description	Handling of influence (How/If not – why)	Influence present? (Yes/No) Description	Handling of influence (How/If not – why)
Radiation intensity	No.	–	No.	–
Temperature	Yes. Corrosion reactions are generally temperature dependent.	Neglected. The influence of galvanic corrosion under oxygen-free, reducing conditions lies within the margins of error for the corrosion rate of the iron insert.	No.	–
Canister geometry	No. There will always be a galvanic contact regardless of geometry.	–	No.	–
Material composition	Yes. Galvanic corrosion requires two metals.	Neglected. The influence of galvanic corrosion under oxygen-free, reducing conditions lies within the margins of error for the corrosion rate of the iron insert.	No.	–
Mechanical stresses	No.	–	Yes. Growth of corrosion products will cause stresses in the canister materials.	Neglected. The influence of galvanic corrosion under oxygen-free, reducing conditions lies within the margins of error for the corrosion rate of the iron insert.

Input data and data uncertainties

The uncertainties are negligible compared to those handled in Section 3.5.1.

3.5.3 Stress corrosion cracking of cast iron insert

Overview/general description

The stress corrosion cracking (SCC) of metals requires a combination of tensile stresses, a specific chemical environment and, a susceptibility of the material. The metal is mostly not attacked on its surface but unfavourable combinations of these conditions can lead to the initiation and propagation of local cracks through the matrix over a period of time.

In a canister with an intact copper shell, nitric acid can form from the radiolysis of residual quantities of nitrogen in moist air (Jones 1959). Nitrate is known to cause SCC in carbon steel in concentrated nitrate solutions with a slip-dissolution mechanism (King 2010), but there are no reports found in the literature that shows SCC would occur in cast iron (Reynaud 2009). Possibly formed nitric acid would rather cause general corrosion, which also would give reduction of the graphite nodules by intruding hydrogen and dissolution of the ferritic matrix and pearlitic structure constituents. This will counteract the formation of sharp cracks with passivated crack walls, which is a prerequisite for stress corrosion cracking with a slip-dissolution mechanism.

A fundamental requirement for a corrosive environment is the presence of water. The presence of water inside the insert cannot be dismissed, however, as discussed in Section 3.5.1 the amount of water would be very limited and in addition it would be consumed relatively fast due to corrosion of the iron insert in a hot and irradiated environment (Spahiu 2021, Henshaw and Spahiu 2021). In the repository, the canister insert is under external pressure and tensile stresses occur on the cast insert only locally and in small areas, according to calculations in Dillström et al. (2010). In addition, there

is a requirement in the design premises (Posiva SKB 2017) to replace the air in the insert with > 90 % argon, which will lower possible amounts of nitrate. It is, therefore, highly improbable that SCC could lead to penetrating cracks in the canister, and above all that this would jeopardise the integrity of the canister.

Dependencies between process and canister variables

Table 3-14 shows how the process influences, and is influenced by, all canister variables.

Boundary conditions

Nitric acid from radiolysis of nitrogen in residual quantities of moist air in the void inside the canister could conceivably cause SCC in areas with tensile stresses in the cast iron insert.

Model studies/experimental studies

See Overview/general description.

Natural analogues/observations in nature

Not applicable.

Time perspective

The effect of radiolysis decreases with time, and is negligable after 300 years due to the decay of Cs-137.

Table 3-14. Direct dependencies between the process "Stress corrosion cracking of cast iron insert" and the defined canister variables and a short note on the handling in the PSAR.

Variable	Variable influence on process		Process influence on variable	
	Influence present? (Yes/No) Description	Handling of influence (How/If not – why)	Influence present? (Yes/No) Description	Handling of influence (How/If not – why)
Radiation intensity	Yes. The agents that may cause SCC are produced through radiolysis.	Neglected. Tensile stresses only occur locally in small areas. Also, if water is present inside the insert it is only expected to be present in small amounts and during a relatively short period.	No.	–
Temperature	Yes.	Neglected, due to small effects.	No.	–
Canister geometry	No.	–	No.	–
Material composition	Yes. Different materials have different sensitivities to SCC.	Actual insert material is considered.	No.	–
Mechanical stresses	Yes. Tensile stresses are required. Compressive stresses prevent SCC.	Neglected. Tensile stresses only occur locally in small areas.	Yes. SCC relaxes tensile mechanical stresses.	Pessimistically neglected.

Handling in the PSAR

Stress corrosion cracking in the cast iron insert, if it occurs, is deemed to be of no importance for the integrity of the canister.

Handling of uncertainties in the PSAR

Uncertainties in mechanistic understanding

There are uncertainties in the understanding of stress corrosion cracking, but they will be of no importance for the safety assessment, since the extent of the process will be limited.

Model simplification uncertainties

Stress corrosion cracking of the insert will not be modelled.

Input data and data uncertainties

The probability of SCC jeopardising the canister integrity is deemed to be small, since only local areas in the insert have tensile stresses. The uncertainty of the quantity of nitrogen that may have been left in the canister is bounded by the design premises of exchanging the atmosphere from air to > 90 % argon. Also, the amount of remaining water is limited to a maximum of 600 g.

3.5.4 Corrosion of copper canister

Overview/general description

A range of studies over several decades (see e.g. King et al. 2001, 2010 for a review) have identified the following substances as capable of corroding the copper canister material under repository conditions:

- oxygen,
  - atmospheric corrosion in the encapsulation plant and repository,
  - corrosion in unsaturated bentonite by oxygen introduced during the repository operating period,
  - corrosion by oxygen trapped in the air-filled pore spaces in the buffer and backfill,
  - corrosion caused by oxygen in penetrating glacial meltwater,
- nitric acid formed by gamma-radiolysis of nitrogen gas in moist air in the gap between canister and buffer,
- oxidants formed by radiolysis of condensed water at the canister surface or bentonite pore water in contact with the canister,
- sulfide transported to the canister surface from the buffer and backfill, or from the groundwater via water bearing fractures in the deposition hole and through the buffer.

The copper shell is the canister's corrosion barrier. Its design purpose is to prevent contact between the encapsulated fuel and the groundwater after deposition of the canister and for as long time as required keeping the dose in the surface biosphere below the risk criteria. The corrosion processes are only marginally affected by the changes in temperature expected in the deep repository. The consequences of corrosion are the formation of corrosion products on the canister surface and a gradual reduction of the thickness of the copper shell. Nevertheless, after very long time spans the corrosion process will penetrate the copper shell, allowing groundwater into the canister.

After the fuel has been encapsulated, the copper canisters will be transported to the geologic repository and deposited. However, some storage time may be inevitable. During that period, the canisters will be exposed to indoor air either at the encapsulation plant or at the repository site and to the atmosphere inside the vessel that will be used for transporting the canister to the repository site.

During transport and handling of the canister it will be inevitable that marks will be incurred from bumping into other objects or from scraping of the surfaces. This will result in locally cold worked areas. It has been known for a hundred years that indentations and scars on a steel surface will stimulate rusting (Cushman and Gardner 1910). It is, therefore, not unreasonable to assume that there will be similar effects on copper. The effects of cold work on corrosion and corrosive wear have been studied by Yin and Li (2005), Li and Li (2005) and Tao and Li (2008). They found that the corrosion potential and the electron work function decreased while the corrosion rate increased with an increase in plastic strain. Yin and Li (2005) measured a decrease in corrosion potential in 0.1 mol/L HNO_3 of about 12 mV for an 80 % reduction in thickness, while in 3.5 % NaCl, the corresponding decrease was 7 mV with the largest decrease at 50 % reduction in thickness. Gubner et al. (2006), using a Kelvin probe measured surface potentials which were 90–200 mV lower in the electron beam weld than in the parent material in a canister lid weld. In a later study, however, no galvanic enhancement of corrosion in the weld could be observed (Gubner and Andersson 2007). As a follow-up, Taxén et al. (2017) compared the potentials of base material copper, cold-worked copper (in a tensile as well as compressive state) and welded (friction stir weld) material in a 0.5 mol/L $MgSO_4$ solution (pH 2.5), but found no significant differences in apparent nobility. It is, therefore, unlikely that a galvanic cell will be established between small cold worked areas or the weld, and the larger non-deformed or non-welded areas on the canister surface.

After emplacement in the deposition holes, it will no longer be possible to actively control the composition of the atmosphere to which the canister is exposed. The buffer and backfill are not saturated with water during the installation and water is provided by the host rock. This wetting process, leading to the final water-saturated conditions around the spent fuel canisters, the form of its progress, and its duration will influence the form and the extent of the corrosion during this phase in the canister service life. The rate at which the buffer resaturates can vary greatly between different deposition holes. Depending on accessibility of water, the time to fully saturate the buffer can range from 10 to several thousands of years (Åkesson et al. 2010).

After water saturation, oxygen may still be present in the canister's surroundings. This oxygen will be consumed by reactions with the copper canister and by reactions with minerals in the bentonite buffer or the host rock. Microbes in the deposition tunnel backfill may also play an important role in oxygen consumption. The density of the backfill is low enough to allow some microbial activity. The effect of microbes would be to shorten the time to reach anoxic conditions in the saturated backfill. Later oxygenated conditions cannot be excluded, as glacial meltwater may reach some canisters positions.

When the oxygen is consumed, the reducing conditions that prevailed before the repository was excavated are expected to be restored. Dissolved sulfides are the only corrosive substances that can react with the copper canister after the oxygen in the repository has been consumed. At the proposed repository depth, the groundwaters have very low sulfide concentrations, mostly much lower than 5×10^{-5} mol/L, and the solubility of the sulfide minerals present in the bentonite is, at most, of the same order of magnitude. This means that the corrosion of the copper canister due to sulfides will be controlled by the availability and supply of sulfides from the groundwater, and the buffer and backfill.

For assessments of corrosion damage and a decrease in copper shell thickness, mostly general corrosion is assumed, which is reasonable in view of the nature of the corrosion. A roughness is often accompanying the general corrosion due to non-permanent separation of anodes and cathodes. More distinct localised attacks are conceivable under certain conditions, which is why localised corrosion is described below, including the mechanically influenced stress corrosion cracking.

A few other corrosion conditions are also evaluated, mostly from a thermodynamic point of view. This includes the reaction of copper with pure water, copper exposed to high chloride conditions, and abiotic corrosion of copper by sulfate.

More detailed elaborations of the different oxidants and corrosion are given under separate subheadings below.

Atmospheric corrosion in the encapsulation plant and repository

The formation of a water film on a metal surface is of fundamental importance to atmospheric corrosion. The thickness of this water film varies from a few monolayers at low relative humidity to thousands of monolayers at 100 % relative humidity (Leygraf 2002). When the relative humidity

exceeds the “critical relative humidity” the corrosion rate increases markedly with increasing humidity. This critical relative humidity depends on the surface conditions of the metal but is generally in the range 50–70 %.

When the thickness of the water film exceeds about three monolayers its properties become similar to those of bulk water (Phipps and Rice 1979). This occurs approximately at the critical relative humidity. As this film thickens, water-soluble pollutants will dissolve in the moisture film in equilibrium with the gaseous phase. The SO_2 present in the air will dissolve forming HSO_3^- and can be oxidised to sulfate by oxidants in the air (e.g. stoichiometrically by ozone, and catalytically by NO_2 (Leygraf and Graedel 2000). The NO_2 present in the air is assumed to be absorbed in the moisture film as HNO_3. The actual indoor humidity will depend on the ventilation of the facility, but will be below the critical humidity at least during the winter months.

The indoor air is expected to have a temperature of about 20 °C. The expected maximum surface temperature for a canister with a heat generation of 1.7 kW is somewhat less than 50 °C when the canister is exposed to freely circulating air. When inside a radiation shield, the temperature may approach 100 °C.

The elevated surface temperature (50 °C) of the copper canister will ensure a relative humidity considerably lower than the critical humidity close to the canister surface. The corrosion rate can, therefore, be assumed to be very low. Rice et al. (1981) have reported corrosion rates for copper exposed at ambient temperature in different atmospheres. The exposure times were 1 to 1.5 years. For city atmospheres, they reported corrosion rates of 6 to 27 nm/year. These rates are in agreement with those for the corrosion of copper in dry air as described by Evans and Miley (1937). They found that a layer of predominantly copper oxide was formed on the surface and that this layer inhibited further corrosion when it had reached a thickness of 9–10 nm. These data refer to room temperature. There are, to the authors’ knowledge, limited data available for the relevant canister temperature. Roy and Sircar (1981) report logarithmic oxidation kinetics in dry air at temperatures between 75 °C and 150 °C, while Pinnel et al. (1979) report parabolic kinetics. Both studies were performed in dry air and, although the rate laws they propose give quite different kinetics for the growth of the oxide layer at 100 °C, they predict a total oxide thickness after a few years exposure in the range 30 to 70 nm.

For mainly logistic reasons the canisters may be transported underground and stored in the repository before deposition. The plans encompass a canister depot with storage of the canisters in empty deposition holes in a dedicated tunnel, typically with storage periods of a couple of months, but up to two years is possible and would take care also of shorter stops in the deposition procedure. The exact design for this storage is to be specified, but forced ventilation of each deposition hole could be foreseen. The atmosphere would anyhow only differ slightly from the industrial atmosphere described above, and the canister temperature will be kept below 100 °C. The loading of canisters in canister transport casks will be done indoors (in Clink), while unloading will take place in the repository (Pers and Sturek 2021), so no further type of atmosphere (e.g. sea spray) is foreseen.

Taxén (2004) describes an atmospheric corrosion study at the Äspö HRL. Copper coupons were exposed to the natural atmosphere of the HRL with and without compacted bentonite present. Tests were performed at ambient temperature and, in the case of the test with bentonite, at 75 °C. Corrosion rates were estimated based on mass loss or from electrochemical stripping of the corrosion products under galvanostatic conditions. Corrosion rates were < 0.1 µm/year. This is significantly lower than typical surface atmospheric corrosion rates in Sweden, which are about 0.5 µm/year in urban atmosphere and can be up to and even over 2 µm/year in coastal areas (Taxén 2004). This suggests that the HRL atmosphere is less corrosive than normal surface atmospheres. It is assumed that the Äspö HRL atmosphere would be typical of the atmosphere in the repository. The only corrosion product detected was $Cu_2(OH)_3Cl$ (paratacamite), although the presence of Cu_2O is also likely and may not have been detected due to sampling artifacts (Taxén 2004).

Storing the copper canisters for extended periods of time before disposal for these conditions will have a negligible effect on their service life after disposal. The total corrosion attack even after two years storage will be less than 1 µm. The corrosion product will most likely be composed of different copper oxides and hydroxides.

Copper corrosion by initially entrapped oxygen

Although the groundwater at repository depth contains virtually no molecular oxygen at all, some limited amount will inevitably be trapped in the buffer and backfill materials during fabrication of the blocks and installation in the repository. In the presence of oxygen, and if the humidity or water is pure, copper is oxidised to Cu_2O and/or CuO, depending on the redox potential. In groundwater a duplex layer is typically formed, composed of an inner layer of Cu_2O and an outer layer of a precipitated basic Cu(II) salt, such as $Cu_2(OH)_3Cl$), $Cu_4(OH)_6SO_4$, or $Cu_2(OH)_2CO_3$. The nature of the Cu(II) phase formed depends on the composition of the groundwater (McNeil and Little 1992). These compounds can also form under atmospheric corrosion conditions.

The rate of O_2 driven corrosion may vary with time and between deposition holes, due to variations in the physico-chemical environment, e.g. increase of relative humidity, spatial variations in the saturation of bentonite, decreasing O_2 concentration due to consumption by corrosion and other processes, and temperature variations. Since the availability of oxygen in the repository will be limited to the finite amounts entrapped in the buffer and backfill materials, the exact rate of O_2 driven corrosion is not important for the assessment of canister integrity and post-closure safety.

The total extent of corrosion under aerobic conditions will be limited by the available amount of oxygen, i.e. the oxygen trapped in the repository after closure. After backfilling the tunnels, the entrapped oxygen can be estimated from the volumes and porosity of the buffer and backfill. The initial state for the buffer and backfill is described in the PSAR Post-closure safety report (SKB 2022a), Section 5.5.3 and 5.6.3 respectively, where the volumes of gas in the installed blocks and pellets are given. A deposition hole contains 3.81 m^3 gas, including the bevel in the tunnel floor for tilting the canister during installation. The deposition tunnel has a gas volume of 25.70 m^3 per 6 m tunnel (the distance between canisters according to the SKB (2019b). As shown in Appendix A2 the amount of oxygen per canister in the repository can be calculated to be about 277 mol. Of this amount, 241 mol comes from the tunnel backfill and 36 mol from the buffer in the deposition hole.

How much of the entrapped oxygen that will reach the canister surface and cause corrosion depends on how fast oxygen is consumed by other processes in comparison with the diffusion of oxygen towards the canister and the rate of copper corrosion. The rate of O_2 consumption by processes other than copper corrosion varies between different models and experimental conditions, as discussed in Section 10.2.5 in the PSAR Post-closure safety report (SKB 2022a). In general, it is likely that the consumption of oxygen by corrosion and other processes, such as microbial activity, reactions with minerals in the clay and at rock surfaces, is heterogeneous and occur on different timescales in saturated and unsaturated regions of the clay system. Consumption of oxygen by corrosion is also dependent on parameters such as relative humidity and temperature.

Probably, not all of the oxygen entrapped in the backfill will be available to corrode the canisters as some of it will be consumed by chemical reactions and microbial activity before it has had time to diffuse all the way to the deposition holes. However, experimental studies have indicated that the initially unsaturated and relatively dry clay system consumes O_2 rather slowly at low temperatures (Giroud et al. 2018, Birgersson and Goudarzi 2018), which is probably due to both the kinetics of chemical reactions and microbial activity being suppressed by low water activity and low temperature. The role of kinetics is corroborated by the strong temperature dependence of the oxygen consumption in experiments by Åkesson and Laitinen (2022). It is therefore, with the current state of knowledge of the kinetics of these processes, not possible to set a limit for the amount of O_2 that will have time to diffuse through the clay system and reach the deposition holes. Instead, the situation can be analysed by different cases of mass-balance, which may be considered as bounding for the extent of O_2 driven corrosion.

Initially, when the canister surface is covered by a very thin oxide film, reactions with O_2 may be rapid enough so that only the upper part of the canister surface consumes O_2 by corrosion. A reasonable estimate for the affected area could be derived on diffusion geometrical ground by “folding” the opening area of the deposition hole over the canister top. This would mean that the uppermost ca 10 % of the canister would be affected by corrosion. Assuming that this area would consume all of the O_2 in the backfill, and that the O_2 in the backfill would be divided equally between the deposition holes, the depth of corrosion would be 3.2 mm by mass-balance (for further details of the calculations, see Appendix A2). A similar analysis was considered in the safety assessment SR-Site. However,

since the corrosion rate of the uppermost canister surface will be significantly reduced as the oxide film grows thicker, O_2 will have time to diffuse also to the lower parts of the canister. If all of the entrapped oxygen in the buffer and backfill would corrode the canister surface evenly, the available amount of O_2 would result in a corrosion depth of 446 μm (Appendix A2). If, however, one allows for a differential corrosion depth due to the diffusion geometry from the backfill and down in the deposition hole, and assumes a linear variation with no corrosion at the bottom of the canister, the maximum corrosion depth (at the canister top) would be 891 μm. It is judged as reasonable that the maximum corrosion depth due to O_2 in the backfill would be somewhere between these two estimates (446 to 891 μm).

Assuming further that the amount of O_2 entrapped in the buffer (36 mol) is consumed by corrosion evenly distributed over the canister surface is pessimistic assumption, neglecting other sinks for O_2 in the deposition holes. The corresponding corrosion depth would be 64 μm by mass-balance (Appendix A2).

Adding up the average corrosion by O_2 from the backfill with the O_2 from the buffer material, and accounting for a differential corrosion depth due to the diffusion geometry from the backfill, it may be reasonable to assume that the maximum corrosion depth caused by O_2 would be less than 1 mm anywhere at the canister surface.

In most of the repository-like field tests that have been conducted, there has been no excess volume of entrapped air such as possibly available from the backfill in the repository. The corrosion measured in these tests can therefore not be directly compared with the situation for the canister in the repository (Gordon et al. 2017, Gordon et al. 2018a, Johansson 2019, Karnland et al. 2009, Johansson et al. 2020, Wendel et al. 2022). It may be noted that most of the O_2 initially entrapped in the LOT test parcels seems to have been consumed by copper corrosion under heated aerobic conditions (Johansson et al. 2020). In LOT, the corrosion products were mainly oxides and the oxide film adherent to the copper surface was generally up to a few μm thick. Measurements of copper in the adjacent bentonite clay were made in order to quantify how much of the corrosion product that had interacted with the clay and it was estimated that the average corrosion depth varied from less than 1 μm up to 14 μm depending on the temperature of the copper surface. In the fullscale field test Lasgit field (Wendel et al. 2022) it was concluded that the initial oxide thickness on the studied copper components was less than 1 μm upon deposition, and a significant portion of the observed corrosion (generally less than 3 μm oxide film, although locally up to 10 μm) could be assumed to have formed during exposure. However, as the studied copper components were subject to ambient conditions for roughly 5 months prior to analysis, it is not possible to quantify with accuracy how much of the oxide formed during exposure, and how much that formed during and after retrieval. The mass-loss of a corrosion specimen from the nearly 20 year long Febex field test corresponded to less than 9 μm corrosion although there was a large amount of initially available O_2 due to its large clay volume (Wersin and Kober 2017). However, it should be noted that Febex differed from other field tests, e.g. LOT, in several important aspects. First of all, the clay volume in Febex was very large compared with e.g. LOT, secondly, the area of the copper corrosion specimens was very small in comparison to the large central heater made of carbon steel, and furthermore, measurements of the gas composition revealed that at some locations in the experiment it took about one year to reach below one percent O_2 in the gas-phase, possibly this was due to a leakage (Giroud 2014).

Localised corrosion under oxic conditions

There are two distinct mechanisms that could lead to localised corrosion during the initial oxygenated conditions, depending on the relative timescales of the development of the redox potential and the wetting of the canister surface (which may be related to the timescale for the resaturation of the clay): non-uniform wetting with possibly droplets formed, and pitting through defects in a passive film.

For deposition holes in the driest parts of the repository, resaturation of the bentonite will be so slow that all O_2 is consumed by corrosion under unsaturated conditions. The initial surface wetting is likely to be non-uniform, either as distinct liquid droplets or in the form of a more or less continuous liquid film of variable thickness. Wetting of the canister surface occurs successively as the near-field bentonite clay gradually saturates. The process is initiated by the deliquescence of a surface salt contaminant, which results in the formation of a droplet. According to the classical Evans droplet

model for localised corrosion, the cathodic reaction preferentially occurs around the periphery of the droplet, as this region has greatest access to O_2. While spatial separation of anodic and cathodic processes under saturated conditions requires breakdown of a passive film, the initiation of localised corrosion under unsaturated conditions is instead a consequence of differential aeration and the geometry of the droplet. Thus, for this mode of localised corrosion, there is no requirement of a passive surface film.

During later years, signs of localised corrosion have been observed in a number of repository-like field tests. These large- or full-scale tests all started out in a state in which the bentonite clay was unsaturated, and in which full saturation and depletion of O_2 occurred over the timescale of the experiments. These tests may thus be regarded as representative of the full extent of localised corrosion due to uneven wetting that may occur during unsaturated conditions. A summary of each field test follows below.

In the full-scale Prototype Repository, two canisters were retrieved after 7 years of exposure in the Äspö HRL. Analysis of corrosion products showed mainly cuprite (Cu_2O) and malachite ($Cu_2(OH)_2CO_3$) and only traces of sulfur (Taxén et al. 2012). In order to examine the canisters for localised corrosion, 240 cross-sections were made from samples taken at six heights of each canister and examined with SEM (scanning electron microscope) in order to count and measure pits and surface defects (Taxén 2013). Among the hundreds of pits and defects observed and measured, the deepest pit found was 7 µm deep. The authors also made an extreme-value analysis based on the data from the two canisters and estimated that pits up to ca 35 µm could be expected somewhere on the canister surfaces. Since the initial state topography of the experiment canisters had not been characterised prior to the start of the experiment, it was not possible to know to what degree the observed topography was related to the actual corrosion process. Metallographic examination of another copper canister, not exposed to the Äspö HRL environment but stored in an indoor environment, revealed a surface topography that was similar to the Prototype canisters with frequently occurring pits and defects up to a few µm deep (Högberg et al. 2017). The surface topography of the canister material is probably due to machining in the canister manufacturing process, both for the Prototype canisters and the indoor stored canister, though the surfaces of the Prototype canisters has been affected by the subsequent corrosion during exposure in the Äspö HRL.

In the large-scale Febex experiment, two copper coupons were embedded next to each other in bentonite clay and were heated up to ca 100 °C for nearly 18 years (Wersin and Kober 2017). While the mass-loss of one coupon corresponded to less than 9 µm average corrosion, microscopic examination of the other coupon revealed an area with plenty of pit-like features on one side of the coupon. The pits found in seven cross-sections examined with SEM were densely distributed and their lateral extension was comparable with their depths. The largest pit found was ca 90 µm deep and ca 400 µm wide, i.e. one order of magnitude deeper than the average corrosion of the other coupon.

In the 20-year long bentonite field tests LOT/S2 and LOT/A3, heated to 90 °C and over 120 °C respectively, weight-loss coupons as well as copper tubes heating the clay were examined for localised corrosion (Johansson et al. 2020). The deepest pit found in cross-sections of the coupons was ca 10 µm deep and a few times as wide, while the average corrosion depth by mass-loss was ca 1 µm. Examination of the coupon surfaces with optical microscopy revealed pits and surface defects up to ca 30 µm deep on both the corroded and reference specimens. Since the reference coupons had been exposed to a dry indoor environment during the whole experiment and their weight-loss corresponded to only 0.1 µm, it is questionable if these pits are related to the exposure in the Äspö HRL. After removal of the corrosion surface products by acid pickling (used for the gravimetric analysis) the surfaces were once again examined with optical microscopy. Now the pits were generally deeper, but the reason for this is unclear as discussed further in Johansson et al. (2020). The deepest pit found on a coupon after removal of the corrosion products was nearly 60 µm deep and about twice as wide. Metallographic cross-sections of the copper tubes were examined with SEM. Similar to what was found for the coupons, pits and surface defects up to ca 10 µm depths occur frequently, while a few pits were up to ca 25 µm deep.

In the 5-year ABM 5 experiment, heated to 80 °C for the main period, copper specimens were examined for weight-loss and surface topography using optical microscopy (Gordon et al. 2018b). The deepest pit found on a corrosion specimen was 21 µm, however, slightly deeper pits were found on reference

specimens kept in dry indoor air during the experiment, and a comparison of the deepest pits found revealed no significant difference between the corroded and reference coupons. These results, together with microscopic inspection of the morphology of the pits, suggested that the pits found were not caused primarily by corrosion during the exposure in the Äspö HRL but are rather due to the mechanical preparation of the coupons. Similar defects have been seen on newly prepared copper coupons in other experiments (Gordon et al. 2018a).

In the full-scale test Lasgit, without heating and designed to be near water saturation at the start, the examination of corrosion showed mainly oxide formation. Examination of cross-sectioned canister material using SEM, showed a relatively smooth surface profile with shallow pits or other, possibly corrosion-induced, defects and a generally thin oxide film (< 3 µm). However, locally there were a few observations of up to 10 µm thick oxide and 5 µm pits or defects (Wendel et al. 2022).

In light of the results from large- and intermediate scale tests summarised above, it may be concluded that the maximum penetration to be expected due to localised corrosion under unsaturated aerobic conditions will be around 100 µm.

The second mechanism through which localised corrosion could occur is via the breakdown of a passive oxide film. This mechanism is conceivable for deposition holes in wetter parts of the repository, for which buffer saturation and even wetting of the canister surface may occur while the conditions are still aerobic. Localised corrosion under saturated aerobic conditions can be assessed based on a number of studies in the literature, of which a relevant set is discussed below.

Pitting of Cu water pipes has been studied extensively since the 1960's, see e.g. (Mattsson 1988, Edwards et al. 1994, Lytle and Nadagouda 2010). At least three types of pitting have been recognised (Mattson 1988). Type I pitting, the most common of all, was reported first by Campbell (1950) and a general theory for pit formation was proposed by Lucey (1967). Type I pitting is associated with cold, hard and moderately hard waters free of naturally occurring inhibitors, but containing HCO_3^-, SO_4^{2-}, Cl^- and O_2, and occurs on Cu pipes with a residual surface carbon film remaining from the manufacturing process (Mattsson 1980). Type II pitting is associated with hot potable waters (> 60 °C) with a pH < 7.4, a HCO_3^- to SO_4^{2-} concentration ratio < 1, and a high O_2 concentration. This type tends to produce pits with a larger depth to width ratio than the approximately hemispherical pits characteristic of Type I pitting. Type III is, like type I, restricted to cold water installations, but does not seem to bear any relation to the presence of a continuous carbon film. The main cause is likely to be found in the water composition. It is observed in cold water with low HCO_3^- and Cl^- content and high O_2 concentration. In some observations the pH has been low (Mattsson 1988), while others report high pH (Edwards et al. 1994).

Although pitting studies in potable waters may not be directly relevant for the assessment of localised corrosion of Cu canisters in saline porewaters, the proposed mechanisms provide some insight into the possibility of localised corrosion in a repository. One could consider three phases in the life of a pit: birth, propagation, and death. Passivation and passivity breakdown are generally regarded as necessary conditions for pitting to initiate on a copper surface, i.e. for the birth of pits. Further, the mechanistic Cu pitting studies indicate that an oxidant (either O_2 or Cu(II)) is a pre-requisite for pit propagation, see e.g. King et al. (2001, 2010). Pitting of Cu water pipes is only sustained because of the high O_2 concentration in fresh water and because it is continually replenished by the movement of water in the pipe. This would not be the case for pits on Cu canisters, both because of the limited amount of O_2 available and because of the restricted mass-transport conditions, which will limit the supply of O_2 to the corrosion sites. Therefore, pits on Cu canisters will be far more likely to die than those on Cu water pipes.

The main anions in the bentonite porewater will be chloride, bicarbonate and sulfate. The assessment of localised corrosion in SR-Site was based on a number of studies of the pitting of Cu in Cl^- and Cl^-/HCO_3^- solutions (King et al. 2001, 2010, SKI 2006). These studies have mainly been concerned with passivity, initiation of pits and the determination of breakdown potentials. The most important and common finding in these studies was that there is a large margin (at least 200 mV_{SHE}) between the breakdown potentials determined in these studies and the corrosion potential of Cu in the repository environment, as determined in Saario et al. (2004). In SR-Site, it was thus concluded that pitting is very unlikely to occur.

Another approach to predict the extent of localised corrosion on longer timescales is to make projections based on the examination of archeological artefacts. Whilst the environmental conditions and Cu alloys differ from those to be used in a repository, these studies have the advantage of having been "conducted" over long periods of time. The corrosion of Cu alloys buried in soil for up to 14 years was studied by Romanoff (1989) who reported a pitting factor of a maximum 25, i.e. the deepest pit found was 25 times deeper than the average corrosion depth. Lightning conductor plates studied by Hallberg et al. (1984) had been buried for 50 to 80 years and the pitting factor estimated was around 5. Finally, Bronze Age artefacts studied by Bresle et al. (1983) had been exposed for an estimated period of 3 000 years and the pitting factors estimated were 2 to 5. These data indicate that, for extended exposure times, a pessimistic estimate of the pitting factor would be 5. Important to note though, the use of a pitting factor will overestimate the pit depth at larger general corrosion depths, since general corrosion destroys the separation of anodes and cathodes required to drive deep pitting.

An alternative use of the same archeological pit depth data has been developed in the Canadian programme (King and Kolár 2000, King and LeNeveu 1992). The data were analysed using extreme-value statistics, and from fits and calculations the time dependence of the cumulative probability can be calculated. Then the probability of a pit of a certain depth can be calculated for the full population of canisters emplaced in the repository. Applying these data to Swedish canisters, there is a probability of 10^{-6} of a pit exceeding about 7.5 mm after 10^6 years. This approach predicts, however, very deep pits after shorter exposure times. With the same probability (10^{-6}) it predicts a 5 mm deep pit after 10 years. These results are consistent with the decreasing pitting factors observed on the archeological artefacts discussed above (Romanoff 1989, Hallberg et al. 1984, Bresle et al. 1983).

Unlike the critical-potential approach to pitting, neither the pitting factor nor the extreme-value analysis approach allows for pit death. Propagation is assumed to continue indefinitely regardless of the evolution in the repository environment, albeit at a diminishing rate in the extreme-value approach. The experimental data used by Romanoff (1989) and Bresle et al. (1983) were obtained under conditions more closely simulating actual disposal conditions, whereas some of the data discussed in the statistical evaluations were obtained after exposure in poorly characterised environments (Bresle et al. 1983). However, they clearly illustrate the tendency of pit growth rates to decrease with exposure time.

Localised corrosion has been reported in a two-year long laboratory exposure of copper in groundwater (Huttunen-Saarivirta et al. 2016). Despite the intention to keep the experiment anoxic, the corrosion potential of the copper electrode and the redox potential measured with a platinum electrode are positive from the start and increase during the time of exposure, which indicates that oxygen has been present and leaked into the experiment. This is also confirmed by the oxygen-containing corrosion products that were found on the copper surfaces after the experiment. On one of the copper samples, a large pit of ca 50 µm depth and similar width was found. EDS (Energy-dispersive X-ray spectroscopy) spectra of corrosion products in the pit contained signals from oxygen and chlorine. This was a relatively large and deep localised corrosion attack compared with the average corrosion of ca 2 µm determined gravimetrically.

In a subsequent study by Huttunen-Saarivirta et al. (2017), corrosion of copper was studied under oxidising conditions in bentonite, and under the influence of aerobic microorganisms. The main corrosion products were cuprite (Cu_2O) and atacamite/paratacamite ($Cu_2(OH)_3Cl$) and no signs of localised corrosion attacks were observed. Similar conclusions were drawn in a study with a multi-electrode, in measurements in water with groundwater composition and bentonite (Kosec et al. 2017).

A literature study of electrochemical data (breakdown and repassivation potentials) in solutions comparable with the repository environment was conducted to further investigate the probability for localised corrosion in the repository (King and Lilja 2013, 2014). The study concluded that pore water compositions in the repository favour general corrosion and not the formation of a passive film, which is a prerequisite for localised corrosion to occur under oxidising conditions.

A new basis for the assessment of localised corrosion under aerobic conditions is the database that the University of Western Ontario has compiled at the request of NWMO in Canada, and summarised in Qin et al. (2017). The database contains a large number of electrode potential measurements under different conditions (temperature, pH, concentrations of chloride, sulfate and carbonate). The main conclusions from the potential measurements do not differ from the earlier literature data and could be summarised as:

- Chloride promotes active dissolution, while carbonate favours the formation of a passive film.
- An increase in alkalinity increases the tendency towards passivation.
- Passivity becomes less likely at higher temperatures.
- Passivity is only expected in $SO_4^{2-}/HCO_3^-/CO_3^{2-}$ solutions at extremely low Cl^- concentrations.

With the new dataset on breakdown and repassivation potentials as an important input, SKB has begun the development of probabilistic models for localised corrosion in order to cover the uncertainty and variability in the data to an even greater extent. As a first development step, the analysis has treated a situation with oxidising conditions where the buffer has been water saturated, keeping in mind that this combination will most likely occur only for a small number of deposition holes for which the resaturation time is short (Åkesson et al. 2010). The modelling is described in Briggs et al. (2020, 2021) and starts with sampling of environmental data (temperature development over time, pH, and concentrations of chloride, sulfate and carbonate) to represent one deposition hole at a time. For every time step the active or passive state is evaluated using the dataset from Qin et al. (2017). Passivity is found to require at least pH 8.9 and $[Cl^-] < 0.06$ mol/L. For passive conditions, the initiation of pitting (and the duration of pitting if initiated) is investigated using regression of the critical potential data. The pit depth is estimated using an empirical pit growth expression. The probabilistic approach uses different machine learning algorithms for regression of the data sets, and is run for up to 1 million realisations (representing on average 145 realisations per deposition hole). For passive conditions, pitting is found to be possible but only during the very earliest period when the O_2 concentration is sufficiently high to increase the corrosion potential. The maximum pit depth is estimated to be 1.22 mm, but the majority of the pits (87 %) are less than 100 µm in depth.

Another, less pronounced effect on the corrosion morphology, is surface roughening due to under-deposit corrosion. Litke et al. (1992) reported non-uniform corrosion in the form of under-deposit corrosion of copper in a laboratory test with bentonite. In this case, the whole surface had been corroded resulting in an uneven general corrosion with variations in corrosion depth of 30 µm for an average corrosion depth of slightly over 40 µm. The extent of surface roughening by under-deposit corrosion has been further studied by Brennenstuhl et al. (2002). The electrochemical noise between coupled identical electrodes, one immersed in bulk solution and the other exposed to a freely swollen 1:1 bentonite:sand mixture, was measured as a function of various factors. Of these, temperature, O_2 concentration and pH had the greatest effect on the extent of localised corrosion. The study is not conclusive, but results suggested that the degree of localised corrosion in a repository should decrease with time as the canister temperature and the O_2 concentration decrease. A mean roughness of 12.4 µm was predicted, with a maximum peak-to-trough surface roughness of 88 µm.

Inevitably, some manufacturing and handling flaws, such as scratches and indentations will remain in the canister when it is deposited. Conceivably, these flaws could act as initiation points for localised corrosion. This possibility has been investigated by King (2004), which concludes that it is unlikely that the presence of pre-existing flaws on the canister surface will impact the service life of the canister as a result of localised corrosion. These flaws will not act as preferential sites for pit initiation, which instead occurs due to the localised breakdown of protective surface films on the scale of a single grain or smaller (King 2004). Environmental factors and the presence of a passive and defected film are more important for pit initiation than the presence of pit-shaped discontinuities on the macroscopic scale.

The conclusions from the probabilistic model correspond well with the surface roughening used as an allowance for localised corrosion in SR-Site. The predictions of the probabilistic model further cover the maximum pit depths observed in laboratory experiments, field tests and archaeological artefacts discussed above.

Copper corrosion by oxygenated glacial meltwater

After consumption of the entrapped oxygen present initially, reducing and sulfidic conditions are generally expected. The only additional identified possibility of oxygen reaching the canister is the penetration of oxygenated glacial meltwater to repository depth that can potentially occur under limited periods of extreme hydraulic conditions during a glacial cycle.

A difference between the initial conditions with entrapped oxygen and the situation with intrusion of oxygenated glacial meltwater, is the state of the copper surface. Initially, the copper surface will have an oxide film due to atmospheric corrosion during storage, but at the time of a glaciation this oxide film is expected to have been replaced by a copper sulfide film.

As an approximate analogue to the canister in the repository, one can consider the corrosion of copper alloy (typically brass or Cu-Ni) heat exchangers exposed to polluted seawater. In these systems, corrosion results from the alternating exposure to anaerobic sulfidic conditions and aerobic conditions. Localised corrosion has been reported and was attributed to the spalling of the corrosion film that occurs under high-flow conditions (Syrett 1981). Even though localised corrosion is not expected under low-flow or stagnant conditions some roughening of the corroding surface could occur (Jacobs and Edwards 2000).

In a situation where glacial meltwater carries enough oxygen to eventually replace the copper sulfide film with a copper oxide film, the situation is then similar to the initial conditions with entrapped oxygen in the buffer. Glacial meltwater is essentially meteoric water and has, consequently, practically no dissolved solids. As an example of glacial meltwater that has interacted with the geological site, Auqué et al. (2006) has discussed groundwater from Grimsel (Hoehn et al. 1998). This specific water has a total amount of dissolved solids of 0.08 g/L and it has been depleted of oxygen. The maximum theoretical oxygen concentration that a meltwater may have as it intrudes at the surface of the host rock is 1.34×10^{-3} mol/L (Sidborn et al. 2010). It should be noted that this concentration is one order of magnitude higher than the solubility of molecular oxygen in saline water under atmospheric conditions, and this supersaturation is due to the potential occurrence of air-filled pores and voids in the melting ice. The possibility that oxygenated melt water reaches the deposition holes is limited by the generally low hydraulic conductivity of the host rock at the Forsmark site. Intrusion of melt water is generally expected to be so slow that oxygen is depleted by the time the water reaches repository depth, but the possibility of some oxygen intrusion cannot be excluded for a few fast flow paths. In the safety assessment SR-Site (SKB 2011) it was found that some tens of canister positions may be affected. In evaluating this corrosion mode, the flow rate and oxygen concentration of glacial melt water reaching a deposition hole need to be considered, as well as the possibility that the bentonite buffer may have been eroded away prior to the melt water intrusion, a condition that may affect a fraction of the deposition positions in the long term. Using the same transport model as for the sulfide flux, it has been estimated that the average corrosion depth due to intruding oxygenated meltwater would be at most 0.3 mm for diffusive conditions, i.e. as long as the bentonite buffer is in place, and maximum 6 mm in deposition holes for which advective conditions are established due to buffer erosion (SKB 2011). This is further discussed in the PSAR Post-closure safety report (SKB 2022a, Section 12.6.2).

Since glacial melt water is very low in chloride, a condition which is found to support localised corrosion of copper under oxic repository conditions, this would then, in line with the assessment of *Localised corrosion under oxic conditions* above, lead to the possibility of additional periods of localised corrosion for the canisters potentially exposed to oxygen concentrations in the ranges of 10^{-3} mol/L during glaciation.

According to the probabilistic model by Briggs et al. (2020, 2021), the maximum pit depth due to corrosion by entrapped air is ~1 mm, while the vast majority of the pits would be less than 100 µm deep. A difference between the situation with entrapped air at disposal and the intrusion of oxygenated meltwater during glaciation is that the entrapped oxygen is expected to be consumed in the scale of weeks or months, while the intrusion of glacial meltwater may occur for much longer times (SKB 2011). In the model by Briggs et al. (2020, 2021), the expression used for the growth of pits is an empirical expression with the time dependence of the pit depth given as $dpit = A \cdot t^n$ (with $A = 89$ mm/(y^n) and $n = 0.59$). This yields for example pit depths of 1.8 mm and 4.6 mm, for exposure times of 200 and 1000 years, respectively; two exposure times pessimistically considered in SR-Site (SKB 2011).

It is emphasized that since the pit initiation depends on passivation and passivity breakdown of a copper oxide film, and since the oxide film will be replaced by a copper sulfide film during the long periods between each (possible) intrusion of glacial meltwater, it is unlikely that the pits resulting from each period of localised corrosion would add to each other. Thus, adding the maximum pit depths from the initial corrosion due to entrapped air with the pit depths caused by oxygen possibly reaching the repository during glaciations, would be pessimistic in terms of penetration depth.

Radiolytic corrosion effects

After emplacement of the canister in the repository, the corrosion environment will be determined by the air present in the initial gap between the canister and the buffer, although some air is also contained in the bentonite porosity. Corrosion by entrapped O_2 is discussed above, however, irradiation of the moist air also leads to the formation of nitric acid, which is an oxidant for copper and thus a potential corrosive agent. After saturation of the buffer, the corrosion environment will be controlled by the groundwater chemistry at Forsmark, together with the chemical properties of the bentonite clay and the radiation fields present at the canister clay interface.

The gamma radiation from the spent fuel is dominated by the decay of Cs-137, with a half-life of ca 30 years. Other gamma emitters have a weaker contribution to the total gamma activity of the fuel and/or a shorter half-life. The radiation field at the canister surface has been evaluated in several reports, and in SR-Site it was concluded that the gamma dose rate, present at the canister surface at the time of encapsulation, is at most 0.18 Gy/h, while the average dose rate at the canister surface is ca 0.055 Gy/h (SKB 2010d). With a half-life of 30 years, the dose rate decreases to ~ 10^{-4} Gy/h in around 300 years, meaning that the canister materials have then been exposed to 99.9 % of the total repository dose. The total repository dose of gamma radiation will thus be on average 20 kGy and maximum 70 kGy at the canister surface (Jonsson 2021b). The neutron dose rate at the canister is initially only 10^{-4} to 10^{-3} of the gamma dose rate, depending on the type of fuel and degree of burnup (Håkansson 2000). Its effect on radiolysis can thus be regarded as negligible as compared with gamma radiolysis.

Since the period of most intense irradiation in the repository corresponds to the early unsaturated phase, a number of studies have been conducted in which copper exposed to humid air has been irradiated. Björkbacka et al. (2017) found that the extent of corrosion was 7–9 times higher in both humid air and humid argon (60 % or 100 % RH) in the presence of radiation (total dose of 45–48 kGy at dose rates of 470–500 Gy/h) when compared with the unirradiated reference tests. The similarity in the extent of corrosion in irradiated air and argon, as compared with the unirradiated systems, led the authors to the conclusion that, although nitrate-containing corrosion products were detected with infrared reflection/absorption spectroscopy (IRAS) in irradiated humid air, the radiolytically produced HNO_3 did not have any major impact on the extent of corrosion.

Ibrahim et al. (2018) also studied the corrosion of copper under irradiation in humid air (70–85 % RH, 75 °C). In the absence of radiation, the copper surface was covered by a thin water film and larger isolated water droplets. The morphology of the corroded surfaces was examined with SEM-EDS. Under the thin water film the surface was passivated due to the formation of a duplex Cu_2O/CuO layer, while thicker, porous and non-passivating deposits were observed under the droplets. After one year of exposure to unirradiated conditions, the porous corrosion products in the droplet regions attained a thickness of 10 µm or less. The local penetration depth in the copper surface was not measured, but it would be expected to be ca 2–3 times lower than the film thickness due to the porosity of the corrosion products. Irradiation at a dose rate characteristic of the canister (0.35 Gy/h) had a relatively minor impact on the corrosion behavior of the copper surface. The thickness of the oxide under the thin water film was the same as in the absence of radiation. Although irradiation did increase the number of water droplets, there was no indication of deeper corrosion attacks on the copper surface. Although no solid nitrate phases were identified on the corroded surfaces, the lateral spreading of the droplets was thought to result from the deliquescence of nitrate species formed from the radiolytically produced HNO_3. It was generally noted that the localised corrosion depth under the droplets was relatively small compared with the lateral spreading of the droplets and there was no evidence for significantly enhanced penetration associated with irradiation.

Gamma irradiation of moist air in the canister-buffer gap leads to the radiolytic formation of nitric acid. Reed and Van Konynenburg (1988) reviewed the effect of ionising radiation on moist air systems. Of the papers reviewed, the study by Jones (1959) of the homogeneous nitrogen/oxygen/water system appears to be directly applicable to repository conditions. Jones (1959) found that the formation of nitric acid was linear with the absorbed dose, and that the formation of nitric acid proceeded to a total concentration that was equivalent to the amount of hydrogen of the water initially present. The *G*-value (in molecules per 100 eV) for the nitric acid production increased with oxygen concentration to a maximum of 2.25 at 15.4 % oxygen and was 2.00 for 20.1 % and 1.2 for air. In a repository, there will be a continuous supply of water and a continuous production of nitric acid can be expected.

Applying the findings and measured *G*-values from Jones (1959) to the repository, assuming an air-filled gap of 1 cm between canister and bentonite, a total production of 0.015 mol of nitric acid is obtained, which, if consumed by uniform corrosion, corresponds to a corrosion depth of less than 7 nm (see Appendix A3).

In an application to the Canadian program for spent fuel disposal (Morco et al. 2017), another type of model has been applied, in which radiolytically produced HNO_3 is dissolved in droplets on the copper surface, i.e. before uniform wetting occurs. The HNO_3 production rate in a condensed water droplet formed on the copper surface was estimated based on the pessimistic assumption that all hydroxyl radicals produced by primary radiolytic processes are converted to HNO_3 in the gas phase, after which it is absorbed in the water droplet and consumed by corrosion of copper. In this way, the corrosion depth induced by humid-air radiolysis is estimated to be 9.4 μm for the whole assessment period. It may be noted that the Canadian repository differs from the Swedish repository in several aspects, e.g regarding canister design and dose rates at the external copper surface, and therefore the model by Morco et al. (2017) is not directly comparable with the KBS-3 repository.

The major component of groundwater is water itself (55 mol/L) and the radiolytic species formed during irradiation of water include oxidising species, e.g. the OH-radical and H_2O_2, but also reducing species, like H_2 and solvated electrons. Earlier mechanistic studies of radiolytic corrosion of copper in water have focused on the effect of gamma radiation on the corrosion potential and corrosion rate. Glass et al. (1986) reported a positive shift of the corrosion potential of ca 100 mV at a very high dose rate of 33×10^3 Gy/h. However, King and Litke (1987) observed no shift of the corrosion potential of copper specimens which were exposed to saline synthetic groundwater and a gamma dose rate of 27 Gy/h (i.e. still two orders of magnitude higher than the initial gamma dose rate at the canister surface). At a dose rate of 13 Gy/h, Simpson (1984) found lower corrosion rates than without irradiation. This observation was corroborated by King and Litke (1987), who used dose rates in the range 14 to 27 Gy/h for irradiation of copper in a saline solution (about 1 mol/L chloride) at 150 °C. The experiments were performed in aerated and de-aerated solutions and the corrosion rates were about a factor of four lower in the presence of radiation. King and Litke (1987) attributed this to the more protective nature of the surface film formed in irradiated solutions. The available information thus shows that there is no indication for shifted corrosion potentials or enhanced corrosion rates caused by gamma radiation at the low dose rates representative for the repository. On the contrary, at least for dose rates in the range of 10–100 Gy/h, the experimental data seem to indicate a lower corrosion rate in the presence of radiation (King et al. 2010).

Several experiments have been performed in which copper samples were immersed in pure water and exposed to gamma radiation doses up to 95 kGy, i.e. doses representative of the repository (Björkbacka et al. 2012, 2013, Björkbacka 2015). The experiments were made using a Cs-137 gamma source and dose rates ranging between 0.02 and 0.3 Gy/s (72 and 1080 Gy/h). These dose rates are considerably higher than the dose rate at the canister surface in the repository, which is at most 5×10^{-5} Gy/s (0.18 Gy/h) and decreasing with the decay, but were used in order to study the effects of full repository dose on a reasonable experimental timescale and to assess the total extent of corrosion. The oxide film formed at the copper surface was mainly composed of cuprite (Cu_2O), although minor amounts of tenorite (CuO) were also identified. The oxide films were of varying thickness and on average at most a few hundred nm thick, as determined by cathodic reduction. For example, for a dose of 69 kGy (dose rate of 720 Gy/h) the oxide film was on average 307 nm thick (calculated assuming a pure Cu_2O film). Since the samples from this particular experiment were pre-oxidized and had an initial oxide layer of ca 46 nm, the oxide growth due to irradiation of water was on average 261 nm which corresponds to a corrosion depth of ca 157 nm (data from Table 4 in Björkbacka 2015). In addition, copper in the solution always corresponded to less than 10 nm of corrosion. Examination of the irradiated surfaces revealed circular localised corrosion features with diameters of up to a few tens of μm and depths of around 1 μm. When the copper specimens were pre-oxidised before irradiation, more irregular localised corrosion features were found after irradiation in water. It is noted that the corrosion observed in these experiments, both the oxide film thickness and the degree of localised corrosion, are negligible contributions to the total corrosion of the canister, and that this corrosion corresponds to a repository-representative dose of gamma radiation.

The mechanism of radiolytic corrosion has been investigated in several studies and different proposals have been made regarding the nature of the oxidants involved (Björkbacka et al. 2015, 2016). Recent experimental studies have shown that molecular O_2, formed by decomposition of H_2O_2 on the oxide

surface, is the dominating oxidant in the copper-water system under radiolysis (Soroka et al. 2021). A computational model based on the mechanistic understanding predicts oxide formation in rather good agreement with experimental findings. For example, 62 nm oxide was formed on polished copper cubes (assuming a compact Cu_2O film) after exposure to a dose of 69 kGy given at a dose rate of 720 Gy/h (Table 5 in Björkbacka 2015), which can be compared to the calculated oxide thickness of 54 nm after exposure to 70 kGy given at a dose rate of 540 Gy/h (Soroka et al. 2021). For an initial dose rate of 0.18 Gy/h (maximum dose rate at the surface of the KBS-3 canister) decreasing with the decay of Cs-137 (total dose of 70 kGy) the same model predicts the formation of ca 2 µm Cu_2O, which corresponds to an average corrosion depth of ca 1.2 µm, due to gamma radiolysis of water (Jonsson 2021b).

Literature studies and further development of the computational model have shown that ground water components such as chloride, sulfate and bicarbonate, will have minor effects on the extent of radiolytic corrosion, as long as the pH is near neutral or alkaline, and as long as the concentration of chloride is not much higher than under repository conditions (Jonsson 2021b).

Some of the spent fuel elements contain fuel rods in which the cladding has been damaged while the fuel was in the reactor, and for which small amounts of water may be present even after the drying procedures. This water could escape into the channels in the cast iron insert and could eventually come in contact with the copper shell in the gap between the insert and the shell. Therefore, in addition to the radiolytic corrosion effects on the outer surface of the copper shell discussed above, there is a possibility of some corrosion on the inside of the copper shell. In SR-Site, it was estimated based on pessimistic assumptions regarding the distribution and encapsulation of damaged fuel rods, that the maximum amount of water that could be present in a single canister due to damaged fuel is 600 g (Posiva SKB 2017). Different mass-balances were evaluated in order to estimate a maximum corrosion depth on the inner copper surface (Neretnieks and Johansson 2013). The most pessimistic assumption, that corrosion only occurs in contact with liquid water formed at the bottom of the gap, gives a corrosion depth of 1.1 mm, while the less pessimistic assumption that corrosion occur over the whole copper surface due to condensation and water film formation, resulted in a depth of 70 µm. Both these estimates were made under the assumption that only copper and not iron corrodes due to the formation of oxidising radiolytic species in the gap. This makes the mass-balances by Neretnieks and Johansson (2013) even more pessimistic, and it may be concluded that corrosion due to water inside the canister is a very limited process.

In addition to estimates of the total extent of corrosion due to water inside the canister, the development of the gas-phase inside the sealed cast iron insert due to radiolysis and residual air and water has been modelled by Henshaw and Spahiu (2021). The modelling predicts formation of low levels of O_2, H_2O_2, H_2, HNO_3 and NH_3, of which the latter, through dissolution and formation of NH_4^+, is a potential SCC agent for copper under oxidizing conditions. For the pessimistic initial condition with 600 g water and 10 % air (90 % argon) inside a canister, up to 0.4 mol NH_3 is predicted, while there is still water present in the canister. After water has been consumed by radiolysis and corrosion of the iron insert, production of NH_3 continues up to 1.3 mol under dry conditions. During the short period (ca 150 days) of NH_3 production under humid conditions, SCC could in principle be of concern if the gas escapes the iron insert and comes in contact with the copper shell and if tensile stresses are present in the material. The same model predicts that by reducing the initial content of air inside the canister to 1 % (99 % argon), still pessimistically assuming 600 g of water initially present, the level of NH_3 produced is lowered to 0.13 mol and, even more important, production of NH_3 starts only after the water has been consumed by corrosion of iron, i.e. under dry conditions. Since electrochemical corrosion processes require an electrolyte, there are no prerequisits for SCC for the initial conditions 1 % air and 600 g water, despite the radiolytic formation of NH_3.

Corrosion due to reaction in O_2-free water

Copper is expected to corrode to an infinitesimal extent in pure, O_2-free water. Since 2007, this view has been challenged by a group of researchers who claim that hydrogen evolution detected in their studies indicates copper corrosion in pure water to an extent far exceeding that predicted by established thermodynamic data (e.g. Szakálos et al. 2007, Hultquist et al. 2011, 2015). The concern was originally raised in Hultquist (1986) and was also contested at that time (Simpson and Schenk 1987, Eriksen et al. 1989). The renewed claim is based on a two-chamber experiment where copper

is immersed in water in a lower chamber separated from an evacuated upper chamber by a palladium foil that allows the passage of hydrogen but no other gases. Hydrogen steady-state pressures of up to 1 mbar were observed in the upper chamber (e.g. Szakálos et al. 2007, Hultquist et al. 2011, 2015). This is about 6 orders of magnitude higher than predicted by established thermodynamic data for the Cu-O-H system. Szakálos et al. (2007) suggest that the hydrogen pressures observed in their experiment may be explained by corrosion of copper by water if a hitherto unknown phase of Cu-O-H exists, which would be the thermodynamic driving force necessary for corrosion.

A fuller introduction to the issue is given in Section 1 of Hedin et al. (2018). In that paper, much of the material summarised below is discussed in more detail, and there are, therefore, frequent references to the paper here. The paper also contains a more complete set of references. The issue has also recently been summarised in Chapter 4 of SKB (2019a) of which the following text is an abbreviated version, with a few additional new references added.

According to established thermodynamic data, the equilibrium pressure of $H_2(g)$ in a closed system with only Cu(s) and $H_2O(l)$ present initially is calculated to be of the order of 10^{-6} mbar at room temperature, when all known solid compounds and solution species of the Cu-O-H system are taken into account, see, e.g., Appendix A in Hedin at al. (2018). Very similar equilibrium calculations have been presented by other authors, see e.g. MacDonald and Sharifi-Asl (2011) and Landolt (2007). This result relies on the assumption that all relevant species in the Cu-O-H system have indeed been identified and included in the calculation. Considerable computational (Korzhavyi et al. 2012, Li et al. 2015) and experimental (Soroka et al. 2013) efforts have been made to identify potential hitherto unknown species of this system. No stable Cu-O-H compound that could act as the thermodynamic driving force of a continuing corrosion reaction in pure, O_2-free water was found. Furthermore, surface reactions between water and the copper or copper oxide surface may lead to the oxidation of about one half of a monolayer of copper at most, potentially releasing a corresponding amount of hydrogen (Lousada et al. 2015, Stenlid et al. 2016). This is far too little to explain the results observed by Hultquist (2011, 2015). A fuller discussion is provided in Section 2 of Hedin et al. (2018). More recently, also Betova et al. (2021) and Senior et al. (2021) have appointed the measured, but very limited, amounts of hydrogen in their experiments to surface reactions,

In an SKB-funded experiment at Uppsala University, the two-chamber hydrogen evolution experiment mentioned above was repeated under more controlled conditions (Boman et al. 2014, Ottosson et al. 2016). No hydrogen evolution ascribable to copper corrosion was detected in the experiment. In similar setups, the Uppsala group also looked for oxidised copper, which would be a more direct piece of evidence of copper corrosion (Ottosson et al. 2017). The water and all relevant surfaces in the setups were examined and in total less oxidised copper than the amount corresponding to a monolayer of the copper surface was found after up to 29 months of exposure. In contrast, the hydrogen evolutions reported in Szakálos et al. (2007) and in Hultquist et al. (2011, 2015), if due to copper corrosion, would have caused corrosion depths of tens of monolayers. A more detailed account of experimental details, results and conclusions is provided in Sections 3.2, 4.4 and 5.2 of Hedin et al. (2018).

An alternative method for studying hydrogen evolution from copper in pure, O_2-free water has been developed in an SKB-funded experiment at Microbial Analytics Sweden AB (Micans). In this method (Bengtsson et al. 2013), typically two copper pieces with a total surface area of 46 cm^2 are submerged in pure O_2-free water in butyl rubber sealed test tubes, leaving a 6 cm^3 N_2-filled gas volume above the water. The gas volume is sampled and analysed at regular intervals. Several combinations of copper qualities and surface treatment methods were exposed for up to 3 years (Johansson et al. 2015). As an example, consider the results from the experiment with the copper quality used in Hultquist et al. (2011, 2015), for a number of surface treatments including the “as received” condition used by Hultquist et al. None of the samples yield hydrogen evolution above background, whereas the expected H_2 evolution rate according to data from Hultquist et al. would have been easily detected by this method. In summary, no continuing hydrogen evolution above background was observed for any of the combinations in the Micans experiment, with the exception of 2 mm thick samples of Cu-OFP where the evolved hydrogen was demonstrated to emanate from the copper sample itself, as the hydrogen evolution took place also when the sample was not exposed to water. Modelling of outgassing of H from Cu-OFP further corroborates that conclusion (Hedin 2019). A more detailed account of the method, the results and conclusions of the test tube study is provided in Sections 3.1, 4.1–4.3 and 5.1 of Hedin et al. (2018). A couple of recent experimental developments with this method, further corroborating the conclusions in the above studies are

presented in SKB (2019a). Finally, Becker et al. (2020) noted a reduction in H content in 2 mm thick Cu-OFP samples from around 0.7 wt.ppm to around 0.3 wt.ppm during 4-week exposures to 10^{-5} mol/L HS^- solutions at 90 °C and suggests that this is due to outgassing, which is compatible with the Micans' results for Cu-OFP.

Another type of glass-contained setup has been used by Senior et al. (2013, 2019) who measured hydrogen evolution rates from thin copper wires immersed in O_2-free water at different temperatures. In the first report, no hydrogen evolution was detected for copper immersed in water at 30 °C. When the temperature was increased to 50 °C, hydrogen was detected around the detection limit of the method used. When the temperature was increased further up to 75 °C a hydrogen evolution was noted, which if interpreted as resulting from corrosion corresponded to a corrosion rate of 0.9 nm/year (Senior et al. 2013). The measurements at 30 °C, 50 °C and 75 °C had then been conducted for 92, 38 and 130 days, respectively. Regarding the temperature effect, these results are similar to the results reported by Johansson et al. (2015) who detected hydrogen gas from 2 mm thick copper samples at 70 °C, but not at 20 °C or 50 °C. In that case it could be shown that the hydrogen gas emanated from the Cu-OFP material itself, and as noted above, that it was thus not related to a corrosion process (Johansson et al. 2015, Hedin 2019). The method and setup used by Senior et al. was developed further in order to measure extremely low levels of hydrogen and to derive bounding corrosion rates for copper in anoxic aqueous solution with the pragmatic purpose to estimate the corrosion from empirical data while disregarding the thermodynamics of the system (Senior et al. 2019). In Senior et al. (2019), the hydrogen evolution rate measured for copper in pure O_2-free water at 75 °C, corresponded to corrosion rates of 1 nm/year. Additionally, Senior et al. (2019) reported exposures to 0.25, 2.5 and 5 mol/L O_2-free NaCl solutions, which resulted in negligible evolution rates below 50 °C. Preliminary results show hydrogen evolution rates corresponding to corrosion of around 10 nm/year at 75 °C for exposures in the NaCl solutions, which seem to decrease with time. The exposures lasted for about one year. The authors do not offer a conclusive explanation for the observed hydrogen evolution in these experiments, but note that some of the exposures yielded inconsistent results when duplicated and mention the hydrogen content and other starting conditions of the copper as factors requiring further investigation. Furthermore, the studied copper was not analysed to determine the presence of corrosion products. Although instrument calibration was performed, it may also be noted that no background measurements of H_2 from the instrument or from a reference cell were reported. Finally, it is noted that the hydrogen evolution rates for Cu in pure, O_2-free water in these experiments are considerably lower than those reported by e.g. Hultquist et al. (2015) for the corresponding temperatures.

Accounts of, and comments on, additional experiments on the issue of copper corrosion in pure, O_2-free water are given in Hedin et al. (2018) and in SKB (2019a).

Even if the material above suggests that the basis for claiming that copper corrodes to an extent that is not compatible with established thermodynamic data is very weak, it is of interest to examine what the data presented by Hultquist et al. (2011, 2015) would mean in terms of corrosion depths in a final repository. Therefore, the temperature-dependent hydrogen evolution rates reported in Hultquist et al. (2015) have been transformed into hypothetical corrosion rates for the temperature development expected in a final repository (Hedin et al. 2017). This yielded a corrosion depth of around 1 mm in the one million year period that needs to be covered in a post-closure safety assessment, when the effect of the elevated temperatures expected during the first few thousand years is also taken into account. It is also noted that the claim made in Hultquist et al. (2015) that their measured hydrogen evolution rates indicate corrosion rates in the range 10–100 nm/year at room temperature lacks support in those authors' own data (Hedin et al. 2017). An alternative approach of a what-if analysis, based on the alleged equilibrium pressures in Hultquist et al. (2011), was also discussed in Hedin et al. (2017) but was found to be less useful in putting a rigorous bound on the extent of corrosion under repository conditions. It can be noted that this approach assuming a constant hydrogen pressure at the canister surface was the one applied in SR-Site (SKB 2010e), using the data at hand at the time.

In this context, it is also noted that the corrosion rates calculated above would be impossible to observe in large-scale *in situ* field tests, where typical average corrosion depths are of the order of 0.1–10 µm. Furthermore, the corrosion observed in field tests (corrosion depth and corrosion products) is fully compatible with processes and parameters included in traditional safety assessment corrosion models, such as the amounts of residual O_2 present in the experiments initially, the thermodynamics of the system, and in some cases the influx of sulfide through the clay (Johansson 2019).

Based on the above account of the issue of copper corrosion in pure, O_2-free water, it is concluded that there is no support for claiming that the extent of this process exceeds that predicted by established thermodynamic data. Experiments on which claims of far higher extents of corrosion are made have been repeated under more controlled conditions. The hydrogen evolution claimed as evidence of copper corrosion was not observed, despite fully sufficient detection levels. Nor was any evidence of oxidised copper found. Also different experimental approaches were used, with the same result. No hitherto unknown stable species of the Cu-O-H system has been found despite both theoretical and experimental efforts. It has also been demonstrated that even if the claims of corrosion of copper in pure O_2-free water were correct, they would correspond to a corrosion depth of about 1 mm in 10^6 years in a final repository.

High chloride concentrations

High chloride concentration in combination with very low pH could cause copper corrosion in oxygen-free water by reduction of H^+ to H_2 (hydrogen gas evolution). In Pourbaix diagrams this is shown as the crossing of the "hydrogen line" with the stability area for copper metal. Beverskog and Puigdomenech (1998) calculated Pourbaix diagrams for chloride concentrations of 0.2 and 1.5 mol/kg, which were later updated for 5 mol/kg (Beverskog and Pettersson 2002). It was found that at 5 mol/kg chloride, copper corrodes below pH 5 at 25 °C to the extent that the total copper concentration in solution is higher then 10^{-6} mol/kg, while for 1.5 mol/kg chloride the corresponding pH value is approximately 3.2. From such thermodynamic calculations SKB derived a safety function indicator criterion for chloride assisted corrosion to be used in SR-Site (SKB 2010a), with the limit set to pH = 4 and $[Cl^-]$ = 2 mol/L. Lilja (2013) gave an extended description of the derivation of the criterion. The approach uses a limit for the total copper concentration of 10^{-6} mol/L, and shows the corrosion would not cause canister failure for any of the deposition positions in Forsmark, either for intact or eroded buffer. The same transport models as used in SR-Site for sulfide corrosion were used. It was also shown how different combinations of pH and chloride concentration can be chosen for the same copper concentration limit.

A new, more elaborate treatment (Appendix A4) using the software PHREEQC and its accompanying databases (Parkhurst and Appelo 2013) takes into account a more complete speciation of copper in chloride solution, an initially low hydrogen pressure and the uncertainties in the activity coefficient models. Also, the limit for when high chloride concentrations become a concern is more adequately expressed as a curve of chloride concentration as a function of pH, than as one specific combination of these entities. As an example, the combination pH = 5 and $[Cl^-]$ = 1.4 mol/L is a point on the curve. For the pH-value of 4, used in the old single-point limit, the calculated upper limit of chloride concentration is around 0.65 mol/L, i.e. lower than the older value of 2 mol/L. The main cause for the difference is the the lower starting hydrogen pressure.

Conversion of copper oxides to copper sulfides

The copper oxides formed on the canister surface due to e.g. entrapped O_2 and radiolysis of water, are not stable in sulfide solution and will be transformed to copper sulfides when sulfide exposure commences. The timescale of this process under repository conditions has not been studied directly, however, complete conversion has been demonstrated on laboratory timescales using preoxidised samples with complex oxide films (Smith et al. 2007, Kristiansen et al. 2015). It is likely that the process is kinetically rapid (and thus controlled by the sulfide flux), since the shifts in corrosion potential are dramatic (Smith et al. 2007), and since both bulk and surface conversion of Cu_2O to Cu_2S are strongly exergonic reactions (Stenlid et al. 2017).

The conversion of Cu_2O to Cu_2S is not in itself a corrosion process, i.e. there is no net oxidation of copper metal in the process. For the conversion of Cu_2O, the experimentally proposed mechanism is a chemical transformation, i.e. without any spatial electrochemical separation (Smith et al. 2007). Quantum chemical modeling of the reaction has further suggested that the conversion mechanism is a direct chemical substitution of O for S, see further Stenlid et al. (2017). For the conversion of Cu(II) oxide and/or hydroxide corrosion products, the experimentally suggested mechanism involves a comproportionation step in which Cu metal and Cu(II) first reacts to form Cu(I), before the sulfidation of Cu(I) occurs, see further Kristiansen et al. (2015).

Copper corrosion by sulfide

The thermodynamic stability of cuprous sulfide (Cu_2S) at potentials below the H_2/H_2O equilibrium line (Pourbaix and Pourbaix 1992) and the presence of sulfide ions in deep Swedish groundwaters, will cause copper canisters to be subjected to corrosion under the long-term reducing conditions expected to develop in the repository. The corrosion products would be Cu_2S, (or other copper sulfides of stoichiometry near Cu_2S), and molecular hydrogen.

The corrosion of copper in sulfide solution has been studied by SKB for a long period, mainly at the University of Western Ontario in Canada. Copper from SKB (Cu-OFP) has been exposed to sulfide solutions with different concentrations. By studying the properties of the films of corrosion products and how they are growing, knowledge can be gained about the corrosion mechanisms. A summary of this work was compiled in Section 5.3 of SKB (2019a), and, here with a few new references added, the main findings were:

- In experiments under natural corroding conditions (no externally applied potential) it is the sulfide flux at the canister surface that determines the type of film formed. At a low flux, the film becomes porous, while a higher flux gives a compact film (Chen J et al. 2014). It is not only the flux in itself that is important, but rather the interfacial concentration, which is the result of the balance between the flux to the surface and the kinetics of the reaction(s) involving sulfide.
- The same dependence of sulfide flux on the film type formed is observed in experiments with an applied potential, so that a high sulfide flux (achieved by using a rotating electrode) is required to get a compact film, while otherwise a porous film is formed (Martino et al. 2017).
- If other anions are present in the solution (as in groundwater), they will influence the film formation process, in at least two ways (Chen et al. 2017a, Martino et al. 2020). Increasing the ionic strength (higher concentration of the added anions Cl^-, SO_4^{2-} or HCO_3^-), decreases the electric field and thus the resistance at the copper-electrolyte interface at the pore bottom, which in turn shifts the control of further film growth to the reaction kinetics of the anodic dissolution, rather than mass-transport. Another effect is from the competition for adsorption sites on the copper surface, and thereby lessened formation of the intermediate $Cu(SH)_{ads}$, which is necessary for the Cu_2S film formation. Although the sulfide concentration influences the morphology of the formed film (e.g. if the film is compact or porous, and in the latter case if the pores are narrow or wider), the presence of other anions can also have an effect, and the ratio $[HS^-]/[X^{n-}]$ needs to be taken into consideration in the subtleties of the film formation process. Competetive adsorption of groundwater ions on low-index Miller surfaces of Cu and Cu_2S has been modelled with quantum chemical tools in order to rationalize the experimental findings further (Halldin Stenlid et al. 2020a, b).
- In the literature it is claimed that the sulfide films formed during electrochemical experiments are passive (e.g. Mao et al. 2014, Dong et al. 2016, Kong et al. 2018), with the sharp increase of the current at higher potentials being the breakdown potential. Other experimental work (Martino et al. 2019a, Guo et al. 2019, 2020) shows that the increase in current is the onset potential for active dissolution of copper, and not breakdown of a passive film. Another argument for passivity is the use of the Point Defect Model (PDM) to describe and interpret the film formation, e.g. in experiments with sulfate-reducing bacteria (Huttunen-Saarivirta et al. 2018), but this has also been criticised (Martino et al. 2019b), rebutted (Huttunen-Saarivirta et al. 2019a) and corrected with an erratum (Huttunen-Saarivirta et al. 2019b). As the PDM is developed to describe a passive film, the interpretation is biased by the inherent assumption of passivity. In Huttunen-Saarivirta et al. (2019a) it is argued that Cu-OFP has a lower pitting susceptibility than pure copper without phosphorus. The same was concluded under oxidising conditions (Bai et al. 2023). Taxén and Sparr (2014) compared the nobility of copper with different amounts of added phosphorus (under oxidising conditions), but found very minor differences.

Thus, the results from natural corrosion and polarization experiments show that the formation of a passive, and thus protecting film, requires a high interfacial concentration of sulfide at the film/electrolyte interface, where the film formation takes place. In turn, the interfacial sulfide concentration depends on the relative rates of supply by transport and consumption by film formation. For a stagnant solution and natural corrosion conditions, a compact and protective film has only been observed at sulfide concentrations $\geq 1 \times 10^{-4}$ mol/L, when the sulfide flux causes the film formation rate to become controlled by the interfacial reaction rate (King et al. 2017, SKB 2019a). This concentration

corresponds to a sulfide flux of the order of 10^{-7} mol/(m^2 s), assuming a diffusion layer of 1 mm and a diffusivity in bulk solution of 10^{-9} m^2/s. As discussed in SKB (2019a) there are uncertainties in evaluating this threshold flux from different types of experiments. Using the linear film growth rate as the indication of a porous film gives the threshold 3×10^{-10} mol/(m^2 s), for an experiment with a sulfide concentration of 5×10^{-4} mol/L. For sulfide fluxes below the threshold, the film growth is controlled by the transport of sulfide in solution (and in the pores of the film), resulting in a porous and non-protective film.

Quantum chemical tools have been used to model the structure and energetics of the Cu–Cu_2O, Cu–Cu_2S, and Cu_2O–Cu_2S interfaces (Halldin Stenlid et al. 2021). This has led to an improved understanding of the properties and stability of these interfaces, which is a fundamental component in the assessment of corrosion behaviour under various conditions involving oxide- and sulfide formation on copper. After the oxygen has been consumed and reducing conditions reinstated, copper corrosion under deep repository conditions will be controlled by the availability of dissolved sulfides. The sulfide in deep groundwater originates most likely from microbially assisted reduction of sulfate (inorganic reduction of sulfate is excluded under repository conditions, see further below in Copper corrosion by sulfate) and possibly also from the dissolution of sulfide minerals. If these processes occur in the rock, the sulfide in the groundwater could be regarded as the source. Within the buffer and backfill, dissolution of accessory minerals (e.g. pyrite and other iron sulfides) could occur (SKB 2022b, Section 3.5.6), as well as microbial activity in the backfill (in the buffer the activity will be limited, see SKB (2022b), Sections 3.5.15 and 4.4.11). In all situations the sulfide needs to be transported through the buffer (and backfill) to reach the canister surface and cause corrosion. The transport limitations are thus the main way of evaluating the sulfide corrosion.

The sulfide transport and the subsequent corrosion have been modelled within the joint SKB-Posiva Integrated Sulfide Project, ISP (Posiva SKB 2021) where 3 slightly different approaches were used, with different degrees of details for the corrosion processes included. The most detailed handling of the corrosion processes is included in the Copper Sulfide Model, CSM (King and Kolář 2019). It must though be pointed out that the model is set up with the assumption of a porous film and active dissolution, and thus localised corrosion could not be handled by this model. Further, the model has a simplified geometry in 1D. The modelling prediction that a large part of the available sulfide will precipitate with iron has not been verified experimentally.

From the “best estimate” simulation with the CSM, the corrosion potential could be evaluated. The first phases consist of initial oxygen in the system oxidising copper to Cu(I) chloro complexes and further to Cu(II), and a period with too low relative humidity to support interfacial electrochemical reactions (corrosion). When the surface re-wets the oxidising conditions will prevail even if all O_2 has been consumed. Copper(II) in the form of Cu^{2+} ions, adsorbed Cu(II) species or precipitated $Cu_2(OH)_3Cl$(s), will oxidise more Cu. From a mass balance (or rather electron balance) point of view this oxidation is not more than if the oxygen oxidised copper to only Cu(I) from the start. Eventually the corrosion potential drops to values to about –0.9 V (vs SCE), which is consistent with experimental data for copper exposed to sulfide solution for 1691 hours (Chen et al. 2010). This lends assurance to the handling of the electrochemical part in the modelling.

With the general corrosion by sulfide being mainly mass transport-limited this corrosion will be evaluted in a broader context in the PSAR, including geochemical and hydrogeolocial data, see further in *Handling in the PSAR* below.

Localised corrosion in sulfide environment

In order for traditional pitting corrosion to occur, i.e. involving the initiation and growth of distinct pits in an otherwise relatively unaffected surface, the film of corrosion products is required to exhibit passive properties, meaning that the film supresses further general corrosion. A defect in the film, can cause a permanent separation of anodic (metal dissolution in the pit) and cathodic (reduction reaction at the film surface) sites, and thus be the driving force for the growth of the pit. In such a case, the anodic area (pits) can become extremely small compared with the cathodic area (surface film), and thus increases the driving force to support growth of distinct and deep pits. A commonly used description of pitting is with an empirical “pitting factor”, i.e. the ratio of the maximum pit depth to the general corrosion depth (so that a pitting factor of 1 means no pits).

SKB made a pessimistic assessment of localised corrosion in sulfide environment in SKB (2019a) using an empirical factor of 20 (for the deposition holes with the highest sulfide flux), but this was built on very limited set of data.

A prerequisite for passivity is that the film is compact, not porous. Such films have been formed in experiments where a potential is applied to the copper electrode at the same time as the sulfide flux is artificially enhanced by rotation the electrode. However, under natural corrosion conditions, i.e. for a stationary copper electrode without an applied potential and at sulfide concentrations representative for the repository environment, the copper sulfide films formed are always porous and non-passive. In case of a non-passive film, corrosion of the metal surface proceeds beyond film formation, meaning that general corrosion competes with the growth of pits and affects the shape of pits during their development, for example making them wider instead of deeper with respect to the general corrosion depth.

The assessement from SKB (2019a) is summarised below, but has also been extended with new data, both from the literature and from new investigations. In the following the word "pit" is used, even though the mechanism for the formation of these localised "features" does not seem to be traditional pitting.

Even though the morphology and properties of the copper sulfide films formed seem to correspond to a rather uniform corrosion process, pits or localised corrosion features have been observed in the copper surface near large grains in the Cu_2S film (Chen et al. 2019). These have been interpreted as signs of micro-galvanic corrosion, resulting from the formation of areas with different film thickness or grain size of copper sulfide crystals. Such micro-galvanic corrosion has also been noted in experiments with forced coupling of electrodes (or electrode parts) with thick and thin layers of sulfide film (Chen et al. 2017b). The mechanistic understanding of this process involves the transport of soluble corrosion products as copper sulfide complexes and clusters (Chen et al. 2018). The lowest sulfide concentration for which pits have been observed is 5×10^{-4} mol/L, with the deepest attacks being about 6 µm. Ongoing work suggests a tendency for the ratio of maximum pit depth to average corrosion to decrease with exposure time.

The development of localised corrosion features has also been studied under electrochemical conditions (Kong et al. 2018). Copper electrodes were polarised in solutions with 5×10^{-4} mol/L sulfide and 0.1 mol/L chloride. The ratio of pit depth to pit mouth diameter (surface width) was measured and was found to decrease with increasing pit volume, i.e. resulting in shallow pits with wide openings.

Caporuscio et al. (2017), exposed copper to artificial groundwaters. The exposure time varied from five weeks up to four months. The temperature was varied during the exposures but all experiments had a peak temperature of 300 °C. The sulfide concentrations were not determined but the formation of a Cu_2S film was verified and measured a thickness of 3 to 8 µm. SEM cross sections of the specimens revealed a dense distribution of pits in the surface beneath the film and generally the pits seemed to be near coalescence. The pits observed ranged from 4 to 14 µm in depth and were at most ca twice as deep as the thickness of the sulfide film.

In a study of stress corrosion cracking (Becker et al. 2020, see further Section 3.5.5) also mechanically unloaded samples were exposed to a sulfide environment (with 0.1 mol/L chloride). The authors reported that no pits were observed, even at a concentration of 10^{-3} mol/L sulfide. The surface was roughened, and with "crystallographic marks" matching in size to the crystals in the inner porous copper sulfide film. At the lower sulfide concentration (10^{-5} mol/L) there was no indication of localised corrosion behaviour.

In slow-strain rate tests for another investigation of stress corrosion cracking (Taxén et al. 2019) the initiation of "cracks" appears at the curved part of the tensile specimens, but the distribution evens out over the full length over time. The interpretation was that transport limitation both affects the initiation and growth of cracks. The higher concentration in concave curvatures causes earlier formation of cracks in those parts. As the cracks are filled with corrosion products the transport is slowed down and the cracks stifle, which is consistent with the observation that the first formed cracks are not deeper then the later formed ones.

As noted in SKB (2019a) corrosion of copper in humid sulfide gas was studied for partial pressures of 10 ppm and 1 % $H_2S(g)$ (Gordon et al. 2018a). In neither case were any signs of localised corrosion found, although the examination of the corroded surface was not extensive.

As was concluded already in SR-Site, the bentonite buffer may erode when contacted by groundwater with low cation concentrations. On a timescale of tens of thousands to hundreds of thousands of years, this may lead to loss of a sufficient amount of buffer to cause advective conditions in the deposition holes exposed to the highest groundwater flow, leaving the copper surface directly exposed to the groundwater. The influx of sulfide to the canister would then no longer be limited by the diffusion resistance of the bentonite buffer but would become controlled by the groundwater flow rate at the deposition hole and the groundwater concentration of sulfide. Also, the high swelling pressure of the buffer suppresses microbial activity in the vicinity of the canister and prevents the formation of a biofilm at the canister surface; a function that could be lost in the case of buffer erosion.

Several studies of copper corrosion morphology in the presence of sulfate reducing bacteria have been published. In a study by Chen S et al. (2014), localised corrosion was reported on copper under an SRB biofilm in rich medium with sulfate (4×10^{-3} mol/L), lactate (47×10^{-3} mol/L) and yeast (1g/L). However, the study was made without evaluation of mass-loss and the extent of general corrosion, meaning that it is not possible to compare the relative importance of general and localised corrosion. The pits observed on the corroded specimens were up to a few µm wide (depths were not measured) after two weeks of exposure in a rich medium which developed ca 2.6×10^{-3} mol/L sulfide.

A systematic study of copper corrosion under an SRB biofilm in nutritious solutions revealed localised as well as general corrosion (Dou et al. 2018). The corrosion exposures were made for ten days with various levels of nutrients. In the most aggressive exposures, the concentration of organics was similar to that used in Chen S et al. (2014) and the sulfide concentration developed to between ca 2×10^{-4} and 3×10^{-3} mol/L during the exposure. It was found that the deepest pits were of similar depth as the average corrosion depth calculated from mass-loss. For example, when copper was exposed to the most aggressive conditions, i.e. the highest levels of organic nutrients, the average corrosion depth determined by mass-loss was ca 45 µm, while the deepest pit found was 44 µm deep. Similar results regarding the degree of localised corrosion with respect to general corrosion have been verified also in a later study by Dou et al. (2020). In the later study, signs of shallow intergranular corrosion were also reported for exposure in nutritious SRB medium which developed high sulfide concentrations.

In a study by Marja-aho et al. (2018), electrical resistance probes made of copper, were exposed to artificial groundwater containing SRB. Localised corrosion was reported for some of the SRB exposures (not all) and SEM cross-sections revealed up to 25 µm penetration. The corresponding extent of general corrosion was not clear. While the reduction of the thickness of the resistance probe was ca 15 µm, weight-loss corresponded to only 2 µm average corrosion depth during the exposure period. This seems to correspond to deeper effects of localised corrosion with respect to the extent of general corrosion as compared with the results of Dou et al. (2018, 2020). One uncertainty in the study by Marja-aho et al. (2018) was that the corrosion products contained not only Cu_2S, but also small amounts of Cu_2O, indicating that initially present O_2 may have affected the corrosion morphology.

In Gordon et al. (2018a) copper was exposed to solutions containing SRB in either growth medium with levels of sulfate and organic carbon as present in groundwater at repository depth, or nutrient rich medium containing higher levels of sulfate and organic carbon (comparable with the studies by Dou et al. discussed above). Reference experiments, in which copper was exposed to nutrient rich solution, without SRB but with sulfide added, were also performed. An enhanced frequency of surface defects (pits), indicated that a localised corrosion mechanism had been operating in some of the experiments with nutrient rich media; however, due to the rough surface finish of the copper specimens used in the experiments, the interpretation of the results was not very clear. Another uncertainty in Gordon et al. (2018a) was that the EDS spectra of corrosion products contained low levels of oxygen. Just as mentioned for the study by Marja-aho et al. (2018), this could mean that the corrosion morphology observed does not reflect the long-term anoxic and sulfidic environment, but rather a transient phase in which low levels of O_2 are present.

It is thus noted that several studies of copper corrosion in SRB supportive environments have demonstrated localised corrosion. These results are though not directly applicable to the repository environment, especially since the concentrations of nutritients (organics and sulfate) are much lower in the deep groundwater than in the laboratory experiments in which localised corrosion has been reported.

As a summary for localised corrosion, it can be noted that the observations of "pits" on copper in sulfide solutions show features that are not growing extensively deeper, but rather deviate less from the average corrosion depth with time, if formed at all. This is consistent with a system that is largely transport-limited (King et al. 2017), and which cannot sustain a localised corrosion process with a penetration depth significantly ahead of the general corrosion front, as the interfacial sulfide concentration at the canister surface is close to zero. The transport resistance for the sulfide is further increased by the precipitation of corrosion products in pits (Chen et al. 2017b), which is also seen in cracks appearing in tensile stress experiments (Taxén et al. 2019). It may be noted that this behaviour, of a pitting factor decreasing with time (or the extent of general corrosion), has been found empirically for archeological artefacts made of copper (see above, *Localised corrosion under oxic conditions*) as well as carbon steel, another non-passive metal (Dillmann et al. 2014).

For the safety assessment it is thus reasonable to describe these localised features in terms of a maximum pit depth to be added to the average corrosion depth. As shown above, the observed features are in the range of 1–15 μm, but it is suggested to pessimistically set the maximum pit depth to be one order of magnitude deeper than the deepest observation, i.e. 150 μm. The experimental results include sulfide concentrations and sulfide fluxes corresponding to the case of eroded buffer (SKB 2019a), which is why this maximum pit depth is applicable also for this situation.

Copper corrosion by sulfate

A direct reaction between metallic copper and sulfate is endergonic, i.e. thermodynamically unfeasible (Swedish Corrosion Institute 1983, Grauer 1990). However, if an additional electron donor such as Fe(II) is available and reduces sulfate to sulfide, copper can react with sulfate to give copper sulfide. It is, however, well known and unanimously accepted in the geochemical literature that purely chemical reduction of sulfate does not occur at temperatures below 100 °C. Grauer (1990) and Goldstein and Aizenshtat (1994) have reviewed abiotic (thermochemical) sulfate reduction. Grauer (1990) concludes that at temperatures relevant for repository conditions, corrosion of copper by sulfate in the absence of sulfate reducing bacteria can be ruled out. Goldstein and Aizenshtat (1994) find that reduction of sulfate through oxidation of certain organic molecules only occurs at geochemically meaningful rates at temperatures above 175 °C. Cross et al. (2004) determined the reaction kinetics for aqueous sulfate reacting with aqueous acetate and elemental sulfur. The half-life of the sulfate was extrapolated to be 1 650 years at 150 °C and 372 000 years at 100 °C. Abiotic reduction of sulfate by hydrogen gas has been studied experimentally under elevated temperatures, varying partial pressures of hydrogen gas and in the presence of elemental sulfur (Truche et al. 2009). The activation energy for this reaction was determined to 131 kJ/mol and the half-life of aqueous sulfate ranges from 210 000 to 2.7×10^9 years at 90 °C and 25 °C, respectively. Truche et al. (2009) also concluded that the rate of sulfate reduction by hydrogen gas in their experimental setup is in line with the kinetics for thermochemical sulfate reduction in oil fields. Due to the limited kinetics demonstrated by the above references, abiotic sulfate corrosion of copper is deemed negligible under repository conditions.

Dependencies between process and canister variables

Table 3-15 shows how the process influences, and is influenced by, all canister variables.

The temperature in the repository will be elevated during the oxidising phase, with a maximum of up to 100 °C on the copper surface. The corrosion reactions are temperature dependent, generally with increasing rates at higher temperatures. This is, however, of subordinate importance, since the diffusion of reactants is rate controlling and diffusivity is much less affected by the temperature. The influence of temperature on the chemical equilibria for the corrosion reactions is completely negligible for the temperature range encountered in the repository.

Boundary conditions

The boundary condition for the copper corrosion process will be the rate of supply of corrosive agents from the near field to the canister – buffer boundary.

Table 3-15. Direct dependencies between the process "Corrosion of copper canister" and the defined canister variables and a short note on the handling in the PSAR.

Variable	Variable influence on process		Process influence on variable	
	Influence present? (Yes/No) Description	**Handling of influence (How/If not – why)**	**Influence present? (Yes/No) Description**	**Handling of influence (How/If not – why)**
Radiation intensity	Yes.	Neglected. Radiation effects on corrosion are negligible.	No.	–
Temperature	Yes. Complex dependence on temperature depending on the relative importance of kinetic and transport steps.	Neglected. The corrosion is modelled using transport control and mass balance.	No.	–
Canister geometry	No.	–	Yes.	Included in modelling of effect of corrosion.
Material composition	Yes. Different materials have different corrosion behaviour.	Actual copper material is considered.	Yes. Corrosion products are formed.	Actual corrosion products formed under the foreseen conditions are considered.
Mechanical stresses	Yes.	Dealt with in Section 3.5.5.	Yes.	Neglected. The growth of corrosion products is limited and does not excert additional pressure on the copper shell.

Model studies/experimental studies

See Overview/general description.

Natural analogues/observations in nature

Corrosion of copper under oxidising conditions can be studied on archaeological artefacts, and such studies have been conducted to assess the risk of pitting (Bresle et al. 1983, Hallberg et al. 1984), see *Localised corrosion under oxic conditions* above. A natural analogue study assessing general corrosion over longer periods of time is reported in Hallberg et al. (1988). They examined a bronze cannon from the Swedish warship Kronan, which had lain buried at a depth of 26 m with its muzzle downward in the mud on the bottom of the Baltic Sea since 1676. Microprobe analysis of a bronze core taken from the muzzle showed concentrations of 96.3 % Cu and 3.3 % Sn and combined Zn and Fe < 0.5 %. The dominant corrosion product was cuprite, Cu_2O. The estimated corrosion rate was 1.5×10^{-5} mm/year with no evident pitting.

Milodowski et al. (2003) present an analysis of the corrosion of native copper plates that have survived in a water-saturated clay environment for more than 176 million years. Although the native copper is affected by corrosion, the study shows that a significant proportion (30–80 % of the original thickness) of the copper sheets is preserved in the saturated compacted clay environment of the Littleham Mudstone. Apart from the recent weathering effects due to exposure at outcrops, petrographical studies demonstrate that most of the observed corrosion and alteration of the native copper is geologically old (i.e. predating the main sediment compaction) and also occurred before the end of the Lower Jurassic Period. This demonstrates that the native copper can remain stable in a saturated and compacted clay environment for geological timescales well in excess of the timescales considered for safety assessment of a deep geologic repository for spent nuclear fuel.

Time perspective

Sulfide corrosion will proceed as long as metallic copper is available and sulfide is present in the buffer, the deposition tunnel backfill or the groundwater. Oxygen corrosion will occur initially and possibly intermittently during deglaciations. The radiolysis will be persistent over a period of a couple of hundred years, but the oxidants may remain for a longer time, but still short on a safety assessment timescale.

Handling in the PSAR

The process is modelled for the main scenario and for the corrosion scenario in the PSAR, see further the PSAR Post-closure safety report (SKB 2022a, Sections 10.2.5, 10.3.13, 10.4.9 and 12.6.2). The modelling, which essentially consists of mass balance and steady-state transport rate expressions, is described in the present report (above and in Appendix A1-A3), and for the sulfide corrosion in further detail in SKB (2010e). The transport models are based on simple diffusion expressions, as well as on integrated flow and corrosion calculations (for example using the concept of equivalent flow), that have been developed and applied to canister corrosion over several decades. In summary, the contributions to the overall corrosion are considered in the following way.

- Corrosion prior to disposal and after emplacement in the deposition hole, but before sealing and backfilling will result in depths less than 1 µm. This is of negligible importance for the service life of the canister.
- Initially entrapped oxygen in the repository will lead to uneven general corrosion, although some localised corrosion cannot be excluded initially when the potential is high. The extent of general corrosion depends on the availability of oxygen entrapped in the buffer and backfill and depends on other processes in the near field. This is discussed further and evaluated in the Post-closure safety report (SKB 2022a, Section 10.2.5), however, already here the maximum corrosion depth could be concluded by pessimistic O_2 mass-balances to be: 64 µm (from buffer) + 891 µm (from backfill) = 955 µm, i.e. < 1 mm. The upper limit of localised corrosion is estimated by adding the maximum pit depths observed in initially unsaturated large-scale field tests (100 µm), with the maximum pit depths predicted probabilistically for saturated conditions (1.22 mm), which adds up to less than 1.5 mm.
- Corrosion by oxygen dissolved in intruding glacial melt water: Intrusion of melt water is generally expected to be so slow that oxygen is depleted by the time the water reaches repository depth, but the possibility of some oxygen intrusion cannot be excluded for a few fast flow paths during transients in a glacial evolution and needs to be evaluated from a hydrogeological and geochemical point of view. The extent of this corrosion form, including the possibilty of localised corrosion, is evaluated in the PSAR Post-closure safety report (SKB 2022a).
- Nitric acid corrosion is neglected due to very minor effects (pessimistically estimated depths of 7 nm).
- Corrosion depths from the radiolysis of water is estimated to be ca 3 µm, considering modelling of general corrosion depth and experimental observations of localised corrosion features.
- Corrosion of copper in pure O_2-free water is deemed to be negligible, based primarily on thermodynamic considerations.
- Chloride assisted corrosion is not considered significant as long as as the pH and chloride concentration is below (at the right-hand side of) the limiting curve for a total copper concentration of 10^{-6} mol/kg in the chloride concentration – pH plot in Figure A4-2, based on thermodynamic calculations. The expected chemical conditions in the repository are assessed and evaluated against the limiting curve in the PSAR Post-closure safety report (SKB 2022a).
- The copper will be corroded by sulfide reaching the canister surface, with the sources being sulfide initially present in the buffer, produced by microbes in the backfill and in the buffer after erosion, and supplied over time by transport in the groundwater. The nature (general, or more rarely localised) and extent of sulfide corrosion need to be evaluated in the safety assessment by comparing the fluxes of sulfide to the canister surface during the different epochs of repository environment to threshold fluxes for the different morfologies. For sulfide fluxes below 3×10^{-10} mol/(m^2 s) the film growth is controlled by the transport of sulfide in solution (and in the pores of the film), giving only

general corrosion. The contributions from uniform corrosion will be modelled as transport-limited and with any kinetic limitations due to interfacial reactions disregarded. To account for localised attacks, that cannot be excluded for sulfide fluxes above 3×10^{-10} mol/(m^2 s) (which could possibly occur e.g. if the protective buffer has been lost), a pessimistic maximum pit depth of 150 µm is used.

- Corrosion effects due to changes in the material (cold work or welding) are deemed to be negligible.

Boundary conditions: The boundary conditions, i.e. the rate of supply of corrosive agents from the near field to the canister – buffer boundary, are explicitly included in the models.

Handling of influences/couplings: Any temperature dependence of reaction rates is pessimistically neglected since all reactions are assumed to be instantaneous. The influence of the material properties is included through mass balance expressions and stoichiometric formulae. The reduction in copper canister thickness is explicitly calculated.

Handling of uncertainties in the PSAR

Uncertainties in mechanistic understanding

There are mechanistic uncertainties regarding the nature and extent of localised corrosion caused by both oxygen and sulfide, and this is treated with pessimistic estimates of maximum pit depths. The extent of corrosion due to the residual oxygen in the repository is determined using an approach with mass balance (and mass transport) and the corrosion rate under reducing conditions is determined by calculating the mass transport flux of corrosive agents to the canister surface. The mechanistic understanding of mass transport is sufficient for the needs of the safety assessment.

Model simplification uncertainties

The model simplifications are pessimistic; e.g. interfacial reaction kinetics are ignored, and steady-state rather than transient transport rate expressions are employed, assuming that the initial concentration of sulfide is much lower than the steady-state concentration.

Input data and data uncertainties

Input data and data uncertainties for the modelling of canister corrosion are discussed in the present report and the **Data report** (SKB 2022d). Important input data include the amount of initially entrapped oxygen in the repository, diffusivities in the buffer, the solubility of sulfide in the buffer material, the initial amount of sulfide present in the buffer, the sulfide concentrations and fluxes in the groundwater over time, and the possible amounts of oxygen that could penetrate to repository depth during transients in a glacial evolution.

3.5.5 Stress corrosion cracking of the copper canister

Overview/general description

Stress corrosion cracking (SCC) is classically described as the consequence of the action of a suitably corrosive environment on a susceptible material in the presence of a tensile stress. In terms of the factors affecting the corrosiveness of copper in the repository environment, the most important are the redox potential, the porewater salinity and pH, temperature, and the presence of specific species that are known to support SCC in copper. The chemical species of interest are those that have been shown to support the SCC of copper under oxidising conditions, namely, nitrite, ammonium, and acetate ions. Those factors that affect the loading on the canister, and hence the level of possible tensile stress, are the hydrostatic head, the bentonite swelling pressure and enhanced loads during future glaciation events. Calculations by Hernelind (2015a, 2019a, b) have shown that there are areas with tensile stresses throughout the copper wall thickness at the flange where the lid is welded onto the tube. King and Newman (2010) compiled a detailed survey of the knowledge of, and mechanisms for, SCC in copper and copper alloys, and under oxidising conditions some of them were concluded to be possible, but conditional on the environment close to the canister. No well-founded mechanism was found for SCC during the long-term anaerobic period (with sulfide present), but, starting with

Taniguchi and Kawasaki (2008), there have also been a few other studies in which micro-cracks observed on copper surfaces exposed to a combination of sulfide in aqueous environments and high tensile stresses, have been interpreted as evidence of SCC. The effect of irradiation on stress corrosion cracking needs also to be taken into consideration.

The four main mechanisms proposed to account for the SCC of Cu (King and Newman 2010) are:

- the film-rupture mechanism,
- the tarnish rupture mechanism,
- the film-induced cleavage model, and
- the surface-mobility model.

The film-rupture mechanism involves crack propagation following the rupture of some form of film at the crack tip. The conditions must be suitable for the formation of a protective film, most likely Cu_2O. Provided the pH inside the crack is not too acidic, a Cu_2O film would be present at potentials achieved in the presence of either O_2 or Cu(II).

The tarnish rupture mechanism is similar to the film rupture mechanism in that it involves a film (tarnish) and dissolution. The environmental requirements for the tarnish rupture mechanism are similar to those for film rupture. A film or tarnish must clearly be present and has been associated in the literature with the formation of Cu_2O.

Mechanisms that require a degree of oxidation or dissolution are only possible whilst an oxidant is present in the repository and then only if other environmental and mechanical loading conditions are satisfied. These constraints will limit the period during which the canisters could be susceptible to cracking via film rupture (slip dissolution) or tarnish rupture mechanisms to the aerobic period after deposition of the canisters

In the film-induced cleavage model, a crack initiates in a surface film and is projected into the underlying ductile metal, inducing a cleavage-like crack. Formation of the surface layer in which the crack initiates requires oxidation of the surface. There is, however, some question about whether a Cu_2S film could play the same role as Cu_2O in promoting SCC via a tarnish rupture (or, indeed, film rupture) mechanism. Under repository conditions, sulfide induced corrosion of copper usually produces a porous, and thus not well-adhered or protective film; see *Copper corrosion by sulfide* in Section 3.5.4.

The surface-mobility model was introduced by Galvele (1987). It postulates that a crack tip under stress captures vacancies, not from the bulk of the material but from the surface, i.e. surface self-diffusion of metal atoms away from the crack tip grows the crack. There are obvious similarities between such a process and creep crack growth and since it relies on a kind of creep, it does not require an oxidising environment or any environment at all. The values of the surface diffusion coefficient are, however, relatively low for bare engineering metals and the model relies on contamination of the surface to increase the values. Galvele (1987) estimates the surface diffusion coefficient from the melting point of the surface compound that is assumed to be present at the crack tip, using an established correlation. King and Newman (2010) discuss flaws in the formulation of their crack growth law, but it will, in a corrected form, predict crack growth rates of the order of 10^{-20} m/s. Therefore, even if cracking were to occur via this mechanism, the crack velocity would be too small to lead to canister failure, even over repository timescales.

There are also other suggested SCC mechanism descriptions, e.g. the adsorption-induced dislocation emission, and vacancy injection and embrittlement (the Aaltonen mechanism), as discussed by King and Newman (2010).

Stress corrosion cracking under oxidising conditions

The classic film rupture and tarnish rupture mechanisms require the presence of a Cu_2O film and sufficient crack-tip strain to either rupture the film to allow crack growth by dissolution or to fracture the tarnish to promote crack growth. These mechanisms would only be possible for the limited period of oxidising conditions in the canister environment in the repository.

To evaluate the possibility of stress corrosion cracking, the threshold concentrations for the various SCC agents could be compared with the concentrations in the water surrounding the canister. There are, however, few threshold values for the concentrations of ions causing SCC, and it may not be enough to consider just the SCC-causing ion in itself, as e.g. chloride may also play a role. There are though laboratory tests showing that ammonium concentrations of approximately 0.1 mol/L (Kinnunen and Varis 2011) or nitrite concentrations of 0.001 mol/L (Benjamin et al. 1988) are required to cause stress corrosion cracking in copper under oxidising conditions. For acetate there is less experimental data available, but according to Kinnunen (2006), stress corrosion cracking did not occur even when the acetate concentration was as high as 10^{-3} mol/L. Lately, Ikäläinen et al. (2021) used an acetate concentration of 0.4 mol/L and still found no signs of stress corrosion cracking in slow strain rate experiments. Earlier experimental results are summarised in King et al. (2010), and conclusions from the experimental results from the Canadian programme are summarised under *Model studies/experimental studies* below.

Stress corrosion cracking in sulfide solution

As described under *Model studies/experimental studies* below, it is unclear if any "classical" stress corrosion cracking has been observed on copper in sulfidic solutions, but there have been observations of superficial cracks in some experiments. As concluded in *Copper corrosion by sulfide* in Section 3.5.4, a passive sulfide film has only been observed in laboratory experiments with increased sulfide flux, and not under natural corroding conditions. This means that the mechanisms requiring the presence of a passive film are not applicable.

In Taxén et al. (2019) a mechanistic description is presented that tries to encompass the results from that study as well as the earlier studies by the same and other researchers. The process is described as an intergranular corrosion aggravated by strain. The tensile stress breaks the sulfide film and corrosion (anodic dissolution) initiates at susceptible grain boundaries and produces small cavities. (The copper atoms in the grain boundary would require somewhat less energy to be oxidised than atoms in the bulk copper matrix.) The intergranular corrosion is aggravated by strain that pulls apart the grains that form the flanks of the cavity. The primary corrosion products are the dissolved copper sulfide complexes, CuHS(aq), $Cu(HS)_2^-$, $Cu_2S(HS)_2^{2-}$, and the anodic corrosion process produces a concentration of dissolved Cu(I). This concentration will increase with increasing temperature and decreasing pH, and if the transport of copper sulfide species is less effective, e.g. at the tip of a crack in the film or on convex surfaces on a rounded test specimen. The increased concentration of copper will promote the precipitation of $Cu_2S(s)$, i.e. as a secondary corrosion product. The precipitation will occur preferably at a growing copper sulfide particles, often outside the crack, but also inside crack. The growth of solid corrosion products will thus tend to block the crack and reduce the transport of sulfide to the crack tip as an effect, and the process will be self limiting. Further, these superficial cracks are only seen for experiments where the bulk sulfide concentration is 10^{-3} mol/L or higher, and the sulfide flux is high enough to give a compact sulfide film (see *Copper corrosion by sulfide* in Section 3.5.4). The porous type of film formed at lower concentrations will not support cracking according to the mechanistic understanding, and thus the stress- and strain effects are not operating. With the experimental results and the mechanism description at hand, it is concluded that strain-enhanced grain boundary corrosion (rather than SCC) only takes place at a bulk sulfide concentration of 10^{-3} mol/L or higher.

The possibility that the Aaltonen mechanism could be an operable SCC mechanism has been revisited (Huotilainen et al. 2018). This mechanism is based on the concept that excess vacancies in the metal can activate dislocations within the material leading to strain localisation at the crack tip and further to crack propagation. There is no intrinsic reason why excess vacancies could not be generated in copper exposed to a sulfide solution and that atomic hydrogen liberated in the corrosion process could enter the material, but observations of effects in laboratory experiments have only been seen at applied currents of the order of 1 mA/cm^2, which would correspond to corrosion from a sulfide flux of 10^{-4} $mol/(m^2\ s)$.

Material aspects

Similar to what was discussed in Section 3.5.4 for corrosion without mechanical load, flaws and scratches on the canister surface could, conceivably, also act as initiation points for SCC. This could happen either through their effect on the local environment or via stress concentration or intensification. According to King (2004), there is no evidence that surface discontinuities will affect the initiation of SCC by ennoblement of the corrosion potential or the formation of locally aggressive conditions. King (2004) also concludes that stress concentration could lead to crack initiation under some circumstances for a pre-existing crack-like flaw, but will be smaller than the minimum threshold stress intensity factor (K_{ISCC}) for copper reported in the literature. Therefore, any cracks that do initiate will tend to become dormant. Copper is ductile and analyses by Björkblad and Faleskog (2018) of materials testing of copper show extensive annihilation of cracks (blunting). There is thus no evidence that weld discontinuities will adversely affect the SCC behaviour of copper canisters. The predicted service life of the canisters is not affected by the presence of such features.

Effects of radiation on SCC

Ammonium and nitrite, the well-known SCC agents for copper under aerobic conditions, could in principle be produced by gamma irradiation of the repository environment since some residual air is present in the clay and in the initial canister-bentonite gap. As noted in *Radiolytic corrosion effects*, Section 3.5.4, radiolysis in the interior of the canister could cause the formation of NH_3 from possible remaining water and air. Earlier studies of the corrosion of copper in humid aerobic environments under irradiation were reviewed in King (1996). Although small amounts of ammonia have been reported (at most 26 volume-ppm in vapour), the predominant radiolytic nitrogen-containing species detected was nitrate (NO_3^-), which is not known to cause SCC of copper. More recent studies of copper exposed to irradiated humid air confirm the formation of nitrate species but neither ammonium nor nitrite were reported (Björkbacka et al. 2017, Ibrahim et al. 2018). These later studies used gamma dose rates between 0.35 and 10^3 Gy/h and the total doses ranged from 0.4 kGy to 100 kGy. Thus irradiation experiments have been performed for both realistic and accelerated conditions and for total doses representative for the canister in the repository.

Stress corrosion cracking of copper under aerobic conditions is associated with a threshold potential (King and Newman 2010). Gamma irradiation can sometimes shift (ennoble) the corrosion potential of metals and alloys to more positive values as a result of the production of oxidising radiolysis products at the metal-solute interface. Although Glass et al. (1986) indeed reported a positive shift of ca 100 mV at a very high dose rate of 33×10^3 Gy/h, King and Litke (1987) observed no shift of the corrosion potential of copper specimens which were exposed to saline synthetic groundwater and a gamma dose rate of 27 Gy/h (i.e. still two orders of magnitude higher than the gamma dose rate at the canister surface).

In addition to the mechanistic arguments above, experimental testing of copper under radiation has shown no signs of SCC. No cracking was observed in stressed copper tear-drop specimens exposed to radiolytic environments in laboratory tests performed by Yunker and Glass (1987) and Yunker (1990). Dose rates of between 19 Gy/h and 4.9×10^3 Gy/h were used with total doses exceeding 10^4 kGy, i.e. approximately 100 times higher than the dose absorbed by the environment at the surface of the copper canister in the repository. Similarly, no sign of cracking was observed on copper U-bend specimens exposed to either a moist vapour phase, synthetic groundwater, or compacted bentonite material at a more representative dose rate of 5 Gy/h (Johnson et al. 1996). These experiments were performed for periods up to 5 years, representing a total dose of the order of 219 kGy. The use of plastically deformed specimens in both of the studies referred to here, either in the shape of tear-drops or a U-bends, ensured the presence of high tensile stresses representing a severe loading condition.

Gamma irradiation of copper at dose rates relevant to the copper canister in the repository appears thus to produce neither significant amounts of SCC agents nor oxidising radiolysis species to shift the corrosion potential of copper into the range for cracking.

Dependencies between process and canister variables

Table 3-16 shows how the process influences, and is influenced by, all canister variables.

Boundary conditions

Concentrations of nitrites, ammonium or acetate at the canister – buffer interface constitute the boundary conditions for this process as are the sulfide fluxes at the canister surface. The stress state at the canister surface is another boundary condition for the process. The dose rate at the copper outer surface constitutes the boundary condition for any effect of irradiation on this process.

Model studies/experimental studies

Work in the Canadian nuclear waste disposal programme has focused on experimental studies of the SCC of OFP (oxygen-free, phosphorus doped) Cu in the three environments (ammonium, acetate and nitrite, under oxidising conditions) known to support cracking (Ikeda and Litke 2004, 2007, 2008, Litke and Ikeda 2006, 2008, 2011). The major conclusions from the experimental work are:

1. except under the most aggressive conditions, OFP copper exhibits largely ductile behaviour in ammonium, acetate, and nitrite solutions,
2. only specimens covered by a visible surface oxide exhibited cracking and only at potentials and pH values consistent with a Cu_2O film,
3. the presence of Cl^- ions inhibits the SCC of OFP copper, and
4. in nitrite solutions, the susceptibility to cracking decreases with increasing temperature.

During the last decade laboratory experiments have been performed by 5 different research groups in trying to investigate if stress corrosion cracking can occur on copper in sulfide solution. Regarding experiments to investigate stress corrosion cracking in sulfide solutions, SKB presented a thorough description in SKB (2019a), with further details in Taxén et al. (2018). The test method has mainly been slow strain rate testing, at various conditions. The results have though not been consistent. In the Japanese work (Taniguchi and Kawasaki 2008) small superficial cracks were noted, but several other observations point to the possibility that this could have been attacks in the grain boundaries and not traditional stress corrosion cracking. SKB had a group at the University of Toronto (Bhaskaran et al. 2013) try to repeat the Japanese experiments, but in spite of aggressive laboratory conditions and variation of many experimental parameters, no cracks were observed. Also a group at VTT Technical Research Centre of Finland tried to repeat the Japanse experiments. First, results were published (Arilahti et al. 2011) that inferred sulfide would quickly go into the copper material, but the authors concluded in a later publication (Sipilä et al. 2014) that the cause of the sulfur ingress was caused by an unsuitable method for specimen analysis. No evidence for SCC was found by this group in either study.

SSM has had further tests being done at Studsvik AB, and material from the exposed test specimens has also been analysed at Aalto University in Finland. In these tests another type of specimen (tapered) was used, and tested at three different sulfide oncentrations (Becker and Öijerholm 2017, Becker et al. 2020, Forsström et al. 2021). As a departure from the earlier test conditions, a phosphate buffer was used to keep the pH stable, and lower, in the test solution. In the first study (Becker and Öijerholm 2017), a strain of 9 % was targeted (exposure time 2 weeks), and at the sulfide concentration of 10^{-3} mol/L some small fractures were observed, with at maximum depth of 50 µm. At a sulfide concentration an order of magnitude lower (10^{-4} mol/L), some smaller superficial defects were noted, but such defects were also found further into the material, and the authors concluded that these defects had another cause, for example the manufacturing of the specimens. The results were further interpreted as indicating that there exists some threshold between those two concentrations for the occurrence of superficial cracks. In the later test (Becker et al. 2020, Forsström et al. 2021), a lower strain rate was used (exposure time 4 weeks), and they instead found corrosion in grain boundaries rather than cracks. At the higher sulfide concentration, 10^{-3} mol/L, the grain boundaries had opened (especially high angle boundaries) and were often filled with corrosion products. At the lower sulfide concentration, 10^{-5} mol/L, no similar opening was found, but still with some slight corrosion in the grain boundaries and slip lines. Mechanically unloaded specimens were also exposed to the same solution, but no similar surface defects were found. Becker et al. (2020) thus concluded that the

opening of the grain boundaries in the high sulfide environment may be attributed to SCC, since no similar surface defects were found in the unloaded specimens exposed to the same environment, meaning that it is not only the corrosion of Cu, but the combination of the stress state and corrosion that dictates the formation of these defects.

At Aalto University the concentration of hydrogen in different samples was analysed. In the specimens from the first study (Forsström et al. 2017), the authors noted higher concentrations of hydrogen in copper after exposure to the sulfide solution. In the second study, there were both strained (SSRT with lower rate than in the first study) and unloaded specimens. As described in Section 3.4.7 the strained samples had a higher concentration than the unloaded samples, exposed to the same sulfide concentration. The authors concluded the surface defect formation on the grain boundaries is most likely related to corrosion of Cu, rather than hydrogen embrittlement of the grain boundaries.

SKB has had Swerea KIMAB (now RISE KIMAB) also try to repeat both the Japanese experiments and the study at Studsvik. The investigations were performed with both round and flat specimens, with different levels of cold work in the material, at different temperatures and with different sulfide concentrations (Taxén et al. 2018). The later work introduced phosphate buffer in the same way as Studsvik did (Taxén et al. 2019). The specimens were analysed with optical microscope and SEM. At rupture the fracture surface showed a ductile fracture. There were signs of attacks in the grain boundaries, which resembles what other researchers sometimes have interpreted as stress corrosion cracking. When a phosphate buffer was present, Kimab observed superficial cracks at high sulfide concentration (10^{-3} mol/L or higher), but not at low (2×10^{-5} mol/L).

The field test MiniCan 4, which was retrieved in 2015, included bent copper samples to investigate crack initiation and pre-cracked samples to measure potential crack growth during exposure in the Äspö HRL's groundwater environment. No crack initiation was observed in either of the two bent samples (Gordon et al. 2017, Johansson et al. 2017). Neither has any growth of the initial crack occurred in any of the pre-cracked samples, corresponding to the results from the previously retrieved MiniCan 3. Small cracks that run from the initial crack were observed, but they are deemed to have been caused by the alternating stresses used to achieve the initial experimental fatigue crack during sample preparation.

Table 3-16. Direct dependencies between the process "Stress corrosion cracking of the copper canister" and the defined canister variables and a short note on the handling in the PSAR.

Variable	Variable influence on process		Process influence on variable	
	Influence present? (Yes/No) Description	Handling of influence (How/If not – why)	Influence present? (Yes/No) Description	Handling of influence (How/If not – why)
Radiation intensity	Yes. High dose rates enhance the corrosion potential and could induce radiation damage in the material.	Neglected, due to small effects.	No.	–
Temperature	Yes. The temperature influences different part of the process in different ways.	Neglected, due to small effects.	No.	–
Canister geometry	No.	–	No.	–
Material composition	Yes. Different materials have different sensitivities to SCC.	Actual copper material is considered.	No.	–
Mechanical stresses	Yes. Tensile stresses at the canister surface are a prerequisite for SCC.	The mechanical stress state is modelled and analysed.	Yes. An SCC crack will relieve the tensile stresses.	Neglected.

Natural analogues/observations in nature

Not applicable.

Time perspective

With different corrosion agents for oxidising and reducing (sulfur containing) conditions, the entire evaluation period of 10^6 years needs to be considered. The oxidising period (from remaining oxygen in the pores of the buffer, and from radiolysis of water) is short, so the SCC mechanism for reducing conditions is to be assessed for most of the time.

Handling in the PSAR

Stress corrosion cracking depends on the fulfilment of several simultaneous conditions, and the presence of sufficient corrosion agent is one of them. For oxidising conditions, the threshold concentrations where SCC have been noticed (ammonium 0.1 mol/L; nitrite 0.001 mol/L; acetate > 0.4 mol/L) is compared to the possible concentrations in water close to the canister, during this short period. For the case of water present in the interior of the canister, also the possible overlapping time periods with radiolytic formation of NH_3 while water still is present, is considered.

For the subsequent long period of reducing conditions the sulfide flux is evaluated. From the laboratory testing it was concluded that SCC, or more correctly described as strain-enhanced grain boundary corrosion, only takes place at a bulk sulfide concentration of 10^{-3} mol/L or higher. This corresponds to a sulfide flux of the order of 10^{-6} mol/(m^2 s), assuming a diffusion layer of 1 mm and a diffusivity in bulk solution of 10^{-9} m^2/s. The sulfide flux in experiments where effects have been observed and could be explained as due to vacancy injection (the Aaltonen mechanism) have been performed at applied currents of the order of 1 mA/cm^2, which would correspond to corrosion from a sulfide flux of 10^{-4} mol/(m^2 s).

As described above tensile stresses cannot be totally excluded. The irradiation effects on the process are small and disregarded.

Handling of uncertainties in the PSAR

Uncertainties in mechanistic understanding

There are uncertainties in the description of the mechanism for the occurrence of superficial cracks that have been seen in laboratory experiments, but the effects are seen mostly in conditions more harsh than in the repository.

Model simplification uncertainties

Stress corrosion cracking is not modelled.

Input data and data uncertainties

Not relevant.

3.5.6 Earth currents – stray current corrosion

Overview/general description

Sources of earth currents

There are several sources for electrical currents in the earth's crust, both natural and anthropogenic. Currents caused by natural sources, earth currents or telluric currents, originate mostly from the interior of the earth, water currents in the ocean, atmospheric discharges, the sun and the space in the universe. Anthropogenic currents are mostly referred to as stray currents and originate mainly from transmission of electric power, rail transport, grounding to the (real) earth of various electric installations and radio communication. An overview of processes occurring in the geosphere is given in the PSAR Geosphere process report (SKB 2022c, Section 5.14).

Another natural source is of an electrochemical nature. Oxidation of sulfide ores coupled to reduction of oxygen can give rise to a “battery-effect”. Natural self-potentials are generally small ranging from a fraction of a millivolt to a few tens of millivolts. Anomalous potentials on the order of a few hundred millivolts are often found in association with ore bodies (Parasnis 1997).

Man-made sources include all types of electrical power installations. High Voltage Direct Current transmissions (HVDC) are locally very strong sources. Monopolar HVDC uses the ground to close the electrical circuit. Thousands of amperes are forced through the earth’s crust over hundreds of kilometres. Although the electrodes are usually located in the sea and major parts of the current stay in the seawater, neighbouring land is usually affected.

Charge carriers

In water, the current is carried by ions, e.g. Na^+ and Cl^- (or other charged particles). Also in the ground, in clay, soil and rock, ions are the dominant charge carriers (Stumm and Morgan 1996). Only certain minerals have significant electronic conductance. The abundant minerals of granite and other rock types of relevance for the Swedish programme are poor conductors, and ions in the porewater of the rock matrix are the dominant charge carriers (Schön 1996).

Alternating and direct currents

Depending on the source, earth currents are either alternating or direct. Most man-made sources are alternating. Although the source may be alternating, it is possible that a direct current component arises. A mineral with rectifying properties could, like a diode in a network of resistors, cause a DC component to arise in the vicinity of the rectifying mineral. Alternating currents do not generally cause corrosion (Koerts and Wetzer 2001), and corrosion effects have only been observed at very high AC densities. HVDC transmission uses, as the name implies, direct current.

Corrosion effects on the canister caused by earth currents

Earth currents in the form of direct current are known to cause corrosion. Primarily, constructions stretching over long distances, such as pipelines, are affected. In this context, a small metallic object such as a five metre high copper canister will be relatively insensitive to direct currents, because the voltage drop across it will be low. As a result of the HVDC electrode located about 30 km north of the Forsmark site (the Fenno-Scan installation), man-made earth currents are a potential source of enhanced corrosion. Such corrosion has been seen on stainless steel logging equipment used at the Forsmark site (Nissen et al. 2005, Thunehed 2017).

The deposited copper canister will be surrounded by partly saturated and/or fully saturated bentonite buffer. Depending on the degree of saturation, the electrical resistance of the bentonite will vary. Generally, the higher the degree of saturation, the lower the electrical resistance becomes. A fully saturated buffer will have an electrical resistivity on the order of 1 ohm.m. The bentonite buffer is surrounded by saturated rock, constituting the walls of the deposition hole. At repository depth at the investigated sites, the rock matrix has a typical resistivity on the order of 10^4 ohm.m, but with some variation (Thunehed and Pitkänen 2007, Thunehed 2018, Löfgren and Sidborn 2018).

The current to affect the copper canister will be propagated from the rock or backfill, through the buffer, and further on to the canister. Metallic copper has negligible resistance and current transport must be electronic, while current in the bentonite will be ionic. Thus, conduction across the copper-buffer interface can be achieved if both thermodynamically possible and kinetically favoured reactions are available for interfacial charge transfer. The rate of such interfacial reactions is inversely proportional to the polarisation resistance across the copper/buffer interface, at least for moderate potentials over the canister (Taxén et al. 2014).

The total corrosion that an external electrical field can cause can be estimated from the resistances in the circuit. The transfer resistance, where current transport changes from ions in the bentonite to electrons in the copper, also known as the polarisation resistance, may be the dominating resistance in the circuit. This value is not constant but varies with the voltage and will decrease strongly above a certain voltage.

The external potential field will be superimposed on the corrosion potential of the canister. The maximal effect is attained when the external current that passes in at one end of the canister will pass out from the other end of the canister. The end where current exits the canister will suffer more corrosion, and the other end will suffer less corrosion than without external field. The initial corrosion processes are likely to be:

$O_2 + 2H_2O + 4e^- \rightarrow 4OH^-$ Cathodic process

$2Cu(s) + 2OH^- \rightarrow Cu_2O(s) + H_2O + 2e^-$ Anodic process

These two processes must balance in terms of charge. With an electrical field, the cathodic process will be stimulated at one end of the canister and suppressed at the other end. In the same way the anodic process will be stimulated at one end and suppressed at the other. The cathodic reduction of oxygen is of course limited by the supply of oxygen. The same arguments apply for Cu(II), earlier formed by oxidation by the molecular oxygen, as the reactant in the cathodic reaction.

The corrosion caused by atmospheric oxygen and oxygen initially remaining in the buffer (and backfill) will cause the formation of a copper oxide layer on the canister. If the buffer at the upper end of the canister becomes positive relative to the buffer at the lower end, the current will gradually "relocate" the initial corrosion and the corrosion products from the upper end to the lower end. If the polarity is the opposite there will be a tendency to "relocate" all corrosion and corrosion products towards the upper end of the canister. (Relocation means here that corrosion products are cathodically reduced at one place and anodically formed at other places, not a physical transport of corrosion products.)

More extensive corrosion than that limited by the supply of oxygen takes place only when an additional cathodic process is possible. The most likely sustainable process is the cleavage of water to form molecular hydrogen:

$2H_2O + 2e^- \rightarrow H_2 + 2OH^-$

The exact potential difference required to drive the cleavage of water at one side of the canister and the oxidation of copper to $Cu_2O(s)$ at the other depends on the equivalent partial pressure of hydrogen. As more reaction products are formed, higher potential differences are required. As an example, stability diagrams (Puigdomenech and Taxén 2000) indicate that at 1.0 atmosphere hydrogen pressure, the potential difference is about 0.5 V at 25 °C and slightly less at 100 °C.

Groundwaters in the Forsmark area frequently have hydrogen contents in the order of 10^{-5} mol/L (Hallbeck and Pedersen 2008), equivalent to a partial pressure in the order of 10^{-2} atmospheres. At a partial pressure of 10^{-2} atmospheres of hydrogen, only potential differences larger than the equilibrium between Cu/Cu_2O at one end of the canister and H_2/H^+ at the other end can drive a corrosion process. At 25 °C a limiting potential difference of about 400 mV is found, while at 100 °C it is 360 mV (estimated from calculations of ΔG for the combined reactions above). At lower potential differences, the ambient partial pressure of 10^{-2} atmospheres hydrogen maintains immunity with respect to the formation of $Cu_2O(s)$.

When sulfide, HS^-, is present, copper can corrode to $Cu_2S(s)$ with evolution of hydrogen. If $Cu_2S(s)$ is considered to be the copper sulfide formed, the corrosion reactions can be written:

$2H_2O + 2e^- \rightarrow H_2 + 2OH^-$ Cathodic process

$2Cu(s) + OH^- + HS^- \rightarrow Cu_2S(s) + H_2O + 2e^-$ Anodic process

The anodic process is here limited by the access of sulfide at the copper surface (King et al. 2017). Thus, the rate of anodic reaction is relatively insensitive to the potential. The process cannot proceed faster than the supply of sulfide allows. Therefore, the corrosion attack by sulfide is expected to be mostly uniform also in the presence of an external electrical field. The cathodic process on the other hand is sensitive to the electrochemical potential. This process is likely to become preferentially located to one end of the canister.

As described in *Localised corrosion under oxic conditions,* Section 3.5.4, pitting corrosion does not occur while the corrosion potential is lower than the breakdown potential of the film. The difference can be regarded as a margin against pitting, and could be estimated to be about 200 mV as a minimum (King 2002), at least for a chloride-containing solution. In order for an external electrical field to cause pitting corrosion, the potential at one end of the canister should be raised by 200 mV. However, the total potential across the canister required to raise the potential at the anodic side by 200 mV is influenced also by the current-potential characteristics of the cathodic reactions that take place at the opposite end of the canister.

With reduction of solid corrosion products or reduction of oxygen under activation control as cathodic reactions, the cathodic current can increase strongly with increasing negative potential. In this case, the shift in potential at the cathodic side may be small compared to a 200 mV shift at the anodic side. During a period when the conditions of an excess supply of oxygen may prevail or when there are reducible corrosion products present, the total voltage across the canister can be approximated with the shift at the anodic side. Thus, a voltage across the canister of 200 mV would, during this period, consume the whole margin against pitting. When there are no reducible corrosion products at the cathodic side of the canister and the oxygen supply is limited by diffusion, there is no strong potential dependence of the cathodic current close to the corrosion potential. The polarisation curve around the corrosion potential is likely to be almost linear over a wide range of potentials or to curve upwards. If the polarisation curve is linear, the total potential across the canister required to consume the margin against pitting is about 400 mV (200 mV + 200 mV). If the polarisation curve curves upwards, the potential difference across the canister must be higher than 400 mV in order to consume the margin against pitting.

When the supply rate of oxygen to the cathode is not enough to drive the anodic processes, hydrogen evolution (reduction of water) can take place. An estimate of the potential across the canister required to drive pitting corrosion is found by considering the free corrosion potentials in Section 3.5.4 as being close to or higher than the potential required to oxidize copper metal to cuprous oxide, at least under neutral or alkaline conditions (King 2004). As described previously in this section, the potential difference between the hydrogen evolution and oxide formation is about 400 mV. An additional 200 mV must be added to reach pitting conditions. Thus, with hydrogen evolution as the cathodic reaction, the potential difference across the canister required to cause pitting corrosion is about 600 mV. The possibilities of pitting in an aerated saturated buffer was evaluated probabilistically in Briggs et al. (2020, 2021) and showed some pitting but only within the first few years. The arguments on the margins to pitting thus do not fully apply for the earliest period.

High concentrations of sulfide have been found to decrease the value of the pitting potential for copper (King et al. 2010). Effects have been found down to sulfide concentrations of 0.001 mol/L, which though is nearly one order of magnitude higher than found in Forsmark (Tullborg et al. 2010). For 0.01 mol/L HS^-, the margin against pitting has been estimated to about 200 mV (King et al. 2010). For sulfide driven copper corrosion, the cathodic process, hydrogen evolution can give currents that increase strongly with increasing cathodic polarisation. The anodic process is the formation of solid copper sulfides, which may be either diffusion controlled or show a passive behaviour. In both cases the polarisation curve is likely to be flat at the anodic side while it can show strong non-linearity at the cathodic side. For these high sulfide concentrations, a potential difference of 200 mV across the canister would consume almost the whole margin against pitting. But, because solid copper sulfides are the only stable corrosion product of copper in this potential range, the growth rate of such a pit would be limited by the diffusion of sulfide to and into the actual pit. There are indications of a threshold effect of sulfide so that the effect of sulfide on the pitting potential disappears below a certain concentration and also that the effect of sulfide decreases with increasing concentrations of other ions in the water (King et al. 2010, SKB 2019a).

Nevertheless, in all cases one effect of an imposed voltage across a canister is that the margin against pitting corrosion is decreased, but the margins increase as the system is depleted of oxygen.

Anodic potentials are also a prerequisite for stress corrosion cracking, and the margins for this process to occur will also be decreased by an imposed voltage across a canister. Still, for stress corrosion cracking to occur, high concentrations of detrimental ions are needed (see Section 3.5.5).

Dependencies between process and canister variables

Table 3-17 shows how the process influences, and is influenced by, all canister variables.

Boundary conditions

The earth currents are generated in the far field and transferred to the canister at the canister/buffer boundary.

Model studies/experimental studies

In SR-Site, measured self-potentials and self-potential gradients at the Forsmark site were used to estimate possible potential gradients due to a High Voltage Direct Current (HVDC) installation over a canister in the planned repository (SKB 2010a). Additional information was sent to SSM (Lilja and Johansson 2014) with an extended analysis (Taxén et al. 2014) investigating the effects of high voltage DC power transmission on copper corrosion in a KBS-3 repository at Forsmark. The influence from the existing sea-based HVDC transmission, the Fenno-Skan installation, was reviewed, and possible locations of new HVDC transmissions in the Forsmark region were found to be limited by the high resistivity bedrock so that a land-based electrode will never be economical in the region. However, major changes in the location of the shoreline due to the combined effect of sea level change and post-glacial crustal rebound may, during some periods, cause the shoreline to be located several kilometers inland from the present position. A sea-based electrode for HVDC transmission could then possibly be located in the vicinity of the repository during such periods. Most of the current from a sea-based electrode is conveyed by the water but large gradient fields arise nearby the electrode. These gradient fields are so large that danger to humans forces the electrodes to be located a few kilometers from the shoreline.

The possible influence of currents from HVDC electrodes on corrosion of the copper canisters is estimated from Finite Element Models (FEM) representing the tunnel system in the repository and the potentials that arise at the most affected positions when the tunnels are located in various electrical fields. Four model types of electrical fields were studied: 1) a uniform horizontal field with a field strength of 50 V/km, 2) Forsmark power station behaving as a secondary electrode, through the groundings and earth lines in overhead power lines, with an output of 20 A through the ground, 3) direct influence from a hypothetical future HVDC sea-based electrode operating at 2 500 A in monopolar mode when the electrode is located directly on top the repository, 4) influence from a hypothetical future HVDC sea-based electrode operating at 2 500 A in monopolar mode at various distances from the repository. The Fenno-Skan installation consists of two electrodes, one in Sweden (placed close to Fågelsundet, approximately 25 km from Forsmark) and one in Finland, and two cables, operated with reverse current directions (bipolar mode). It is for monopolar mode (one cable disconnected, or unbalanced operation with different currents in the cables) that causes currents to go trhrough the earth.

In all cases, calculations include conditions where the tunnels are oriented to represent the maximum influence at the site of the deposition holes. For short distances between the repository and the electrode, where electrode design may be of importance, a representation consisting of 8 sub-electrodes in a ring with 100 m radius was used. An equal current is fed to all sub-electrodes.

The result from the extended modelling was that the highest value of the potential that will develop along the height of a canister surrounded by bentonite is about 0.46 V, under reducing conditions with sulfide available. The maximum additional corrosion rate is lower than 0.20 µm/year for a monopolar operation of the Fenno-Skan installation. During the initial oxidizing conditions, where the cathodic reaction is reduction of oxygen gas or earlier formed corrosion products, corrosion would consume these oxidants so that the presence of an electrical field under these conditions would not cause any additional corrosion.

With the electrical fields from the present Fenno-Skan installation, the voltages that arise along the height of a canister will be low also for conditions with ‘as-deposited’ bentonite. Estimated from the highest local field strength observed (1.5 V/km) the voltage may be about 0.008 V, corresponding to a corrosion rate of about 0.003 µm/year. These values are expected to decrease as the conductivity of the surrounding bentonite increases when its water content increases.

Table 3-17. Direct dependencies between the process "Earth currents – stray current corrosion" and the defined canister variables and a short note on the handling in the PSAR.

Variable	Variable influence on process		Process influence on variable	
	Influence present? (Yes/No) Description	Handling of influence (How/If not – why)	Influence present? (Yes/No) Description	Handling of influence (How/If not – why)
Radiation intensity	No.	–	No.	–
Temperature	Yes. Temperature will influence the stability of copper and tendency for pitting.	Neglected due to small effects, and only in short term.	No.	–
Canister geometry	Yes. The dimensions of the canister determine its conductance.	The length of the canister in included in the modelling, but other details of the canister geometry are neglected due to small effects.	Yes. To the extent that the process occurs, the effect would be a reduction of canister thickness.	Treated as a stylised case of future human action.
Material composition	Yes. Different materials have different electrical conductivities.	Neglected due to small effects.	No.	–
Mechanical stresses	No.	–	No.	–

In the study of possible future HVDC installations the most pessimistic modelling case resulted in a corrosion rate of < 0.2 µm/year. With an assumtion of an operation period of 100 years in monopolar mode (unrealistic for economic reasons) the corrosion would be 20 µm at the most exposed canister. If hypothetically one and the same canister should be the most exposed one, at 100 occasions during 10^6 years, the total corrosion would not be more than 2 mm.

Natural analogues/observations in nature

See "General description/Overview" and "Model studies/experimental studies".

Time perspective

Earth currents generated by natural causes may be present throughout the one million year time period of the safety assessment. Man made earth currents in general are expected not to occur during glaciations and other periods of no habitation, but could be possible during periods when the shoreline is in the vincinity of the repository site (Taxén et al. 2014). The analysis in the complementary material sent to SSM (Lilja and Johansson 2014) assumed operation of an HVDC installation for 100 years, and such installations at 100 times during the one million year assessment period.

Handling in the PSAR

The effect of natural earth currents on canister corrosion can be neglegted as it is unlikely that sufficiently large potential gradients can be maintained over the deposition hole to affect the copper corrosion.

The corrosion of the canister in the presence of an external field would still be limited by the availability of groundwater constituents for either the cathodic reaction (oxygen), the anodic reaction (sulfide), or ions causing stress corrosion cracking (nitrite, ammonium, acetat). Cathodic reactions would also be counteracted by any dissolved hydrogen gas present.

For the current situation of potential gradients over the canister at the Forsmark site, the estimates in the extended modelling are in line with those estimated in the safety assessment SR-Site. The study additionally addresses influences of possible future HVDC electrodes. The results show that, with pessimistic assumptions on future HVDC locations, the influences may be larger than today.

However, also with the very pessimistic assumptions of a location directly on top of the shaft that connects the repository level and ground level, the effect is limited to about 2 mm for the most exposed canister positions in the repository. The process will be treated with a stylised case of future human action.

Handling of uncertainties in the PSAR

Uncertainties in mechanistic understanding

There are no uncertainties in the mechanistic understanding of any importance for the safety assessment.

Model simplification uncertainties

The model simplifications are generally pessimistic.

Input data and data uncertainties

There are uncertainties in the determination of the rock resisitivity in Forsmark (Thunehed and Pitkänen 2007). In the modelling of the effect of HVDC installations (Taxén et al. 2014) this is handled by using 6 different functions for the rock resistivity dependence of depth. Likewise there are uncertainties in the assumption on the future location of the shoreline.

The value of the polarization resistance and the extent of the potential range over which it is applied must be regarded together with the chemical environment it is intended to represent. For the study in Taxén et al. (2014) a constant polarisation resistance was used for potentials up to 0.5 V across the canister for the long time period with no oxygen and with transport-limited sulfide corrosion. For short term behavior the linear region is smaller, but as long as the cathodic reaction is the reduction of molecular oxygen or reduction of previously formed corrosion products, an external electrical field does not cause more corrosion, but possibly relocates and collects the corrosion products to the anodic side of the canister.

3.5.7 Deposition of salts on the canister surface

Overview/general description

In the present design, the heat generation in the fuel is 1 700 W (at a maximum), resulting in an increased canister surface temperature. The temperature development will, among other things, depend on heat transfer to the surrounding bentonite. In the safety assessment SR-Site, the maximum canister surface temperature was calculated to be 90 °C, which is lower than the 100 °C required to compromise the chemical stability of the bentonite, see further Section 3.5.8 in the PSAR Buffer, backfill and closure process report (SKB 2022b). At elevated temperatures, the corrosion reactions may proceed with enhanced rates, but this will be of negligible importance since the corrosion processes involved are either under mass transport or mass balance control. A more important consequence of the higher canister surface temperature is the possible redistribution and enrichment of salts in the bentonite and their deposition onto the canister surface. The extent to which this may occur will depend on the salt content of the groundwater and of the bentonite porewater. The salts that may be of concern are chlorides and sulfates from the groundwater, and sulfates and carbonates from the accessory minerals in the bentonite. The redistribution and enrichment of salts in the buffer material is further discussed in Section 3.3.1 of the Buffer, backfill and closure process report (SKB 2022b).

Salt enrichment has been studied in a number of repository-like field tests. In the Long Term Test of Buffer Materials (LOT), copper heaters are embedded in compacted bentonite and exposed to groundwater in the Äspö HRL. The two pilot packages S1 and A0, heated to copper surface temperatures of 90 °C and 130 °C, respectively, were retrieved after one year (Karnland et al. 2000). Examination of the heaters showed that in both packages the copper surfaces were covered with a thin layer of calcium sulfate and/or calcium carbonate. No chloride enrichments were apparent even though the groundwater had a chloride content of over 8 000 mg/L.

Precipitates of calcium sulfate and calcium carbonate were found also in the LOT/A2 package, retrieved after 6 years exposure at 130 °C. The longer exposure did not, however, seem to cause precipitation of larger amounts of these phases on the heater surface (Karnland et al. 2009). The

bentonite pore water concentration of chloride was measured as a function of the distance from the central heater for both colder and warmer parts of the LOT/A2 package. The chloride concentration was nearly constant in both the axial and radial directions in the blocks examined, and the total content was very close to that of a mixture of salt content of the original bentonite and the salt content of the amount of Äspö groundwater needed for saturation. The total amount of chloride was actually a little lower than that of a mixture, which could be explained by ion equilibrium, as described by Birgersson and Karnland (2009).

The LOT/S2 and A3 test parcels were heated to 90 °C and 120 °C, respectively, and were exposed to the Äspö environment for 20 years. As for the earlier test parcels in the LOT series, precipitates of calcium sulfate were present at the copper clay interfaces, which was verified with XRD (Johansson et al. 2020). The copper surfaces were examined extensively using SEM-EDS at different magnifications. It was generally found that the levels of chlorine on the copper surfaces was less than one at.%, however, at high magnification, local spots could be found where the levels of chlorine were up to a few at.%. The corrosion product $Cu_2(OH)_3Cl$ was identified on the bottom plates of the test parcels, however, this is not regarded as the result of salt deposition but rather a different corrosion environment, since the bottom plate was in contact with sand (Johansson et al. 2020).

Examination of the bentonite from two of the deposition holes in the Prototype Repository, in which full-scale copper canisters were heated and and exposed to the Äspö groundwater for 7 years, showed results very similar to LOT/A2 (Olsson S et al. 2009). No systematic variation of the chloride concentration was found in the pore water from bentonite at different distances from the heated canisters in the test, and the measured chloride concentrations were found to result from proportional mixing of the initial pore water and the Äspö groundwater.

An enrichment of chloride at the bentonite/heater interface has been reported in the large scale experiment Febex, performed by Nagra at the Grimsel test site (Fernández et al. 2018). However, near the interface, the bulk of the bentonite was depleted in chloride compared to the initial concentration. The observed enrichment could have been caused by the condensation and evaporation that is expected during the saturation process and which would lead to a redistribution of the initial chloride content. The enrichment close to the heater could also be an effect of leakage through the cabling system (Giroud 2014). The data show no overall accumulation of chloride in the buffer surrounding the heater, rather a loss to the groundwater in the rock.

It is at this time not established whether or not the precipitation of the sulfates and the carbonates were caused by evaporation of water or by the lower solubility of the calcium salts at elevated temperatures. In the latter case, they are likely to redissolve as the temperature decreases again. Alternatively, the deposits can be redissolved when contacted with water undersaturated with respect to calcium carbonate and calcium sulfate. Deposits of calcium sulfate and calcium carbonate have been observed in all packages retrieved from the LOT series and in the Prototype Repository. Similar salt deposits were also observed in a heater experiment performed in Stripa (Pusch et al. 1992). Since these deposits are not electrically conductive, they are not expected to increase the risk of localised corrosion, see e.g. Adeloju and Duan (1994). Furthermore, higher chloride concentrations have been found to promote active dissolution of oxic corrosion products in the repository environment and would thus lower the susceptibility of copper to localised corrosion during the oxic phase (King et al. 2001, Briggs et al. 2020, 2021).

In summary, temperatures up to and above 100 °C are not expected to lead to deposition of salts on the canister surface to an extent that would affect the corrosion behaviour of the copper canister.

Dependences between process and canister variables

Table 3-18 shows how the process influences, and is influenced by, all canister variables.

Boundary conditions

The heat flux at the canister-buffer interface and the abundance of salts dissolved in water (or water vapour) at the surface constitute the boundary conditions for this process. The flux of salts to the surface and what limits this flux is discussed in Section 3.3.1 in the Buffer, backfill and closure process report (SKB 2022b).

Model studies/experimental studies

See above.

Table 3-18. Direct dependencies between the process "Deposition of salts on the canister surface" and the defined canister variables and a short note on the handling in the PSAR.

Variable	Variable influence on process		Process influence on variable	
	Influence present? (Yes/No) Description	Handling of influence (How/If not – why)	Influence present? (Yes/No) Description	Handling of influence (How/If not – why)
Radiation intensity	No.	–	No.	–
Temperature	Yes. The temperature affects the precipitation of salts.	Neglected, due to small effects.	No.	–
Canister geometry	No.	–	No.	–
Material composition	No.	–	Yes. Surface deposits may occur.	Neglected. The process has no implications for safety.
Mechanical stresses	No.	–	No.	–

Natural analogues/observations in nature

Not applicable.

Time perspective

Elevated temperatures will remain for several hundred years. The effects discussed above will, however, only occur during the bentonite saturation phase.

Handling in the PSAR

Deposition of salts has small consequences and is only relevant during the bentonite saturation phase. The process has no implications for safety and is, therefore, neglected.

Handling of uncertainties in the PSAR

Uncertainties in mechanistic understanding

There are uncertainties concerning the mechanisms for possible salt deposition. There are no major uncertainties in understanding the consequences of such a deposit on the lifetime of the canister.

Model simplification uncertainties

Not applicable.

Input data and data uncertainties

Not applicable.

3.6 Radionuclide transport

See Section 2.6 "Radionuclide transport ".

References

SKB's (Svensk Kärnbränslehantering AB) publications can be found at www.skb.com/publications. SKBdoc documents will be submitted upon request to document@skb.se, with the exception of internal documents.

Adeloju S B, Duan Y Y, 1994. Influence of bicarbonate ions on stability of copper oxides and copper pitting corrosion. British Corrosion Journal 29, 315–320.

Agrenius L, Spahiu K, 2016. Criticality effects of long-term changes in material compositions and geometry in disposal canisters. SKB TR-16-06, Svensk Kärnbränslehantering AB,

Albinsson Y, Ödegaard-Jensen A, Oversby V M, Werme L, 2003. Leaching of spent fuel under anaerobic and reducing conditions. In Finch R J, Bullen D B (eds). Scientific basis for nuclear waste management XXVI. Warrendale, PA: Materials Research Society. (Materials Research Society Symposium Proceedings 757, 407–413.

Allen A O, 1961. The radiation chemistry of water and aqueous solutions. Princeton, NJ: Van Nostrand.

Alvarez Holston A-M, Stjärnsäter J, 2017. On the effect of temperature on the threshold stress intensity factor of delayed hydride cracking in light water reactor fuel cladding. Nuclear Engineering and Technology 49, 663–667.

Alverlind L, 2016. Isostatic pressure load of canister with scaled iron material model. Report 5000484-1, Revision 4, Inspecta Technology AB. SKBdoc 1089758 ver 3.0, Svensk Kärnbränslehantering AB.

Andersson-Östling H C M, 2020. Creep testing of copper intended for nuclear waste disposal – overview of studies from 1985 to 2018. SKB TR-20-06, Svensk Kärnbränslehantering AB.

Arilahti E, Lehtikuusi T, Olin M, Saario T, Varis P, 2011. Evidence for internal diffusion of sulphide from groundwater into grain boundaries ahead of crack tip in Cu OFP copper. Corrosion Engineering, Science and Technology 46, 134–137.

Askeljung C, Granfors M, Roth O, 2019. Release of ^{108m}Ag from irradiated PWR control rod absorbers under deep repository conditions. SKB R-19-21, Svensk Kärnbränslehantering AB.

ASME, 2008. ASME boiler and pressure vessel code. Section III – Rules for construction of nuclear power plant components – Divisions 1 and 2. New York: American Society of Mechanical Engineers.

Auqué L F, Gimeno M J, Gómez J B, Puigdomenech I, Smellie J, Tullborg E-L, 2006. Groundwater chemistry around a repository for spent nuclear fuel over a glacial cycle. Evaluation for SR-Can. SKB TR-06-31, Svensk Kärnbränslehantering AB.

Bai X, Guo R, Mao F, Macdonald D M, 2023. Effect of microalloying element P on the pitting behavior of copper. Corrosion Science 211, 110858.

Bauhn L, Ekberg C, Fors P, Spahiu K, 2017. The effect of bromide on oxygen yields in homogeneous α-radiolysis. MRS Advances Volume 2, Issue 13 (Scientific Basis for Nuclear Waste Management XL) 201, 711–716.

Bauhn L, Hansson N, Ekberg C, Fors P, Delville R, Spahiu K, 2018a. The interaction of molecular hydrogen with α-radiolytic oxidants on a (U,Pu)O_2 surface. Journal of Nuclear Materials 505, 54–61.

Bauhn L, Ekberg C, Fors P, Spahiu K, 2018b. The fate of hydroxyl radicals produced during H_2O_2 decomposition on the SIMFUEL surface in the presence of dissolved hydrogen, Journal of Nuclear Materials 507, 38–43.

Becker R, Öijerholm J, 2017. Slow strain rate testing of copper in sulfide rich chloride containing deoxygenated water at 90 °C. Stockholm: Swedish Radiation Safety Authority. (SSM 2017:02)

Becker R Forsström A, Yagodzinskyy Y, Heikkilä M, Hänninen H, 2020. Sulphide-induced stress corrosion cracking and hydrogen absorption in copper exposed to sulphide and chloride containing deoxygenated water at 90 °C. SSM report 2020:01, Swedish Radiation Safety Authority.

BEFAST III, 1997. Further analysis of extended storage of spent fuel. Final report of a Co-ordinated Research Programme on the Behaviour of Spent Fuel Assemblies during Extended Storage (BEFAST III) 1991–1996. IAEA-TECDOC-944, International Atomic Energy Agency.

Behrenz P, Hannerz K, 1978. Criticality in a spent fuel repository in wet crystalline rock. SKB TR 108, Svensk Kärnbränslehantering AB.

Bengtsson A, Chukharkina A, Eriksson L, Hallbeck B, Halbeck L, Johansson J, Johansson L, Pedersen K, 2013. Development of a method for the study of H_2 gas emission in sealed compartments containing canister copper immersed in O_2-free water. SKB TR-13-13, Svensk Kärnbränslehantering AB.

Benjamin L A, Hardie D, Parkins R N, 1988. Stress corrosion resistance of pure coppers in ground waters and sodium nitrite solutions. British Corrosion Journal 23, 89–95.

Berner U, 2002. Project Opalinus Clay. Radionuclide concentration limits in the near field of a repository for spent fuel and vitrified high level waste. Nagra NTB 02-10, Nagra, Switzerland.

Berner U, Curti E, 2002. Radium solubilities for SF/HLW wastes using solid solution and co-precipitation models. Internal Report TM-44-02-04, Paul Scherrer Institute, Villigen, Switzerland.

Betova I, Bojonov M, Lilja C, 2021. Influence of ionic strength on hydrogen generation during interaction of copper with deoxygenated neutral solution. Corrosion Science 188, 109552. doi:10.1016/j.corsci.2021.109552

Beverskog B, Pettersson S-O, 2002. Pourbaix diagrams for the copper in 5 m chloride solution, SKI Report 02:23, Swedish Nuclear Power Inspectorate.

Beverskog B, Puigdomenech I, 1998. Pourbaix diagrams for the copper-chlorine system at 5–100 °C. SKI Report 98:19, Swedish Nuclear Power Inspectorate.

Bhaskaran G, Carcea A, Ulaganathan J, Wang S, Huang Y, Newman R C, 2013. Fundamental as-pects of stress corrosion cracking of copper relevant to the Swedish deep geologic repository con-cept. SKB TR-12-06, Svensk Kärnbränslehantering AB.

Bienvenu P, Cassette P, Andreoletti G, Bé M-M, Comte J, Lépy M-C, 2007. A new determination of ^{79}Se half-life. Applied Radiation and Isotopes 65, 355–364.

Birgersson M, Goudarzi R, 2018. Investigations of gas evolution in an unsaturated KBS-3 repository. SKB TR-18-11, Svensk Kärnbränslehantering AB.

Birgersson M, Karnland O, 2009. Ion equilibrium between montmorillonite interlayer space and an external solution – Consequences for diffusional transport. Geochimica et Cosmochimica Acta 73, 1908–1923.

Björck M, Pehkonen H, Vuori L, Tigerström M, Lahtonen K, Valden M, Purhonen T, Cederqvist L, 2017. Evaluation of a gas shield for friction stir welding of copper canisters. Posiva SKB Report 02, Posiva Oy, Svensk Kärnbränslehantering AB.

Björck M, Taxén C, Vuoristo T, Elger R, Zavalis T, Wikström L, Sparr M, 2019. Embedded oxide particles in Friction Stir Welds. Effect on creep and corrosion properties. Posiva SKB Report 10, Posiva Oy, Svensk Kärnbränslehantering AB.

Björkbacka Å, 2015. Radiation induced corrosion of copper. PhD thesis. Royal Institute of Technology, Sweden.

Björkbacka Å, Hosseinpour S, Leygraf C, Jonsson M, 2012. Radiation induced corrosion of copper in anoxic aqueous solution. Electrochemical and Solid-State Letters 15, C5–C7.

Björkbacka Å, Hosseinpour S, Johnson M, Leygraf M, Jonsson M, 2013. Radiation induced corrosion of copper for spent nuclear fuel storage. Radiation Physics and Chemistry 92, 80–86.

Björkbacka Å, Yang M, Gasparrini C, Leygraf C, Jonsson M, 2015. Kinetics and mechanism of reaction between H_2O_2 and copper and copper oxides. Dalton Transactions 44, 16045–16051.

Björkbacka Å, Johnson C M, Leygraf C, Jonsson M, 2016. Role of the oxide layer in radiation-induced corrosion of copper in anoxic water. The Journal of Physical Chemistry C 120, 11450–11455.

Björkbacka Å, Johnson C M, Leygraf C, Jonsson M, 2017. Radiation induced corrosion of copper in humid air and argon atmospheres. Journal of The Electrochemical Society 164, C201–C206.

Björkblad A, Faleskog J, 2018. Evaluation of Cu-OFP creep crack growth and theoretical fracture models for Cu-OFP. Posiva SKB Report 03, Posiva Oy, Svensk Kärnbränslehantering AB.

Blackwood D J, Naish C C, Sharland S M, Thompson A M, 2002. Experimental and modelling study to assess the initiation of crevice corrosion in stainless steel containers for radioactive waste. Report AEAT/ERRA-0300, AEA Technology, Abingdon, UK.

Boman M, Ottosson M, Berger R, Andersson Y, Hahlin M, Björefors F, Gustafsson T, 2014. Corrosion of copper in ultrapure water. SKB R-14-07, Svensk Kärnbränslehantering AB.

Bond A E, Hoch A R, Jones G D, Tomczyk A J, Wiggin R M, Worraker W J, 1997. Assessment of a spent fuel disposal canister. Assessment studies for a copper canister with cast steel inner component. SKB TR 97-19, Svensk Kärnbränslehantering AB.

Bosbach D, Böttle M, Volker M, 2010. Experimental study of Ra^{2+} uptake by barite ($BaSO_4$). Kinetics of solid solution formation via $BaSO_4$ dissolution and $Ra_xBa_{1-x}SO_4$ (re) precipitation. SKB TR-10-43, Svensk Kärnbränslehantering AB.

Bowman C D, Venneri F, 1994. Underground supercriticality from plutonium and other fissile material. LA-UR-94-4022A, Los Alamos National Laboratory. (Also published in Science and Global Security 5, 279–320.)

Bradbury M, Bayens B, 2003. Far field sorption databases for the performance assessment of high level waste repository in undisturbed Opalinus Clay host rock. Nagra Technical Report 02-18, Nagra, Switzerland.

Brandt F, Curti E, Klinkenberg M. Rozov K, Bosbach D, 2015. Replacement of barite by a (Ba,Ra)SO4 solid solution at close-to-equilibrium conditions: A combined experimental and theoretical study. Geochimica et Cosmochimica Acta 155, 1–15.

Brennenstuhl A M, McBride A, Ramamurthy S, Davidson R, 2002. The effects of microstructural and environmental factors on underdeposit corrosion of oxygen-free phosphorous-doped copper. Report 06819-REP-01200-10079-R00, Ontario Power Generation, Nuclear Waste Management Division.

Bresle Å, Saers J, Arrhenius B, 1983. Studies in pitting corrosion on archaeological bronzes. Copper. SKB TR 83-05, Svensk Kärnbränslehantering AB.

Brissonneau L, Barbu A, Bocquet J-L, 2004. Radiation effects on the long-term ageing of spent fuel storage containers. Packaging, Transport, Storage and Security of Radioactive Material 15, 121–130.

Briggs S, Lilja C, King F, 2020. Probabilistic model for the pitting of copper canisters under aerobic, saturated conditions. SKB TR-20-01, Svensk Kärnbränslehantering AB.

Briggs S, Lilja C, King F, 2021. Probabilistic model for pitting of copper canisters. Materials and Corrosion 72, 308–316.

Broczkowski M E, Noël J J, Shoesmith D W, 2005. The inhibiting effects of hydrogen on the corrosion of uranium dioxide under nuclear waste disposal conditions. Journal of Nuclear Materials 346, 16–23.

Broczkowski M E, Goldik J S, Santos B G, Noël J J, Shoesmith D W, 2006. Corrosion of nuclear fuel inside a failed copper nuclear waste container. In Dunn D, Poinssot C, Begg B (eds). Scientific Basis for Nuclear Waste Management XXX. Warrendale, PA: Materials Research Society. (Materials Research Society Symposium Proceedings 985), 3–14.

Broczkowski M E, Noël J J, Shoesmith D W, 2007. The influence of dissolved hydrogen on the surface composition of doped uranium dioxide under aqueous corrosion conditions. Journal of Electroanalytical Chemistry 602, 8–16.

Broczkowski M E, Keech P G, Noel J J, Shoemsith D W, 2010. Corrosion of uranium dioxide containing simulated fission products in dilute hydrogen peroxide and dissolved hydrogen. J Electrochem Soc 157, C275–C281.

Brookins D G, 1975. Coffinite-uraninite stability relations in the Grants mineral belt. American Association of Petroleum Geologists Bulletin 59, 905.

Brown P, Cera E, G B, Ekberg C, 2005. Chemical thermodynamics. Vol. 8. Chemical thermodynamics of zirconium. Amsterdam: Elsevier.

Bruno J, Cera E, de Pablo J, D L, Jordana S, Savage D, 1997. Determination of radionuclide solubility limits to be used in SR 97. Uncertainties associated to calculated solubilities. SKB TR 97-33, Svensk Kärnbränslehantering AB.

Bruno J, Cera E, Duro L, Pon J, de Pablo J, Eriksen T, 1998. Development of a kinetic model for the dissolution of the UO_2 spent nuclear fuel. Application of the model to the minor radionuclides. SKB TR-98-22, Svensk Kärnbränslehantering AB.

Bruno J, Bosbach D, Kulik D, Navrotsky A, 2007. Chemical thermodynamics. Vol. 10. Chemical thermodynamics of solid solutions of interest in radioactive waste management. Paris: Nuclear Energy Agency, OECD.

BSC, 2004. Aqueous corrosion rates for waste package materials. ANL-DSD-MD-000001 Rev 01. Las Vegas: Bechtel SAIC Company.

Börgesson L, Johannesson L-E, Raiko H, 2009. Uneven swelling pressure on the canister simplified load cases derived from uneven wetting, rock contours and buffer density distribution. SKBdoc 1206894 ver 1.0, Svensk Kärnbränslehantering AB.

Campbell H S, 1950. Pitting corrosion in copper water pipes caused by films of carbonaceous material produced during manufacture. Journal of the Institute of Metals 77, 345–356.

Caporuscio F A, Palaich S E M, Cheshire M C, Jove Colon C F 2017. Corrosion of copper and authigenic sulfide mineral growth in hydrothermal bentonite experiments. Journal of Nuclear Materials 485, 137–146.

Carbol P, Cobos-Sabate J, Glatz J-P, Grambow B, Kienzler B, Loida A, Martinez Esparza Valiente A, Metz V, Quiñones J, Ronchi C, Rondinella V, Spahiu K, Wegen D H, Wiss T, 2005. The effect of dissolved hydrogen on the dissolution of ^{233}U doped UO_2(s), high burn-up spent fuel and MOX fuel. SKB TR-05-09, Svensk Kärnbränslehantering AB.

Carbol P, Fors P, Gouder T, Spahiu K, 2009a. Hydrogen suppresses UO_2 corrosion. Geochimica et Cosmochimica Acta 73, 4366–4375.

Carbol P, Fors P, Van Winckel S, Spahiu K, 2009b. Corrosion of irradiated MOX fuel in the presence of dissolved H_2. Journal of Nuclear Materials 392, 45–54.

Casella A, Hanson B, Miller W, 2008. Factors affecting UO_2 dissolution under geological disposal conditions. In Proceedings of the 12th International High-Level Waste Management Conference. Las Vegas, Nevada, 7–11 September 2008. New York: American Nuclear Society, 388–394.

Casteels F, Dresselaars G, Tas H, 1986. Corrosion behaviour of container materials for geological disposal of high level waste. Commission of European Communities Report, EUR 10398, 3–40.

Cera E, Bruno J, Duro L, Eriksen T, 2006. Experimental determination and chemical modelling of radiolytic processes at the spent fuel/water interface. Long contact time experiments. SKB TR-06-07, Svensk Kärnbränslehantering AB.

Chan K S, 2013. An assessment of delayed hydride cracking in zirconium alloy cladding tubes under stress transients, International Materials Reviews 58, 349–373.

Chang Z, 2015. Multiscale modelling of radiation-enhanced diffusion phenomena in metals. PhD thesis. Royal Institute of Technology, Sweden.

Chaouadi R, Gérard R, 2005. Copper precipitate hardening of irradiated RPV materials and implications on the superposition law and re-irradiation kinetics. Journal of Nuclear Materials 345, 65–74.

Chen J, Qin Z, Shoesmith D W, 2010. Kinetics of corrosion film growth on copper in neutral chloride solutions containing small concentrations of sulfide. Journal of The Electrochemical Society 157, C338–C345.

Chen J, Qin Z, Shoesmith D W, 2014. Key parameters determining structure and properties of sulphide films formed on copper corroding in anoxic sulphide solutions. Corrosion Engineering, Science and Technology 49, 415–419.

Chen J, Qin Z, Martino T, Shoesmith D W, 2017a. Effect of chloride on Cu corrosion in anaerobic sulphide solutions. Corrosion Engineering, Science and Technology 52, 40–44.

Chen J, Qin Z, Martino T, Shoesmith D W, 2017b. Non-uniform film growth and micro/macro-galvanic corrosion of copper in aqueous sulphide solutions containing chloride. Corrosion Science 114, 72–78.

Chen J, Qin Z, Martino T, Guo M, Shoesmith D W, 2018. Copper transport and sulphide sequestration during copper corrosion in anaerobic aqueous sulphide solutions. Corrosion Science 131, 245–251.

Chen J, Guo M, Martino T, Ramamurthy S, Noël J J, Shoesmith D, Lilja C, Johansson A J, 2019. The distribution of corrosion damage to copper surfaces exposed to aqueous sulphide solutions. SKBdoc 1706406 ver 1.0, Svensk Kärnbränslehantering AB.

Chen S, Wang P, Zhang D, 2014. Corrosion behaviour of copper under biofilm of sulfate reducing bacteria. Corrosion Science 87, 407–415.

Christensen H, Bjergbakke E, 1982. Radiolysis of groundwater from HLW stored in copper canisters. SKBF/KBS TR 82-02, Svensk Kärnbränslehantering AB.

Christensen H, Bjergbakke E, 1984. Radiolysis of cozncrete. SKBF/KBS TR 84-02, Svensk Kärnbränslehantering AB.

Clarens F, Serrano-Purroy D, Martínez-Esparza A, Wegan D, Gonzalez-Robles E, de Pablo J, Casas I, Giménez J, Christiansen B, Glatz J-P, 2008. RN fractional release of high burn-up fuel: effect of HBS and estimation of accessible grain boundary. In Lee W E, Roberts J W, Hyatt N C, Grimes R W (eds). Scientific Basis for Nuclear Waste Management XXXI. Warrendale, PA: Materials Research Society. (Materials Research Society Symposium Proceedings 1107), 439–446.

Clavier N, Szenknect S, Costin D T, Mesbah A, Ravaux J, Poinssot C, Dacheux N, 2013. Purification of uranothorite solid solutions from polyphase systems, Journal of Nuclear Materials 441, 73–83.

Cliffe K A, Kelly M, 2006. COMP23 version 1.2.2. User's manual. SKB R-04-64, Svensk Kärnbränslehantering AB.

Cramer J, Smellie J (eds), 1994. Final report of the AECL/SKB Cigar Lake analog study. SKB TR 94-04, Svensk Kärnbränslehantering AB.

Cross M M, Manning D A C, Bottrell S H, Worden R H, 2004. Thermochemical sulphate reduction (TSR): experimental determination of reaction kinetics and implications of the observed reaction rates for petroleum reservoirs. Organic Geochemistry 35, 393–404.

Cui D, Spahiu K, 2002. The reduction of U(VI) on corroded iron under anoxic conditions. Radiochimica Acta 90, 623–628.

Cui D, Low J, Sjöstedt C J, Spahiu K, 2004. On Mo-Ru-Tc-Pd-Rh-Te alloy particles extracted from spent fuel and their leaching behavior under Ar and H_2 atmospheres. Radiochimica Acta 92, 551–555.

Cui D, Ekeroth E, Fors P, Spahiu K, 2008. Surface mediated processes in the interaction of spent fuel or α-doped UO_2 with H_2. In Shuh D K, Chung B W, Albrecht-Schmitt T, Gouder T, Thompson J D (eds). Actinides 2008 – basic science, applications and technology. Warrendale, PA: Materials Research Society. (Materials Research Society Symposium Proceedings 1104), 87–99.

Curti E, Kulik D A, 2020. Oxygen potential calculations for conventional and Cr-doped UO_2 fuels based on solid solution thermodynamics. Journal of Nuclear Materials 534, 152140.

Curti E, Puranen A, Grolimund D, Jädernas D, Sheptyakova D, Mesbah A, 2015. Characterization of selenium in UO_2 spent nuclear fuel by micro X-ray absorption spectroscopy and its thermodynamic stability. Environmental Science: Processes & Impacts 17, 1760–1768.

Cushman A S, Gardner H A, 1910. The corrosion and preservation of iron and steel. New York: McGraw-Hill.

Desgranges L, Ripert M, Piron J P, Kodja H, Gallier J P, 2003. Behaviour of fission gases in an irradiated nuclear fuel under α external irradiation. Journal of Nuclear Materials 321, 324–330.

Dillmann P, Neff D, Féron D, 2014. Archaeological analogues and corrosion prediction: from past to future. A review. Corrosion Engineering, Science and Technology 49, 567–576.

Dillström P, 2014. Probabilistic analysis of BWR canister inserts for spent nuclear fuel in the case of an earthquake induced rock shear load. Inspecta Technical Report 50014130-1, Revision 5. SKBdoc 1412158 ver 1.0, Svensk Kärnbränslehantering AB.

Dillström P, 2015. Damage tolerance analysis of BWR-canister inserts for spent nuclear fuel in the case of an earthquake induced rock shear load – Influence of using more detailed models. Report 5000264-1, Revision 2, Inspecta Technology AB. SKBdoc 1450913 ver 1.0, Svensk Kärnbränslehantering AB.

Dillström P, Bolinder T, 2010. Damage tolerance analysis of canister inserts for spent nuclear fuel in the case of an earthquake induced rock shear load. SKB TR-10-29, Svensk Kärnbränslehantering AB.

Dillström P, Manngård T, 2017. Probabilistic analysis of BWR canister inserts for spent nuclear fuel in the case of an isostatic pressure load. Report 5001090-1, Revision 4, Inspecta Technology AB. SKBdoc 1585534 ver 1.0, Svensk Kärnbränslehantering AB.

Dillström P, Alverlind L, Andersson M, 2010. Framtagning av acceptanskriterier samt skadetålighets-analyser av segjärnsinsatsen. SKB R-10-11, Svensk Kärnbränslehantering AB. (In Swedish.)

Doerner H A, Hoskins W M, 1925. Co-precipitation of radium and barium sulphates. Journal of the American Chemical Society 47, 662–675.

Dong C, Mao F, Gao S, Sharifi-Asl S, Lu P, Macdonald D D, 2016. Passivity breakdown on copper: influence of temperature. Journal of The Electrochemical Society 163, C707–C717.

Dou W, Jia R, Jin P, Liu J, Chen S, Gu T, 2018. Investigation of the mechanism and characteristics of copper corrosion by sulfate reducing bacteria. Corrosion Science 144, 237–248.

Dou W, Pu Y, Han X, Song Y, Chen S, Gu T, 2020. Corrosion of Cu by a sulfate reducing bacterium in anaerobic vials with different headspace volumes. Bioelectrochemistry 133, 107478. doi:10.1016/j.bioelechem.2020.107478

Duro L, Grivé M, Cera E, Domenech C, Bruno J, 2006a. Update of a thermodynamic database for radionuclides to assist solubility limits calculation for performance assessment. SKB TR-06-17, Svensk Kärnbränslehantering AB.

Duro L, Grivé M, Cera E, Gaona X, Domènech C, Bruno J, 2006b. Determination and assessment of the concentration limits to be used in SR-Can. SKB TR-06-32, Svensk Kärnbränslehantering AB.

Edwards M, Ferguson J F, Reiber S H, 1994. The pitting corrosion of copper. Journal of American Water Works Association 86, 74–90.

Ekeroth E, Low J, Zwicky H-U, Spahiu K, 2009. Corrosion studies with high burnup LWR fuel in simulated groundwater. In Hyatt N C, Pickett D A, Rebak R B (eds). Scientific Basis for Nuclear Waste Management XXXII. Warrendale, PA: Materials Research Society. (Materials Research Society Symposium Proceedings 1124), Q02–07.

Ekeroth E, Granfors M, Schild D, Spahiu K, 2020. The effect of temperature and fuel surface area on spent nuclear fuel dissolution kinetics under H_2 atmosphere. Journal of Nuclear Materials 531, 151981. doi:10.1016/j.jnucmat.2019.151981

EN 1563:1997. Founding. Spheroidal graphite cast iron. Brussels: European Committee for Standardization.

EN 1976:1988. Copper and copper alloys. Cast unwrought copper products. Brussels: European Committee for Standardization.

Eriksen T, Jonsson M, 2007. The effect of hydrogen on dissolution of spent fuel in 0.01 mol × dm^{-3} $NaHCO_3$ solution. SKB TR-07-06, Svensk Kärnbränslehantering AB.

Eriksen T E, Ndalamba P, Grenthe I, 1989. On the corrosion of copper in pure water. Corrosion Science 29, 1241–1250.

Eriksen T E, Jonsson M, Merino J, 2008. Modelling time resolved and long contact time dissolution studies of spent nuclear fuel in 10 mM carbonate solution: a comparison between two different models and experimental data. Journal of Nuclear Materials 375, 331–339.

Eriksen T E, Shoesmith D W, Jonsson M, 2012. Radiation induced dissolution of UO_2 based nuclear fuel – A critical review of predictive modelling approaches. Journal of Nuclear Materials 420, 409–423.

Evans U R, Miley H A, 1937. Measurements of oxide films on copper and iron. Nature 139, 282–283.

Evins L Z, 2013a. Treatment of silver in solubility calculations. SKBdoc 1396561 ver 1.0, Svensk Kärnbränslehantering AB.

Evins L Z, 2013b. Treatment of redox in SR-Site solubility calulations. SKBdoc 1396559 ver 1.0, Svensk Kärnbränslehantering AB.

Evins L Z, 2020. On the barrier function of spent fuel cladding. SKBdoc 1912057 ver 1.0, Svensk Kärnbränslehantering AB.

Evins L Z, Hedin A, 2020. Failed fuel and their potential contribution to risk calculated in the post-closure safety for the spent nuclear fuel repository. SKBdoc 1872793 ver 1.0, Svensk Kärnbränslehantering AB.

Evins L Z, Jensen K A, 2012. Review of spatial relations between uraninite and coffinite – implications for alteration mechanisms. MRS Online Proceedings Library Archive, 1475 doi:10.1557/opl.2012.559

Evins L Z, Jensen K A, Ewing R C, 2005. Uraninite recrystallization and Pb loss in the Oklo and Bangombé natural fission reactors, Gabon. Geochimica et Cosmochimica Acta 69, 1589–1606.

Evins L Z, Juhola P, Vähänen M, 2014. REDUPP Final report. Posiva Working Report 2014-12. Posiva Oy, Finland.

Evins L Z, Bosbach D, Duro L, Farnan I, Metz V, Riba O, 2022. Final Scientific Report. Deliverable D1.26, DisCo project, (Grant Agreement 755443), Euratom Research and Training Programme on Nuclear Energy, Horizon 2020 Framework Programme, European Commission. Availabe at: https://cordis.europa.eu/project/id/755443/results

Fernández A M, Sánchez-Ledesma D M, Melón A, Robredo L M, Rey J J, Labajo M, Clavero M A, Carretero S, González A E, 2018. Thermo-hydro-geochemical behaviour of a Spanish bentonite after of the FEBEX in situ test at the Grimsel Test Site. Technical report CIEMAT/DMA/2G216/03/16. Nagra Arbeitsbericht NAB 16–25, Nagra, Switzerland.

Ferry C, Poinssot C, Broudic V, Cappelaere C, Desgranges L, Garcia P, Jégou C, Lovera P, Marimbeau A, Piron J P, Poulesquen A, Roudil D, Gras J M, Bouffioux P, 2005. Synthesis on the spent fuel long term evolution. Report CEA-R-6084, Commissariat à l'Énergie Atomique.

Ferry C, Piron J-P, Poulesquen A, Poinssot C, 2008. Radionuclides release from spent fuel under disposal conditions: re-evaluation of the Instant Release Fraction. In Lee W E, Roberts J W, Hyatt N C, Grimes R W (eds). Scientific Basis for Nuclear Waste Management XXXI. Warrendale, PA: Materials Research Society. (Materials Research Society Symposium Proceedings 1107), 447–454.

Ferry C, Piron J-P, Ambard A, 2010. Effect of helium on the microstructure of spent fuel in the repository. Journal of Nuclear Materials 407, 100–109.

Ferry C, Radwan J, Palancher H, 2016. Review about the effect of He on the microstructure of spent nuclear fuel in a repository. MRS Advances 1, 4147–4156.

Fidalgo A, Roth O, Puranen A, Evins L, Spahiu K, 2020. Aqueous leaching of ADOPT and standard UO_2 spent nuclear fuel under H_2 atmosphere. MRS Advances 5, 167–175.

Finch R, Murakami T, 1999. Systematics and paragenesis of uranium minerals. Reviews in Mineralogy and Geochemistry 38, 91–179.

Fors P, Carbol P, Van Winkel S, Spahiu K, 2008. High burn-up UO_2 fuel corrosion under reducing conditions. In Proceedings of the 12th International High-Level Waste Management Conference. Las Vegas, Nevada, 7–11 September 2008. New York: American Nuclear Society, 380–387.

Forsström A, 2019. Localized deformation in spent nuclear fuel disposal canisters. PhD thesis. Aalto University, Finland. (Also published as Forsström A, Yagodzinskyy Y, Hänninen H, 2019. Hydrogen effects on mechanical performance of nodular cast iron. Corrosion Reviews 37, 441–454.

Forsström A, Becker R, Öijerholm J, Yagodzinskyy Y, Hänninen H, Linder J, 2017. Hydrogen absorption in copper as a result of corrosion reactions in sulphide and chloride containing deoxygenated water at 90 °C in simulated spent nuclear fuel repository conditions. In Proceedings of EUROCORR, 2017, The Annual Congress of the European Federation of Corrosion, 20th International Corrosion Congress and Process Safety Congress, Prague, Czechia, 3–7 September 2017.

Forsström A, Yagodzinskyy Y, Hänninen H, 2019. Hydrogen effects on mechanical performance of nodular cast iron. Corrosion Reviews 37, 441–454.

Forsström A, Becker R, Hänninen H, Yagodzinskyy Y, Heikkilä M, 2021. Sulphide-induced stress corrosion cracking and hydrogen absorption of copper in deoxygenated water at 90 °C. Materials and Corrosion 72, 317–332.

Forsyth R, 1995. Spent nuclear fuel. A review of properties of possible relevance to corrosion processes. SKB TR 95-23, Svensk Kärnbränslehantering AB.

Forsyth R, 1997. The SKB Spent Fuel Corrosion Programme. An evaluation of results from the experimental programme performed in the Studsvik Hot Cell laboratory. SKB TR 97-25, Svensk Kärnbränslehantering AB.

Forsyth R S, Werme L O, 1992. Spent fuel corrosion and dissolution. Journal of Nuclear Materials 190, 3–19.

Forsyth R S, Mattsson O, Schrire D, 1988. Fission product concentration profiles (Sr, Xe, Cs and Nd) at the individual grain level in power-ramped LWR fuel. SKB TR 88-24, Svensk Kärnbränslehantering AB.

Forsyth R S, Eklund U-B, Werme L O, 1994. A study of fission product migration and selective leaching by means of a power-bump test. In Barkatt A, Van Konynenburg R (eds). Scientific Basis for Nuclear Waste Management XVII. Pittsburgh, PA: Materials Research Society. (Materials Research Society Symposium Proceedings 333), 385–390.

Fuchs L H, Hoekstra H R, 1959. The preparation and properties of uranium (IV) silicate. American Mineralogist 44, 1057–1063.

Galvele J R, 1987. A stress corrosion cracking mechanism based on surface mobility. Corrosion Science 27, 1–33.

Gamsjäger H, Bugajski J, Gajda T, Lemire R J, Preis W, 2005. Chemical thermodynamics. Vol. 6. Chemical thermodynamics of nickel. Amsterdam: Elsevier.

Gamsjäger H, Gajda T, Sangster J, Saxena S K, Voigt W, 2012. Chemical thermodynamics of tin. Paris: Nuclear Energy Agency, OECD.

Ganchenkova M G, Yagodzinskyy Y N, Borodin V A, Hänninen H, 2014. Effects of hydrogen and impurities on void nucleation in copper: Simulation point of view. Philosophical Magazine 94, 3522–3548.

Gdowski G E, Bullen D B, 1988. Survey of degradation modes of candidate materials for high-level radioactive-waste disposal containers. Vol 2, Oxidation and corrosion. Report UCID-21362, Lawrence Livermore National Laboratory, University of California.

Giroud N, 2014. FEBEX – Assessment of Redox Conditions in Phase 2 before Dismantling. NAB 14-55, Nagra, Switzerland.

Giroud N, Tomonaga Y, Wersin P, Briggs S, King F, Vogt T, Diomidis N, 2018. On the fate of oxygen in a spent fuel emplacement drift in Opalinus Clay, Applied Geochemistry 97, 270–278.

Glass R S, Van Konynenburg R A, Overturf G E, 1986. Corrosion processes of austenitic stainless steels and copper-based materials in gamma-irradiated aqueous environments. In Proceedings of Corrosion/86, Houston, TX, 17–21 March 1986. Paper 258.

Goldschmidt B, 1940. Étude du fractionnement par crystallisation mixte à l'aide des radioéléments. Annales de Chimie, Serie XI, 13, 88–174. (In French.)

Goldstein T P, Aizenshtat Z, 1994. Thermochemical sulfate reduction: a review. Journal of Thermal Analysis and Calorimetry 42, 241–290.

Gordon A, Sjögren L, Taxén C, Johansson A J, 2017. Post-test examination of packages 4 and 5 of the MiniCan field experiment. SKB TR-16-12, Svensk Kärnbränslehantering AB.

Gordon A, Johansson J, Pahverk H, Börjesson E, Sjögren L, 2018a. Corrosion morphology of copper in anoxic sulphide environments. SKB TR-18-14, Svensk Kärnbränslehantering AB.

Gordon A, Pahverk H, Börjesson E, Johansson A J, 2018b. Examination of copper corrosion specimens from ABM 45, package 5. SKB TR-18-17, Svensk Kärnbränslehantering AB.

Grambow B, Loida A, Dressler P, Geckeis H, Gago J, Casas I, de Pablo J, Gimenez J, Torrero M E, 1996. Long-term safety of radioactive waste disposal: chemical reaction of fabricated and high burnup spent UO_2 fuel with saline brines. Final report. Wissenschaftliche Berichte FZKA 5702, Forschungszentrum Karlsruhe.

Grambow B, Loida A, Martínez-Esparza A, Díaz-Arocas P, de Pablo J, Paul J-L, Marx G, Glatz J-P, Lemmens K, Ollila K, Christensen H, 2000. Source term for performance assessment of spent fuel as a waste form. EUR 19140, European Commission.

Grandia F, 2013. Reply to comments and questions from SSM concerning Ba-Ra sulphate co-precipitation in canister. SKBdoc 1416537 ver 1.0, Svensk Kärnbränslehantering AB.

Grandia F, Merino J, Bruno J, 2008. Assessment of the radium-barium co-precipitation and its potential influence on the solubility of Ra in the near-field. SKB TR-08-07, Svensk Kärnbränslehantering AB.

Granfors M, 2017. Round-robin of hydrogen content in copper determined by melt extraction and gas analysis. SKB R-17-15, Svensk Kärnbränslehantering AB.

Gras J-M, 2014. State of the art of ^{14}C in Zircaloy and Zr alloys-^{14}C release from zirconium alloy hulls (D 3.1) Deliverable in the FP7 European project CAST.

Grauer R, 1990. The reducibility of sulphuric acid and sulphate in aqueous solution (translated from German). SKB TR 91-39, Svensk Kärnbränslehantering AB.

Gray W J, 1999. Inventories of iodine-129 and cesium-137 in the gaps and grain boundaries of LWR spent fuels. In Wronkiewicz D J, Lee J H (eds). Scientific Basis for Nuclear Waste Management XXII. Warrendale, PA: Materials Research Society. (Materials Research Society Symposium Proceedings 556), 487–494.

Gray W J, Strachan D M, Wilson C N, 1992. Gap and grain boundary inventories of Cs, Tc and Sr in spent LWR fuel. In Sombret C G (ed). Scientific Basis for Nuclear Waste Management XV. Warrendale, PA: Materials Research Society. (Materials Research Society Symposium Proceedings 257), 353–360.

Grenthe I, Fuger J, Konings R J M, Lemire R, Muller A B, Nguen-Trung C, Wanner H, 1992. Chemical thermodynamics. Vol. 1. Chemical thermodynamics of uranium. Amsterdam: Elsevier.

Grenthe I, Gaona X, Plyasunov A V, Rao L, Runde H, Grambow B, Konings R J M, Smith A L, Moore E E, 2020. Second update of the chemical thermodynamics of U, Np, Pu, Am and Tc. Chemical thermodynamics. Vol. 14. Boulogne-Billancourt: Nuclear Energy Agency, OECD.

Grigoriev V, 1996. Hydrogen embrittlement of zirconium alloys. Report STUDSVIK/M-96/73, Studsvik Material AB.

Grivé M, Domènech C, Montoya V, Garcia D, Duro L, 2010a. Simple Functions Spreadsheet tool presentation. SKB TR-10-61, Svensk Kärnbränslehantering AB.

Grivé M, Domènech C, Montoya V, Garcia D, Duro L, 2010b. Determination and assessment of the concentration limits to be used in SR-Can. Supplement to TR-06-32. SKB R-10-50, Svensk Kärnbränslehantering AB.

Grivé M, García D. Campos I, Idiart A, Duro L, 2013a. Simple Functions Spreadsheet tool: Phosphates update and Temperature assessment. Amphos21 Final report. SKBdoc 1415884 ver 1.0, Svensk Kärnbränslehantering AB.

Grivé M, Idiart A, Colàs E, Duro L, 2013b. Handling of uncertainty in thermodynamic data. Amphos21 Final report. SKBdoc 1396560 ver 1.0, Svensk Kärnbränslehantering AB.

Gubner R, Andersson U, 2007. Corrosion resistance of copper canister weld material. SKB TR-07-07, Svensk Kärnbränslehantering AB.

Gubner R, Andersson U, Linder M, Nazarov A, Taxén C, 2006. Grain boundary corrosion of copper canister weld material. SKB TR-06-01, Svensk Kärnbränslehantering AB.

Guilbert S, Sauvage T, Erramli H, Barthe M-F, Desgardin P Blondiaux G, Corbel C, Piron J P, 2003. Helium behavior in UO_2 polycrystalline disks. Journal of Nuclear Materials 321, 121–128.

Guillaumont R, Fanghänel T, Fuger J, Grenthe I, Neck V, Palmer D A, Rand M H, 2003. Chemical thermodynamics. Vol. 5. Update on the chemical thermodynamics of uranium, neptunium, plutonium, americium and technetium. Amsterdam: Elsevier.

Guinan M W, 2001. Radiation effects in spent nuclear fuel canisters. SKB TR-01-32, Svensk Kärnbränslehantering AB.

Guo M, Chen J, Martino T, Biesinger M, Noël J J, Shoesmith D W, 2019. The susceptibility of copper to pitting corrosion in borate-buffered aqueous solutions containing chloride and sulfide. Journal of The Electrochemical Society 166, C550–C558.

Guo M, Chen J, Lilja C, Dehnavi V, Behazin M, Noël J J, Shoesmith D W, 2020. The anodic formation of sulfide and oxide films on copper in borate-buffered aqueous chloride solutions containing sulphide. Electrochimica Acta 362, 137087. doi:10.1016/j.electacta.2020.137087

Guo X, Szenknect S, Mesbah A, Clavier N, Poinssot C, Ushakov S V, Curtius H, Bosbach D, Ewing R C, Burns P C, Dacheux N, 2015. Thermodynamics of formation of coffinite, $USiO_4$. Proceedings of the National Academy of Sciences 112, 6551–6555.

Hahn O, 1936. Applied radiochemistry. Ithaca, NY: Cornell University Press.

Hallbeck L, Pedersen K, 2008. Explorative analysis of microbes, colloids and gases. SDM-Site Forsmark. SKB R-08-85, Svensk Kärnbränslehantering AB.

Hallbeck L, Johansson L, Edlund J, Pedersen K, 2017. Microbial analyses of groundwater, bentonite and surfaces, post-test analysis of packages 4 (A05) and 5 (A06), retrieved from the MiniCan experiment at Äspö laboratory. SKB TR-16-13, Svensk Kärnbränslehantering AB.

Hallberg R O, Engvall A-G, Wadsten T, 1984. Corrosion of copper lightning conductor plates. British Corrosion Journal 19, 85–88.

Hallberg R O, Östlund P, Wadsten T, 1988. Inferences from a corrosion study of a bronze cannon, applied to high level nuclear waste disposal. Applied Geochemistry 3, 273–280.

Halldin Stenlid J, Campos dos Santos E, Bagger A, Johansson A J, Rossmeisl J, Pettersson L G M, 2020a. Electrochemical interface during corrosion of copper in anoxic sulfide-containing groundwater – A computational study. The Journal of Physical Chemistry C 124, 469−481.

Halldin Stenlid J, Campos dos Santos E, Arán-Ais R M, Bagger A, Johansson A J, Cuenya B R, Rossmeisl J, Pettersson L G M, 2020b. Uncovering the electrochemical interface of low-index copper surfaces in deep groundwater environments. Electrochimica Acta 362, 137111. doi:10.1016/j.electacta.2020.137111

Halldin Stenlid J, Campos dos Santos E, Johansson A J, Pettersson L G M, 2021. Properties of interfaces between copper and copper sulphide/oxide films. Corrosion Science 183, 109313. doi:10.1016/j.corsci.2021.109313

Hanson B, 2008. Examining the conservatisms in dissolution rates of commercial spent nuclear fuel. In Proceedings of the 12th International High-Level Waste Management Conference. Las Vegas, Nevada, 7–11 September 2008. New York: American Nuclear Society, 404–411.

Hanson B D, Stout R B, 2004. Reexamining the dissolution of spent fuel: a comparison of different methods for calculating rates. In Hanchar J M, Stroes-Gascoyne S, Browning L (eds). Scientific Basis for Nuclear Waste Management XXVIII. Warrendale, PA: Materials Research Society. (Materials Research Society Symposium Proceedings 824), 89–94.

Hanson B D, Friese J I, Soderquist C Z, 2004. Initial results from dissolution testing of spent fuel under acidic conditions. In Hanchar J M, Stroes-Gascoyne S, Browning L (eds). Scientific Basis for Nuclear Waste Management XXVIII. Warrendale, PA: Materials Research Society. (Materials Research Society Symposium Proceedings 824), 113–118.

Hansson N L, Tam P L, Ekberg C, Spahiu K, 2021. XPS study of external α-radiolytic oxidation of UO_2 in the presence of argon or hydrogen. Journal of Nuclear Materials 543, 152604.

Harrington J F, Birchall D J, 2007. Sensitivity of total stress to changes in externally applied water pressure in KBS-3 buffer bentonite. SKB TR-06-38, Svensk Kärnbränslehantering AB.

He H, Keech P G, Broczkowski M E, Noël J J, Shoesmith D W, 2007. Characterization of the influence of fission product doping on the anodic reactivity of uranium dioxide. Canadian Journal of Chemistry 85, 702–713.

He M, Jiang S, Jiang S, Chen Q, Qin J, Wu S, Dong Y, Zhao Z, 2000. Measurement of ^{79}Se and ^{64}Cu with PXAMS. Nuclear Instruments and Methods in Physics Research Section B: Beam Interactions with Materials and Atoms 172, 177–181.

He M, Jiang S, Jiang S, Diao L, Wu S, Li C, 2002. Measurements of the half-life of ^{79}Se with PX-AMS. Nuclear Instruments and Methods in Physics Research Section B: Beam Interactions with Materials and Atoms 194, 393–398.

Heberling F, Metz V, Böttle M, Curti E, Geckeis H, 2018. Barite recrystallization in the presence of ^{226}Ra and ^{133}Ba. Geochimica et Cosmochimica Acta 232, 124–139.

Hedin A, 2004. Integrated near-field evolution model for a KBS-3 repository. SKB R-04-36, Svensk Kärnbränslehantering AB.

Hedin A, 2019. Scoping calculations of hydrogen degassing from Cu-OFP. SKBdoc 1716281 ver 1.0, Svensk Kärnbränslehantering AB.

Hedin A, Evins L Z, Spahiu K, 2013. What if criticality in the final repository? SKBdoc 1417199 ver 1.0, Svensk Kärnbränslehantering AB.

Hedin A, Lilja C, Johansson A J, 2017. Copper corrosion in pure water – scientific and post-closure safety aspects. Proceedings of the 16th International High-Level Radioactive Waste Management Conference, Charlotte, NC, 9–13 April 2017. American Nuclear Society.

Hedin A, Johansson A J, Lilja C, Boman M, Berastegui P, Berger R, Ottosson M, 2018. Corrosion of copper in pure O_2-free water? Corrosion Science 137, 1–12.

Hemingway B S, 1982. Thermodynamic properties of selected uranium compounds and aqueous species at 298.15 K and 1 bar and at higher temperatures; preliminary models for the origin of coffinite deposits. Open File Report 82-619, US Geological Survey.

Henshaw J, 1994. Modelling of nitric acid production in the Advanced Cold Process Canister due to irradiation of moist air. SKB TR 94-15, Svensk Kärnbränslehantering AB.

Henshaw J, Spahiu K, 2021. Radiolysis calculations of air, argon and water mixtures in a KBS-3 canister. SKB TR-21-11, Svensk Kärnbränslehantering AB.

Henshaw J, Hoch A, Sharland S M, 1990. Further assessment studies of the Advanced Cold Process Canister. AEA-D&R-0060, AEA Decommissioning & Radwaste.

Hernelind J, 2010. Modelling and analysis of canister and buffer for earthquake induced rock shear and glacial load. SKB TR-10-34, Svensk Kärnbränslehantering AB.

Hernelind J, 2015a. Analysis of creep in the KBS-3 copper canister due to internal and external loads. SKBdoc 1399768 ver 2.0, Svensk Kärnbränslehantering AB.

Hernelind J, 2015b. Detailed models for PWR-canisters for earthquake induced rock shearing. SKBdoc 1439730 ver 1.0, Svensk Kärnbränslehantering AB.

Hernelind J, 2015c. Hydrostatic pressure for detailed BWR/PWR-canisters. SKBdoc 1454226 ver 1.0, Svensk Kärnbränslehantering AB.

Hernelind J, 2017. Effect of changing design criterion for buffer to swelling pressure 10 MPa. SKBdoc 1516736 ver 1.0, Svensk Kärnbränslehantering AB.

Hernelind J, 2019a. Extended canister analyses with emphasis on tensile stresses and uneven swelling pressure. SKBdoc 1614038 ver 1.0, Svensk Kärnbränslehantering AB.

Hernelind J, 2019b. Design parameters effect on tensile stresses for the copper shell. SKBdoc 1707582 ver 2.0, Svensk Kärnbränslehantering AB.

Hernelind J, Börgesson L, 2018. Global analyses to validate buffer properties corresponding to swelling pressures of 3–10 MPa and sensitivity analyses of buffer and steel tube properties. SKBdoc 1550977 ver 1.0, Svensk Kärnbränslehantering AB.

Hocking W H, Duclos A M, Johnson L H, 1994. Study of fission-product segregation in used CANDU fuel by X-ray photoelectron spectroscopy (XPS) II. Journal of Nuclear Materials 209, 1–26.

Hoehn E, Eikenberg J, Fierz T, Drost W, Reichlmayr E, 1998. The Grimsel Migration Experiment: field injection–withdrawal experiments in fractured rock with sorbing tracers. Journal of Contaminant Hydrology 34, 85–106.

Honeycombe R W K, 1968. Creep in pure metals and alloys. In The plastic deformation of metals. London: Arnold, 352–396.

Hua F, Mon K, Pasupathi P, Gordon G, Shoesmith D, 2005. A review of the corrosion of titanium grade 7 and other titanium alloys in nuclear waste repository environments. Corrosion 61, 987–1003.

Hultquist G, 1986. Hydrogen evolution in corrosion of copper. Corrosion Science 26, 173–176.

Hultquist G, Graham M J, Szakalos P, Sproule G I, Rosengren A, Gråsjö L, 2011. Hydrogen gas production during corrosion of copper by water. Corrosion Science 53, 310–319.

Hultquist G, Graham M J, Kodra O, Moisa S, Liu R, Bexell U, Smialek J L, 2015. Corrosion of copper in distilled water without O_2 and the detection of produced hydrogen. Corrosion Science 95, 162–167.

Hummel W, Anderegg G, Puigdomenech I, Rao L, Tochiyama O, 2005. Chemical thermodynamics of compounds and complexes of U, Np, Pu, Am, Tc, Se, Ni and Zr with selected organic ligands. Paris: Nuclear Energy Agency, OECD.

Huotilainen C, Saario T, Toivonen A, 2018. Review of the Aaltonen-mechanism. SKB R-18-03, Svensk Kärnbränslehantering AB.

Huttunen-Saarivirta E, Rajala P, Carpén L, 2016. Corrosion behaviour of copper under biotic and abiotic conditions in anoxic ground water: electrochemical study. Electrochimica Acta 203, 350–365.

Huttunen-Saarivirta E, Rajala P, Bomberg M, Carpén L, 2017. EIS study on aerobic corrosion of copper in ground water: influence ofmicro-organisms. Electrochimica Acta 240, 163–174.

Huttunen-Saarivirta E, Ghanbari E, Mao F, Rajala P, Carpén L, Macdonald D, 2018. Kinetic properties of the passive film on copper in the presence of sulfate-reducing bacteria. Journal of The Electrochemical Society 165, C450–C460.

Huttunen-Saarivirta E, Rajala P, Carpén L, Wang J, Liu F, Ghanbari E, Mao F, Dong C, Yang J, Sarifi-Asl S, Macdonald D D, 2019a. Response to Comments on E. Huttunen-Saarivirtaet al. "Kinetic Properties of the Passive Film on Copper in the Presence of Sulfate-Reducing Bacteria" [J. Electrochem. Soc., 165, C450 (2018)]. Journal of The Electrochemical Society 166, Y17–Y26.

Huttunen-Saarivirta E, Ghanbari E, Mao F, Rajala P, Carpén L, Macdonald D D, 2019b. Erratum: Kinetic properties of the passive film on copper in the presence of sulfate-reducing bacteria" [J. Electrochem. Soc., 165, C450 (2018)]. Journal of The Electrochemical Society 166, X5–X5.

Håkansson R, 2000. Beräkning av nuklidinnehåll, resteffekt, aktivitet samt doshastighet för utbränt kärnbränsle. SKB R-99-74, Svensk Kärnbränslehantering AB. (In Swedish.)

Håkansson L, Lundgren K, 2009. Källstyrkor för bränsleelement under driftskede för Clink, slutförvarsanläggning och slutförvar. Rapport 06-0038R, Rev. 3. Alara Engineering. SKBdoc 1198314 ver 1.0, Svensk Kärnbränslehantering AB.

Högberg C-J, Karlsson O, Randelius M, Johansson A J, 2017. Surface morphology and elemental composition of copper canisters for disposal of spent nuclear fuel. SKB P-17-11, Svensk Kärnbränslehantering AB.

Hökmark H, Lönnqvist M, Fälth B, 2010. THM-issues in repository rock. Thermal, mechanical, thermo-mechanical and hydro-mechanical evolution of the rock at the Forsmark and Laxemar sites. SKB TR-10-23, Svensk Kärnbränslehantering AB.

IAEA, 2003. Spent fuel performance assessment and research, Final report of the co-ordinated research project SPAR. IAEA-TECDOC-1343, International Atomic Energy Agency.

Ibrahim B, Zagidulin D, Behazin M, Ramamurthy S, Wren J C, Shoesmith D W, 2018. The corrosion of copper in irradiated and unirradiated humid air. Corrosion Science 141, 53–62.

Ikeda B M, Litke C D, 2004. Status report for 2003 on stress corrosion cracking of OFP copper in ammonia. Report 06819-REP-01300-10078-R00, Ontario Power Generation, Nuclear Waste Management Division.

Ikeda B M, Litke C D, 2007. Stress corrosion cracking of copper in nitrite/chloride mixtures at elevated temperatures. NWMO TR-2007-04, Nuclear Waste Management Organization, Canada.

Ikeda B M, Litke C D, 2008. The effect of high chloride concentration on stress corrosion cracking behaviour of copper. NWMO TR-2008-12, Nuclear Waste Management Organization, Canada.

Ikonen K, 2006. Fuel temperature in disposal canisters. Posiva Working Report 2006-19, Posiva Oy, Finland.

Ikonen K, 2020. Temperatures inside SKB and Posiva type disposal canisters for spent fuel. Posiva SKB Report 12, Posiva Oy, Svensk Kärnbränslehantering AB.

Ikonen K, Kuutti J, Raiko H, 2018. Thermal dimensioning for the Olkiluoto Repository – 2018 update. Posiva Working Report 2018-26, Posiva Oy, Finland.

Ikäläinen T, Jäppinen E, Saario T, 2021. Susceptibility of Cu-OFP to SCC by acetate under aerated conditions. Posiva Working Report 2020-21, Posiva Oy, Finland.

Jacobs S, Edwards M, 2000. Sulfide scale catalysis of copper corrosion. Water Research 34, 2798–2808.

Janeczek J, Ewing R C, 1992. Coffinitization – a mechanism for the alteration of UO_2 under reducing conditions. In Sombret C G (ed). Scientific Basis for Nuclear Waste Management XV. Warrendale, PA: Materials Research Society. (Materials Research Society Symposium Proceedings 257), 497–504.

Janeczek J, Ewing R C, Oversby V M, Werme L O, 1996. Uraninite and UO_2 in spent nuclear fuel: a comparison. Journal of Nuclear Materials 238, 121–131.

Jansson P, Renström P, Sarnet J, Sjöland A, 2022. A new methodology for thermal analysis of geological disposal of spent nuclear fuel using integrated simulations of gamma heating and finite element modeling. Annals of Nuclear Energy 172, 109082. doi:10.1016/j.anucene.2022.109082

Jégou C, Peuget S, Broudic V, Roudil D, Deschanels X, Bart J M, 2004. Identification of the mechanism limiting the alteration of clad spent fuel segments in aerated carbonated groundwater. Journal of Nuclear Materials 326, 144–155.

Jégou C, Muzeau B, Brudic V, Poulesquen A, Roudil D, Jorion F, Corbel C, 2005. Effect of alpha radiation on UO_2 surface reactivity in aqueous media. Radiochimica Acta 93, 35–42.

Jiang S, Guo J, Jiang S, Li C, Cui A, He M, Wu S, Li S, 1997. Determination of the half-life of ^{79}Se with the accelerator mass spectrometry technique. Nuclear Instruments and Methods in Physics Research Section B 123, 405–409.

Jin L-Z, Sandström R, 2009. Non-stationary creep simulation with a modified Armstrong-Frederick relation applied to copper canisters. Computational Materials Science 46, 339–346.

Johansson A J, 2019. Corrosion of copper in repository-like field tests: compilation and analysis of data. SKBdoc 1713264 ver 1.0, Svensk Kärnbränslehantering AB.

Johansson A J, Lilja C, Sjögren L, Gordon A, Hallbeck L, Johansson L, 2017. Insights from post-test examination of three packages from the MiniCan test series of coppercast iron canisters for geological disposal of spent nuclear fuel: impact of the presence and density of bentonite clay. Corrosion Engineering, Science and Technology 52, 54–60.

Johansson A J, Svensson D, Gordon A, Pahverk H, Karlsson O, Brask J, Lundholm M, Malmström D, Gustavsson F, 2020. Corrosion of copper after 20 years exposure in the bentonite field tests LOT S2 and A3. SKB TR-20-14, Svensk Kärnbränslehantering AB.

Johansson F, Kierkegaard J, Zetterström P, 2019. Kriticitetsanalys för slutförvaring av använt kärnbränsle. SKBdoc 1605532 ver 1.0, Svensk Kärnbränslehantering AB. (In Swedish.) (Internal report.)

Johansson J, Blom A, Chukharkina A, Pedersen K, 2015. Study of H_2 gas emission in sealed compartments containing copper immersed in O_2-free water. SKB TR-15-03, Svensk Kärnbränslehantering AB.

Johnson L H, McGinnes D F, 2002. Partitioning of radionuclides in Swiss power reactor fuels. Nagra NTB 02-07, Nagra, Switzerland.

Johnson L H, Tait J C, 1997. Release of segregated nuclides from spent fuel. SKB TR 97-18, Svensk Kärnbränslehantering AB.

Johnson L H, LeNeveu D M, King F, Shoesmith D W, Kolar M, Oscarson D W, Sunder S, Onofrei C, Crosthwaite J L, 1996. The disposal of Canada's nuclear fuel waste: a study of postclosure safety of in-room emplacement of used CANDU fuel in copper containers in permeable plutonic rock. Volume 2: vault model. Report AECL-11494-2, COG-96-552-2, Atomic Energy of Canada.

Johnson L H, Poinssot C, Ferry C, Lovera P, 2004. Estimates of the instant release fraction of UO_2 and MOX fuel at $t = 0$. Nagra NTB 04-08, Nagra, Switzerland.

Johnson L, Ferry C, Poinssot C, Lovera P, 2005. Spent fuel radionuclide source-term model for assessing spent fuel performance in geological disposal. Part I: Assessment of the instant release fraction. Journal of Nuclear Materials 346, 56–65.

Johnson L, Gunther-Leopold I, Kobler Waldis J, Linder H P, Low J, Cui D, Ekeroth E, Spahiu K, Evins L Z, 2012. Rapid aqueous release of fission products from high burn-up LWR fuel: Experimental results and correlations with fission gas release. Journal of Nuclear Materials 420, 54−62.

Jones A R, 1959. Radiation–induced reactions in the N_2–O_2–H_2O system. Radiation Research 10, 655–663.

Jonsson M, 2021a. Impact of H_2 and Ar on the production of corrosive species in vapour exposed to gamma irradiation in canisters for spent nuclear fuel. SKB R-21-14, Svensk Kärnbränslehantering AB.

Jonsson M, 2021b. Impact of groundwater constituents on radiation-induced corrosion of copper. SKBdoc 1883483 ver 1.0, Svensk Kärnbränslehantering AB.

Jonsson M, Nielsen F, Roth O, Ekeroth E, Nilsson S, Hossain M M, 2007. Radiation induced spent nuclear fuel dissolution under deep repository conditions. Environmental Science & Technology 41, 7087–7093.

Jonsson M, Emilsson G, Emilsson L, 2018. Mechanical design analysis for the canister. Posiva SKB Report 04, Posiva Oy, Svensk Kärnbränslehantering AB.

Josefsson J, Andersson-Östling H C M, 2019. SSRT testing of Cu. SKB R-18-09, Svensk Kärnbränslehantering AB.

Jörg G, Buhnemann R, Hollas S, Kivel N, Kossert K, Van Winkel S, Gostowski C L, 2010. Preparation of isotopically pure Se-79 and highly precise determination of its half life. Applied Radiation and Isotopes 68, 2339–2351.

Kamimura K, 1992. FP gas release behaviour of high burn-up MOX fuels for thermal reactors. In Fission gas release and fuel rod chemistry related to extended burnup. Proceeding of a Technical Committee Meeting held in Pembroke, Ontario, Canada, 28 April–1 May 1992. IAEA-TECDOC-697, International Atomic Energy Agency, 82–88.

Karnland O, Sandén T, Johannesson L-E, Eriksen T E, Jansson M, Wold S, Pedersen K, Motamedi M, Rosborg B, 2000. Long term test of buffer material. Final report on the pilot parcels. SKB TR-00-22, Svensk Kärnbränslehantering AB.

Karnland O, Olsson S, Dueck A, Birgersson M, Nilsson U, Hernan-Håkansson T, Pedersen K, Nilsson S, Eriksen T E, Rosborg B, 2009. Long term test of buffer material at the Äspö Hard Rock Laboratory, LOT project. Final report on the A2 test parcel. SKB TR-09-29, Svensk Kärnbränslehantering AB.

Kelm M, Bohnert E, 2004. A kinetic model for the radiolysis of chloride brine, its sensitivity against model parameters and a comparison with experiments. FZK Wissenschaftliche Berichte FZKA 6977, Forschungszentrum Karlsruhe.

Kelm M, Bohnert E, 2005. Gamma radiolysis of NaCl brine: effect of dissolved radiolysis gases on the radiolytic yield of long-lived products. Journal of Nuclear Materials 346, 1–4.

Kienzler B, Duro L, Lemmens K, Metz V, de Pablo J, Valls A, Wegen D, Johnson L, Spahiu K, 2017. Summary of the Euratom collaborative project FIRST-Nuclides and conclusions for the safety case. Nuclear Technology 198, 260–276.

King F, 1996. The potential for stress corrosion cracking of copper containers in a Canadian nuclear fuel waste disposal vault. Report AECL-11550, COG-96-94, Atomic Energy of Canada.

King F, 2002. Corrosion of copper in alkaline chloride environments. SKB TR-02-25, Svensk Kärnbränslehantering AB.

King F, 2004. The effect of discontinuities on the corrosion behaviour of copper canisters. SKB TR-04-05, Svensk Kärnbränslehantering AB.

King F, 2010. Stress corrosion cracking of carbon steel used fuel containers in a Canadian deep geological repository in sedimentary rock. NWMO TR-2010-21, Nuclear Waste Management Organization, Canada.

King F, Kolár M, 2000. The copper container corrosion model used in AECL's second case study. 06819-REP-01200-10041-R00, Ontario Power Generation, Nuclear Waste Management Division.

King F, Kolář M, 2019. Copper Sulfide Model (CSM). Model improvements, sensitivity analyses, and results from the Integrated Sulfide Project inter-model comparison exercise. SKB TR-18-08, Svensk Kärnbränslehantering AB.

King F, LeNeveu D, 1992. Prediction of the lifetimes of copper nuclear waste containers. In Proceedings of the Topical Meeting on Nuclear Waste Packaging, Focus '91. Las Vegas, 30 September – 2 October 1991. La Grange Park: American Nuclear Society, 253–261.

King F, Lilja C, 2013. Localised corrosion of copper canisters in bentonite pore water. SKB TR-13-27, Svensk Kärnbränslehantering AB.

King F, Lilja C, 2014. Localised corrosion of copper canisters. Corrosion Engineering and Technology 49, 420–424.

King F, Litke C D, 1987. The corrosion of copper in synthetic groundwater at 150 °C. Part I. The results of short term electrochemical tests. Technical Record TR-428, Atomic Energy of Canada Ltd.

King F, Newman R, 2010. Stress corrosion cracking of copper canisters. SKB TR-10-04, Svensk Kärnbränslehantering AB.

King F, Ahonen L, Taxén C, Vuorinen U, Werme L, 2001. Copper corrosion under expected conditions in a deep geologic repository. SKB TR-01-23, Svensk Kärnbränslehantering AB.

King F, Lilja C, Pedersen K, Pikänen P, Vähänen M, 2010. An update of the state-of-the-art report on the corrosion of copper under expected conditions in a deep geologic repository. SKB TR-10-67, Svensk Kärnbränslehantering AB.

King F, Chen J, Qin Z, Shoesmith D, Lilja C, 2017. Sulphide mass-transport control of the corrosion of copper canisters. Corrosion Engineering, Science and Technology 52, 210−216.

King F, Puigdomenech I, Lilja C, 2021. Effect of high groundwater chloride concentration on the corrosion of copper canisters. Posiva Working Report 2021-10, Posiva Oy, Finland.

Kinnunen P, 2006. Stress corrosion cracking investigation of copper in groundwater with acetate ions. Posiva Working Report 2006-18, Posiva Oy, Finland.

Kinnunen P, Varis P, 2011. Stress corrosion cracking investigation of copper in groundwater with ammonium under potential polarisation. Posiva Working Report 2011-05, Posiva Oy, Finland.

Klinkenberg M, Brandt F, Breuer U, Bosbach D, 2014. Uptake of Ra during the recrystallization of barite: a microscopic and time of flight-secondary ion mass spectrometry study. Environmental Science & Technology 48, 6620−6627.

Knopp R, Neck V, Kim J I, 1999. Solubility, hydrolysis and colloid formation of plutonium(IV). Radiochimica Acta 86, 101–108.

Koerts H C, Wetzer J M, 2001. Literature survey on corrosion of underground metallic structures induced by alternating currents. KEMA Report 40030204-TDP 01-16792A, KEMA, The Netherlands.

Kolár M, King F, 1996. Modelling the consumption of oxygen by container corrosion and reaction with Fe(II). In Murphy W M, Knecht D (eds). Scientific Basis for Nuclear Waste Management XIX. Warrendale, PA: Materials Research Society. (Materials Research Society Symposium Proceedings 412), 547–554.

Kong D, Dong C, Wei X, Man C, Lei X, Mao F, Li X, 2018. Size matching effect between anion vacancies and halide ions in passive film breakdown on copper. Electrochimica Acta 292, 817–827.

Konings R J M, Plyasunov A, 2016. Comment on ‘‘First experimental determination of the solubility constant of coffinite”[Geochim. Cosmochim. Acta 181 (2016) 36–53]. Geochimica et Cosmochimica Acta 212, 372–373.

Korzhavyi P, Gorbatov O, Selleby M, 2018. Precipitation of late blooming phases in iron-based Alloys. Theoretical modelling. SKB R-16-07, Svensk Kärnbränslehantering AB.

Korzhavyi P A, Sandström R, 2014. Monovacancy in copper: Trapping efficiency for hydrogen and oxygen impurities. Computational Materials Science 84, 122–128.

Korzhavyi P A, Soroka I L, Isaev E I, Lilja C, Johansson B, 2012. Exploring monovalent copper compounds with oxygen and hydrogen. PNAS 109, 686–689.

Kosec T, Hren M, Andraž Legat A, 2017. Monitoring copper corrosion in bentonite by means of a coupled multi-electrode array. Corrosion Engineering, Science and Technology 52, sup1, 70–77.

Kristiansen P T, Massel F, Werme L, Lilja C, Duda L C, 2015. Sulfidation of singlephase oxide on copper and as powder studied using soft X-ray spectroscopy. Journal of The Electrochemical Society 162, C785–C791.

Kursten B, Smailos E, Azkarate I, Werme L, Smart N R, Marx G, Cuñado M A, Santarini G, 2004. COBECOMA. State-of-the-art document on the corrosion behaviour of container materials. Final report. Brussels: European Commission.

Landolt D, 2007. Corrosion and surface chemistry of metals. Lausanne, Switzerland: EPFL Press.

Langmuir D, 1978. Uranium solution-mineral equilibria at low temperatures with applications to sedimentary ore deposits. Geochimica et Cosmochimica Acta 42, 547–569.

Langmuir D, Chatham J R, 1980. Groundwater prospecting for sandstone-type uranium deposits: a preliminary comparison of the merits of mineral-solution equilibria, and single tracer methods. Journal of Geochemical Exploration 13, 201–219.

Larson F R, Miller J, 1952. A time-temperature relationshop for rupture and creep stresses. Transactions of ASME 74, 765–775.

Leijon G, Ahlström J, Andersson-Östling H C M, 2018. In situ hydrogen charging of OFP copper during creep. SKB R-17-17, Svensk Kärnbränslehantering AB.

Lemire R J, Fuger J, Nitsche H, Potter P, Rand M H, Rydberg J, Spahiu K, Sullivan J C, Ullman W J, Vitorge P, Wanner H, 2001. Chemical thermodynamics. Vol. 4. Chemical thermodynamics of neptunium and plutonium. Amsterdam: Elsevier.

Lemire R J, Berner U, Musicas C, Palmer D A, Taylor P, Tochiyama O, 2013. Chemical thermodynamics of of iron, Part 1. Paris: Nuclear Energy Agency, OECD.

Lemmens K, E. Gonzalez-Robles E, Kienzler B, Curti E, Serrano-Purroy D, Sureda R, Martínez-Torrents A, Roth O, Slonszki E, Mennecart T, Günther-Leopold, Hozer Z, 2017. Instant release of fission products in leaching experimentswith high burnup nuclear fuels in the framework of the Euratom project FIRST- Nuclides. Journal of Nuclear Materials 484, 307–323.

Leygraf C, 2002. Atmospheric corrosion. In Marcus P (ed). Corrosion mechanisms in theory and practice. 2nd ed. New York: Marcel Dekker, 529–562.

Leygraf C, Graedel T E, 2000. Atmospheric corrosion. New York: Wiley.

Li W, Li D Y, 2005. Variations of work function and corrosion behaviors of deformed copper surfaces. Applied Surface Science 240, 388–395.

Li Y, 2015. Ab initio based modeling of defects and disorder in industrial materials. PhD thesis. Royal Institute of Technology, Stockholm, Sweden.

Li Y, Korzhavyi P A, 2015. Interactions of point defects with stacking faults in oxygen-free phosphorus-containing copper. Journal of Nuclear Materials 462, 160–164.

Li Y, Lousada C M, Soroka I I, Korzhavyi P A, 2015. Bond network topology and antiferroelectric order in cuprice CuOH. Inorganic Chemistry 54, 8969–8977.

Li Y, Korzhavyi P, Sandström R, Lilja C, 2017. Impurity effects on the grain boundary cohesion in copper. Physical Review Materials 1, 070602(R). doi:10.1103/PhysRevMaterials.1.070602

Lilja C, 2012a. Inre övertryck i kapseln. SKBdoc 1333208 ver 2.0, Svensk Kärnbränslehantering AB. (In Swedish.)

Lilja C, 2012b. Svar på begäran om kompletteringar angående kapselfrågor. SKBdoc 1333256 ver 2.0, Svensk Kärnbränslehantering AB. (In Swedish.)

Lilja C, 2013. Influence of high chloride concentration on copper corrosion. SKBdoc 1398014 ver 1.0, Svensk Kärnbränslehantering AB.

Lilja C, Johansson J, 2014. Svar till SSM på begäran om komplettering avseende degraderingsprocesser för kapseln. SKBdoc 1398013 ver 4.0, Svensk Kärnbränslehantering AB. (In Swedish.)

Lilja C, King F, Puigdomenech I, Pastina B, 2021. Speciation of copper in high chloride concentrations, in the context of corrosion of copper canisters. Materials and Corrosion 72, 293–299.

Litke C D, Ikeda B M, 2006. The effect of acetate concentration, chloride concentration and applied current on stress corrosion cracking of OFP copper. Report 06819-REP-01300-10005, Ontario Power Generation, Nuclear Waste Management Division.

Litke C D, Ikeda B M, 2008. The stress corrosion cracking behaviour of copper in acetate solutions. NWMO TR-2008-21, Nuclear Waste Management Organization, Canada.

Litke C D, Ikeda B M, 2011. Status report on the stress corrosion cracking behaviour of OFP copper in nitrite and ammonia solutions. NWMO TR-2011-06, Nuclear Waste Management Organization, Canada.

Litke C D, Ryan S R, King F, 1992. A mechanistic study of the uniform corrosion of copper in compacted clay-sand soil. AECL-10397, COG-91-304, Atomic Energy of Canada Ltd.

Liu N, Zack Qin Z, Noel J J, Shoesmith D W, 2017. Modelling the radiolytic corrosion of α-doped UO_2 and spent nuclear fuel. Journal of Nuclear Materials 494, 87–94.

Loida A, Grambow B, Geckeis H, 1996. Anoxic corrosion of various high burnup spent fuel samples. Journal of Nuclear Materials 238, 11–22.

Lousada C M, Korzhavyi P A, 2020a. Segregation of P and S impurities to a Σ9 grain boundary in Cu. Metals 10, 1362. doi:10.3390/met10101362

Lousada C M, Korzhavyi P A, 2020b. Hydrogen sorption capacity of crystal lattice defects and low Miller index surfaces of copper. Journal of Materials Science 55, 6623–6636.

Lousada C, Trummer M, Jonsson M, 2013. Reactivity of H_2O_2 towards different UO_2-based materials: The relative impact of radiolysis products revisited. Journal of Nuclear Materials 434, 434–439.

Lousada C M, Johansson A J, Korzhavyi P, 2015. Thermodynamics of H_2O splitting and H_2formation at the Cu(110)–water interface. The Journal of Physical Chemistry C 119, 14102–14113.

Lousada C M, Soroka I L, Yagodzinskyy Y, Tarakina N V, Todoshchenko O, Hänninen H, Korzhavyi P A, Jonsson M, 2016. Gamma radiation induces hydrogen absorption by copper in water. Nature Scientific Reports 6, 24234. doi:10.1038/srep24234

Lovera P, Ferry C, Poinssot C, Johnson L, 2003. Synthesis report on the relevant diffusion coefficients of fission products and helium in spent nuclear fuels. Report CEA-R-6039, Commisariat à l'Énergie Atomique.

Lucey V F, 1967. Mechanisms of pitting corrosion of copper in supply waters. British Corrosion Journal 2, 175–187.

Lui T S, Chao C G, 1989. High-temperature properties of ferritic spheroidal graphite cast iron. Journal of Materials Science 24, 2503–2507.

Lundgren K, 2017. Radiation dose to water for an U-233 doped pellet compared to a long time decayed irradiated pellet. SKB R-17-08, Svensk Kärnbränslehantering AB.

Lytle D A, Nadagouda M N, 2010. A comprehensive investigation of copper pitting corrosion in a drinking water distribution system. Corrosion Science 52, 1927–1938.

Löfgren M, Sidborn M, 2018. Modelling of bounding corrosion rates of reactor pressure vessels in SFR due to earth currents. SKB R-16-14, Svensk Kärnbränslehantering AB.

MacDonald D D, Sharifi-Asl S, 2011. Is copper immune to corrosion when in contact with water and aqueous solutions? SSM Report 2011:09, Swedish Radiation Safety Authority.

Magnusson H, 2017. Thermodynamic evaluation of impurity elements in OFP copper. SKB R-17-20, Svensk Kärnbränslehantering AB.

Maier A C, Kegler P, Klinkenberg, M, Baena A, Finkeldei S, Brandt F, Jonsson M, 2020. On the change in UO_2 redox reactivity as a function of H_2O_2 exposure. Dalton Transactions 49, 1241–1248.

Manson S S, Haferd A M, 1953. A linear time-temperature relation for extrapolation of creep and stress-rupture data. Technical note 2890. Washington: National Advisory Committee For Aeronautics.

Mao F, Dong C, Sharifi-Asl S, Lu P, Macdonald D D, 2014. Passivity breakdown on copper:influence of chloride ion. Electrochimica Acta 144, 391–399.

Marion G M, Kargel J S, Catling D C, Jakubowski S D, 2005. Effect of pressure on aqueous chemical equilibria at subzero temperatures with applications to Europa. Geochimica et Cosmochimica Acta 69, 259–274.

Marja-aho M, Rajalaa P, Huttunen-Saarivirtaa E, Legat A, Kranjc A, Kosec T, Carpéna L, 2018. Copper corrosion monitoring by electrical resistance probes in anoxicgroundwater environment in the presence and absence of sulfatereducing bacteria. Sensors and Actuators A 274, 252–261.

Marsh G P, 1990. A preliminary assessment of the advanced cold process canister. Report AEA-InTec-0011, AEA Technology.

Martin G, Maillard S, Van Brutzel L, Garcia P, Dorado B, Valot C, 2009. A molecular dynamics study of radiation induced diffusion in uranium dioxide. Journal of Nuclear Materials 385, 351–357.

Martin O, Nilsson K-F, Jakšić N, 2009. Numerical simulation of plastic collapse of copper cast iron canister for spent nuclear fuel. Engineering Failure Analysis 16, 225–241.

Martino T, Chen J, Qin Z, Shoesmith D W, 2017. The kinetics of film growth and their influence on the susceptibility to pitting of copper in aqueous sulphide solutions. Corrosion Engineering, Science and Technology 52, 61–64.

Martino T, Smith J, Chen J, Quin Z, Noël J J, Shoesmith D W, 2019a. The properties of electro-chemically-grown copper sulphide films. Journal of The Electrochemical Society 166, C9–C18.

Martino T, Chen J, Guo M, Ramamurthy S, Shoesmith D W, Noël J J, 2019b. Comments on E. Huttunen-Saarivirtaet al. “Kinetic properties of the passive film on copper in the presence of sulfate-reducing bacteria” [J. Electrochem. Soc. 165 C450 (2018)]. Journal of The Electrochemical Society 166, Y13–Y16.

Martino T, Chen J, Nöel J J, Shoesmith D W, 2020. The effect of anions on the anodic formation of copper sulphide films on copper. Electrochimica Acta 331, 135319. doi:10.1016/j.electacta.2019.135319

Martinsson Å, Sandström R, 2012. Hydrogen depth profile in phosphorus-doped, oxygen-free copper after cathodic charging. Journal of Materials Science 47, 6768–6776.

Martinsson Å, Wu R, Sandström R, 2009. Influence of hydrogen on mechanical properties of nodular cast iron. KIMAB-2009-118, Swerea KIMAB AB, Sweden.

Martinsson Å, Andersson-Östling H C M, Seitisleam F, Wu R, Sandström R, 2010. Creep testing of nodular iron at ambient and elevated temperatures. SKB R-10-64, Svensk Kärnbränslehantering AB.

Martinsson Å, Sandström R, Lilja C, 2013. Hydrogen in oxygen-free, phosphorus-doped copper: charging techniques, hydrogen contents and modelling of hydrogen diffusion and depth profile. SKB TR-13-09, Svensk Kärnbränslehantering AB.

Matsuno K, Matsunaga H, Endo M, Yanase K, 2012. Effect of hydrogen on uniaxial tensile behaviour of a ductile cast iron. International Journal of Modern Physics: Conference Series 6, 407–412.

Matsuo T, 2017. The effect of pearlite on the hydrogen-induced ductility loss in ductile cast irons. Journal of Physics: Conference Series 843, 012012.

Matsunaga H, Usuda T, Yanase K, Endo M, 2014. Ductility loss in ductile cast iron with internal hydrogen. Metallurgical and Materials Transactions A 45, 1315–1326.

Matthiesen H, Hilbert L R, Gregory D J, 2003. Siderite as a corrosion product on archaeological iron from a waterlogged environment. Studies in Conservation 48, 183–194.

Matthiesen H, Hilbert L R, Gregory D, Sørensen B, 2007. Corrosion of archaeological iron artefacts compared to modern iron at the waterlogged site Nydam, Denmark. In Dillmann P, Piccardo P, Matthiesen H, Beranger G (eds). Corrosion of metallic heritage artefacts: investigation, conservation and prediction for long-term behaviour. Cambridge: Woodhead Publishing, 272–292.

Mattsson E, 1980. Corrosion of copper and brass: practical experience in relation to basic data. British Corrosion Journal 15, 6–13.

Mattsson E, 1988. Counteracting of pitting in copper water pipes by bicarbonate dosing. Materials and Corrosion 39, 499–503.

Mattsson H, Olefjord I, 1984. General corrosion of Ti in hot water and water saturated bentonite clay. SKB/KBS TR 84-19, Svensk Kärnbränslehantering AB.

Mattsson H, Olefjord I, 1990. Analysis of oxide formed on titanium during exposure in bentonite clay. I. The oxide growth. Materials and Corrosion 41, 383–390.

Mattsson H, Li C, Olefjord I, 1990. Analysis of oxide formed on Ti during exposure in bentonite clay. II. The structure of the oxide. Materials and Corrosion 41, 578–584.

Matzke H, Spino J, 1997. Formation of the rim structure in high burnup fuel. Journal of Nuclear Materials 248, 170–179.

Mazeina L, Navrotsky A, Greenblatt M, 2008. Calorimetric determination of energetics of solid solutions of UO_{2+x} with CaO and Y_2O_3. Journal of Nuclear Materials 373, 39–43.

McNeil M B, Little B J, 1992. Corrosion mechanisms for copper and silver objects in near-surface enviroments. Journal of the American Institute for Conservation 31, 355–366.

Miller M K, Russell K F, 2007. Embrittlement of RPV steels: an atom probe tomography perspective. Journal of Nuclear Materials 371, 145–160.

Milodowski A E, Styles M T, Werme L, Oversby V M, 2003. The corrosion of more than 176 million year old native copper plates from a deposit in mudstone in South Devon, United Kingdom. Paper 03681. In Corrosion 2003 (NACE International Conference), San Diego, 16–20 March 2003, 1–10.

Morco R P, Joseph J M, Hall D S, Medri C, Shoesmith D W, Wren J C, 2017. Modelling of radiolytic production of HNO_3 relevant to corrosion of a used fuel container in deep geologic repository environments. Corrosion Engineering, Science and Technology 52 sup1, 141–147.

Motta A T, Capolungo L, Chen L Q, Cinbiz M N, Daymond M R, Koss D A, Lacroix E, Pastore G, Simon P C A, Tonks M R, Wirth B D, 2019. Hydrogen in zirconium alloys: A review. Journal of Nuclear Materials 518, 440–460.

Muzeau B, 2007. Mecanismes de l'alteration sous eau du combustible irradie de type UOX. PhD thesis. University Paris XI.

Muzeau B, Jégou C, Delaunay F, Broudic V, Brevet A, Catalette H, Simoni E, Corbel C, 2009. Radiolytic oxidation of UO_2 pellets doped with alpha emitters ($^{238/239}Pu$). Journal of Alloys and Compounds 467, 578–589.

Nagra, 2002. Project Opalinus Clay. Safety report. Demonstration of disposal feasibility for spent fuel, vitrified high-level waste and long-lived intermediate-level waste (Entsorgungsnachweis). Nagra NTB-02-05, Nagra, Switzerland.

Naudet R, 1991. Oklo: des réacteurs nucléaires fossiles, étude physique. Paris: Commisariat à l'Énergie Atomique. (In French.)

Necib S, Bucur C, Caes S, Cochin F, Cvetković B Z, Fulger M, Gras J M, Herm M, Kasprzak L, Legand S, Metz V, Perrin S, Sakuragi T, Suzuki-Muresan T, 2018. Overview of ^{14}C release from irradiated zircaloys in geological disposal conditions. Radiocarbon 60, 1757–1771.

Neck V, Altmaier M, Seibert A, Yun J I, Marquardt C M, Fanghänel T, 2007. Solubility and redox reactions of Pu(IV) hydrous oxide: Evidence for the formation of PuO_{2+x}(s, hyd). Radiochimica Acta 95, 193–207.

Neff D, Dillmann P, Beranger G, 2003. An analytical study of corrosion products formed on buried ferrous archaeological artefacts. In Féron D, Macdonald D D (eds). Prediction of long term corrosion behaviour in nuclear waste systems (EFC 36). Leeds: Maney Publishing, 295–315.

Neff D, Dillmann P, Bellot-Gurlet L, Beranger G, 2005. Corrosion of iron archaeological artefacts in soil: characterisation of the corrosion system. Corrosion Science 47, 515–535.

Neff D, Dillmann P, Descostes M, Beranger G, 2006. Corrosion of iron archaeological artefacts in soil: estimation of the average corrosion rates involving analytical techniques and thermodynamic calculations. Corrosion Science 48, 2947–2970.

Neretnieks I, Johansson A J, 2013. Corrosion of the copper canister inside due to radiolysis of remaining water in the insert. SKBdoc 1419961 ver 1.0, Svensk Kärnbränslehantering AB.

Nicot J-P, 2008. Methodology for bounding calculations of nuclear criticality of fissile material accumulations external to a waste container at Yucca Mountain, Nevada. Applied Geochemistry 23, 2065–2081.

Nilsson K F, Lofaj F, Burström M, Andersson C-G, 2005. Pressure tests of two KBS-3 canister mock-ups. SKB TR-05-18, Svensk Kärnbränslehantering AB.

Nilsson S, Jonsson M, 2008. On the catalytic effect of Pd(s) on the reduction of UO_2^{2+} with H_2 in aqueous solution. Journal of Nuclear Materials 374, 290–292.

Nilsson S, Jonsson M, 2011. H_2O_2 and radiation induced dissolution of UO_2 and SIMFUEL pellets. Journal of Nuclear Materials 410, 89–93.

Nissen J, Gustafsson J, Sandström R, Wallin L, Taxén C, 2005. Forsmark site investigation. Some corrosion observations and electrical measurements at drill sites DS4, DS7 and DS8. SKB P-05-265, Svensk Kärnbränslehantering AB.

Nordström E, 2009. Fission gas release data for Ringhals PWRs. SKB TR-09-26, Svensk Kärnbränslehantering AB.

Northwood D O, Kosasih U, 1983. Hydrides and delayed hydrogen cracking in zirconium and its alloys. International Metals Reviews 28, 92–121.

Norris S, Capouet M, 2018. Overview of CAST Project. Radiocarbon 60, 1649–1656.

Ochs M, Talerico C, 2004. SR-Can. Data and uncertainty assessment. Migration parameters for the bentonite buffer in the KBS-3 concept. SKB TR-04-18, Svensk Kärnbränslehantering AB.

Odette G R, Lucas G E, 1998. Recent progress in understanding reactor pressure vessel steel embrittlement. Radiation Effects and Defects in Solids 144, 189–231.

Odette G R, Nanstad R K, 2009. Predictive reactor pressure vessel steel irradiation embrittlement models: issues and opportunities. JOM 61, 17–23.

Odorowski M, 2015. Étude de l'altération de la matrice $(U,Pu)O_2$ du combustible irradié en conditions de stockage géologique: Approche expérimentale et modélisation géochimique. PhD thesis. Mines Paris Tech, France. (In French.)

Odorowski M, Jégou C, De Windt L, Broudic V, Peuget S, Magnin M, Tribet M, Martin C, 2016. Oxidative dissolution of unirradiated Mimas MOX fuel (U/Pu oxide) in carbonated water unde oxic and anoxic conditions. Journal of Nuclear Materials 468, 17–25.

Odorowski M, Jégou C, De Windt L, Broudic V, Jouan G. Peuget S, Martin C, 2017. Effect of metallic iron on the oxidative dissolution of UO_2 doped with a radioactive alpha emitter in synthetic Callovo-Oxfordian water. Geochimica et Cosmochimica Acta 219, 1–21.

Okinaka Y, Straschil H K, 1986. Effect of inclusions on the ductility of electroless copper deposits. Journal of The Electrochemical Society 133, 2608–2615.

Olander D, 2004. Thermal spike theory of athermal diffusion of fission products due to alpha decay of actinides in spent fuel (UO_2). SKB TR-04-17, Svensk Kärnbränslehantering AB.

Oldberg K, 2009. Distribution of fission gas release in 10 × 10 fuel. SKB TR-09-25, Svensk Kärnbränslehantering AB.

Olin Å, Noläng B, Osadchii E, Öhman L, Rosen E, 2005. Chemical thermodynamics. Vol. 7. Chemical thermodynamics of selenium. Amsterdam: Elsevier.

Ollila K, 2006. Dissolution of unirradiated UO_2 and UO_2 doped with ^{233}U in 0.01 M NaCl under anoxic and reducing conditions. Posiva 2006-08, Posiva Oy, Finland.

Ollila K, 2008. Dissolution of unirradiated UO_2 and UO_2 doped with ^{233}U in low and high ionic strength NaCl under anoxic and reducing conditions. Posiva Working Report 2008-50, Posiva Oy, Finland.

Ollila K, Oversby V M, 2005. Dissolution of unirradiated UO_2 and UO_2 doped with ^{233}U under reducing conditions. SKB TR-05-07, Svensk Kärnbränslehantering AB.

Ollila K, Oversby V, 2006. Testing of uranium dioxide enriched with ^{233}U under reducing conditions. In Van Iseghem P (ed). Scientific Basis for Nuclear Waste Management XXIX. Warrendale, PA: Materials Research Society. (Materials Research Society Symposium Proceedings 932), 167–173.

Ollila K, Albinsson Y, Oversby V, Cowper M, 2003. Dissolution rates of unirradiated UO_2, UO_2 doped with ^{233}U, and spent fuel under normal atmospheric conditions and under reducing conditions using an isotope dilution method. SKB TR-03-13, Svensk Kärnbränslehantering AB.

Ollila K, Myllykylä E, Tanhua-Tyrkkö M, Lavonen T, 2013. Dissolution rate of alpha-doped UO_2 in natural groundwater. Journal of Nuclear Materials 442, 320–325.

Olsson P, Chang Z, Yousfi A, Thuvander M, Boizot B, Brysbaert G, Metayer V, Gorse-Pomonti D, 2013. Electron irradiation accelerated Cu-precipitation experiment. Testing of canister insert cast iron and an FeCu model alloy. SKB R-13-50, Svensk Kärnbränslehantering AB.

Olsson S, Jensen V, Johannesson L-E, Hansen E, Karnland O, Kumpulainen S, Kiviranta L, Svensson D, Hansen S, Lindén J, 2013. Prototype Repository. Hydro-mechanical, chemical and mineralogical characterization of the buffer and backfill material from the outer section of the Prototype repository. SKB TR-13-21, Svensk Kärnbränslehantering AB.

Ottosson M, Boman M, Berastegui P, Andersson Y, Hahlin M, Korvela M, Berger R, 2016. Copper in ultrapure water. SKB TR-16-01, Svensk Kärnbränslehantering AB.

Ottosson M, Boman M, Berastegui P, Andersson Y, Hahlin M, Korvela M, Berger R, 2017. Copper in ultrapure water, a scientific issue under debate. Corrosion Science 122, 53–60.

Oversby V M, 1996. Criticality in a high level waste repository. A review of some important factors and an assessment of the lessons that can be learned from the Oklo reactors. SKB TR 96-07, Svensk Kärnbränslehantering AB.

Oversby V M, 1998. Criticality in a repository for spent fuel: lessons from Oklo. In McKinley I G, McCombie C (eds). Scientific Basis for Nuclear Waste Management XXI. Warrendale, PA: Materials Research Society. (Materials Research Society Symposium Proceedings 506), 781–788.

Padovani C, Pletser D, Jurkschat K, Armstrong D, Dugdale S, Brunt D, Faulkner R, Was G, Johansson A J, 2019. Assessment of microstructural changes in copper due to gamma radiation damage. SKB TR-19-12, Svensk Kärnbränslehantering AB.

Panagopoulos C N, Zacharopoulos N, 1994. Cathodic hydrogen charging and mechanical properties of copper. Journal of Materials Science 29, 3843–3846.

Parasnis D S, 1997. Principles of applied geophysics. 5th ed. London: Chapman & Hall.

Parkhurst D L, Appelo C A J, 2013. Description of input and examples for PHREEQC version 3. U.S. Geological Survey Techniques and Methods, Book 6, Chap. A43. Denver, Colorado: U.S. Geological Survey; available only at http://pubs.usgs.gov/tm/06/a43.

Pastina B, LaVerne J A, 2001. Effect of molecular hydrogen on hydrogen peroxide in water radiolysis. Journal of Physical Chemistry A 105, 9316–9322.

Pastina B, Isabey J, Hickel B, 1999. The influence of water chemistry on the radiolysis of primary coolant water in pressurized water reactors. Journal of Nuclear Materials 264, 309–318.

Penny R K, Marriott D L, 1995. Design for creep. 2nd ed. London: Chapman & Hall.

Pers K, Sturek M, 2021. Produktionsrapport kapsel. SKBdoc 1407944 ver 2.0, Svensk Kärnbränslehantering AB. (In Swedish.) (Internal document.)

Phipps P B P, Rice D W, 1979. The role of water in atmospheric corrosion. In Brubaker G R, Phipps P B P (eds). Corrosion chemistry. Washington, D.C.: American Chemical Society. (ACS Symposium Series 89), 235–261.

Pinnel M R, Tompkins H G, Heath D E, 1979. Oxidation of copper in controlled clean air and standard laboratory air at 50 °C to 150 °C. Applications of Surface Science 2, 558–577.

Poinssot C, Ferry C, Poulesquen A, 2007. New perspectives for the spent nuclear fuel radionuclides release model in a deep geological repository. In Dunn D, Poinssot C, Begg B (eds). Scientific Basis for Nuclear Waste Management XXX. Warrendale, PA: Materials Research Society. (Materials Research Society Symposium Proceedings 985), 111–116.

Posiva SKB, 2017. Safety functions, performance targets and technical design requirements for a KBS-3V repository. Conclusions and recommendations from a joint SKB and Posiva working group. Posiva SKB Report 01, Posiva Oy, Svensk Kärnbränslehantering AB.

Posiva SKB, 2021. The Integrated Sulfide Project – Summary report. A collaboration project 2014–2018. Posiva SKB Report 09, Posiva Oy, Svensk Kärnbränslehantering AB.

Pourbaix M, Pourbaix A, 1992. Potential-pH equilibrium diagrams for the system S–H_2O from 25 to 150 °C: influence of access of oxygen in sulphide solutions. Geochimica et Cosmochimica Acta 56, 3157–3178.

Puigdomenech I, 2012. Hydrogeochemistry: SR-Site and comparative analysis. SKBdoc 1262945 ver 1.0, Svensk Kärnbränslehantering AB. (Internal document.)

Puigdomench I, Taxén C, 2000. Thermodynamic data for copper. Implications for the corrosion of copper under repository conditions. SKB TR-00-13, Svensk Kärnbränslehantering AB.

Puranen A, Barreiro A, Evins L Z, Spahiu K, 2017. Spent fuel leaching in the presence of corroding iron. MRS Advances 2, 681–686.

Puranen A, Roth O, Evins L Z, Spahiu K, 2018. Aqueous leaching of high burnup UO2 fuel under hydrogen conditions. MRS Advances 3, 1013–1018.

Puranen A, Barreiro Fidalgo A, Evins L Z, Spahiu K, 2020. Spent fuel corrosion and the effect of iron corrosion products – The effects of hydrogen generation and formation of iron corrosion products. Journal of Nuclear Materials 542, 152423.

Puranen A, Evins L Z, Barreiro A, Roth O, Spahiu K, 2022. Very high burnup spent fuel corrosion & leaching under hydrogen conditions. Journal of Nuclear Materials 572, 154027.

Pusch R, Karnland O, Lajudie A, Lechelle J, Bouchet A, 1992. Hydrothermal field test with French candidate clay embedded steel heater in the Stripa mine. SKB TR 93-02, Svensk Kärnbränslehantering AB.

Qin Z, Daljeet R, Ai M, Farhangi N, Noël J J, Ramamurthy S, Shoesmith D, King F, Keech P, 2017. The active/passive conditions for copper corrosion under nuclear waste repository environment. Corrosion Engineering and Technology 52, 45–49.

Rai D, Yui M, Moore D A, 2003. Solubility and solubility product at 22 °C of UO_2(c) precipitated from aqueous U(IV) solutions. Journal of Solid State Chemistry 32, 1–17.

Rand M, Fuger J, Grenthe I, Neck V, Rai D, 2009. Chemical thermodynamics of thorium. Paris: Nuclear Energy Agency, OECD.

Rard J A, Rand M H, Anderegg G, Wanner H, 1999. Chemical thermodynamics. Vol. 3. Chemical thermodynamics of technetium. Amsterdam: Elsevier.

Raynaud P, Bielen A, 2011. Cladding hydrogen based regulations in the United States. In 2011 Water Reactor Fuel Performance Meeting, Chengdu, China, 11–14 September 2011. Available at: http://citeseerx.ist.psu.edu/viewdoc/download?doi=10.1.1.740.4642&rep=rep1&type=pdf

Reed D T, Van Konynenburg R A, 1988. Effects of ionizing radiation on moist air systems. In Apted M J, Westerman R E (eds). Scientific basis for nuclear waste management XI. Pittsburgh, PA: Materials Research Society. (Materials Research Society Symposium Proceedings 112), 393–404.

Renström P, 2020a. Beräkningar av temperaturer i kopparhöljet och bufferten i förenklade parameterstudier. SKB R-19-27, Svensk Kärnbränslehantering AB. (In Swedish.)

Renström P, 2020b. Numerical study of the influence from deposited gamma radiation energy on canister temperature in the Spent Fuel Repository. SKB R-19-26, Svensk Kärnbränslehantering AB.

Reynaud A, 2009. Corrosion of cast irons. In Cottis B, Graham M, Lindsay R, Lyon S, Richardson T, Scantlebury D, Stott H (eds). Shreir's corrosion. 4th ed. Volume 3: Corrosion and degradation of engineering materials, 1737–1788.

Rice D W, Peterson P, Rigby E B, Phipps P B P, Cappel R J, Tremoureux R, 1981. Atmospheric corrosion of copper and silver. Journal of The Electrochemical Society 128, 275–284.

Robit-Pointeau V, Poinssot C, Vitorge p, Grambow B, Cui D, Spahiu K, Catalette H, 2006. Assessment of the relevance of coffinite formation within the near-field environment of spent nuclear fuel geological disposals. In Van Iseghem P (ed). Scientific Basis for Nuclear Waste Management XXIX. Warrendale, PA: Materials Research Society. (Materials Research Society Symposium Proceedings 932), 89–96.

Rodríguez-Villagra N, Riba O, Milena-Pérez A, Cobos J, Jimenez-Bonales L, Fernández-Carretero S, Coene E, Silva O, Duro L, 2022. Dopant effect on the spent fuel matrix dissolution of new advanced fuels: Cr-doped UO_2 and Cr/Al-doped UO_2. Journal of Nuclear Materials 568, 153880.

Romanoff M, 1989. Underground corrosion. Houston: NACE International.

Rondinella V, Wiss T, 2010. The high burnup structure in nuclear fuel, Materials today 13, 24–32.

Rondinella V V, Cobos J, Wiss T, 2004. Leaching behaviour of low-activity alpha-doped UO_2. In Hanchar J M, Stroes-Gascoyne S, Browning L (eds). Scientific Basis for Nuclear Waste Management XXVIII. Warrendale, PA: Materials Research Society. (Materials Research Society Symposium Proceedings 824), 167–173.

Roth O, 2015. A study of instant release fractions and matrix dissolution rate of two fuel samples irradiated in Olkiluoto 1. Posiva Working Report 2015-19, Posiva Oy, Finland.

Roth O, Jonsson M, 2008. Oxidation of UO_2 in aqueous solutions. Central European Journal of Chemistry 6, 1–14.

Roth O, Granfors M, Puranen A, Spahiu K, 2015. Release of ^{108}Ag from irradiated PWR control rod absorbers under deep repository. MRS Online Proceedings Library Archive 1744, 217–222.

Roth O, Cui D, Askeljung C, Puranen A, Evins L Z, Spahiu K, 2019. Leaching of spent nuclear fuels in aerated conditions: Influences of sample preparation on radionuclide release patterns. Journal of Nuclear Materials 527, 151789. doi:10.1016/j.jnucmat.2019.151789

Roth O, Askeljung C, Puranen A, Johnson K, Jädernäs D, Barreiro Fidalgo, A. Evins L Z, Spahiu K, 2021. Investigation of secondary phases formed during long-term aqueous leaching of spent nuclear fuel. MRS Advances 6, 90–94.

Rothman A J, 1984. Potential corrosion and degradation mechanisms of Zircaloy cladding on spent fuel in a tuff repository. Report UCID-20172, Lawrence Livermore National Laboratory.

Roudil D, Deschanels X, Trocellier P, Jégou C, Peuget S, Bart J-M, 2004. Helium thermal diffusion in a uranium dioxide matrix. Journal of Nuclear Materials 325, 148–158.

Roudil D, Jégou C, Broudic V, Muzeau B, Peuget S, Deschanels X, 2007. Gap and grain boundary inventories from pressurized water reactor spent fuels. Journal of Nuclear Materials 362, 411–415.

Roudil D, Bonhoure J, Pik R, Cuney M, Jégou C, Gauthier-Lafaye F 2008. Diffusion of radiogenic helium in natural uranium oxides. Journal of Nuclear Materials 378, 70–78.

Roy S K, Sircar S C, 1981. A critical appraisal of the logaritmic rate law in thin-film formation during oxidation of copper and its alloys. Oxidation of Metals 15, 9–20.

Saario T, Betova I, Heinonen J, Kinnunen P, Lilja C, 2004. Effect of the degree of compaction of bentonite on the general corrosion rate of copper. In Prediction of long term corrosion behaviour in nuclear waste systems. Proceedings of the 2nd International Workshop. Nice, 12–16 September 2004. ANDRA (Agence Nationale pour la Gestion des Déchets RadioActifs).

Sahiluoma P, Yagodzinskyy Y, Forsström A, Hänninen H, Bossuyt S, 2021. Hydrogen embrittlement of nodular cast iron. Materials and Corrosion 72, 245–254.

Salas J, Gimeno M J, Auqué L, Molinera J, Gómez J, Juárez I, 2010. SR-Site – hydrogeochemical evolution of the Forsmark site. SKB SKB TR-10-58, Svensk Kärnbränslehantering AB.

Sandberg N, Korzhavyi P, 2009. Theoretical study of irradiation induced hardening and embrittlement in spent nuclear fuel holders, relevant for the Swedish long-term storage. SKB R-09-15, Svensk Kärnbränslehantering AB.

Sandström R, 1999. Extrapolation of creep strain data for pure copper. Journal of Testing and Evaluation 27, 31–35.

Sandström R, 2012. Basic model for primary and secondary creep in copper. Acta Materialia 60, 314–322.

Sandström R, 2016. The role of cell structure during creep of cold worked copper. Materials Science & Engineering A 674, 318–327.

Sandström R, 2017. Formation of a dislocation back stress during creep of copper at low temperatures. Materials Science & Engineering A 700, 622–630.

Sandström R, Andersson H, 2008a. Creep in phosphorus alloyed copper during power-law breakdown. Journal of Nuclear Materials 372, 76–88.

Sandström R, Andersson H, 2008b. The effect of phosphorus on creep in copper. Journal of Nuclear Materials 372, 66–75.

Sandström R, Lousada C M, 2021. The role of binding energies for phosphorus and sulphur at grain boundaries in copper. Journal of Nuclear Materials 544, 152682. doi:10.1016/j.jnucmat.2020.152682

Sandström R, Sui F, 2021. Modeling of tertiary creep in copper at 215 and 250 °C. Journal of Engineering Materials and Technology 143, 031001. doi:10.1115/1.4049241.

Sarnet J, 2022. Några mätningar av segjärns åldring. SKB R-22-04, Svensk Kärnbränslehantering AB. (In Swedish.)

Schön J H, 1996. Physical properties of rock: fundamentals and principles of petrophysics. Oxford: Pergamon.

Science and Global Security, 1996. Vol. 5, No. 3, (Special issue).

Scott T B, Allen G C, Heard P J, Randel M G, 2005. Reduction of U(VI) to U(IV) on the surface of magnetite. Geochimica et Cosmochimica Acta 69, 5639–5646.

Senior N A, Newman R C, Abghari B, Keech P G, 2013. Influence of pH, temperature, and salinity upon anoxic copper corrosion. In Proceedings of 16th International Conference on Environmental Degradation of Materials in Nuclear Power Systems – Water Reactors, Asheville, North Carolina, 11–15 August 2013.

Senior N A, Newman R C, Artymowicz D, Binns W J, Keech P G, Hall D S, 2019. Communication – A method to measure extremely low corrosion rates of copper metal in anoxic aqueous media. Journal of The Electrochemical Society 166, C3015–C3017.

Senior N A, Martino T, Binns J, Keech P, 2021. The anoxic corrosion behaviour of copper in the presence of chloride and sulphide. Materials and Corrosion 72, 282–292.

Shoesmith D W, Zagidulin D, 2011. The corrosion of zirconium under deep geologic repository conditions. Journal of Nuclear Materials 418, 292–306.

Sidborn M, Sandström B, Tullborg E-L, Salas J, Maia F, Delos A, Molinero J, Hallbeck L, Pedersen K, 2010. SR-Site: Oxygen ingress in the rock at Forsmark during a glacial cycle. SKB TR-10-57, Svensk Kärnbränslehantering AB.

Silva R J, Bidoglio G, Rand M H, Robouch P B, Wanner H, Puigdomenech I, 1995. Chemical thermodynamics. Vol. 2. Chemical thermodynamics of americium. Amsterdam: Elsevier.

Simpson J P, 1984. Experiments on container materials for Swiss high-level waste disposal projects Part II. Nagra NTB 84-01, Nagra, Switzerland.

Simpson J P, Schenk R, 1987. Hydrogen evolution from corrosion of pure copper. Corrosion Science 27, 1365–1370.

Sipilä K, Arilahti E, Lehtikuusi T, Saario T, 2014. Effect of sulphide exposure on mechanical prop-erties of CuOFP. Corrosion Engineering, Science and Technology 49, 410–414.

SKB, 2006. Long-term safety for KBS-3 repositories at Forsmark and Laxemar – A first evaluation. Main report of the SR-Can project. SKB TR-06-09, Svensk Kärnbränslehantering AB.

SKB, 2010a. Fuel and canister process report.for the safety assessment SR-Site. SKB TR-10-46, Svensk Kärnbränslehantering AB.

SKB, 2010b. FEP report for the safety assessment SR-Site. SKB TR-10-45, Svensk Kärnbränslehantering AB.

SKB, 2010c. Handling of future human actions in the safety assessment SR-Site. SKB TR-10-53, Svensk Kärnbränslehantering AB.

SKB, 2010d. Spent nuclear fuel for disposal in the KBS-3 repository. SKB TR-10-13, Svensk Kärnbränslehantering AB.

SKB, 2010e. Corrosion calculations report for the safety assessment SR-Site. SKB TR-10-66, Svensk Kärnbränslehantering AB.

SKB, 2011. Long-term safety for the final repository for spent nuclear fuel at Forsmark. Main report of the SR-Site project. SKB TR-11-01, Svensk Kärnbränslehantering AB.

SKB, 2017. Svar till SSM på begäran om komplettering kring försprödningsmekanismer för kapseln. SKBdoc 1602500 ver 1.0, Svensk Kärnbränslehantering AB. (In Swedish.)

SKB, 2019a. Supplemetary information on canister integrity issues. SKB TR-19-15, Svensk Kärnbränslehantering AB.

SKB, 2019b. Referensutformning PSAR. SKBdoc 1178459 ver 5.0, Svensk Kärnbränslehantering AB. (In Swedish.) (Internal document.)

SKB, 2020. Post-closure safety for the final repository for spent nuclear fuel at Forsmark – Climate and climate related issues, PSAR version, SKB TR-20-12, Svensk Kärnbränslehantering AB.

SKB, 2022a. Post-closure safety for the final repository for spent nuclear fuel at Forsmark. Main report, PSAR version. SKB TR-21-01, Svensk Kärnbränslehantering AB.

SKB, 2022b. Post-closure safety for the final repository for spent nuclear fuel at Forsmark – Buffer, backfill and closure process report, PSAR version, SKB TR-21-03, Svensk Kärnbränslehantering AB.

SKB, 2022c. Post-closure safety for the final repository for spent nuclear fuel at Forsmark – Geosphere process report, PSAR version. SKB TR-21-04, Svensk Kärnbränslehantering AB.

SKB, 2022d. Post-closure safety for the final repository for spent nuclear fuel at Forsmark – Data report, PSAR version. SKB TR-21-06, Svensk Kärnbränslehantering AB.

SKB, 2022e. Post-closure safety for the final repository for spent nuclear fuel at Forsmark – Radionuclide transport report, PSAR version. SKB TR-21-07, Svensk Kärnbränslehantering AB.

SKB, 2021a. Använt kärnbränsle att hantera i KBS-3-systemet. SKBdoc 1380282 ver 3.0, Svensk Kärnbränslehantering AB. (In Swedish.) (Internal report.)

SKB, 2021b. Hantering av använt kärnbränsle inom KBS-3-systemet. SKBdoc 1380283 ver 2.0, Svensk Kärnbränslehantering AB. (In Swedish.) (Internal report.)

SKI, 2006. Engineered barrier system – Assessment of the corrosion properties of copper canisters. Report from a workshop at Lidingö, Sweden, April 27–29, 2005. SKI Report 2006:11, Swedish Nuclear Power Inspectorate.

Smart N R, Adams R, 2006. Natural analogues for expansion due to the anaerobic corrosion of ferrous materials. SKB TR-06-44, Svensk Kärnbränslehantering AB.

Smart N R, Rance A P, 2005b. Effect of radiation on anaerobic corrosion of iron. SKB TR-05-05, Svensk Kärnbränslehantering AB.

Smart N R, Blackwood D J, Werme L, 2002a. Anaerobic corrosion of carbon steel and cast iron in artificial groundwaters: Part 1 – Electrochemical aspects. Corrosion 58, 547–559.

Smart N R, Blackwood D J, Werme L, 2002b. Anaerobic corrosion of carbon steel and cast iron in artificial groundwaters: Part 2 – Gas generation. Corrosion 58, 627–637.

Smart N R, Rance A P, Fennell, P, Werme L, 2003. Expansion due to anaerobic corrosion of steel and cast iron: experimental and natural analogue studies. In Féron D, Macdonald D D (eds). Prediction of long term corrosion behaviour in nuclear waste systems (EFC 36). Leeds: Maney Publishing, 280–294.

Smart N R, Blackwood D J, Marsh G P, Naish C C, O'Brien T M, Rance A P, Thomas M I, 2004. The anaerobic corrosion of carbon and stainless steels in simulated cementitious environments: a summary review of Nirex research. Report AEAT/ERRA-0313, AEA Technology.

Smart N R, Rance A P, Fennell P A H, 2005. Galvanic corrosion of copper-cast iron couples. SKB TR-05-06, Svensk Kärnbränslehantering AB.

Smart N R, Rance A P, Fennell P A H, 2006. Expansion due to anaerobic corrosion of iron. SKB TR-06-41, Svensk Kärnbränslehantering AB.

Smart N, Rance A, Reddy B, Fennell P, Winsley R, 2012. Analysis of SKB MiniCan. Experiment 3. SKB TR-12-09, Svensk Kärnbränslehantering AB.

Smart N, Reddy B, Nixon D, Rance A, Johansson A J, 2015. A Miniature Canister (MiniCan) Corrosion experiment. Progress report 5 for 2008–2013. SKB P-14-19, Svensk Kärnbränslehantering AB.

Smith J M, Wren J C, Odziemkowski M, Shoesmith D W, 2007. The electrochemical response of pre-oxidized copper in aqueous sulfide solutions. Journal of The Electrochemical Society 154, C431–C438.

Soroka I L, Shchukarev A, Jonsson M, Tarakina N V, Korzhavyi P A, 2013. Cuprous hydroxide in a solid form: does it exist? Dalton Transactions 42, 9585–9594.

Soroka I, Chae N, Jonsson M, 2021. On the mechanism of γ-radiation-induced corrosion of copper in water. Corrosion Science 182, 109279. doi:10.1016/j.corsci.2021.109279

Spahiu K, 2012. Svar till SSM på begäran om komplettering om inverkan av vätgas på bränsle-upplösning. SKBdoc 1372969 ver 1.0, Svensk Kärnbränslehantering AB. (In Swedish.)

Spahiu K, 2021. Residual water and gases in a KBS-3 canister and their effect on post-closure safety. SKB TR-21-12, Svensk Kärnbränslehantering AB.

Spahiu K, Evins. L Z, 2013. Metal alloy particles in spent nuclear fuel. SKBdoc 1415408 ver 1.0, Svensk Kärnbränslehantering AB.

Spahiu K, Evins L Z, 2014. Svar till SSM på begäran om förtydligande angående bränsleupplösning. SKBdoc 1452302 ver 1.0, Svensk Kärnbränslehantering AB. (In Swedish.)

Spinks J W T, Woods R J, 1990. An introduction to radiation chemistry. 3rd ed. New York: Wiley.

Stefanescu D M (ed), 2017. ASM Handbook, Volume 1A – Cast Iron Science and Technology. Materials Park, Ohio: ASM International.

Stenlid J H, Soldemo M, Johansson A J, Leygraf C, Göthelid M, Weissenrieder J, Brinck T, 2016. Reactivity at the $Cu_2O(100)$:Cu–H_2O interface: a combined DFT and PES study. Physical Chemistry Chemical Physics 18, 30570.

Stenlid J H, Johansson A J, Leygraf C, Brinck T, 2017. Computational analysis of the early stage of cuprous oxide sulfidation: a top-down process. Corrosion Engineering, Science and Technology 52, 50–53.

Stroes-Gascoyne S, 1996. Measurements of instant-release source terms for ^{137}Cs, ^{90}Sr, ^{99}Tc, ^{129}I and ^{14}C in used CANDU fuels. Journal of Nuclear Materials 238, 264–277.

Stumm W, Morgan J J, 1996. Aquatic chemistry: chemical equilibria and rates in natural waters. 3rd ed. New York: Wiley.

Sui F, Sandström R, 2018. Basic modelling of tertiary creep of copper. Journal of Materials Science 53, 6850–6863.

Sui F, Sandström R, Wu R, 2018. Creep tests on notched specimens of copper. Journal of Nuclear Materials 509, 62–72.

Sundström R, Andersson-Östling H C M, Hagström J, 2020. Recrystallization of copper with phosphorus and Auger microscopy studies of the phosphorus content. SKB TR-20-07, Svensk Kärnbränslehantering AB.

Swanton S W, Baston G M N, Smart N R, 2015. Rates of steel corrosion and carbon-14 release from irradiated steels – state of the art review (D2.1). Deliverable in the FP7 Euratom project CAST.

Swedish Corrosion Institute, 1983. Corrosion resistance of a copper canister for spent nuclear fuel. SKBF/KBS TR 83-24, Svensk Kärnbränsleförsörjning AB.

Syrett B C, 1981. The mechanism of accelerated corrosion of copper-nickel alloys in sulphide-polluted seawater. Corrosion Science 21, 187–209.

Szakálos P, Hultquist G, Wikmark G, 2007. Corrosion of copper by water. Electrochemical and Solid-State Letters 10, C63–C67.

Szenknect S, Costin D T, Clavier N, Mesbah A, Poinssot C, Vitorge P, Dacheux N, 2013. From uranothorites to coffinite: a solid solution route to the thermodynamic properties of $USiO_4$. Inorganic Chemistry 52, 6957–6968.

Szenknect S, Mesbah A, Cordara T, Clavier N, Brau H P, Le Goff X, Poinssot C, Ewing R C, Dacheux N, 2016. First experimental determination of the solubility constant of coffinite. Geochimica et Cosmochimica Acta 181, 36–53.

Szenknect S, Dacheux N, Ewing R C, Navrotsky A, 2017. Reply to comment by Konings and Plyasunov on; First experimental determination of the solubility constant of coffinite;[Geochim. Cosmochim. Acta 181 (2016) 36–53]. Geochimica et Cosmochimica Acta 212, 374–376.

Szenknect S, Alby D, García M L, Wang C, Podor R, Miserque F, Mesbah A, Duro L, Evins L Z, Dacheux N, Bruno, J, Ewing R, 2020. Coffinite formation from UO_{2+x}. Scientific Reports 10, 12168.

Tait J C, Cornett R J J, Chant L A, Jirovec J, McConnell J, Wilkin D L, 1997. Determination of Cl impurities and 36Cl instant release from used CANDU fuels. In: Scientific Basis for Nuclear Waste Management XX, Eds: Triay I, Gray WJ. Proceedings of the Materials Research Society Symposium, Boston, USA, December 2–6 1996. MRS, Pittsburgh, Pennsylvania, 503–510.

Taniguchi N, Kawasaki M, 2008. Influence of sulfide concentration on the corrosion behavior of pure copper in synthetic seawater. Journal of Nuclear Materials 379, 154–161.

Tao S, Li D Y, 2008. Nanocrystallization effect on the surface electron work function of copper and its corrosion behaviour. Philosophical Magazine Letters 88, 137–144.

Taxén C, 2004. Atmospheric corrosion of copper 450 metres underground. Results from three years exposure in the Äspö HRL. In Oversby V M, Werme L O (eds). Scientific Basis for Nuclear Waste Management XXVII. Warrendale, PA: Materials Research Society. (Materials Research Society Symposium Proceedings 807), 423–428.

Taxén C, 2013. Ytprofiler på kopparkapslar från deponeringshål 5 och 6 i försöksserien Prototyp. SKB P-13-50, Svensk Kärnbränslehantering AB. (In Swedish.)

Taxén C, Sparr M, 2014. Corrosion properties of copper materials. SKB R-14-15, Svensk Kärnbränslehantering AB.

Taxén C, Lundholm M, Persson D, Jakobsson D, Sedlakova M, Randelius M, Karlsson O, Rydgren P, 2012. Analyser av koppar från prototypkapsel 5 och 6. SKB P-12-22, Svensk Kärnbränslehantering AB. (In Swedish.)

Taxén C, Strandberg B, Lilja C, 2014. Possible influence from stray currents from high voltage DC power transmission on copper canisters. SKB TR-14-15, Svensk Kärnbränslehantering AB.

Taxén C, Wickström L, Sparr M, 2017. Corrosion properties of cold worked or welded copper materials. SKB R-17-09, Svensk Kärnbränslehantering AB.

Taxén, C, Flyg J, Bergqvist H, 2018. Stress corrosion testing of copper in sulfide solutions. SKB TR-17-16, Svensk Kärnbränslehantering AB.

Taxén C, Flyg J, Bergqvist H, 2019. Stress corrosion testing of copper in near neutral sulfide solutions. SKB TR-19-13, Svensk Kärnbränslehantering AB.

Thomas L E, Guenther R J, 1989. Characterization of low-gas-release LWR fuels by transmission electron microscopy. In Lutze W, Ewing R C (eds). Scientific Basis for Nuclear Waste Management XII. Pittsburgh, PA: Materials Research Society. (Materials Research Society Symposium Proceedings 127), 293–300.

Thomas L E, Beyer C E, Charlot L A, 1992. Microstructural analysis of LWR spent fuels at high burnup. Journal of Nuclear Materials 188, 80–89.

Thunehed H, 2017. Compilation and evaluation of earth current measurements in the Forsmark area. SKB R-14-34, Svensk Kärnbränslehantering AB.

Thunehed H, 2018. Measurements of potential fields caused by earth currents and estimation of the bulk electric resistivity between deep boreholes at Forsmark. SKB P-18-06, Svensk Kärnbränslehantering AB.

Thunehed H, Pitkänen T, 2007. Forsmark site investigation Transient electromagnetic soundings at Forsmark and the regional surroundings Estimations of depth to saline groundwater. SKB P-07-165, Svensk Kärnbränslehantering AB.

Truche L, Berger G, Destrigneville C, Pages A, Guillaume D, Giffaut E, Jacquot E, 2009. Experimental reduction of aqueous sulphate by hydrogen under hydrothermal conditions: Implication for the nuclear waste storage. Geochimica et Cosmochimica Acta 73, 4824–4835

Trummer M, Jonsson M, 2010. Resolving the H_2 effect on radiation induced dissolution of UO_2 based spent nuclear fuel. Journal of Nuclear Materials 396, 163–169.

Trummer M, Nilsson S, Jonsson M, 2008. On the effects of fission product noble metal inclusions on the kinetics of radiation induced dissolution of spent nuclear fuel. Journal of Nuclear Materials 378, 55–59.

Trummer M, Roth O, Jonsson M, 2009. H_2 inhibition of radiation induced dissolution of spent nuclear fuel. Journal of Nuclear Materials 383, 226–230.

Tullborg E-L, Smellie J, Nilsson A-C, Gimeno M J, Brüchert V, Molinero J, 2010. SR-Site – sulphide content in the groundwater at Forsmark. SKB TR-10-39, Svensk Kärnbränslehantering AB.

Unosson M, 2016. Numerical simulation of earthquake induced rock shear through a deposition hole – Crack initiation and propagation in an insert with pre-existing intertubular and edge crack planes. SKBdoc 1474363 ver 1.0, Svensk Kärnbränslehantering AB.

Valls A, Grivé M., Riba O, Morales M, Spahiu K, 2014. Estimation of the long term helium production in high burn-up spent fuel due to alpha decay and consequences for the canister. MRS Online Proceedings Library Archive 1665, 297–302.

Van Brutzel L, Crocombette J-P, 2007. Atomic scale modelling of the primary damage state of irradiated UO_2 matrix. In Aktaa J, Samaras M, Serrano de Caro M, Victoria M, Wirth B (eds). Structural and refractory materials for fusion and fission technologies. Warrendale, PA: Materials Research Society. (Materials Research Society Symposium Proceedings 981E), JJ01-01.

Van Konynenburg R A, 1995. Comments on the draft paper "Underground supercriticality from plutonium and other fissile material" written by C. D. Bowman and F. Venneri (LANL). Report UCRL-ID-120990 COM, University of California.

Viertel M, 2016. Strålskärmsberäkningar för kopparkapslar innehållande BWR, MOX och PWR bränsleelement. Studsvik rapport 07-0014R Rev 2. SKBdoc 1077122 ver 4.0, Svensk Kärnbränslehantering AB.

Wada R, Nishimura T, Fujiwara K, Tanabe M, Mihara M, 1999. Experimental study on hydrogen gas generation rate from corrosion of Zircaloy and stainless steel under anaerobic alkaline conditions. In Proceedings of the 7th International Conference on Radioactive Waste Management and Environmental Remediation, ICEM '99. Nagoya, Japan, 26–30 September 1999. New York: American Society of Mechanical Engineers.

Wampler W R, Schober T, Lengeler B, 1976. Precipitation and trapping of hydrogen in copper. Philosophical Magazine 34, 129–141.

Weber J, Barthel J, Klinkenberg M, Bosbach D, Kruth M, Brandt F, 2017. Retention of ^{226}Ra by barite: The role of internal porosity. Chemical Geology 466, 722–732.

Wendel E, Gordon A, Johansson A J, Svensson D, Bergendal E, 2022. Analysis of corrosion products on filter housings in the Lasgit field experiment. SKB TR-22-01, Svensk Kärnbränslehantering AB.

Werme L O, Forsyth R S, 1988. Spent UO_2 fuel corrosion in water: release mechanisms. In Apted M J, Westerman R E (eds). Scientific basis for nuclear waste management XI. Pittsburgh, PA: Materials Research Society. (Materials Research Society Symposium Proceedings 112), 443–452.

Werme L O, Johnson L H, Oversby V M, King F, Spahiu K, Grambow B, Shoesmith D W, 2004. Spent fuel performance under repository conditions: a model for use in SR-Can. SKB TR-04-19, Svensk Kärnbränslehantering AB.

Wersin P, Kober F (eds), 2017. FEBEX-DP. Metal corrosion and iron–bentonite interaction studies. Nagra Arbeitsbericht NAB 16-16, Nagra, Switzerland.

Wersin P, Bruno J, Spahiu K, 1993. Kinetic modelling of bentonite – canister interaction. Implications for Cu, Fe and Pb corrosion in a repository for spent nuclear fuel. SKB TR 93-16, Svensk Kärnbränslehantering AB.

White A F, Brantley S L, 2003. The effect of time on the weathering of silicate minerals: why do weathering rates differ in the laboratory and field? Chemical Geology 202, 479–506.

White J H, Yaniv A E, Schick H, 1966. The corrosion of metals in the water of the Dead Sea. Corrosion Science 6, 447–460.

Wikramaratna R S, Goodfield M, Rodwell W R, Nash P J, Agg P J, 1993. A preliminary assessment of gas migration from the copper/steel canister. SKB TR 93-31, Svensk Kärnbränslehantering AB.

Wu R, Freeman A J, Olson G B, 1992. On the electronic basis of the phosphorus intergranular embrittlement of iron. Journal of Materials Research 7, 2403–2411.

Wu R, Ahlström J, Magnusson H, Frisk K, Martinsson Å, 2015. Charging, degassing and distribution of hydrogen in cast iron. SKB R-13-45, Svensk Kärnbränslehantering AB.

Xu H, Wang Y, 1999. Electron energy-loss spectroscopy (EELS) study of oxidation states of Ce and U in pyrochlore and uraninite – natural analogues for Pu- and U-bearing waste forms, Journal of Nuclear Materials 265, 117–123.

Yagodzinskyy Y, Malitckii E, Saukkonen T, Hänninen H, 2012. Hydrogen-enhanced creep and cracking of oxygen-free phosphorus-doped copper. Scripta Materialia 67, 931–934.

Yagodzinskyy Y, Malitckii E, Tuomisto F, Hänninen H, 2018. Hydrogen-induced strain localisation in oxygen-free copper in the initial stage of plastic deformation. Philosophical Magazine 98, 727–740.

Yang Q, Toijer E, Olsson P, 2019. Analysis of radiation damage in the KBS-3 canister materials. SKB TR-19-14, Svensk Kärnbränslehantering AB.

Yang Q, Yang Q, Chang Z, Messina L, Sandberg N, Castin N, Yousfi A, Toijer E, Thuvander M, Boizot B, Metayer V, Gorse-Pomonti D, Olsson P, 2022. Cu precipitation in electron-irradiated iron alloys for spent-fuel canisters. Journal of Nuclear Materials 572. doi:10.1016/j.jnucmat.2022.154038

Yin S, Li D Y, 2005. Effects of prior cold work on corrosion and corrosive wear of copper in HNO_3 and NaCl solutions. Materials Science and Engineering A 394, 266–276.

Yunker W H, 1990. Corrosion behavior of copper-base materials in a gamma-irradiated environment. Report WHC-EP-0188, Westinghouse Hanford Company, Richland, Washington.

Yunker W H, Glass R S, 1987. Long-term corrosion behaviour of copper-base materials in a gamma-irradiated environment. In Bates J K, Seefeldt W B (eds). Scientific basis for nuclear waste management X: symposium held in Boston, Massachusetts, USA, 1–4 December 1986. Pittsburgh, PA: Materials Research Society. (Materials Research Society Symposium Proceedings 84), 579–590.

Zwicky H-U, Low J, Ekeroth E, 2011. Corrosion studies with high burnup light water reactor fuel. Release of nuclides into simulated groundwater during accum lated contact time of up to two years. SKB TR-11-03, Svensk Kärnbränslehantering AB.

Zänker H, Hennig C, 2014. Colloid-borne forms of tetravalent actinides: a brief review. Journal of Contaminant Hydrology 157, 87–105.

Åkesson M, Laitinen H, 2022. Gas phase composition during the unsatured period, Status report June 2022. SKBdoc 1983850 ver 1.0, Svensk Kärnbränslehantering AB.

Åkesson M, Kristensson O, Börgesson L, Dueck A, Hernelind J, 2010. THM modelling of buffer, backfill and other system components. Critical processes and scenarios. SKB TR-10-11, Svensk Kärnbränslehantering AB.

Appendix A

Supporting calculations of copper corrosion

A1 Corrosion depth for general corrosion

The copper corrosion depth, d_{corr} for general corrosion can be calculated from the amount of corrodant according to

$$d_{corr} = \frac{N_i f_i M_{Cu}}{A_{corr} \rho_{Cu}} \qquad \text{A1-1}$$

where N_i is the amount of oxidant i, f_i is the stoichiometric factor for the corrosion reaction, M_{Cu} is the molar mass of copper, ρ_{Cu} is the density of copper and A_{corr} is area exposed to the corrosion attack.

The stochimetric factor is the amount Cu (in mol) corroded per mol oxidant

$$f_i = \frac{N_{Cu}}{N_i} \qquad \text{A1-2}$$

For calculations of corrosion with mass balances or simple mass transport evaluations, the summary reactions are used. Four different corrosion reactions are treated (or mentioned) in this report, with their respective accompanying stoichiometric factors:

In the early phase copper is corroded by oxygen, pessimistically assuming only oxidation to Cu(I)

$4Cu + O_2 \rightarrow 2Cu_2O$ $\qquad f_{O2} = 4$

The main corrosion reaction in the long-term is oxidation of water (protons) driven by stability of copper sulfide

$2Cu + HS^- + H^+ \rightarrow Cu_2S(s) + H_2$ $\qquad f_{HS} = 2$

Chloride in solution will form complexes with especially Cu(I) , so that oxidation by water (protons) is possible (with n=1, 2 or 3). The formation of Cu(II) complexes are much weaker and disregarded.

$Cu(s) + nCl^- + H^+ \rightleftarrows CuCl_n^{(n-1)-} + ½H_2$ $\qquad f_{Cl} = 1$

Copper can be oxidised by nitric acid, forming different NO or NO_2 species, depending on concentration. A pessimistic stoichiometry, $f_{HNO3} = 1$, is used.

A2 Initially entrapped oxygen

The corrosion from the initially entrapped oxygen is calculated with mass balances from the void filled with gas in the buffer and backfill. The initial state for the buffer and backfill is described in the PSAR Post-closure safety report (SKB 2022a), Section 5.5.3 and 5.6.3 giving the gas-filled pore volumes $V_{void,dephole} = 3.81$ m^3 and the $V_{void,backfill} = 25.70$ m^3/(6 m tunnel) respectively. The distance between canisters is 6 m according to SKB (2019b).

With 21 % oxygen in air and a gas molar volume of 0.0224 m^3/mol (at 273 K) this gives the amounts of oxygen for a deposition hole

$$N_{O2,dephole} = \frac{V_{dephole} \cdot 0.21}{0.0224 \ \frac{\text{m}^3}{\text{mol}}} = \frac{3.81 \ \text{m}^3 \cdot 0.21}{0.0224 \ \frac{\text{m}^3}{\text{mol}}} = 35.7 \ \text{mol} \qquad \text{A2-1}$$

The corresponding amounts of oxygen in the backfill in 6 m tunnel is 240.9 mol (see Table A2-1), with the sum being 277 mol. (The dissolved oxygen represents only a small fraction of that present in the gas phase and is ignored.) About 2 % (5.37/240.9 = 0.02) of the oxygen in the backfill would corrode the canister if the oxygen is diffusing outwards in all directions and only the part corresponding to the deposition hole area goes to the canister. Different assumptions could be made on how and where the oxygen is consumed, by corrosion or other processes. The corrosion depth assuming general corrosion is calculated from Eq A1-1, with $f_{O2} = 4$ (pessimistically assuming that copper is only oxidised

to Cu_2O) and different corroding areas, A_{corr}, according to Table A2-2. The resulting corrosion ranges from some tens of µm up to 3.2 mm, the latter for the most pessimistic case with all tunnel oxygen corroding the lid and upper part of the canister.

Table A2-1 Amount of oxygen entrapped in a deposition hole and in the backfill, available for corrosion of the canister.

	Void volume or expression, V_{void} [m³]	Amount of oxygen, N_{O2} [mol]
Deposition hole, incl. bevel	3.81	35.7
Backfill, 6 m tunnel	25.70	240.9
Backfill, 6 m, only part corresponding to dep. hole area	$\frac{\pi r_h^2}{6\times 2\left(w_t + h_t\right)} \times 25.70 = 0.572$	5.37

Table A2-2 Corrosion depth calculated as mass balances for corrosion of copper by entrapped oxygen, for different assumptions on oxygen consumption and transport.

Assumptions	Amount of oxygen, $N_{O2,dephole}$ [mol]	Corroding area, A_{corr}		Corrosion depth, d_{corr} [mm]
		Calculated as	Value [m²]	
All oxygen uniformly on all canister surface	276.7	$\pi\left(2r_{can}h_{can} + 2r^2_{can}\right)$	17.68	0.446
Tunnel oxygen on lid and 10 % of cylindrical surface	276.7	$\pi\left(0.1\times 2r_{can}h_{can} + r^2_{can}\right)$	2.46	3.20
Tunnel oxygen, only dep. hole area part of tunnel cross section, on lid + 10 % of cylindrical surface	5.37	$\pi\left(0.1\times 2r_{can}h_{can} + r^2_{can}\right)$	2.46	0.062
Deposition hole oxygen on cylindrical surface	35.7	$\pi 2r_{can}h_{can}$	15.9	0.064
Deposition hole oxygen, half diffusing outwards	17.9	$\pi 2r_{can}h_{can}$	15.9	0.032

A3 Nitric acid formation

Gamma irradiation of moist air in the canister-buffer gap leads to the formation of nitric acid, which could cause corrosion. Jones (1959) found that the formation of nitric acid was linear with the absorbed dose. The rate of its formation will be given by

$$\frac{dN_{HNO3}}{dt} = \frac{GV_{air}\rho_{air}D_0}{N_A}e^{-\ln 2\frac{t}{T_{1/2}}} \qquad \text{A3-1}$$

and the total amount of HNO_3 produced as a function of time

$$N_{HNO3} = \frac{GV_{air}\rho_{air}D_0}{N_A}\frac{T_{1/2}}{\ln 2}\left(1 - e^{-\ln 2\frac{t}{T_{1/2}}}\right) \qquad \text{A3-2}$$

where G is the G-value (in number of molecules/eV), V_{air} the irradiated air volume, ρ_{air} the density of the air, D_0 the initial dose rate outside the canister, N_A Avogadro's number, t the irradiation time and $T_{½}$ the half-life (years) of the radiation source.

The irradiated volume is taken as a gap of air, d_{gap}, between the canister and the buffer, giving a volume of

$$V_{air} = h_{can} \cdot \pi \left(\left(r_{can} + d_{gap} \right)^2 - r_{can}^2 \right) \qquad \text{A3-3}$$

A gap of 1 cm (d_{gap}=0.01 m) gives the volume 0.161 m^3. With an initial dose rate of 1 Gy/h assumed to decay as Cs-137 ($T_{½}$=30 year), and a G-value of 0.02 molecules/eV (from Jones 1959), Equation A3-2 would give a total production of 0.015 mol of nitric acid. This would, if consumed uniformly over the cylindric canister surface, correspond to a corrosion depth of 7 nm. A 1:1 stoichiometry for HNO_3 oxidising Cu to Cu(I) is assumed, i.e. f_{HNO3}=1 when using Eq. A1-1. The calculation is made for a pessimistic initial dose rate and should thus be regarded as a bounding estimate for the corrosion depth.

A4 Limit for corrosion in high chloride concentrations

The derivation of an updated limit for the criterion for corrosion by high chloride concentrations (Lilja et al. 2021) uses the same approach as earlier (SKB 2010a, Lilja 2013) where combinations of pH and chloride concentrations are sought so that the total copper concentration is below a specified value. The updating of the limit for the criterion takes into account:

- A total copper concentration of 10^{-6} mol/kg is used as the limit, and verified to not cause any canister failures, either for intact or eroded buffer. For this evaluation the mass transport models for sulfide corrosion used in SR-Site (SKB 2010e) were applied, with the appropriate stoichiometry (f_{Cl}=1 instead of f_{HS}=2). In earlier assessments this limit was more arbitrarily chosen from standard Pourbaix diagrams which commonly are drawn for a total concentration of 10^{-6} mol/L (or mol/kg, at low concentrations the difference is negligible).
- In SR-Site a simplified calculation was done for only the formation of the complex $CuCl_3^{2-}$ (SKB 2010a). In Lilja (2013), both $CuCl_2^-$ and $CuCl_3^{2-}$ were used. It was further shown how different copper concentrations limits as well as different models for activity coefficients could influence how to choose a suitable combination of pH and chloride concentration. For the criteria to be used in the PSAR a more complete thermodynamic speciation calculation was performed, using the software PHREEQC version 3.4 with the LLNL database (Parkhurst and Appelo 2013).
- The earlier, simplified calculations were also performed assuming a hydrogen gas pressure set to 1 atm, as also often is used in Pourbaix diagrams. In the updated speciation calculation no initial hydrogen is present, which causes the corrosion reaction to proceed further.

The choice of the LLNL database, among several databases available for PHREEQC, was based on an evaluation against data for the solubility of CuCl(s), for details see Lilja et al. (2021) and King et al. (2021). The different databases not only have their own set of species and reactions with equilibrium constants, but also different models for calculating activity coefficients. The databases Minteq.v4, Wateq4f and LLNL were compared to data from three published sets of data, see Figure A4-1. The chloride concentration and the ionic strength were varied separately in the experiments by using perchloric acid. For ionic strengths below 1 mol/kg and chloride concentrations below 0.3 mol/kg, all the 3 databases can be used, but at higher ionic strengths and chloride concentrations, the LLNL database reproduces the experimental data best. For lower copper concentrations, as for example the 10^{-6} mol/kg used in the PSAR, the difference between the databases are smaller, even at higher chloride concentrations.

Using PHREEQC with the LLNL database, a curve representing a total copper concentration of 10^{-6} mol/kg could be derived, see Figure A4-2. This will be used as the limit for the safety indicator criterion to avoid corrosion due to high chloride concentration. This approach is consistent with Posiva's handling of corrosion in high chloride concentration (King et al. 2021). Posiva is using the same thermodynamic data for their assessment, with the difference that the total copper concentration in water is calculated and various transport cases are evaluated to give corrosion rates.

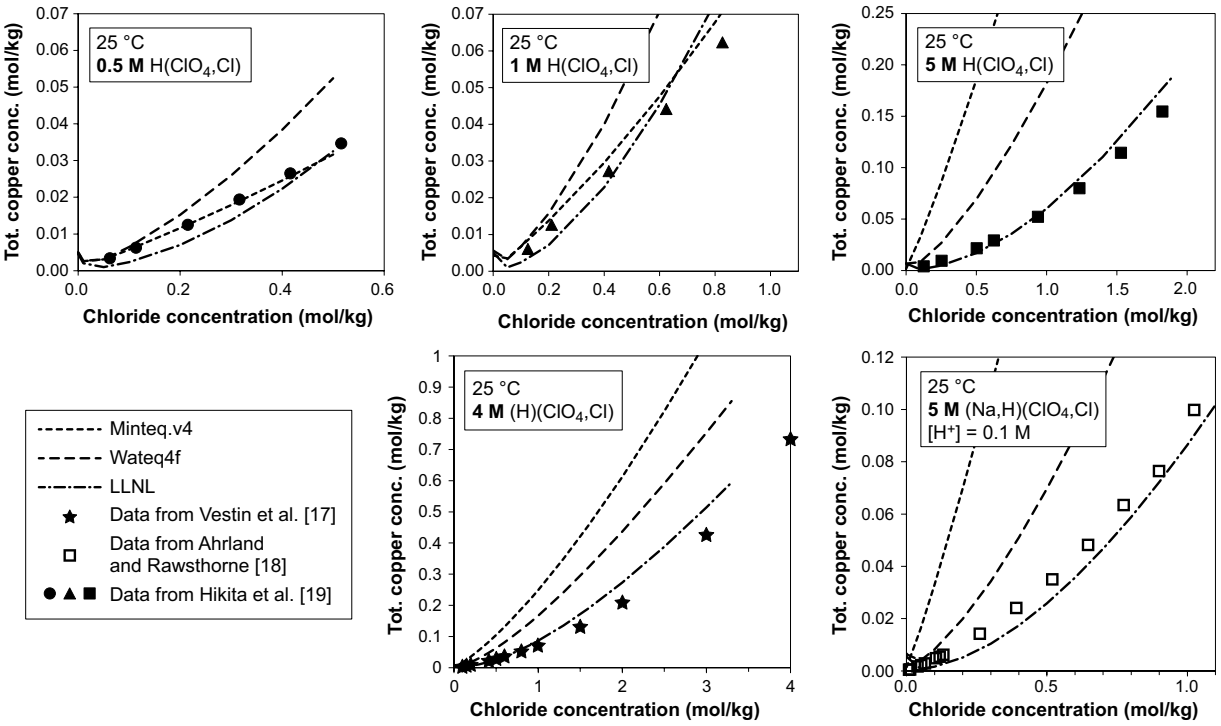

Figure A4-1. *Experimentally determined solubility of CuCl(s) in solutions with different ionic strengths, with varying amounts of added chloride, compared with PHREEQC calculations using the three investigated databases (Lilja et al. 2021).*

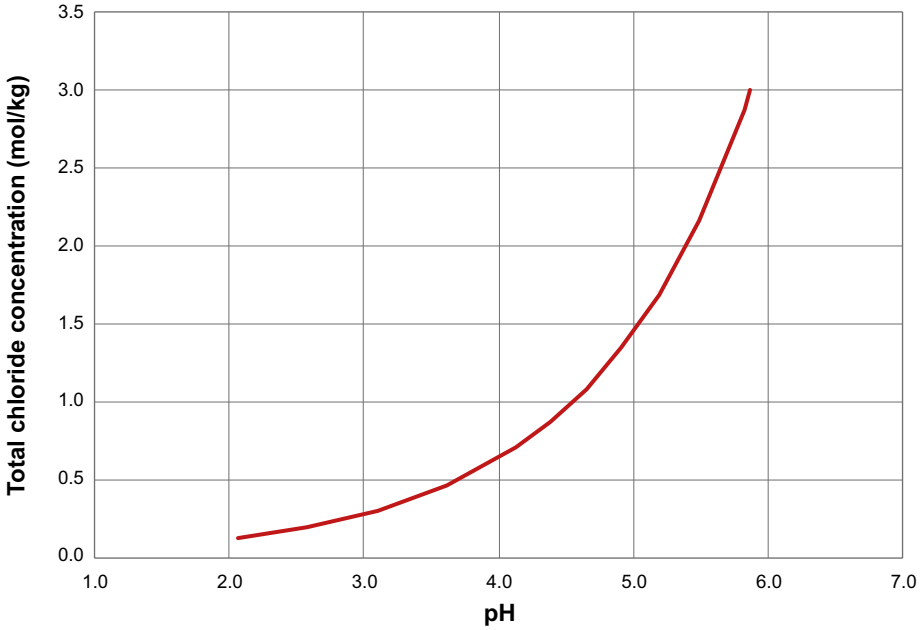

Figure A4-2. *Curve showing the combinations of pH and chloride concentration that gives a total copper concentration in the solution of 10^{-6} mol/kg, using PHREEQC with database LLNL (Parkhurst and Appelo 2013). The calculation is performed for 25 °C and no initial hydrogen in the solution.*

Appendix B

Notation and data used

Notation	Description	Data used		Notes	Reference
		Value	Unit		
A_{corr}	Area exposed to corrosion		m^2	Different assumptions	
A_{α}	Alpha activity per volume		Bq/m^3	Section 2.4.2	
d_{corr}	Corrosion depth		m	Calculated	
d_{FeCu}	Thickness of the gap between iron and copper	0.00175	m	Pessimistically including tolerances when calculated from outer diameter of insert and inner diameter of copper shell.	Pers and Sturek (2021)
d_{gap}	Air gap between canister and buffer	0.01	m	Calculated from inner diameter of the ring-shaped bentonite blocks and canister outer diameter	SKB (2022a, Section 5.5.2)
D_0	Initial dose rate	1	Gy/h		Posiva SKB (2017)
D_{FeCu}	Average canister diameter for the gap between iron and copper	0.9505	m	Calculated from nominal values of outer diameter of insert and inner diameter of copper shell.	Pers and Sturek (2021)
D_{α}	Diffusion coefficient accelerated by α self-irradiation		m^2/s	Section 2.4.2	
f_i	Stoichiometric factor (amount of Cu (in mol) per mol oxidant)		–	Various values, see Appendix A1	
G	G-value	0.02	molecules/eV		Jones (1959)
h_{can}	Height of the canister	4.835	m		Pers and Sturek (2021)
h_t	Height of tunnel	4.8	m		SKB (2019b)
k_{eff}	Effective neutron multiplication factor			Section 2.1.3	
L_{fuel}	Length of fuel elements generating the heat	3.68	m		Ikonen (2006)
M_{Cu}	Molar mass of copper	63.55	g/mol		
N_A	Avogadro's number	6.022×10^{23}	molecules/mol		
N_i	Amount of specie *i*		mole	Calculated	
P	Power output from the canister	1700	W		SKB (2022a, Section 5.3.4)
r_{can}	Radius of the canister	0.525	m		Pers and Sturek (2021)
r_h	Radius of the deposition hole	0.875	m		SKB (2022a, Section 5.5.2)
t	Time		year	General	
$T_{1/2}$	Half life	30	year	For Cs-137	SKB (2022d, Table 3-5)

Notation	Description	Data used		Notes	Reference
		Value	Unit		
T_{Cu}	Temperature in the copper	375	K	Pessimistic value used in SR-Site	SKB (2011, Section 10.3.13)
T_{Fe}	Temperature in the iron		K	Calculated	
V_{air}	Irradiated volume of air		m^3	Calculated	
V_{void}	Gas-filled initial pore volume in buffer or backfill		m^3	Various assumtions	
w_t	Tunnel width	4.2	m		SKB (2019b)
ε_{tot}	Combined emissivity of the two materials in the gap			$\varepsilon_{tot} = \frac{1}{\frac{1}{\varepsilon_{Fe}} + \frac{1}{\varepsilon_{Cu}} - 1}$ $\varepsilon_{Fe} = 0.6$; $\varepsilon_{Cu} = 0.02$	Ikonen (2006) Value for copper emissivity assumed for highly polished copper
ρ_{air}	Density of air	1.184	kg/m^3		
ρ_{Cu}	Density of copper	8 920	kg/m^3	The same value used in corrosion and criticality analyses	Pers and Sturek (2021)
σ	Stefan-Boltzmann constant	5.6697×10^{-8}	$W/(m^2K^4)$		Hedin (2004)
λ_{gas}	Thermal conductivity of the gas in the gap	0.0178	W/m,K	For argon	Ikonen (2006)

Arkitektkopia AB, Bromma, 2022

SKB is responsible for managing spent nuclear fuel and radioactive waste produced by the Swedish nuclear power plants such that man and the environment are protected in the near and distant future.

skb.se